ΕΘΝΙΚΟ ΜΕΤΣΟΒΙΟ ΠΟΛΥΤΕΧΝΕΙΟ
ΣΧΟΛΗ ΕΦΑΡΜΟΣΜΕΝΩΝ ΜΑΘΗΜΑΤΙΚΩΝ
ΚΑΙ ΦΥΣΙΚΩΝ ΕΠΙΣΤΗΜΩΝ

Αριθμητικές εφαρμογές καταστατικών προσομοιώσεων εντός του πλαισίου Κρίσιμης Κατάστασης Εδαφομηχανικής με προσανατολισμένη δομή

ΔΙΔΑΚΤΟΡΙΚΗ ΔΙΑΤΡΙΒΗ

ΑΛΕΞΑΝΔΡΟΥ Ι. ΘΕΟΧΑΡΗ

Διπλωματούχου Πολιτικού Μηχανικού Ε.Μ.Π.

ΕΠΙΒΛΕΠΩΝ:

Ι. Φ. ΔΑΦΑΛΙΑΣ

Ομ. Καθηγητής Ε.Μ.Π.

Αθήνα, Ιούνιος 2017

ΕΘΝΙΚΟ ΜΕΤΣΟΒΙΟ ΠΟΛΥΤΕΧΝΕΙΟ
ΣΧΟΛΗ ΕΦΑΡΜΟΣΜΕΝΩΝ ΜΑΘΗΜΑΤΙΚΩΝ
ΚΑΙ ΦΥΣΙΚΩΝ ΕΠΙΣΤΗΜΩΝ

Αριθμητικές εφαρμογές καταστατικών προσομοιώσεων εντός του πλαισίου Κρίσιμης Κατάστασης Εδαφομηχανικής με προσανατολισμένη δομή

ΔΙΔΑΚΤΟΡΙΚΗ ΔΙΑΤΡΙΒΗ

ΑΛΕΞΑΝΔΡΟΥ Ι. ΘΕΟΧΑΡΗ

Διπλωματούχου Πολιτικού Μηχανικού Ε.Μ.Π.

ΤΡΙΜΕΛΗΣ ΣΥΜΒΟΥΛΕΥΤΙΚΗ ΕΠΙΤΡΟΠΗ

1. Ι. ΔΑΦΑΛΙΑΣ
2. Γ. ΜΠΟΥΚΟΒΑΛΑΣ
3. Α. ΠΑΠΑΔΗΜΗΤΡΙΟΥ

ΕΠΤΑΜΕΛΗΣ ΕΞΕΤΑΣΤΙΚΗ ΕΠΙΤΡΟΠΗ

1. Ι. ΔΑΦΑΛΙΑΣ
2. Γ. ΜΠΟΥΚΟΒΑΛΑΣ
3. Α. ΠΑΠΑΔΗΜΗΤΡΙΟΥ
4. Ε. Ε. ΘΕΟΤΟΚΟΓΛΟΥ
5. Ε. ΚΟΝΤΟΥ - ΔΡΟΥΓΚΑ
6. F. DARVE
7. G. VIGGIANI

Αθήνα, Ιούνιος 2017

General Contents

Περίληψη

Η Θεωρία Κρίσιμης Κατάστασης (ΘΚΚ) είναι κυρίαρχη στον τομέα της Εδαφομηχανικής και στην κοινότητα που ασχολείται με τα κοκκώδη υλικά, ήδη από την θεμελίωση της πριν από 60 χρόνια. Αποτελεί το κύριο πλαίσιο για τα περισσότερα καταστατικά προσομοιώματα των κοκκωδών και εδαφικών υλικών καθώς προβλέπει την κρίσιμη και σταθερή κατάσταση (critical and steady state) στην οποία τα υλικά αυτά φτάνουν μετά από εκτεταμένη παραμόρφωση, κατά τη διάρκεια φόρτισής τους. Η βάση της ΘΚΚ συντίθεται από δυο ικανές και αναγκαίες συνθήκες για την επίτευξη και διατήρηση της κρίσιμης κατάστασης, με την πρώτη να προσδιορίζει τον αποκλίνοντα λόγο τάσεων ως σταθερά του υλικού και την δεύτερη να ορίζει τον δείκτη πόρων ως μοναδική συνάρτηση της ισοτροπικής τάσης. Η ΘΚΚ υποθέτει ότι σε αυτήν την οριακή κατάσταση το υλικό δεν διαθέτει σημαντική εσωτερική δομή, καθώς δεν αναφέρεται καθόλου σε αυτή. Μολαταύτα, σύγχρονες έρευνες υποστηρίζουν ότι μία εξαιρετικά ισχυρή ανισοτροπία ενυπάρχει κατά την ΚΚ, λόγω της προσανατολισμένης εσωτερικής δομής του, και επιδρά σημαντικά στη συμπεριφορά του υλικού.

Η διατριβή είναι κυρίως επικεντρωμένη στην δομή των κοκκωδών υλικών και συγκεκριμένα, των γεωυλικών. Αν και η εσωτερική δομή του εδάφους (fabric) αποτελεί ένα από τα πλέον σημαντικά χαρακτηριστικά για την μηχανική απόκρισή του, εκτεταμένη έρευνα γύρω από το θέμα εμφανίζεται μόλις τις τελευταίες δύο δεκαετίες. Το έδαφος, παρότι αποτελεί κοκκώδες υλικό, στην έρευνα και στην πράξη συνηθίζεται να προσομοιώνεται και να εξετάζεται με βάση τις θεωρίες συνεχούς μέσου. Αυτό σημαίνει ότι η εσωτερική δομή του, και ειδικά ο προσανατολισμός αυτής, που επιδρά σημαντικά στην μακροσκοπική απόκριση του εδάφους, δεν λαμβάνεται υπόψη, ή σε κάποιες περιπτώσεις λαμβάνεται υπόψη αλλά όχι επαρκώς.

Ο προσανατολισμός της εσωτερικής δομής και η σχέση της με την μηχανική συμπεριφορά της άμμου εμφανίζεται τόσο σημαντική, ώστε εδώ και 5 χρόνια έχει προταθεί μία νέα θεωρία, η Θεωρία Ανισοτροπικής Κρίσιμης Κατάστασης (ΘΑΚΚ), η οποία τροποποιεί την αρχική ΘΚΚ προσθέτοντας μία επιπλέον συνθήκη σχετική με την εσωτερική δομή του υλικού και την κατεύθυνση φόρτισης ως ένα απαραίτητο βήμα, για να γίνει η θεωρία πλήρης. Η ΘΑΚΚ έχει χρησιμοποιηθεί με μεγάλη επιτυχία ως ένα γενικό πλαίσιο καταστατικών προσομοιωμάτων και η προσθήκη της συνθήκης εσωτερικής δομής στο πλαίσιο της ΘΑΚΚ δίδει ευελιξία και ιδιαίτερες δυνατότητες στα προσομοιώματα που τη χρησιμοποιούν. Όμως, παρόλη την αυξημένη ακρίβεια και εφαρμοσιμότητά της, η νέα αυτή θεωρία δεν έχει αποδειχθεί ότι ισχύει αυτόνομα ως θεωρία μέχρι σήμερα. Η αιτία είναι ότι πολύ ειδικές πειραματικές συνθήκες πρέπει να συντρέχουν, ώστε να μπορεί να εξεταστεί κατά πόσον η αναφερόμενη ΘΑΚΚ είναι απαραίτητο συμπλήρωμα της ΘΚΚ, καθώς σε τυπικές συνθήκες φόρτισης (π.χ. κλασική τριαξονική φόρτιση) η ΘΚΚ εμφανίζεται πλήρης και η επιπλέον συνθήκη ικανοποιείται ταυτόχρονα με τις δυο προαναφερθείσες αρχικές κλασσικές συνθήκες της ΘΚΚ. Όμως, για διαφορετικές και πιο σύνθετες, αλλά φυσικές και συχνά εμφανιζόμενες διαδρομές

φόρτισης (π.χ. στροφή των κυρίων αξόνων των τάσεων), είναι πολύ δύσκολο να ελεγχθεί εάν οι συνθήκες της ΘΚΚ είναι πλήρεις, με την έννοια του αν είναι αναγκαίες και ικανές.

Στη παρούσα έρευνα χρησιμοποιήθηκε η Μέθοδος Διακριτών Στοιχείων (ΜΔΣ), μία σύγχρονη μέθοδος με την οποία μπορεί να προσομοιωθεί ένα κοκκώδες υλικό στην διακριτή του φύση. Πραγματοποιήθηκαν καινοτόμα αριθμητικά πειράματα τριών σταδίων φόρτισης (τριών φάσεων) σε δύο και τρεις διαστάσεις με τα οποία αποδείχθηκε ότι η ΘΚΚ είναι πράγματι μη πλήρης.

Το αριθμητικό δείγμα έφτασε αρχικά στην Κρίσιμη Κατάσταση (ΚΚ) κατά τη φάση 1 και κατόπιν επιβλήθηκε η στροφή των κύριων αξόνων (ΚΑ) της τάσης, διατηρώντας σταθερές τις κύριες τιμές των τάσεων κατά τη φάση 2. Η στροφή των ΚΑ προκάλεσε μείωση του δείκτη πόρων και, κατά συνέπεια, εγκατάλειψη της ΚΚ, παρά το γεγονός ότι οι δύο συνθήκες της ΘΚΚ ικανοποιούνταν κατά την έναρξη της διαδικασίας. Η πρόσφατα προταθείσα ΘΑΚΚ θεραπεύει αυτή την ατέλεια της ΘΚΚ συμπληρώνοντας τις δύο συνθήκες με μία τρίτη, η οποία σχετίζεται με την κρίσιμη κατάσταση της ανισοτροπίας της δομής. Αυτή η τρίτη συνθήκη παραβιάζεται από την στροφή των ΚΑ των τάσεων και μπορεί να εξηγήσει την προαναφερθείσα μείωση του δείκτη πόρων και επομένως την απομάκρυνση από την ΚΚ.

Μια επιπλέον τρίτη φάση, παρόμοια με την αρχική τριαξονική ακτινική διαδρομή των τάσεων της φάσης 1, εφαρμόζεται στο δείγμα σε διάφορα στάδια της φάσης 2. Συμπεραίνεται ότι ο δείκτης πόρων αδιαμφισβήτητα επιστρέφει στην κρίσιμη τιμή μαζί με τον αποκλίνοντα λόγο τάσεων, ο οποίος, αφού φτάσει μία μέγιστη τιμή, επιστρέφει και αυτός στην κρίσιμη τιμή του. Η ΘΑΚΚ μπορεί επίσης να εξηγήσει την απόκριση του δείγματος κατά τη δεύτερη και την τρίτη φάση φόρτισης, τα χαρακτηριστικά των οποίων δεν μπορούν να αντιμετωπιστούν από την κλασσική ΘΚΚ, που δεν λαμβάνει υπόψη την ανισοτροπία της δομής. Αυτές οι φάσεις φόρτισης έχουν εφαρμοστεί και μπορούν να συγκριθούν σε 2 και 3 διαστάσεις, παρέχοντας ποιοτικά τους ίδιους μηχανισμούς, ενώ η 3Δ ανάλυση παρέχει επίσης αποτελέσματα ποσοτικά συγκρίσιμα με πραγματικές άμμους.

Συμπερασματικά, μετά από το αριθμητικό πείραμα που πραγματοποιήθηκε με τη ΜΔΣ, οι τρεις συνθήκες της ΘΑΚΚ κρίνονται αναγκαίες και ικανές για την επίτευξη και διατήρηση της ΚΚ. Επιπλέον επιβεβαιώνεται η εγκυρότητα της πρόσθετης προτεινόμενης συνθήκης και η ΘΑΚΚ αποδεικνύεται πιο ακριβής και πλήρης θεωρία για την περιγραφή και την πρόβλεψη της γενικής συμπεριφοράς του εδάφους.

Εκτεταμένη περίληψη

Ευχαριστίες

Θα ήθελα να εκφράσω την ευγνωμοσύνη μου σε όλους όσους συνέβαλαν με διάφορους τρόπους, όλα αυτά τα χρόνια, για να ολοκληρωθεί η παρούσα εργασία.

Καταρχάς θα ήθελα να ευχαριστήσω εγκαρδίως τον επιβλέποντα καθηγητή Ιωάννη Δαφαλιά, για τη συνεχή υποστήριξή του και την καθοδήγηση κατά τη διάρκεια της διδακτορικής μου διατριβής, αλλά και για την ευκαιρία να διεξαγάγω έρευνα μαζί του. Δεν θα μπορούσα να ελπίζω σε έναν καλύτερο επιβλέποντα, τόσο από την πλευρά της επιστημονικής αριστείας, όσο και από την άποψη του χαρακτήρα. Ευχαριστώ επίσης τον καθηγητή Γιώργο Μπουκοβάλα που υπήρξε ανεκτίμητος δάσκαλος και φίλος εδώ και πολλά χρόνια, από το προπτυχιακό μου δίπλωμα. Οι ειλικρινείς ευχαριστίες μου και στον καθηγητή Αχιλλέα Παπαδημητρίου, για την πολύ παραγωγική συνεργασία που είχαμε και τα εξαιρετικά σχόλια και προτάσεις του. Επίσης, ευχαριστώ ιδιαιτέρως τον καθηγητή Cino Viggiani για την εμπνευστική παρουσία του και τα σχόλιά του και για την καθηγήτρια Μαρίνα Πανταζίδου για την καθοδήγησή της.

Επιπροσθέτως ευχαριστώ πολύ τον Δρ. Μανώλη Βαϊρακτάρη για τη συνεχή παρουσία του, τις παρατηρήσεις, τα σχόλια και τις προτάσεις του και γενικότερα για την εξαιρετική συνεργασία που είχαμε.

Θέλω να εκφράσω την εκτίμηση μου στην ερευνητική ομάδα του εργαστηρίου των γεωϋλικών και την ομάδα του SOMEF. Ιδιαιτέρως ευχαριστώ τον Αλέξανδρο και τον Νίκο, τον Κώστα και την Μυρσίνη για όλες τις στιγμές εργασίας και διασκέδασης που περάσαμε μαζί, και τον Γιάννη για τη φιλία του και τη συνδρομή του τα τελευταία χρόνια. Πολύ ευχαριστώ τους φίλους μου και ιδιαίτερα τους Πέτρο, Κυριάκο, Παναγιώτη, Θοδωρή, και Σωτήρη, για όλες τις στιγμές που περάσαμε μαζί. Ένα ιδιαίτερο ευχαριστώ στον δάσκαλό μου της κιθάρας Morten και στην Τίνα και στον Δημήτρη για την υποστήριξή τους.

Αυτό το έργο δεν θα είχε υλοποιηθεί χωρίς την υποστήριξη των γονέων μου, στους οποίους αξίζει επίσης να αποδοθούν εύσημα για αυτό το επίτευγμα. Τους ευχαριστώ για όλη τους τη φροντίδα, τις προσπάθειες, την έμπνευση και την ενθάρρυνση. Επιπλέον, ευχαριστώ από καρδιάς τη γιαγιά μου, την αδελφή μου και τον αδελφό μου. Τέλος, ευχαριστώ την Ελίνα για την αγάπη της, την ηθική αλλά και πρακτική υποστήριξη της, και τη Σάλλυ που έκανε την κάθε μέρα καλύτερη.

Η έρευνα που οδήγησε σε αυτά τα αποτελέσματα χρηματοδοτήθηκε από το Ευρωπαϊκό Συμβούλιο Έρευνας (European Research Council) στα πλαίσια του έβδομου πλαισίου-προγράμματος της Ευρωπαϊκής Ένωσης FP7-ERC-IDEAS Advanced Grant Agreement n° 290963 (SOMEF). Ευχαριστώ το ΕΣΕ για αυτήν την υποστήριξη.

Αφιέρωση

Στους γονείς μου …

1. Εισαγωγή

Το έδαφος είναι ένα κοκκώδες υλικό ιδιαίτερου ενδιαφέροντος, το οποίο, δεδομένης της εμφάνισής του στην επιφάνεια της Γης, έχει ονομαστεί «το δέρμα της Γης» (Miller, 1953). Το έδαφος είναι κυριολεκτικά η βάση κάθε βήματος μας, αποτελεί το θεμέλιο της σύγχρονης ανθρώπινης ζωής και, επομένως, δικαίως αποδίδεται ιδιαίτερη σημασία στη συμπεριφορά του. Συνιστά ένα κρίσιμο υλικό για την κατασκευή, την εξόρυξη, τις κατολισθήσεις και γενικά για σχεδόν όλες τις πτυχές της σύγχρονης υποδομής και της οικονομικής ανάπτυξης. Επιπλέον χρησιμεύει ως βάση θεμελίωσης για τις περισσότερες κατασκευές, αποτελεί το περιβάλλον για τις επιφανειακές και βαθιές εξορύξεις και είναι το κύριο δομικό υλικό για υποδομές, όπως δρόμους και φράγματα. Το πλέον σημαντικό είναι ότι τα εδαφικά υλικά είναι σε πολλές περιπτώσεις τα κρίσιμα αίτια για αστοχίες μεγάλης κλίμακας και αντίστοιχες καταστροφές, όπως μεγάλες κατολισθήσεις και αστοχίες επιχωμάτων. Είναι ζωτικής σημασίας για την ανάπτυξη και, συχνά, την επιβίωση των ανθρώπων, η βελτίωση της κατανόησης και της ακριβούς πρόβλεψης της μηχανικής συμπεριφοράς του εδάφους.

Ορόσημο στην ανάλυση και προσομοίωση της μηχανικής συμπεριφοράς του εδάφους, υπήρξε η δημιουργία της Θεωρίας Κρίσιμης Κατάστασης - ΘΚΚ (Critical State Theory). Οι Roscoe, Schofield και Wroth (1958) και οι Schofield και Wroth (1968) πρότειναν ένα γενικό πλαίσιο με εφαρμογή τόσο σε αργίλους, όσο και σε άμμους (οι δύο κύριοι τύποι εδαφικών υλικών), για την ευσταθή κατάσταση που αυτές επιτυγχάνουν μετά από «επαρκή διάτμηση». Αυτό το πλαίσιο έχει υπάρξει κυρίαρχο για τον τομέα της μηχανικής του εδάφους και εφαρμόζεται με επιτυχία μέχρι σήμερα τόσο στην έρευνα, όσο και στην πρακτική. Επιπροσθέτως η ΘΚΚ βρίσκεται στον πυρήνα της πλειονότητας των καταστατικών προσομοιωμάτων που ειδικεύονται σε κοκκώδη υλικά (π.χ., Vermeer, 1978, Jeremic, Runesson & Sture, 1999, Dafalias, Papadimitriou & Li, 2004, Taiebat & Dafalias, 2008). Αυτά τα προσομοιώματα βασίζονται κυρίως στις θεωρίες του συνεχούς μέσου, ενισχυμένες με χαρακτηριστικά όπως η εξάρτηση της επιφάνειας διαρροής από την υδροστατική τάση, η δυνατότητα πλαστικών ογκομετρικών παραμορφώσεων και η διαστολικότητα, τα οποία αποτελούν βασικές ιδιότητες των εδαφών.

Ένα σημαντικό και ενδεχομένως βασικό στοιχείο της συμπεριφοράς του εδάφους, που εξετάζεται ευρέως στην ανάλυση και στην προσομοίωση της μηχανικής απόκρισης του εδάφους μόλις τις τελευταίες δύο δεκαετίες, είναι η δομή (fabric) του εδάφους. Ακόμη και αν το έδαφος προσομοιώνεται με βάση τις θεωρίες του συνεχούς μέσου, είναι ένα διακριτό μέσο, και διαθέτει εσωτερική δομή η οποία καθορίζει, με αποφασιστικό τρόπο, την μακροσκοπική απόκρισή του. Ο προσανατολισμός της εσωτερικής δομής του εδάφους, η οποία εδώ θα αποδίδεται μόνο με τον όρο δομή (fabric), προσδιορίζεται κυρίως από το σχήμα των κόκκων, το δίκτυο των επαφών μεταξύ των σωματιδίων, καθώς και από τη χωρική κατανομή των κενών. Προηγμένα καταστατικά προσομοιώματα έχουν ενσωματώσει τη δομή και τη έχουν συμπεριλάβει σε ένα συνεχές προσομοίωμα (Li & Dafalias, 2002, Muhunthan, Chameau & Masad, 1996, Muhunthan & Chameau 1997, Papadimitriou, Li & Dafalias, 2012).

Η δομή και η σχέση της με τη μηχανική απόκριση της άμμου είναι τόσο σημαντική, ώστε οι Li & Dafalias (2012) πρότειναν μια νέα θεωρία, την Θεωρία Ανισοτροπικής Κρίσιμης Κατάστασης - ΘΑΚΚ (Anisotropic Critical State Theory) για την τροποποίηση της κλασικής ΘΚΚ προσθέτοντας μια παράμετρο που σχετίζεται με τη δομή. Παρόλο που η ΘΑΚΚ έχει εφαρμοστεί με επιτυχία ως πλαίσιο καταστατικών προσομοιωμάτων, μέχρι τώρα δεν έχει αποδειχθεί ως μία αυτόνομη θεωρία. Η προσθήκη μιας παραμέτρου δομής στο πλαίσιο της ΘΑΚΚ παρέχει ξεχωριστές δυνατότητες στα προσομοιώματα που την εφαρμόζουν, αλλά η θεωρία αυτή καθαυτή, δεν υποστηρίζεται ούτε διαψεύδεται μέσω πειραμάτων. Αυτό συμβαίνει διότι απαιτούνται ειδικές συνθήκες, ώστε να ελεγχθεί εάν είναι απαραίτητη η τροποποίηση της ΘΚΚ, η οποία ισχύει ως έχει στις τυπικές καταστάσεις για τις οποίες και προτάθηκε (π.χ. κλασική τριαξονική συμπίεση). Ωστόσο, για διαφορετικές και πιο σύνθετες διαδρομές τάσεων, που συχνά εμφανίζονται στη φύση (π.χ. στροφή των κυρίων αξόνων των τάσεων) δεν είναι σαφές εάν οι συνθήκες της ΘΚΚ είναι πλήρεις.

Ένας από τους σημαντικότερους στόχους αυτής της διατριβής ήταν να παράσχει ένα πείραμα που θα μπορούσε να επιλύσει αυτήν την αμφιβολία με οριστικό τρόπο. Μια τέτοια δοκιμή θα δημιουργούσε τις προϋποθέσεις υπό τις οποίες θα εξετάζονταν τόσο η ΘΚΚ, όσο και η ΘΑΚΚ. Αυτό το ειδικό πείραμα έχει βρεθεί ότι είναι η στροφή των κύριων αξόνων του τανυστή των τάσεων στην Κρίσιμη Κατάσταση (ΚΚ)διατηρώντας παράλληλα τις κύριες τιμές των τάσεων σταθερές.

Λόγω της δυσκολίας υλοποίησης της προτεινόμενης διαδικασίας σε φυσικά πειράματα, αλλά και επειδή η δομή του εδάφους είναι πολύ δύσκολο ακόμη να μετρηθεί σε αυτά, χρησιμοποιήθηκε η Μέθοδος Διακριτών Στοιχείων (ΜΔΣ), ώστε να προσομοιωθούν τα περιγραφόμενα πειράματα. Αυτή η αριθμητική μέθοδος έχει εφαρμοστεί στη Γεωμηχανική από το 1979 (Cundall & Strack, 1979), αλλά αναπτύχθηκε και χρησιμοποιήθηκε ευρέως τα τελευταία 20 χρόνια. Το κυρίαρχο πλεονέκτημά της είναι ότι αποτελεί έναν τρόπο προσομοίωσης κοκκώδους μέσου και της διακριτής του φύσης, χωρίς να χρειάζεται να χρησιμοποιηθεί η παραδοχή ενός μακροσκοπικού προσομοιώματος. Αυτό επιτρέπει την ανάλυση της μικροδομής του εδαφικού υλικού, προκειμένου να προκύψουν αποτελέσματα σχετικά με τη μηχανική συμπεριφορά του και να επανεξεταστούν οι υποθέσεις που χρησιμοποιούνται από τα καταστατικά προσομοιώματα. Το μειονέκτημα της ΜΔΣ είναι ότι, καθώς ασχολείται με τα στερεά σωματίδια του διακριτού μέσου και τις αλληλεπιδράσεις μεταξύ τους, είναι επί του παρόντος αδύνατο να εφαρμοστεί με μεγάλο αριθμό κόκκων, π.χ. όσους θα υπήρχαν σε προβλήματα συνοριακών συνθηκών.

Εκτενέστερη ανάλυση σχετική με τις δυνατότητες ποσοτικοποίησης της δομής θα πραγματοποιηθεί στην επόμενη ενότητα. Κατόπιν θα παρουσιαστεί η Θεωρία Κρίσιμης Κατάστασης, ενώ η Θεωρία Ανισοτροπικής Κρίσιμης Κατάστασης θα παράσχει το κίνητρο και το πλαίσιο για τα πειράματα και την ανάλυση που ακολουθεί. Στη συνέχεια θα πραγματοποιηθεί το διδιάστατο καινοτόμο αριθμητικό πείραμα μέσω της ΜΔΣ. Αυτή η 2Δ αναπαράσταση του κοκκώδους υλικού έχει αποδειχθεί εξαιρετικά χρήσιμη, κυρίως για την ευκολότερη - σε σύγκριση με την 3Δ - ερμηνεία των αποτελεσμάτων και την ταχύτητα της ανάλυσης. Το εν λόγω αριθμητικό πείραμα βασίζεται στην στροφή των κυρίων αξόνων των τάσεων. Η ανάλυση αυτού του εικονικού πειράματος θα αποκαλύψει την μη πληρότητα της ΘΚΚ και την θεραπεία που μπορεί να προσφέρει η ΘΑΚΚ. Επιπλέον, θα ακολουθήσει μία μονοτονική ακτινική φόρτιση, μετά την φάση της στροφής των κυρίων αξόνων, η οποία θα αποδείξει την γενική ισχύ του φαινομένου της ΚΚ. Επιπλέον, αφού παρουσιαστεί το ίδιο αριθμητικό πείραμα σε 3 διαστάσεις, θα εξετασθούν εν συντομία οι ομοιότητες και οι διαφορές των αποτελεσμάτων για 2 και 3 διαστάσεις. Η συνεκτίμηση της τρίτης διάστασης δημιουργεί περιορισμούς στη διαδικασία, αλλά τα αποτελέσματα θα επιβεβαιώσουν την ανεπάρκεια της ΘΚΚ. Στην εφαρμογή των εικονικών πειραμάτων ξεπεράστηκαν αρκετές τεχνικές δυσκολίες

δημιουργώντας νέες δυνατότητες στην εφαρμογή της ΜΔΣ, κυρίως στην περιοχή της ΚΚ. Τέλος, θα εξαχθούν τα κύρια συμπεράσματα.

2. Η δομή του εδάφους

Το έδαφος είναι ένα πολυφασικό κοκκώδες υλικό, το οποίο αποτελείται από στερεούς κόκκους και κενά. Τα σωματίδια αποτελούν τη στερεά φάση του εδάφους, ενώ το υπόλοιπο μέρος είναι τα κενά, τα οποία μπορούν να εμπεριέχουν υγρά ή αέρια. Έτσι, τα κενά μπορούν επίσης να χωριστούν σε δύο υπο-φάσεις: την υγρή και την αέρια. Σε συνήθη εδάφη το υγρό είναι νερό και το αέριο είναι απλός ατμοσφαιρικός αέρας, αλλά μπορεί να παρουσιαστούν και άλλα υγρά ή ακόμη και αέρια (π.χ. λάδι, υγρά απόβλητα ή διοξείδιο του άνθρακα).

Εκτός από τον πολυφασικό χαρακτήρα των εδαφών, μια άλλη σημαντική πτυχή με σημαντική επίδραση, ειδικά στην ανισότροπη μηχανική συμπεριφορά, είναι η χωρική κατανομή των στερεών και ο προσανατολισμός τους καθώς και η χωρική κατανομή και ο προσανατολισμός και των σχετικών κενών. Ο όρος δομή (fabric) χρησιμοποιείται, για να περιγράψει τη συνολική χωρική και γεωμετρική διαμόρφωση των εδαφικών στοιχείων (Brewer, 1964, Oda, 1972a).

Τρία είναι τα βασικά είδη δομής του εδάφους: ο προσανατολισμός των κυρίων αξόνων των κόκκων με βάση το σχήμα τους, ο προσανατολισμός των διανυσμάτων που είναι κάθετα στις διεπαφές μεταξύ των στερεών σωματιδίων και η κατανομή και ο προσανατολισμός των κενών. Και τα τρία αυτά είδη θεωρούνται σημαντικά για τη γενική συμπεριφορά ενός κοκκώδους υλικού. Στην παρούσα διερεύνηση θα εξετασθεί κυρίως η δομή με βάση τα διανύσματα διεπαφών, ενώ για 2Δ θα εξετασθεί και ο προσανατολισμός των κενών του υλικού. Στη συνέχεια ορίζονται συνοπτικά και τα τρία είδη δομής για την ανάλυση των βασικών εννοιών πίσω από τους ορισμούς αυτούς και για την πληρότητα της παρουσίασης.

Οι κόκκοι του εδάφους δεν είναι ούτε σφαιρικοί ούτε ελλειψοειδείς, μολαταύτα είναι δυνατό να καθοριστεί ένας κύριος άξονας για το σχήμα τους. Για διάφορα, ακανόνιστα σχήματα (όπως στο Σχήμα 1) ένας κύριος, μέγιστος άξονας, μπορεί να υπολογιστεί λαμβάνοντας υπόψη τον προσανατολισμό του κόκκου. Στη συνέχεια ορίζονται δύο μοναδιαία διανύσματα στον κύριο άξονα (Σχήμα 1), που είναι χαρακτηριστικά του

προσανατολισμού των κόκκων ($\mathbf{n}_p$,$-\mathbf{n}_p$). Με βάση αυτά τα διανύσματα, η δομή που σχετίζεται με τον προσανατολισμό αυτού του ενός σωματιδίου «p» ισούται με $\mathbf{n}_p \otimes \mathbf{n}_p$, όπου το $\otimes$ συμβολίζει το τανυστικό γινόμενο και μόνο το $\mathbf{n}_p$ (χωρίς το $-\mathbf{n}_p$) χρησιμοποιείται. Εάν χρησιμοποιηθούν και τα δύο διανύσματα, πρέπει να εφαρμοστεί συντελεστής 0.5 μπροστά από το τανυστικό γινόμενο, αποδίδοντας ακριβώς το ίδιο αποτέλεσμα. Τα χαρακτηριστικά αυτά διανύσματα μπορούν να αναλυθούν σε καρτεσιανό σύστημα αξόνων οπότε και να ποσοτικοποιθούν τόσο αυτά, όσο και το τανυστικό τους γινόμενο.

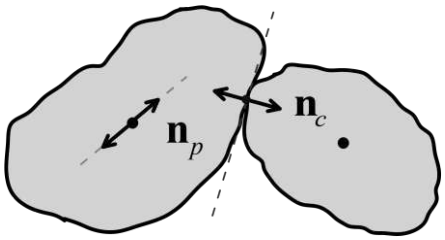

Σχήμα 1: Διανύσματα για την περιγραφή της δομής των κοκκωδών υλικών: $\mathbf{n}_p$ για τον προσανατολισμό των κόκκων, $\mathbf{n}_c$ για τα κάθετα διανύσματα διεπαφών

Για ένα δείγμα εδάφους, ο τανυστής εσωτερικής δομής για τον προσανατολισμό των σωματιδίων ορίζεται ως το άθροισμα όλων των τανυστικών γινομένων όλων των κόκκων του εδάφους (Oda, 1982, Satake, 1982, Kanatani, 1984):

$$\mathbf{G}_p = \frac{1}{N_p} \sum_{k_p=1}^{N_p} \mathbf{n}_p^{k_p} \otimes \mathbf{n}_p^{k_p} \qquad (1)$$

$\mathbf{n}_p$ είναι τα διανύσματα που ορίζουν τον προσανατολισμό της δομής των κόκκων, $\otimes$ είναι το τανυστικό γινόμενο, με $\sum$ εννοείται η άθροιση σε όλους τους κόκκους, το k_p χαρακτηρίζει τον k_p κόκκο, και N_p είναι ο συνολικός αριθμός των κοκκωδών σωματιδίων στο δείγμα. Σε πολλές περιπτώσεις το αποκλίνον μέρος του τανυστή της δομής είναι το πλέον ενδιαφέρον, δεδομένου ότι είναι απαλλαγμένο από το υδροστατικό στοιχείο και παρέχει την σημαντική δομική ανισοτροπία. Αυτός ο αποκλίνων τανυστής προκύπτει σε 2Δ ως:

$$\mathbf{F}_p = \mathbf{G}_p - \frac{1}{2}\mathbf{I} = \frac{1}{N_p} \sum_{k_p=1}^{N_p} \mathbf{n}_p^{k_p} \otimes \mathbf{n}_p^{k_p} - \frac{1}{2}\mathbf{I} \qquad (2)$$

Σε μία 3Δ κατάσταση ο συντελεστής $1/2$ θα πρέπει να αντικατασταθεί με $1/3$.

Στο διδιάστατο χώρο ο τανυστής δομής έχει δύο βαθμούς ελευθερίας, δεδομένου του ότι έχει μηδενικό ίχνος εξ ορισμού (ή εάν αφορά τον πλήρη τανυστή $\mathbf{G}_p$ μοναδιαίο ίχνος). Συνεπώς η εσωτερική ανισοτροπία της δομής μπορεί να ποσοτικοποιηθεί χρησιμοποιώντας μόνο τη διαφορά των δύο κυρίων τιμών ($a_p = F_{pI} - F_{pII}$) και μία γωνία, π.χ. εκπεφρασμένη μέσω ενός χαρακτηριστικού άξονα (π.χ. του οριζοντίου άξονα) και της κατεύθυνσης της μέγιστης κύριας τάσης (θ_p). Αυτός ο τρόπος ορισμού της έντασης της ανισοτροπίας της δομής είναι συνήθης στην ανάλυση με τη ΜΔΣ (Fu & Dafalias, 2011a; Yishmiri & Soga, 2011). Επιπροσθέτως αυτή η ένταση αποδεικνύεται ότι είναι ποιοτικά και ποσοτικά ταυτόσημη με το μέτρο (ή νόρμα) του τανυστή $F = \sqrt{tr\mathbf{F}^2} = \sqrt{2}\left|F_I\right| = \sqrt{2}\left|F_{II}\right| = (1/\sqrt{2})\left|F_I - F_{II}\right|$. Σε 3Δ, η νόρμα του τανυστή είναι ο πλέον κατάλληλος τρόπος για την ποσοτικοποίηση της έντασης της ανισοτροπίας (Li & Dafalias, 2012).

Ένας άλλος τρόπος για τον ορισμό της δομής με βάση τη στερεά φάση είναι μέσω του επιπέδου που καθορίζει την κατεύθυνση της διεπαφής (διανύσματα διεπαφών). Αυτό το επίπεδο (ή γραμμή σε 2Δ) ορίζεται ως εκείνο που διέρχεται από το σημείο διεπαφής δύο κόκκων και είναι εφαπτόμενο στα σωματίδια που έρχονται σε επαφή. Κάθετα σε αυτό το επίπεδο (ή γραμμή), και με αρχή το σημείο διεπαφής, ορίζονται δύο μοναδιαία διανύσματα, τα οποία ονομάζονται κάθετα διανύσματα διεπαφής (Σχήμα 1).

Με βάση αυτόν τον ορισμό του επιπέδου διεπαφής και των διανυσμάτων διεπαφής ο τανυστής δομής μπορεί να οριστεί ως (Oda, 1982, Satake, 1982, Kanatani, 1984):

$$\mathbf{G}_c = \frac{1}{N_c}\sum_{k_c=1}^{N_c} \mathbf{n}_c^{k_c} \otimes \mathbf{n}_c^{k_c} \qquad (3)$$

όπου $\mathbf{G}_c$ είναι ο τανυστής δομής για τα διανύσματα διεπαφής, το υπογεγραμμένο "c" δηλώνει ότι χρησιμοποιούνται τα διανύσματα διεπαφής (contact normal vectors), $\mathbf{n}_c^{k_c}$ είναι το μοναδιαίο κάθετο διάνυσμα που περιγράφει τη δομή για την $k_c th$ διεπαφή και το $\sum$ εννοεί την άθροιση σε όλες τις επαφές N_c που υπάρχουν μεταξύ των N_p κόκκων.

Ένα άλλο ουσιαστικό στοιχείο για τη δομή των κοκκωδών μέσων είναι η κατανομή και ο προσανατολισμός των κενών. Η ποσοτικοποίηση των χαρακτηριστικών των κενών

είναι κατά βάση πολύ διαφορετική από την περιγραφή της στερεάς φάσης. Αυτό συμβαίνει λόγω των θεμελιωδών διαφορών μεταξύ των δύο φάσεων. Ο κενός χώρος ορίζεται απλώς ως ο χώρος που δεν πληρούται με στερεά σωματίδια. Αυτό οδηγεί σε διάφορα ζητήματα για την περιγραφή των κενών, όπως το μη κυρτό και ιδιόμορφο σχήμα τους και η συνεχής και τυχαία εξέλιξη του κενού χώρου, χωρίς προκαθορισμένα σχήματα. Επιπλέον τα κενά μεταξύ των κόκκων, ειδικά σε 3 διαστάσεις, αλληλοσυνδέονται, έτσι ώστε στην πράξη να υπάρχει μόνο ένα ενιαίο κενό, ή λίγα μεγάλα. Όλα αυτά τα χαρακτηριστικά καθιστούν την εν λόγω φάση πολύ διαφορετική, όσον αφορά στη δομή της, από τον στερεό χώρο. Παρ'όλα αυτά είναι προφανές και έχει αναφερθεί (Li & Li, 2009, Theocharis et al., 2014, Fu & Dafalias, 2015) ότι κατά τη δομή τους τα κενά και τα στερεά συνδέονται, όπως αναμένεται, και επιπλέον συσχετίζονται ποσοτικά. Εν συντομία, για να ποσοτικοποιήσουμε τη δομή των κενών, όλα τα χαρακτηριστικά τους έχουν σημασία - όπως το μέγεθος, το σχήμα και η συνδεσιμότητα των κενών - ενώ για τα στερεά είναι απλούστερο να εστιάσει κανείς μόνο στο σχήμα των σωματιδίων ή στα διανύσματα διεπαφής.

Σε μία πρόσφατη δημοσίευση (Theocharis et al., 2017b, υπό εξέταση) εξετάσθηκε συστηματικά μία εξόχως διαδεδομένη μέθοδος για την ποσοτικοποίηση της δομής των κενών: η μέθοδος ανάλυσης των κενών με παράλληλες γραμμές σάρωσης. Τα αποτελέσματα της ανάλυσης αυτής περιλαμβάνουν την απόδειξη (με αναλυτικό και αριθμητικό τρόπο) ύπαρξης προβλημάτων στους μέχρι τώρα ορισμούς που έχουν χρησιμοποιηθεί με βάση αυτήν τη μέθοδο, ενώ παρουσιάστηκαν και δύο νέες εναλλακτικές λύσεις για έναν πιο φυσικό και ορθό ορισμό του τανυστή δομής.

Συγκεκριμένα, με μια σχετικά απλή τροποποίηση του αρχικού ορισμού, όπως αυτός δόθηκε από τους Oda et al. (1985), ορίζεται ένας νέος τανυστής δομής με βάση τη μέθοδο παράλληλων γραμμών σάρωσης που μπορεί να ποσοτικοποιήσει επαρκώς την ανισοτροπία:

$$\mathbf{G}_v^{co} = \frac{1}{L}\sum_{\theta=-90^0}^{\theta=90^0} l^\theta \, \mathbf{n}^\theta \otimes \mathbf{n}^\theta; \quad L = \sum_{\theta=-90^0}^{\theta=90^0} l^\theta; \quad l^\theta = \frac{\sum_{i=1}^{N^\theta} l_i^\theta}{N^\theta} \quad \text{για} \;\; l_i^\theta > \text{"cut off" τιμή} \qquad (4)$$

όπου $\mathbf{n}^\theta$ είναι το μοναδιαίο διάνυσμα κατά μήκος της εκάστοτε γραμμής που βρίσκεται υπό γωνία θ, το $\mathbf{n}^\theta \otimes \mathbf{n}^\theta$ χρησιμοποιείται για το τανυστικό γινόμενο του $\mathbf{n}^\theta$ με τον

εαυτό του, ο l_i^θ χαρακτηρίζει το μήκος i κατά τη γωνία θ, το N^θ είναι ο αριθμός των μηκών των κενών l_i^θ για κάθε γωνία θ, το l^θ είναι το μέσο μήκος όλων των μηκών των κενών για τη κάθε γωνία θ και $L = \sum_{\theta=-90^0}^{\theta=90^0} l^\theta$ είναι το άθροισμα όλων των μέσων μηκών l^θ για όλες τις γωνίες θ, ενώ η άθροιση λαμβάνει χώρα σε προκαθορισμένα διαστήματα του θ μέσα στον χώρο $[-90^0, 90^0]$. Ο μέσος όρος των μηκών l^θ παρέχει την σημαντική ανισοτροπία των τανυστών $\mathbf{n}^\theta \otimes \mathbf{n}^\theta$ και η στατιστική κατανομή του καθορίζει τον προσανατολισμό της δομής. Στην περίπτωση που το l^θ είναι ίσο για κάθε θ, θα απαλειφθεί από τον αριθμητή και τον παρανομαστή της Εξ. (4), και, ολοκληρώνοντας για κάθε θ προκύπτει ο μισός μοναδιαίος τανυστής $(1/2)\mathbf{I}$ που σχετίζεται με πλήρως ισοτροπική δομή.

Ένας άλλος, νέος ορισμός ενός τανυστή με τη μέθοδο γραμμών σάρωσης, ο οποίος αποδεικνύεται και αυτός αποτελεσματικός στη μέτρηση ανισοτροπίας των κενών και προτείνεται από τους Theocharis et al. (2017b) είναι:

$$\mathbf{G}_{v2} = \frac{1}{\sum_{\theta=-90^0}^{\theta=90^0} \left(\sum_{i=1}^{N^\theta} l_i^{\theta^2} \right)} \sum_{\theta=-90^0}^{\theta=90^0} \left(\sum_{i=1}^{N^\theta} l_i^{\theta^2} \right) \mathbf{n}^\theta \otimes \mathbf{n}^\theta \qquad (5)$$

Τα σύμβολα παραμένουν ίδια όπως και πριν. Σε αυτήν την περίπτωση, το στατιστικό βάρος του τανυστή δομής, που χαρακτηρίζει την ανισοτροπία της δομής των κενών, είναι το τετράγωνο του μήκους των μηκών των κενών, σε αντίθεση με τους προηγούμενους ορισμούς, όπου χρησιμοποιείται το ίδιο το μήκος. Αμφότεροι οι παραπάνω νεοδημιουργηθέντες τανυστές δομής κενών, στις εξισώσεις (4) και (5), μπορούν να ποσοτικοποιήσουν επαρκώς την ανισοτροπία των κενών και θα εφαρμοστούν στη συνέχεια για την ποσοτικοποίηση της δομής των κενών σε 2Δ μέσω αριθμητικών πειραμάτων ΜΔΣ. Υπογραμμίζεται ότι οι παράλληλες γραμμές σάρωσης εφαρμόζονται σε όλο το δείγμα και όχι μόνο σε μία αντιπροσωπευτική περιοχή, όπως σε άλλες μεθόδους.

3. Η Θεωρία Κρίσιμης Κατάστασης και η κληρονομιά της

3.1 Η κλασική Θεωρία Κρίσιμης Κατάστασης

Η έννοια της Κρίσιμης Κατάστασης (ΚΚ) έχει εισαχθεί από τους Roscoe, Schofield & Wroth (1958) και από τους Schofield & Wroth (1968) στο έργο-ορόσημό τους πριν από μισό περίπου αιώνα. Οι συγγραφείς την περιγράφουν ως: «η γενική ιδέα ότι το έδαφος και άλλα κοκκώδη υλικά, αν παραμορφώνονται συνεχώς μέχρι να ρέουν ως ρευστό τριβής, θα εισέλθουν σε μια καλά καθορισμένη κρίσιμη κατάσταση που καθορίζεται από δύο εξισώσεις» (Schofield & Wroth, 1968 - Ενότητα 1.8 , Σελ. 12). Αυτές οι δύο εξισώσεις αναφέρονται στις μακροσκοπικές ιδιότητες του υλικού και ορίζονται με βάση τις τάσεις και τον όγκο.

Καταρχάς είναι σημαντικό να ξεχωρίσουμε την Θεωρία Κρίσιμης Κατάστασης από το αντίστοιχο φαινόμενο. Η Κρίσιμη Κατάσταση (ΚΚ) αναφέρεται στην κατάσταση των κοκκωδών υλικών όπου το υλικό συνεχίζει να παραμορφώνεται συνεχώς διατμητικά, ενώ οι τάσεις και ο όγκος του παραμένουν σταθερά. Η αναλυτική έκφραση αυτής της κατάστασης συνεπώς προκύπτει ως:

$$\dot{p}=0, \quad \dot{q}=0, \quad \dot{\varepsilon}_v=0, \quad \dot{\varepsilon}_q\neq 0 \qquad (6)$$

όπου q είναι η αποκλίνουσα τάση, p είναι η υδροστατική τάση, ε_v είναι η ογκομετρική τροπή και ε_q είναι η αποκλίνουσα τροπή, η μόνη η οποία εξελίσσεται στην ΚΚ. Η υπερτιθέμενη τελεία πάνω από τις παραμέτρους υποδηλώνει την μερική παράγωγο με το χρόνο.

Οι Roscoe, Schofield & Wroth (1958) και Schofield & Wroth (1968) περιέγραψαν το φαινόμενο αλλά πρότειναν επίσης και μία θεωρία βασισμένη στην ΚΚ. Αυτή η θεωρία υποδηλώνει ότι η κρίσιμη κατάσταση μπορεί να οριστεί ρητά από δύο συνθήκες, οι οποίες είναι ικανές και αναγκαίες για να επιτευχθεί και να διατηρηθεί η ΚΚ. Αυτές οι δύο εξισώσεις καθορίστηκαν καταρχάς στον τριαξονικό χώρο και στην αρχική τους μορφή εκφράστηκαν ως:

$$q=\mathrm{M}p; \quad \Gamma=v+\lambda\ln p \qquad (7)$$

όπου πάλι q είναι η αποκλίνουσα τάση, p είναι η υδροστατική τάση, v είναι ο ειδικός όγκος του υλικού, M, Γ και λ είναι ιδιότητες του εδαφικού υλικού. Το πρώτο μέρος της εξίσωσης (7) αναφέρεται σε τάσεις και προκύπτει ότι στην ΚΚ η αποκλίνουσα και η υδροστατική τάση σχετίζονται γραμμικά μέσω μιας σταθεράς, που εξαρτάται μόνο από το υλικό. Το δεύτερο μέρος της εξ. (7) υπαγορεύει ότι ο ειδικός όγκος, ο οποίος είναι ο συνολικός όγκος που καταλαμβάνεται από μοναδιαίο όγκο στερεών κόκκων, μειώνεται γραμμικά καθώς αυξάνεται ο λογάριθμος της υδροστατικής πίεσης, ενώ το δείγμα βρίσκεται πάντα στην ΚΚ. Τα δύο μέρη της εξίσωσης (7) παρουσιάζονται ποιοτικά στο Σχήμα 2.

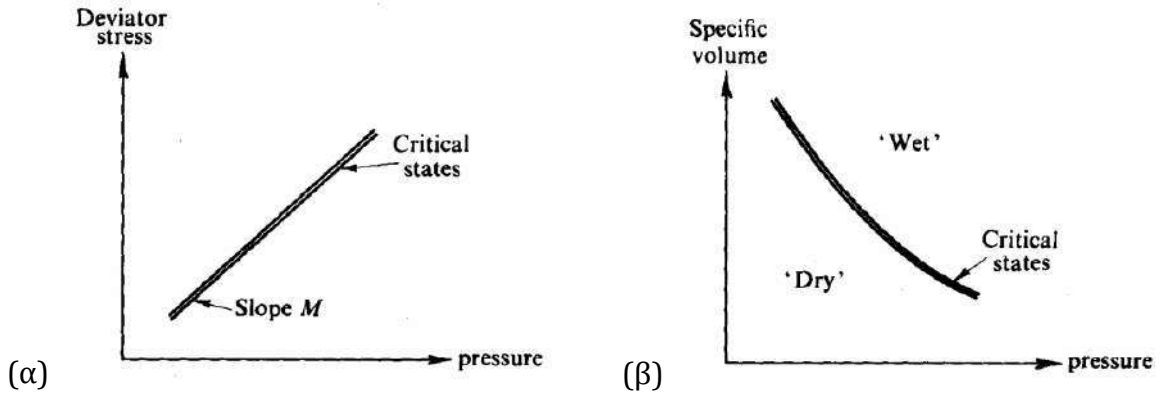

Σχήμα 2: Κρίσιμη Κατάσταση σύμφωνα με τις Εξ. (6): (α) η αποκλίνουσα σε σχέση με την υδροστατική τάση (β) ο ειδικός όγκος σε σχέση με την υδροστατική τάση (Schofield & Wroth, 1968 – Ενότητα 1.8, σελ. 12)

Η Κρίσιμη Κατάσταση δεν είναι απλώς μια σταθερή κατάσταση στην οποία φθάνει ένα κοκκώδες υλικό υπό κάποια ιδιαίτερη διαδικασία φόρτισης, αλλά αποτελεί μια γενική "βάση αναφοράς" για αυτό το είδος υλικών. Σε οποιοδήποτε δεδομένο δείγμα εδάφους το ερώτημα είναι εάν είναι "χαλαρότερο" ή "πυκνότερο" από την ΚΚ. "Χαλαρότερη" είναι η κατάσταση κατά την οποία, υπό παραμόρφωση, το υλικό θα συμπυκνωθεί, ο ειδικός όγκος του θα μειωθεί, δηλ. θα σημειωθεί μείωση των κενών μεταξύ του μοναδιαίου όγκου των κόκκων και αναφέρεται ως "Υγρή (Wet)" στο Σχ. 2(β). Από την άλλη πλευρά η "πυκνότερη" είναι η αντίθετη κατάσταση στην οποία το δείγμα θα διασταλεί, δηλαδή η παραμόρφωση θα προκαλέσει αύξηση του ειδικού όγκου. Αυτή είναι η "Ξηρή (Dry)" περιοχή στο Σχ. 2(β). Είναι πλέον σαφές ότι η ΚΚ δεν είναι απλώς μια σταθερή κατάσταση, αλλά ένα πολύ σημαντικό και ισχυρό πλαίσιο που υπαγορεύει την συμπεριφορά του εδάφους. Αυτή η συμπεριφορά, αποτελεί τη βάση για την

ανάπτυξη της Θεωρίας Κρίσιμης Κατάστασης (ΘΚΚ), ένα σημαντικό επίτευγμα της Εδαφομηχανικής.

Μία ακόμη συνήθης μορφή των συνθηκών της ΘΚΚ είναι η εξής:

$$\eta=\frac{q}{p}=\eta_c=\mathrm{M},\quad e=e_c=\hat{e}_c(p) \tag{8}$$

όπου ο η είναι το σύμβολο για τον αποκλίνοντα λόγο τάσεων (deviatoric stress ratio) και η_c για τον αποκλίνοντα λόγο τάσεων στην ΚΚ, εξ ορισμού ίσος με M. Ο δείκτης πόρων (ή λόγος κενών - void ratio) ($e=1+v$) αντικαθιστά τον ειδικό όγκο, καθώς έχουν σχέση ένα προς ένα, και ισούται με e_c στην ΚΚ. Το $\hat{e}_c(p)$ χρησιμοποιείται για να υπογραμμίσει ότι ο δείκτης πόρων στην ΚΚ εξαρτάται μόνο από την υδροστατική τάση. Η σχέση μεταξύ της υδροστατικής τάσης και του δείκτη πόρων αποτελεί την προβολή της επιφάνειας της ΚΚ στο χώρο $e-p$ και εδώ αναφέρεται ως Γραμμή Κρίσιμης Κατάστασης (ΓΚΚ).

3.2 Ερωτήματα σχετικά με τη Θεωρία Κρίσιμης Κατάστασης

Ως κυρίαρχο επίτευγμα του επιστημονικού πεδίου η ΘΚΚ έχει προσελκύσει έντονη κριτική. Είναι σημαντικό να έχουμε κατά νου ότι, τη στιγμή που αναπτύχθηκε η ΘΚΚ, δεν υπήρχε παρόμοια τέτοια θεωρία και ότι η επιστήμη της γεωμηχανικής βρισκόταν στα πρώτα της στάδια. Κατόπιν της εισαγωγής της όμως, έχουν εγερθεί αρκετά σχετικά ζητήματα, ειδικά δεδομένου ότι πρόκειται για μια θεωρία βασισμένη κυρίως σε πειραματικά αποτελέσματα, χωρίς ισχυρό θεωρητικό υπόβαθρο. Τα δύο σημαντικά ζητήματα που έχουν προσελκύσει την προσοχή της έρευνας τα τελευταία χρόνια είναι η μοναδικότητα της ΚΚ και οι ικανές και αναγκαίες συνθήκες επίτευξής της (Poulos, 1981, Chu, 1995, Riemer & Seed, 1997, Mooney, Finno & Viggiani, 1998, Li & Dafalias, 2012, Zhao & Guo, 2013).

3.2.1 Είναι η Κρίσιμη Κατάσταση μοναδική;

Η μοναδικότητα ή όχι της ΘΚΚ συνδέεται κυρίως με την Γραμμή Κρίσιμης Κατάστασης (ΓΚΚ). Είναι πλέον γενικώς αποδεκτό ότι η τιμή του αποκλίνοντα λόγου των τάσεων q/p στην ΚΚ, είναι μοναδική (π.χ., Mooney et al., 1998). Το πρόβλημα της μοναδικότητας της ΓΚΚ έχει διερευνηθεί, χωρίς να έχει επιτευχθεί πλήρης και σαφής

κατάληξη. Πολλά πρακτικά προβλήματα περιορίζουν μέχρι στιγμής τα εργαστηριακά αποτελέσματα, όπως η ανάπτυξη διατμητικών ζωνών παραμόρφωσης, περιοχών στένωσης διατομών και άλλων μη ομοιόμορφων παραμορφώσεων, με αποτέλεσμα η ΚΚ να μην μπορεί να επιτευχθεί σε όλο το δείγμα και έτσι μόνο λίγα δείγματα να φτάνουν ομοιόμορφα στην ΚΚ.

Η Μέθοδος των Διακριτών Στοιχείων (ΜΔΣ) (Cundall & Strack, 1979) είναι ένα νέο, ελπιδοφόρο, αριθμητικό εργαλείο που παρέχει απαντήσεις σε αυτό το πεδίο. Αυτή η αριθμητική μέθοδος μπορεί να εφαρμόσει διάφορες συνοριακές συνθήκες και συνθήκες φόρτισης, και να δώσει μετρήσεις σε οποιαδήποτε περιοχή των δειγμάτων που χρησιμοποιήθηκαν, έτσι ώστε τα πρακτικά προβλήματα των φυσικών πειραμάτων να μπορούν να ξεπεραστούν. Η έρευνα με τη ΜΔΣ έχει ήδη δώσει πειστικές αποδείξεις για τη μοναδικότητα της ΚΚ και τις παραμέτρους που η μοναδικότητα αυτή μπορεί να συνεπάγεται (Rothenburg & Kruyt, 2004, Sitharam & Vinod, 2008, Fu & Dafalias, 2011b, Yang & Luo, 2015, Yang & Wu, 2016).

3.2.2 Είναι οι συνθήκες της ΘΚΚ ικανές και αναγκαίες;

Μετά την παρουσίαση της κύριας έννοιας της ΘΚΚ, οι Schofield & Wroth (1968) περιγράφουν με μεγαλύτερη ακρίβεια τη συμπεριφορά στην ΚΚ. Στην ενότητα 6.8, σελ. 104-105, η ΚΚ ορίζεται ως: "[...] η κατάσταση του υλικού που ρέει ως υγρό τριβής σε σταθερό ειδικό όγκο, τότε και μόνο τότε, όταν η αποτελεσματική υδροστατική πίεση p και η αποκλίνουσα τάση q ικανοποιούν [...]" εδώ τις Εξ. (8). Αυτή η υπόθεση υποδηλώνει σαφώς ότι οι συνθήκες (8) περιγράφουν τις ικανές και αναγκαίες συνθήκες, για να οριστεί η κρίσιμη κατάσταση. Η υπόθεση αυτή συνδέεται προφανώς και με το ζήτημα της μοναδικότητας που περιγράφεται παραπάνω. Το πλήρες σύνολο των καταστατικών μεταβλητών που θα ορίζαν με ακρίβεια την μοναδική ΚΚ, θα καθόριζαν επίσης τις ικανές και αναγκαίες συνθήκες. Αυτά τα δύο ζητήματα, αν και σχετίζονται σαφώς, δεν είναι το ίδιο πρόβλημα.

3.3 Θεωρία Ανισοτροπικής Κρίσιμης Κατάστασης

Μία από τις βασικές παραδοχές της ΘΚΚ ήταν η μικρή σημασία της εσωτερικής δομής του εδάφους στην ΚΚ. Όπως δήλωσαν ρητά: «Θα ασχοληθούμε με τις ισοτροπικές μηχανικές ιδιότητες του υλικού, ιδιαίτερα του αναμοχλευμένου εδάφους που στερείται

δομής» (Schofield & Wroth (1968) - Τμήμα 1.9, σελ. 14). Αυτό αντικατοπτρίζεται στην Εξ. (8) από το γεγονός ότι χρησιμοποιείται ο δείκτης πόρων, αλλά καμία ποσότητα σχετική με τη δομή. Αυτή η συγκεκριμένη υπόθεση, μολονότι ίσως ήταν αρχικώς λογική ή ακόμη και αναγκαία, για να οικοδομηθεί το πρότυπο της ΘΚΚ εκείνη την εποχή, έχει προσελκύσει σοβαρή κριτική (Li & Dafalias, 2012, Dafalias, 2016).

Τα τελευταία 20 χρόνια, αρκετά μικροδομικά στοιχεία αποδεικνύουν ότι στην ΚΚ η δομή παρουσιάζει έντονη ανισοτροπία (π.χ. Masson & Martinez, 2001, Li & Li, 2000, Fu & Dafalias, 2011b, Theocharis et al., 2017a). Στη σύγχρονη έρευνα έχει καταστεί προφανές ότι η ΚΚ φέρει κάποια εξάρτηση από τη δομή, μια επιπλέον μεταβλητή που αναδεικνύεται ως αναγκαιότητα. Η επιρροή της δομής στην ανισοτροπική φύση της Κρίσιμης Κατάστασης και η μοναδικότητά της, έχει βαθιές συνέπειες για την καθολικά αποδεκτή ΘΚΚ (Seed et al., 2003).

Έτσι οι Li & Dafalias (2012) δημιούργησαν την Θεωρία Ανισοτροπικής Κρίσιμης Κατάστασης – ΘΑΚΚ, όπου η δομή είναι μια πρόσθετη καταστατική μεταβλητή. Αυτή η θεωρία διατυπώθηκε για κοκκώδη υλικά ως ένα γενικό πλαίσιο, χωρίς να απαιτεί συγκεκριμένο προσομοίωμα, και χρησιμοποιείται μέσα στο ευρύτερο πεδίο της ελαστοπλαστικότητας, ακριβώς στο ίδιο πνεύμα με τη ΘΚΚ. Στον πυρήνα της ΘΑΚΚ είναι η δομή, η οποία εκφράζεται μέσω της Μεταβλητής Ανισοτροπίας Δομής - ΜΑΔ (Fabric Anisotropy Variable) που ορίζεται ως:

$$A = \mathbf{F} : \mathbf{n} = F\mathbf{n}_F : \mathbf{n} = FN \qquad (9)$$

όπου A είναι η Μεταβλητής Ανισοτροπίας Δομής, $\mathbf{F}$ είναι ο αποκλίνων τανυστής δομής ο οποίος μπορεί να αναλυθεί σε νόρμα (F) και έναν μοναδιαίας-νόρμας τανυστή κατεύθυνσης $\mathbf{n}_F$, $\mathbf{n}$ είναι ο μοναδιαίος τανυστής της κατεύθυνσης της φόρτισης, το βαθμωτό μέγεθος $N = \mathbf{n}_F : \mathbf{n}$ ποσοτικοποιεί τη σχετική κατεύθυνση των $\mathbf{F}$ και $\mathbf{n}$, με την άνω-κάτω τελεία να δηλώνει το ίχνος του γινομένου των δύο προσκείμενων τανυστών. Για την παρούσα εφαρμογή, αλλά και ως γενική αρχή, η κατεύθυνση φόρτισης $\mathbf{n}$ επιλέγεται συγγραμική πάντα με τον αποκλίνοντα τανυστή του πλαστικού ρυθμού παραμόρφωσης. Αυτή η επιλογή αίρει την ανάγκη ο τανυστής αυτός να σχετιστεί με κάποιο συγκεκριμένο προσομοίωμα. Συνεπώς η Μεταβλητής Ανισοτροπίας Δομής ποσοτικοποιεί τη δομή σε όρους έντασης, αλλά και σε όρους σχετικής κατεύθυνσης με

τη φόρτιση. Η ένταση της δομής F ορίζεται ως το μέτρο του τανυστή δομής, κανονικοποιημένο με την τιμή του στην ΚΚ.

Η εξέλιξη της $\mathbf{F}$ μπορεί να μετρηθεί με τη ΜΔΣ, με βάση τον ορισμό της δομής, ενώ μία συνεχής εξίσωση εξέλιξης προτάθηκε από τους Li & Dafalias (2012) που βασίστηκαν σε παρατηρήσεις της ΜΔΣ. Προηγούμενες έρευνες ΜΔΣ (Li and Li, 2009, Fu and Dafalias, 2011b) έχουν δείξει ότι, καθώς εξελίσσεται ο τανυστής δομής με την πλαστική παραμόρφωση, η κατεύθυνση του $\mathbf{n}_F$ τείνει να ευθυγραμμιστεί με το $\mathbf{n}$ και γίνεται συγγραμική στην ΚΚ (εάν δεν έχει ήδη γίνει), ενώ η νόρμα F, τείνει προς το 1 στην ΚΚ. Συνεπώς, στην ΚΚ έχουμε: $N = N_c = \mathbf{n}_F : \mathbf{n} = \mathbf{n} : \mathbf{n} = 1$ (δεδομένων των μοναδιαίων $\mathbf{n}_F$ και $\mathbf{n}$), $F = 1$ και $\mathbf{F} = \mathbf{F}_c = \mathbf{n}$. Ως εκ τούτου, βασιζόμενοι στον ορισμό του A στην Εξ. (9), έπεται η τρίτη συνθήκη της ΘΑΚΚ, $A = A_c = 1$. Πλέον οι νέες συνθήκες για την ΑΘΚΚ είναι:

$$\eta = \eta_c = (q/p)_c = M,\ e = e_c = \hat{e}_c(p),\ A = A_c = 1 \qquad (10)$$

Με βάση και την παραπάνω ανάλυση γίνεται σαφές ότι η Μεταβλητής Ανισοτροπίας Δομής λαμβάνει και αρνητικές τιμές, με βάση το N που αλλάζει πρόσημο π.χ. στην περίπτωση τριαξονικού εφελκυσμού. Επιπλέον, η ΜΑΔ μπορεί να λάβει τιμές και μεγαλύτερες του 1, όταν το μέτρο της ανισοτροπίας της δομής γίνει μεγαλύτερο του 1.

3.4 Η πληρότητα της ΘΚΚ και η εγκυρότητα της ΘΑΚΚ

Ενώ η Μεταβλητής Ανισοτροπίας Δομής είναι πολύ χρήσιμη στην καταστατική προσομοίωση, για να αποδείξει την αναγκαιότητά της ως μια επιπλέον, τρίτη αναγκαία συνθήκη ΚΚ που υπεισέρχεται στις Εξ. (8), πρέπει κανείς να είναι σε θέση να δείξει ότι, αν ικανοποιηθούν οι πρώτες δύο κλασικές συνθήκες αλλά όχι η τρίτη, τότε δεν μπορεί να επιτευχθεί ΚΚ. Μέχρι στιγμής, με την εκτέλεση προσομοιώσεων ΜΔΣ έχει παρατηρηθεί ότι, όταν πληρούνται οι δύο πρώτες προϋποθέσεις, η τρίτη συνθήκη ικανοποιείται πάντοτε ταυτόχρονα (Fu και Dafalias, 2011b). Συνεπώς δεν έχει καταστεί δυνατό να δημιουργηθεί μια περίπτωση όπου οι δύο πρώτες συνθήκες επιτυγχάνονται χωρίς η τρίτη να επιτευχθεί ταυτόχρονα. Έτσι, θα μπορούσε κανείς να συμπεράνει ότι η τρίτη προϋπόθεση είναι απλώς ένα βολικό συμπλήρωμα, το οποίο συμβαίνει ταυτόχρονα με τις δύο πρώτες συνθήκες στην ΚΚ, αλλά δεν μπορεί να σταθεί στο

επίπεδο μιας απαραίτητης και ανεξάρτητης τρίτης προϋπόθεσης για την εμφάνιση της ΚΚ.

Αναφέρεται λοιπόν το ακόλουθο νοητικό πείραμα και η σχετική ερώτηση: ένα δείγμα εδάφους φορτίζεται σε τριαξονική συμπίεση έως ότου φθάσει στην Κρίσιμη Κατάσταση, δηλαδή στην κατάσταση στην οποία αναπτύσσεται συνεχής παραμόρφωση υπό σταθερές τάσεις χωρίς μεταβολή όγκου. Ενώ βρίσκεται στην ΚΚ, επιβάλλεται στροφή των κύριων αξόνων (ΚΑ) της τάσης, με τις κύριες τιμές της τάσης να διατηρούνται σταθερές. Το ερώτημα που τίθεται είναι: θα συνεχίσει το δείγμα να βρίσκεται στην ΚΚ ή όχι;

Το προτεινόμενο πείραμα, όπου η στροφή των κυρίων αξόνων της τάσης συμβαίνει στην ΚΚ, διατηρώντας παράλληλα τις κύριες τιμές της τάσης, είναι ακριβώς το πείραμα που απαιτείται για την καταρχάς αντιμετώπιση των ζητημάτων που τέθηκαν στην προηγούμενη παράγραφο. Το αρχικό ερώτημα είναι αν το δείγμα θα εξακολουθούσε να είναι στην ΚΚ ή όχι, όταν επιβάλλεται τέτοια στροφή. Εφόσον η συνθήκη του κρίσιμου λόγου τάσεων ($\eta = \eta_c = M$) δεν θα αλλάξει για σταθερές τιμές κύριων τάσεων και ο δείκτης πόρων βρίσκεται ήδη στην τιμή κρίσιμης κατάστασης ($e = e_c$) για το δεδομένο p που παραμένει επίσης ίδιο, αν οι κλασικές συνθήκες της ΘΚΚ που δίδονται από τις εξισώσεις (8) είναι επαρκείς για την ΚΚ, τότε το δείγμα πρέπει να παραμείνει στην ΚΚ κατά τη διάρκεια της στροφής των κυρίων αξόνων τάσης και, κατά συνέπεια, δεν πρέπει να παρατηρηθεί καμία αλλαγή του δείκτη πόρων.

Ωστόσο, εάν κάποιος μετρά μια αλλαγή του δείκτη πόρων όταν ξεκινά η στροφή ΚΑ, αυτό σημαίνει ότι οι Εξ. (8) είναι αναγκαίες, αλλά όχι ικανές για τη διατήρηση της ΚΚ και επομένως η κλασική ΘΚΚ είναι ελλιπής. Στην περίπτωση αυτήν κάτι άλλο πρέπει να συμβαίνει κατά τη διάρκεια αυτής της διαδικασίας που μετακινεί το δείγμα μακριά από την ΚΚ. Σύμφωνα με την ΘΑΚΚ αυτό το "κάτι άλλο" σχετίζεται με την παραβίαση της τρίτης, σχετιζόμενης με τη δομή, συνθήκης στις Εξ. (10). Στροφή των κυρίων αξόνων της τάσης και συναφείς παρατηρήσεις έχουν ήδη παρουσιαστεί με τη ΜΔΣ (π.χ. Li και Yu, 2010, Tong et al, 2014), αλλά το χαρακτηριστικό γνώρισμα της παρούσας εργασίας είναι ότι αυτή η στροφή ξεκινά από την ΚΚ, πείραμα που δεν επετεύχθη ποτέ πριν. Την παραπάνω ανάλυση σχετικά με το ζήτημα της πληρότητας ή όχι της ΘΚΚ, καθώς και την πρόταση για ένα πείραμα ΜΔΣ με εναλλαγή των κυρίων αξόνων των τάσεων στην ΚΚ για επιβεβαίωση ή άρνηση της πληρότητας της ΘΚΚ και για επικύρωση της ανάγκης

εισαγωγής της ΘΑΚΚ, πρωτοανέφερε και επεξεργάστηκε, σε υποθετική βάση ο Dafalias (2016). Ένας από τους κύριους στόχους του παρόντος έργου είναι η πραγματοποίηση αυτής της υποθετικής πρότασης.

4. Αριθμητικά πειράματα 2Δ με τη ΜΔΣ– Η απόδειξη της μη πληρότητας της ΘΚΚ και η θεραπεία της

Για τη διδιάστατη προσομοίωση αυτής της ενότητας υπάρχουν μόνο δύο κύριες τάσεις και τροπές: $\sigma_i (i=1,2)$ και $\varepsilon_i (i=1,2)$. Οι διαξονικές εκφράσεις των τριαξονικώς ορισμένων αρχικά παραμέτρων, p (υδροστατική πίεση), q (αποκλίνουσα τάση), ε_v (ογκομετρική τροπή) και ε_q (αποκλίνουσα τροπή) ορίζονται ως: $p=1/2\left(\sigma_1+\sigma_2\right)$, $q=\sigma_1-\sigma_2$, $\varepsilon_v=\varepsilon_1+\varepsilon_2$ και $\varepsilon_q=1/2\left(\varepsilon_1-\varepsilon_2\right)$. Οι προσομοιώσεις των πειραμάτων πραγματοποιήθηκαν με το λογισμικό PFC 2D v4.0© (Itasca, 2013; Cundall and Strack, 1979) και οι παράμετροι που χρησιμοποιήθηκαν περιγράφονται στον Πίνακα 1. Οι τεχνικές λεπτομέρειες και τα προβλήματα που έπρεπε να λυθούν, ώστε να πραγματοποιηθεί η παρούσα ανάλυση είναι σημαντικά και αναλυτικά περιγράφονται πέρα από την παρούσα εργασία και στο Theocharis et al. (2017a), αλλά το κύριο ενδιαφέρον εστιάζεται στα αποτελέσματα, τα οποία και παρουσιάζονται παρακάτω.

Υπογραμμίζεται ότι η διδιάστατη ανάλυση που ακολουθεί αποτελεί καθαρή ανάλυση 2 διαστάσεων και όχι ανάλυση επίπεδης έντασης ή επίπεδης παραμόρφωσης. Λόγω αυτού, οι τιμές των διαφόρων περαμέτρων (π.χ. του δείκτη πόρων) δεν είναι σχετικές με τις αντίστοιχες τιμές τους σε 3Δ και μπορούν να συγκριθούν με αυτές μόνο ποιοτικά.

Αριθμός κόκκων	20,000
Μέση ακτίνα κόκκου (m)	0.001
Συντελεστής ομοιομορφίας (Cu = d_{60}/d_{10});r_{min} (m); r_{max} (m)	1.8 ; 0.0005 ; 0.0015
Πλάτος του δείγματος εκτός επιπέδου (t) (m)	1
Ακτίνα κυκλικού δοκιμίου (m)	0.165
Ισοτροπική και μέση πίεση (kPa)	200
Πυκνότητα κόκκων (kg/m^3)	1000
k_n (N/m)	5x10^8
k_s / k_n (N/m)	1
Συντελεστής τριβής (disk-disk; disk-boundary disk)	0.5; 0.0
Λόγος απόσβεσης	0.7

Πίνακας 1: Ιδιότητες των κόκκων και του δοκιμίου για τα 2Δ πειράματα ΜΔΣ

4.1 Μακροσκοπικά Αποτελέσματα

Φάση 1: Διαξονική φόρτιση μέχρι την ΚΚ

Η διαξονική φόρτιση εφαρμόστηκε αυξάνοντας τη θλιπτική, κύρια τάση σ_1 κατά τον κατακόρυφο άξονα και μειώνοντας ισόποσα την ελάχιστη κύρια τάση σ_2 κατά τον οριζόντιο άξονα. Ως εκ τούτου προκύπτει $\Delta\sigma_1 = -\Delta\sigma_2 > 0$. Καθώς οι κατευθύνσεις των κυρίων τάσεων παραμένουν σταθερές κατά τη διάρκεια της φάσης αυτής, ένα πεδίο ταχυτήτων με σταθερές κατευθύνσεις εφαρμόστηκε στους συνοριακούς κόκκους. Η μακροσκοπική συμπεριφορά του αρχικώς στρογγυλού δείγματος παρουσιάζεται στο Σχήμα 3 (α και β) με μαύρες γραμμές και εμφανίζει μία τυπική συμπεριφορά λόγου τάσεων και ογκομετρικής παραμόρφωσης για χαλαρά εδάφη. Το αριθμητικό δείγμα φτάνει στην ΚΚ περίπου στο 10% της αξονικής παραμόρφωσης κατά τον κατακόρυφο (y) άξονα, ενώ οι υπολογισμοί συνέχισαν μέχρι η παραμόρφωση αυτή να φτάσει στο 30%, καθώς ο λόγος τάσεων και ο δείκτης πόρων διατήρησαν τις τιμές της ΚΚ τους, δηλαδή $\eta = \eta_c = M \approx 0.57$ και $e = e_c = \hat{e}_c(200\text{kPa}) \approx 0.23$.

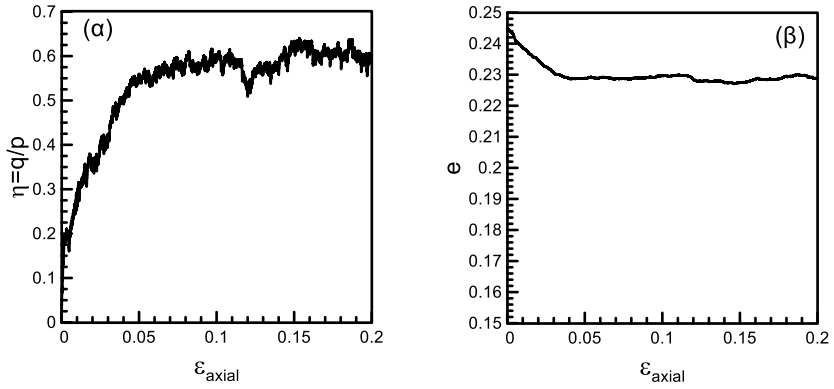

Σχήμα 3: Διαξονική φόρτιση ενός χαλαρού κοκκώδους υλικού: (α) αποκλίνων λόγος τάσεων η και (β) δείκτης πόρων e, σε σχέση με την κατακόρυφη αξονική τροπή ε_{axial}

Φάση 2: Στροφή των κυρίων αξόνων των τάσεων

Η στροφή των κυρίων αξόνων των τάσεων, διατηρώντας τις κύριες τιμές σ_1, σ_2 σταθερές, επιβλήθηκε στο δείγμα, όταν αυτό έφτασε το 20% της αξονικής παραμόρφωσης κατά τη φάση 1, ενώ βρισκόταν αδιαμφισβήτητα στην ΚΚ. Η στροφή κυρίων αξόνων ποσοτικοποιήθηκε μέσω της γωνίας θ_σ που σχηματίζει ο άξονας της σ_1 με τον κατακόρυφο άξονα, και η οποία αυξάνεται κατά 180ο για κάθε πλήρη στροφή. Το Σχήμα 4 δείχνει σχηματικά την διαδρομή των τάσεων που ακολουθείται από την σ_{xy} με την $(\sigma_{yy}-\sigma_{xx})/2$. Η κάθε βηματική αύξηση τάσης είναι εφαπτομενική στην περιφέρεια του κύκλου με σταθερή ακτίνα $(\sigma_1-\sigma_2)/2$.

Καθώς το δείγμα βρίσκεται στην ΚΚ, όπου $q/p=M$, επακολουθεί ότι η ακτίνα του κύκλου είναι ίση με $(1/2)Mp$. Η γωνία που σχηματίζει η ακτίνα με τον άξονα $(\sigma_{yy}-\sigma_{xx})/2$ ισούται με $2\theta_\sigma$. Ο σερβομηχανισμός που χρησιμοποιήθηκε στην ΜΔΣ ορίζει το κατάλληλο πεδίο ταχυτήτων των συνοριακών κόκκων, ώστε να επιτευχθεί η στροφή κυρίων αξόνων των τάσεων, ελέγχοντας την περιοδική μεταβολή των τάσεων $\sigma_{xx}, \sigma_{yy}, \sigma_{xy}$ όπως φαίνεται στο Σχήμα 5(α), με τις ορθές τάσεις να μεταβάλλονται με διπλάσια συχνότητα από τις διατμητικές.

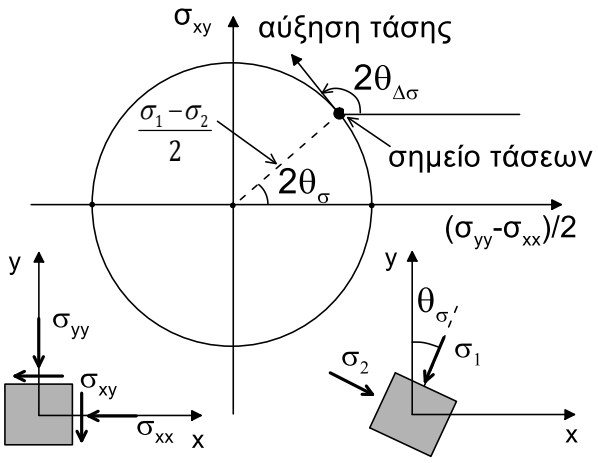

Σχήμα 4: Απεικόνιση της διαδρομής των τάσεων για στροφή των κυρίων αξόνων των τάσεων κατά τη φάση 2 και σχηματικά παρουσίαση των τάσεων

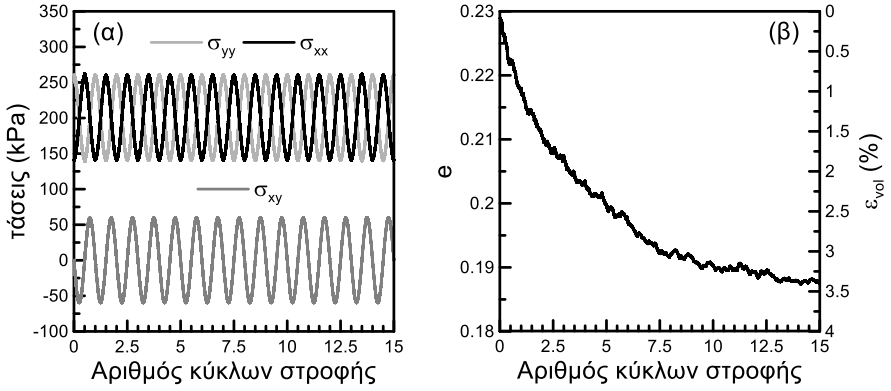

Σχήμα 5: (α) Μεταβολή των τάσεων και (β) του δείκτη πόρων και της ογκομετρικής τροπής με βάση τους κύκλους στροφής των κυρίων αξόνων των τάσεων στη φάση φόρτισης 2

Το Σχήμα 5(β) αποτελεί ένα σχήμα-κλειδί. Δείχνει μείωση του δείκτη πόρων και της αντίστοιχης ογκομετρικής τροπής κατά τη διάρκεια της στροφής των ΚΑ. Ο δείκτης πόρων μειώνεται συνεχώς, κύκλο με τον κύκλο, από την αρχική τιμή $e_c = 0.23$ του στην ΚΚ, σε μία τιμή περίπου $e = 0.188$ η οποία αντιστοιχεί σε μία ογκομετρική τροπή 3.4% από την αρχή της δεύτερης φάσης, βαίνοντας με μειούμενο ρυθμό προς τη σταθεροποίηση μετά από 15 κύκλους. Αυτό το αποτέλεσμα ενσωματώνει ένα πολύ σημαντικό συμπέρασμα: η αρχική μείωση του δείκτη πόρων από την τιμή της ΚΚ, από την αρχή της στροφής των κυρίων αξόνων είναι η σημαντική παρατήρηση που αποδεικνύει τη μη πληρότητα των κλασικών συνθηκών της ΚΚ. Η νέα ΘΑΚΚ μπορεί να περιγράψει και να εξηγήσει την παραπάνω συμπεριφορά, με βάση την τρίτη των συνθηκών της Εξ. (11), όπως θα δειχθεί παρακάτω.

Φάση 3: Διαξονική φόρτιση μετά την στροφή των κυρίων αξόνων των τάσεων και επισκόπηση όλων των φάσεων

Η φόρτιση της τρίτης φάσης, είναι παρόμοια με αυτήν της πρώτης, αλλά περιστραμμένη κατά μία γωνία θ_σ του άξονα της σ_1 με βάση τον κατακόρυφο άξονα, όπου και σταμάτησε η προηγούμενη φάση. Ο σκοπός αυτης της ακτινικής φόρτισης είναι η διερεύνηση της απόκρισης της τάσης και του δείκτη πόρων, ο οποίος είχε μειωθεί κατά την προηγούμενη φάση, και η εξέταση εάν η ΚΚ θα ξαναεπιτευχθεί και πώς. Με στόχο να είναι δυνατή μία επισκόπηση όλης της συμπεριφοράς από την αρχή, τα αποτελέσματα της τρίτης φάσης θα παρουσιαστούν παράλληλα με τα αποτελέσματα των δύο προηγουμένων σε κοινά διαγράμματα, στα Σx. 6 και 7, για δύο επιλογές γωνίας θ_σ. Για την ενιαία παρουσίαση θα χρησιμοποιηθεί η ισοδύναμη αθροιστική αποκλίνουσα τροπή $e_{eq} = \int \sqrt{(1/2)\dot{e}_{ij}\dot{e}_{ij}}\,dt$, με e_{ij} την αποκλίνουσα τροπή σε 2 διαστάσεις. Σε όλα αυτά τα διαγράμματα η φάση 1 παρουσιάζεται με γκρι ανοιχτό, η φάση 2 με μαύρο και η φάση 3 με γκρι σκούρο.

Τα Σχήματα 6(α) και 7(α) δείχνουν τη διαδρομή των τάσεων στο χώρο σ_{xy} και $(\sigma_{yy} - \sigma_{xx})/2$, όπως και στο Σχήμα 4, για όλες τις φάσεις, η τρίτη για θ_σ = 210ο και 0ο μετά από 10 κύκλους αντιστοίχως. Η ακτίνα με γκρι ανοιχτό, ο μαύρος κύκλος και η γκρι ακτίνα εκτός του κύκλου, καθώς και η ομάδα σημείων στην ΚΚ αντικατοπτρίζουν ζωηρά την ιστορία της τάσης σε καθεμιά από τις φάσεις. Η ακτινική έξωθεν του κύκλου τάση (ανεπαίσθητη στο Σχ. 6(α) αλλά εμφανής στο Σχ. 7(α)) περιγράφει την αύξηση του λόγου τάσεων στην αρχή της τρίτης φάσης, όπως φαίνεται και στα επακόλουθα Σχ. 6(β) και 7(β).

Τα Σχ. 6(β) και 7(β) παρουσιάζουν την μεταβολή του λόγου τάσης $\eta = q/p$ με την e_{eq} με τις αναμενόμενες διακυμάνσεις λόγω της ΜΔΣ και στις τρεις φάσεις. Ανεξαρτήτως της τιμής της θ_σ στο τέλος τη φάσης 2 ο λόγος τάσεων η είναι ίσος με αυτόν της ΚΚ M, αλλά αμέσως μετά την έναρξη της τρίτης φάσης εμφανίζεται αύξηση της τιμής του η πάνω από το M (αρχή των γκρι γραμμών στα Σχ. 6(β) και 7(β)), με την αύξηση αυτή να είναι εξεχόντως σημαντική μετά από την πιο έντονη συμπύκνωση στην περίπτωση $\theta_\sigma = 0^o$ μετά από 10 κύκλους και κατόπιν ο λόγος τάσεων πέφτει και παραμένει στην τιμή $\eta = M$.

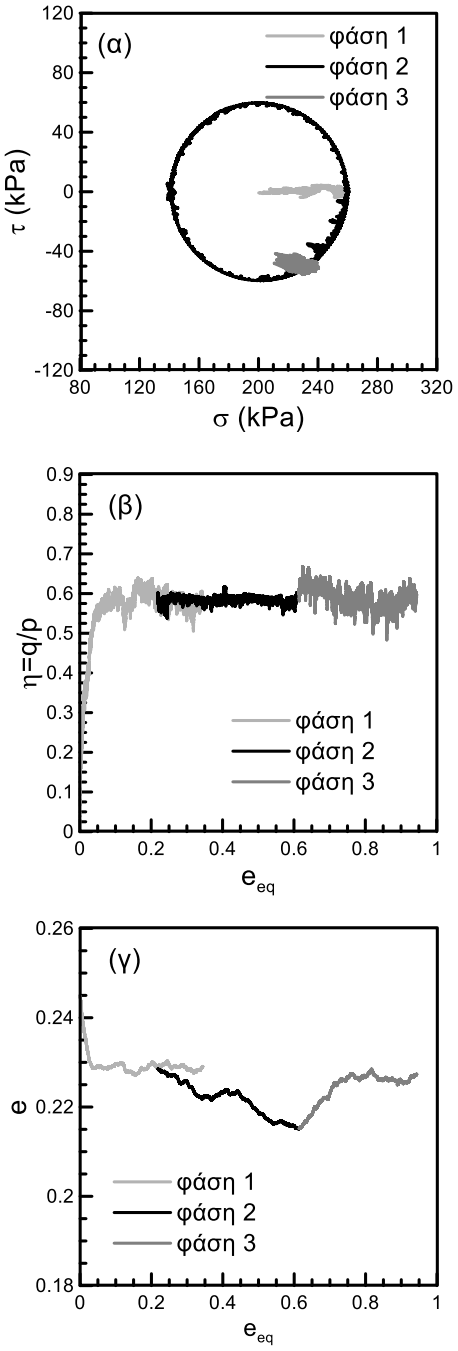

Σχήμα 6: Διαγράμματα για την τριφασική φόρτιση με την τρίτη φάση για $\theta_\sigma = 210^o$: (α) η διαδρομή των τάσεων (β) ο λόγος τάσεων q/p με την e_{eq} (γ) ο δείκτης πόρων e με την e_{eq}

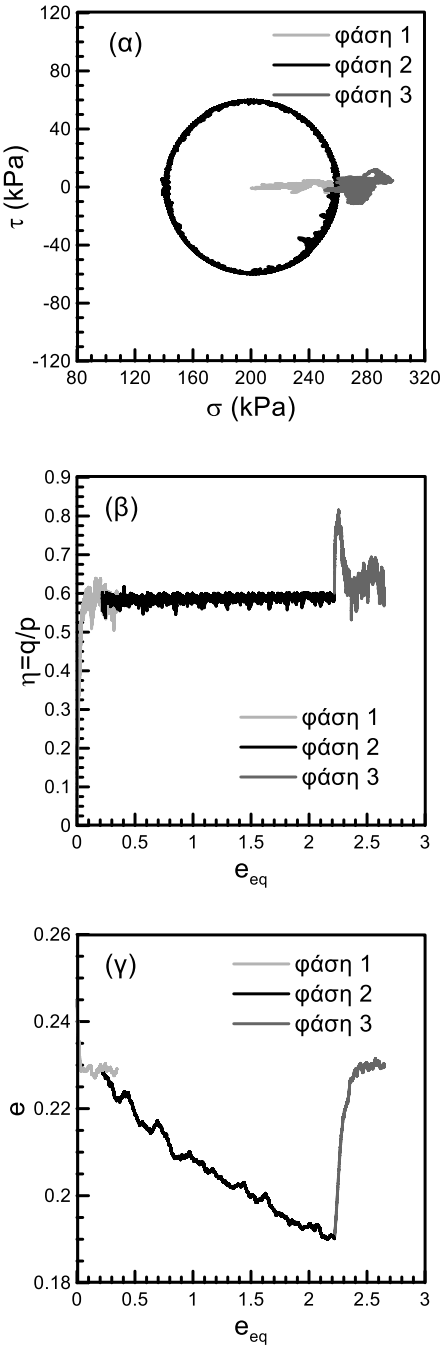

Σχήμα 7. Διαγράμματα για την τριφασική φόρτιση με την τρίτη φάση για $\theta_\sigma = 0^o$ μετά από 10 κύκλους: (α) η διαδρομή των τάσεων (β) ο λόγος τάσεων q/p με την e_{eq} (γ) ο δείκτης πόρων e με την e_{eq}

Τέλος τα Σχήματα 6(γ) και 7(γ) παρουσιάζουν την μεταβολή του δείκτη πόρων καθόλη τη διάρκεια της φόρτισης των τριών φάσεων, με την τρίτη φάση για τις επιλογές των θ_σ = 210ο και 0ο μετά από 10 κύκλους αντιστοίχως. Η βασική παρατήρηση παραμένει και πάλι η δραματική μείωση του δείκτη πόρων κατά τη διάρκεια της δεύτερης φάσης. Ένα πολύ ενδιαφέρον νέο στοιχείο δίδεται από την τρίτη φάση φόρτισης: ο δείκτης πόρων επιστρέφει στην τιμή του στην ΚΚ και παραμένει εκεί, δηλαδή η μείωση του δείκτη πόρων η οποία παρατηρήθηκε κατά τη δεύτερη φάση έχει αντιστραφεί πλήρως και αυτό συμβαίνει ανεξάρτητα των κύκλων φόρτισης που προηγήθηκαν, των τιμών της θ_σ και του e_{eq}. Σε συνδυασμό με το ότι $\eta = M$ υποδηλώνεται ότι η ΚΚ έχει αποκατασταθεί.

4.2 Εξέλιξη της δομής κατά τη διάρκεια του 2Δ πειράματος της ΜΔΣ

Μέχρις εδώ τα αποτελέσματα του αριθμητικού πειράματος απέδειξαν την μη πληρότητα της κλασικής ΘΚΚ δείχνοντας ότι οι δύο κλασικές συνθήκες της Εξ. (9) δεν είναι ικανές ώστε να διατηρηθεί η ΚΚ. Είναι όμως σημαντικό να προταθεί και μία εναλλακτική θεωρία, η οποία θα μπορεί με πληρότητα να περιγράψει τα αποτελέσματα αυτά. Όπως ήδη αναφέρθηκε, αυτή είναι η ΘΑΚΚ των Li & Dafalias (2012) και το νέο στοιχείο είναι ο ρόλος της δομής του υλικού στην ΚΚ. Συνεπώς η εξέλιξη της δομής και οι ποσότητες που σχετίζονται με την ΘΑΚΚ θα παρουσιαστούν σε αυτό το τμήμα, σε ενιαία διαγράμματα, ομοίως όπως στην προηγούμενη ενότητα, ακολουθώντας και την ίδια χρωματική σύμβαση.

Ο τανυστής δομής $\mathbf{F}$ καταρχάς ποσοτικοποιήθηκε μέσω της Εξ. (3) για τα διανύσματα διεπαφών κόκκων. Ο $\mathbf{F}$ κατόπιν αναλύεται μέσω δύο βαθμωτών μεγεθών: τη νόρμα του F που δίδεται ως: $F = \sqrt{tr\mathbf{F}^2} = \sqrt{2}\left|F_I\right| = \sqrt{2}\left|F_{II}\right| = (1/\sqrt{2})\left|F_I - F_{II}\right|$ και τη διαφορά των γωνιών τάσης - δομής ($\theta_\sigma - \theta_F$) που μετράει τη διαφορά της γωνίας θ_F που ορίζεται μέσω της μέγιστης κύριας δομής F_I, από τη γωνία θ_σ του άξονα της σ_1 (Σχ. 4.3) με αναφορά και για τις δύο γωνίες τον κατακόρυφο άξονα y.

Στα Σχήματα 8(α) και 9(α) παρουσιάζονται τα διαγράμματα για τα F και $\theta_\sigma - \theta_F$ και για τις τρεις φάσεις, η τρίτη για θ_σ = 210ο και 0ο μετά 10 κύκλους αντίστοιχα. Το F

αυξάνεται από το μηδέν στην τιμή του στην ΚΚ ($F_c = 1$) κατά τη φάση 1, όπως αναπτύσσεται η ανισοτροπία της δομής, παραμένει ίσο με 1 κατά τη διάρκεια της δεύτερης φάσης, παρόλο που το υλικό εγκαταλείπει την ΚΚ όπως φαίνεται από τη μείωση του δείκτη πόρων και μετά από μία δραματική αύξηση πάνω από το 1 στην αρχή της τρίτης φάσης, επιστρέφει στην τιμή της ΚΚ, $F_c = 1$. Στο ίδιο σχήμα η διαφορά $\theta_\sigma - \theta_F$ παραμένει, κατά μέσο όρο μηδέν κατά τη διάρκεια της πρώτης φάσης με κάποιες διακυμάνσεις από -3° έως 3° λόγω της ασταθούς κατάστασης του δείγματος, το οποίο βρίσκεται σε εξαιρετικά χαλαρή κατάσταση, ενώ κατά την τρίτη φάση η διαφορά $\theta_\sigma - \theta_F$ είναι πρακτικά μηδέν χωρίς διακυμάνσεις (λόγω πυκνότερης κατάστασης).

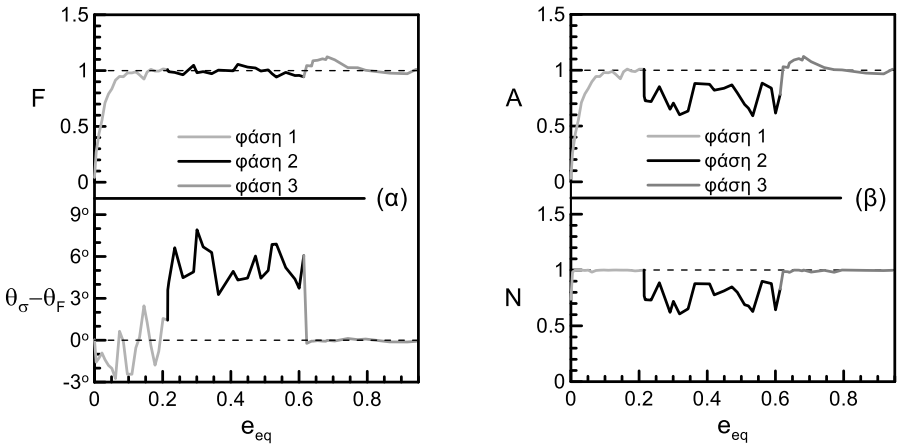

Σχήμα 8: Διαγράμματα ποσοτήτων δομής κατά την τριφασική φόρτιση με την φάση 3 για $\theta_\sigma = 210^o$: (a) F και $\theta_\sigma - \theta_F$ (β) $A = F\mathbf{n}_F : \mathbf{n}$ και $N = \mathbf{n}_F : \mathbf{n}$

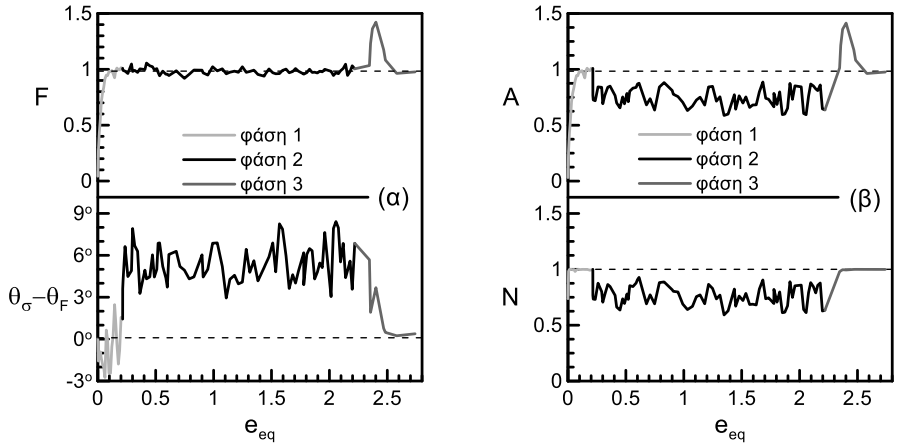

Σχήμα 9: Διαγράμματα ποσοτήτων δομής κατά την τριφασική φόρτιση με την φάση 3 για $\theta_\sigma = 0^o$ μετά από 10 κύκλους: (α) F και $\theta_\sigma - \theta_F$ (β) $A = F\mathbf{n}_F : \mathbf{n}$ και $N = \mathbf{n}_F : \mathbf{n}$

Κατά τη διάρκεια της δεύτερης φάσης η διαφορά $\theta_\sigma - \theta_F$ κυμαίνεται μεταξύ 3^0 και 8^0 και για τις δύο περιπτώσεις γωνίας θ_σ. Η αύξηση από 0^0 (κατά μέσο όρο στη φάση 1) λαμβάνει χώρα με μία αρκετά γρήγορη μεταβολή μέσα στο πρώτο τέταρτο του πρώτου κύκλου της δεύτερης φάσης, ενώ έτσι συμβαίνει και στην αντιστροφή της, από τη φάση 2 στην 3. Η εν λόγω ανάλυση καταδεικνύει ότι η τάση και η δομή είναι συγγραμικές κατά τις φάσεις 1 και 3, ενώ στη δεύτερη φάση γυρίζουν ταυτόχρονα, με τους κύριους άξονες της δομής να ακολουθούν αυτούς της τάσης με καθυστέρηση περίπου $\theta_\sigma - \theta_F = 5^o$ κατά μέσο όρο.

Παρόμοια αποτελέσματα για τις τάσεις και για τη δομή κατά την στροφή των κυρίων αξόνων έχουν παρουσιαστεί στη βιβλιογραφία, για 2Δ, αλλά χωρίς να ξεκινούν από την ΚΚ. Αυτή η διαφοροποίηση όμως είναι που αποτελεί την πλέον σημαντική διαφορά στην παρούσα εργασία. Ειδικώς στους Li & Yu (2010) και Fu & Dafalias (2015) η ένταση της δομής, η οποία ορίζεται ως $\alpha_F = \sqrt{2}F$, παραμένει κατά προσέγγιση σταθερή κατά τη στροφή, ενώ η διαφορά $\theta_\sigma - \theta_F$ κυμαίνεται από –4^o έως 8^o και από 5^o έως 8^o για τις δύο προαναφερόμενες εργασίες, πολύ κοντά στα παρόντα ευρήματα.

Τα Σχ. 8(β) και 9(β) παρουσιάζουν τα διαγράμματα των N και A κατά τις τρεις φάσεις φόρτισης, η τρίτη σε θ_σ = 210^o και 0^o μετά από 10 κύκλους, αντιστοίχως. Κατά τις φάσεις 1 και 3 $N = 1$, ενώ κατά τη δεύτερη φάση το N κυμαίνεται περίπου στο 0.8. Με βάση την Εξ. (3.5) προκύπτει $N = \mathbf{n}_F : \mathbf{n} = \cos 2\varphi$ με $\varphi = \theta_n - \theta_F$ τη γωνία μεταξύ των κατευθύνσεων των $\mathbf{n}$ και $\mathbf{F}$ (μέσω του $\mathbf{n}_F$), εκπεφρασμένο μέσω της διαφοράς των γωνιών θ_n και θ_F. Συνεπώς, $\theta_n - \theta_F = (1/2)\cos^{-1} N$ το οποίο καταλήγει σε $\theta_n - \theta_F = 0$ για $N = 1$ κατά τις φάσεις 1 και 3 υποδηλώνοντας συγγραμικότητα των $\mathbf{F}$ και $\mathbf{n}$, και $\theta_n - \theta_F = 18^o$ για $N \simeq 0.8$, περίπου, κατά τη φάση 2, υποδηλώνοντας ότι οι κύριοι άξονες του $\mathbf{F}$ ακολουθούν με μία διαφορά φάσης 18^o αυτούς του $\mathbf{n}$ κατά την στροφή των αξόνων της τάσης. Συνδυάζοντας την προηγούμενη παρατήρηση, ότι κατά τη φάση 2 $\theta_\sigma - \theta_F = 5^o$ κατά μέσο όρο, ακολουθεί ότι $\theta_n - \theta_\sigma = 18^o - 5^o = 13^o$, δηλαδή οι κύριοι άξονες της τάσης ακολουθούν με μία διαφορά φάσης 13^o τους κύριους άξονες του $\mathbf{n}$ κατά την στροφή των αξόνων του δευτέρου.

Συνοψίζοντας κατά τις φάσεις 1 και 3 οι κυρίοι αξόνες της τάσης του $\mathbf{F}$ και του $\mathbf{n}$ είναι συγγραμικές, με απότομη μεταβολή προς και από τη δεύτερη φάση κατά την οποία οι

κύριοι άξονες του **F** ακολουθούν αυτούς της τάσης με μία διαφορά φάσης 5^o, ενώ οι κύριοι άξονες της τάσης ακολουθούν αυτούς του **n** με διαφορά φάσης 13^o, ενώ όλα τα ζευγάρια στρέφονται ταυτοχρόνως. Υπογραμμίζεται ότι, εάν για την ποσοτικοποίηση της δομής του υλικού χρησιμοποιηθεί η δομή των κενών (μέσω των εξισώσεων 4 ή και 5) αντί της δομής των διανυσμάτων διεπαφής, ποιοτικά τα αποτελέσματα παραμένουν ίδια. Η μόνη ουσιαστική διαφορά έγκειται στην μεγαλύτερη καθυστέρηση στροφής των κυρίων αξόνων της δομής των κενών σε σχέση με αυτή των διανυσμάτων διεπαφής. Συνεπώς, εάν λαμβάναμε υπόψη στην στροφή των κυρίων αξόνων και αυτούς της δομής των κενών, αυτοί θα έρχονταν τελευταίοι με διαφορά περίπου 6^o από τους κύριους άξονες της δομής των διανυσμάτων διεπαφής.

Με βάση την παραπάνω ανάλυση στο τέλος των φάσεων 1 και 3 η Μεταβλητής Ανισοτροπίας Δομής $A = A_c = 1$, κατά μέσον όρο με μικρές διακυμάνσεις, όπως επίσης και τιμές του λόγου τάσεων και του δείκτη πόρων έχουν φτάσει σε αυτές της ΚΚ, Σχ. 6(b και c), 7(b και c). Κατά τη δεύτερη φάση προκύπτει ότι $A \simeq 0.8 < 1$ για τα Σχ. 8(b) και 9(b), ενώ κατά την πρώτη περίοδο της φάσης 3 $A \simeq 1.1 > 1$ (Σχ. 8(b)), και $A \simeq 1.25 > 1$ (Σχ. 9(b)), κατά μέσον όρο. Καθώς $A = FN$ από την Εξ. (9), η εξέλιξη του A είναι πολύ κοντά στο N όταν $F \approx 1$ κατά μέσο όρο στο τέλος της φάσης 1, κατά τη διάρκεια της φάσης 2 και τέλος κοντά στο τέλος της τρίτης φάσης.

5. Αριθμητικά πειράματα 3Δ με τη ΜΔΣ

Κατόπιν της υλοποίησης του επιθυμητού ειδικού αριθμητικού πειράματος σε 2Δ, πραγματοποιήθηκε η επέκταση της μεθόδου και η εφαρμογή του και σε 3Δ. Ένα εύλογο ερώτημα θα ήταν ποια η ανάγκη επέκτασης των αποτελεσμάτων που έχουν ήδη επιτευχθεί και, επιπλέον, γιατί να παρουσιάζονται εν γένει αποτελέσματα σε 2Δ, αντί κατευθείαν η ανάλυση να πραγματοποιείται σε 3Δ. Στο δεύτερο ερώτημα οι λόγοι για τα 2Δ αποτελέσματα σχετίζονται κυρίως με δύο βασικούς παράγοντες: τη σημαντική διαφορά σε όρους υπολογιστικού χρόνου (γι' αυτόν τον λόγο τα λογισμικό 2Δ ΜΔΣ χρησιμοποιούνται ακόμα, ευρύτερα από τα 3Δ) και την ευκολότερη ερμηνεία των αποτελεσμάτων σε 2Δ. Έτσι, σε περιπτώσεις όπου το επιτρέπει η φυσική πραγματικότητα, οι 2Δ απλοποιήσεις μπορούν να παρέχουν τους μηχανισμούς που περιγράφουν διάφορα φυσικά φαινόμενα με πολύ μικρότερο κόστος. Επιπλέον τα 2Δ αποτελέσματα παρουσιάζονται απλώς σε ένα επίπεδο (δυνάμεις, ταχύτητες κλπ.). Αυτή

η άμεση απεικόνιση των πληροφοριών δίνει μια πληρέστερη και απλούστερη εικόνα για τους μηχανισμούς, που, πολλές φορές, είναι αδύνατο να απεικονιστεί σε 3Δ.

Η 2Δ ΜΔΣ έχει αποδειχθεί επαρκής σε αρκετά προβλήματα και χρησιμοποιείται σήμερα εκτενώς. Κατά τα τελευταία έτη τα 2Δ αποτελέσματα είναι σταθερά περισσότερα από αυτά των 3Δ. Παρ' όλα αυτά η ανάλυση 2Δ προφανώς δεν διαθέτει την 3η διάσταση και αυτόματα υποδηλώνεται ότι οποιοδήποτε αποτέλεσμα είναι καθαρά ποιοτικό. Τα συμπεράσματα που εξάγονται από τις 2Δ μπορούν να εκτιμηθούν μόνο ποιοτικά από άποψη μηχανισμών και εννοιών, οι οποίες μερικές φορές πρέπει να επιβεβαιωθούν και σε τρεις διαστάσεις. Οι 2Δ αναλύσεις μπορούν να αποτελέσουν μια εξαιρετική βάση επί της οποίας στη συνέχεια να εκτελεσθούν και να ερμηνευθούν ευκολότερα αυτά των 3Δ με τη βοήθεια της 2Δ απεικόνισης. Απαιτείται μεγάλη προσοχή όταν χρησιμοποιούνται αποτελέσματα 2Δ χωρίς επέκταση σε 3Δ. Ποσοτικά, σε 3Δ, οι ιδιότητες της μάζας, οι τιμές του δείκτη κενών και του μέσου όρου των επαφών ανά σωματίδιο, αναμένεται να είναι πολύ διαφορετικοί από τις 2Δ. Επομένως η ανάλυση 3Δ προτείνεται να ακολουθεί πάντοτε οποιαδήποτε σημαντικά αποτελέσματα, όπως η ατέλεια μιας σημαντικής θεωρίας, που εξάγονται από 2Δ. Ένα επιπλέον κέρδος σε αυτήν την περίπτωση είναι η σύγκριση της συχνά εφαρμοζόμενης 2Δ ΜΔΣ, με τα αποτελέσματα σε 3Δ, σε ένα σημαντικό πείραμα.

Αν και οι έννοιες και οι αρχές για τις παρούσες πειραματικές διαδικασίες και τα αναμενόμενα αποτελέσματα ήταν ποιοτικά τα ίδια όπως στις 2Δ, η εξέταση της 3ης διάστασης δημιούργησε πολλές πρακτικές προκλήσεις. Καταρχάς η απεικόνιση των αποτελεσμάτων είναι πιο δύσκολη και σε πολλές περιπτώσεις μπορεί να προκαλέσει σύγχυση, παρά σαφήνεια.

Επιπροσθέτως ένας επιπλέον άξονας σημαίνει τρία επιπλέον στοιχεία όσον αφορά τους - συμμετρικούς – τανυστές δεύτερης τάξης (τάση, τροπή και δομή). Έτσι υπάρχουν τρεις κύριες τιμές και τρεις κύριες ιδιοκατευθύνσεις, η καθεμία εκ των οποίων χρειάζεται τουλάχιστον δύο παραμέτρους, για να οριστεί (π.χ. δύο γωνίες, ως προς τις σφαιρικές συντεταγμένες). Όμως και πάλι μπορεί να χρησιμοποιηθεί μόνο μία νόρμα για την ποσοτικοποίηση της έντασης του τανυστή (βλ. Li & Dafalias, 2012). Επιπλέον η εφαρμογή ενός πεδίου ταχυτήτων επί των συνοριακών κόκκων στην γενική περίπτωση, όπως εφαρμόστηκε στις 2Δ, προσέθεσε σημαντική πολυπλοκότητα. Οι τεχνικές της εφαρμογής των ειδικών μεθόδων που χρησιμοποιήθηκαν στο προηγούμενο κεφάλαιο, για την 2Δ περίπτωση, χρειάστηκε να επεκταθούν πλήρως σε

3Δ.

Οι τρεις πειραματικές φάσεις που εφαρμόστηκαν και στην περίπτωση αυτήν ήταν: φάση 1 τριαξονική φόρτιση, φάση 2 στροφή των κύριων αξόνων (ΚΑ) της τάσης στην κρίσιμη κατάσταση (ΚΚ) και φάση 3 ακτινική φόρτιση ίδιου τύπου με το αρχικό τριαξονικό φορτίο της φάσης 1. Τα αποτελέσματα αναμένονταν να είναι ποιοτικά παρόμοια. Για τις 3 διαστάσεις, όπου το πείραμα έλαβε χώρα, οι τρεις κύριες τάσεις και τροπές είναι $\sigma_i (i=1,2,3)$ και $\varepsilon_i (i=1,2,3)$. Οι παράμετροι p (υδροστατική τάση), q (αποκλίνουσα τάση), ε_v (ογκομετρική τροπή) και ε_q (αποκλίνουσα τροπή) ορίζονται ως $p=1/3(\sigma_1+\sigma_2+\sigma_3)$, $q=\sqrt{\left((\sigma_1-\sigma_2)^2+(\sigma_2-\sigma_3)^2+(\sigma_1-\sigma_3)^2\right)/2}$, $\varepsilon_v=\varepsilon_1+\varepsilon_2+\varepsilon_3$ και $\varepsilon_q=2/3\sqrt{\left((\varepsilon_1-\varepsilon_2)^2+(\varepsilon_2-\varepsilon_3)^2+(\varepsilon_1-\varepsilon_3)^2\right)/2}$.

5.1 Μακροσκοπικά Αποτελέσματα

Τα σημαντικότερα συμπεράσματα από τα 2Δ εικονικά πειράματα, δηλαδή η μη πληρότητα της ΘΚΚ και η υποστήριξη της ΘΑΚΚ των Li & Dafalias (2012), υποστηρίζονται ακόμη περισσότερο από τα αποτελέσματα στις 3Δ. Οι ίδιοι μηχανισμοί αποκαλύπτονται στην εγκατάλειψη της ΚΚ κατά τη διάρκεια της στροφής των κυρίων αξόνων των τάσεων που καθιστά την κλασική ΘΚΚ ατελή. Επιπροσθέτως στην μακροσκοπική και μικροσκοπική ανάλυση ισχύουν παρόμοια ποιοτικά συμπεράσματα στις 2 και στις 3 διαστάσεις. Πρόκειται κυρίως για τις ομοιότητες των εφαρμογών 2Δ και 3Δ της ΜΔΣ, που επικυρώνουν τα προηγούμενα συμπεράσματα, καθώς τα συμπεράσματα αυτά ήταν κυρίως εννοιολογικής μορφής.

Το 3Δ πείραμα ΜΔΣ και η επακόλουθη ανάλυση αποκάλυψαν σημαντικές ομοιότητες με μακροσκοπικά αποτελέσματα από φυσικά πειράματα και άλλες λεπτομέρειες, που το 2Δ δεν μπορούσε να συλλάβει με ακρίβεια. Η τριαξονική διαδικασία της φάσης 1 έχει μια μακροσκοπική απόκριση που είναι πολύ ρεαλιστική παρουσιάζοντας διαστολή μετά από αρχική, μικρή συστολή, και οι τιμές που λαμβάνονται για τις παραμέτρους κρίσιμης κατάστασης είναι πολύ κοντά σε εκείνες για πραγματικές άμμους. Έτσι τα αποτελέσματα είναι ποσοτικά συγκρίσιμα και με αυτά των φυσικών πειραμάτων με παρόμοια υλικά (Σχήμα 10).

Φάση 1: Τριαξονική φόρτιση μέχρι την ΚΚ

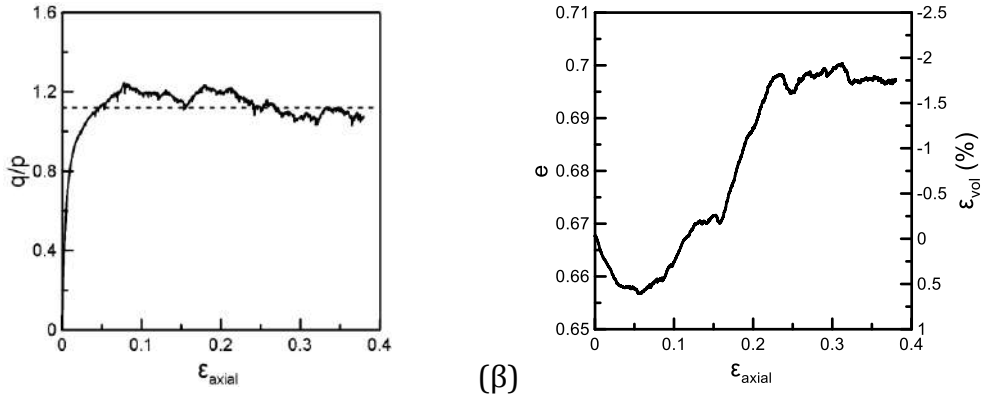

Σχήμα 10: Μακροσκοπική συμπεριφορά της τριαξονικής φόρτισης (φάση 1) (α) λόγος τάσεων η και (β) δείκτης πόρων e, με την κατακόρυφη αξονική τροπή ε_{axial}

Φάση 2: Στροφή των κυρίων αξόνων των τάσεων

Η εξέλιξη του δείκτη πόρων κατά τη διάρκεια της φάσης 2 έχει σαφή τάση για συστολή, αλλά με σαφείς, μικρότερες περιόδους διαστολής (Σχήμα 11), όπως σε φυσικά πειράματα, γεγονός που δεν εμφανίστηκε στις 2Δ. Επιπροσθέτως η συστολή της φάσης 2 πραγματοποιήθηκε σε μεγάλο βαθμό κατά τη διάρκεια των δύο αρχικών κύκλων στροφής, καθώς στη συνέχεια η ογκομετρική τροπή ήταν σημαντικά μικρότερη σε σχέση με τη συνολική. Η συνολική ογκομετρική αλλαγή της φάσης 2 φαίνεται να είναι μεγαλύτερη από ό,τι σε φυσικά πειράματα με άμμο. Υπάρχουν διάφοροι λόγοι που θα μπορούσαν να υποστηρίξουν αυτές τις διαφορές, αλλά θα χρειαζόταν περαιτέρω έρευνα για τη πλήρη διευκρίνιση αυτού του ζητήματος.

Φάση 3: Τριαξονική φόρτιση μετά τη στροφή των κυρίων αξόνων των τάσεων και επισκόπηση όλων των φάσεων

Επιπλέον η φάση 3 αποκαλύπτει την επιστροφή στην ΚΚ, κάτω από την ίδια τιμή του δείκτη πόρων και του λόγου τάσεων, όπως επίσης προτάθηκε σε 2Δ. Ανεξάρτητα από τον προσανατολισμό της τριαξονικής φόρτισης, για την ίδια υδροστατική πίεση, το υλικό θα επιστρέψει στην ίδια ΚΚ, όπως αναμενόταν. Αυτό το συμπέρασμα υποστηρίζει την ανεξαρτησία της ΚΚ στη διαδρομή φόρτισης καθώς, ακόμη και αν η ενδιάμεση φάση 2 αναγκάζει το δείγμα να εγκαταλείψει την ΚΚ, το υλικό εξακολουθεί να αναγνωρίζει την ίδια (Σχήμα 12).

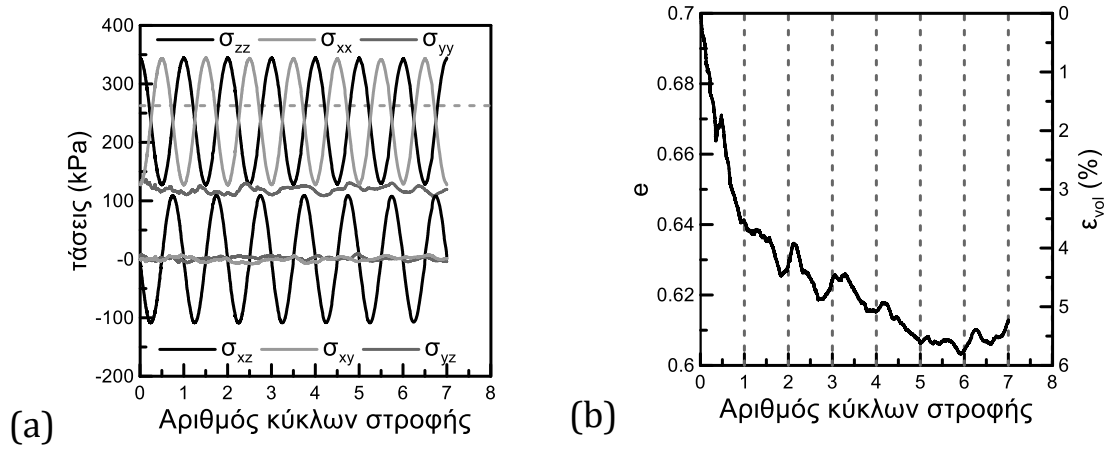

Σχήμα 11: (a)Μεταβολή των τάσεων και (b) μεταβολή του δείκτη πόρων και της ογκομετρικής τροπής, με τον αριθμό των κύκλων φόρτισης (φάση 2)

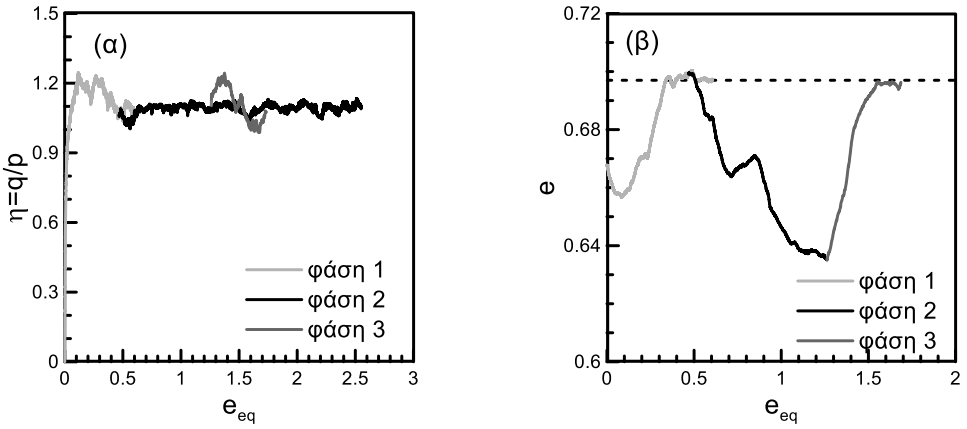

Σχήμα 12: Διαγράμματα κατά την τριφασική φόρτιση για $\theta_\sigma = 90^o$ μετά από 1 κύκλο: (α) ο λόγος τάσεων q/p και (β) ο δείκτης πόρων e με την e_{eq}

5.2 Εξέλιξη της δομής κατά τη διάρκεια του 3Δ πειράματος της ΜΔΣ

Η ανάλυση της δομής της τριφασικής διαδικασίας σε 3Δ αποκαλύπτει παρόμοιες τάσεις με τις 2Δ (Σχήμα 13). Καθώς τα βαθμωτά μεγέθη που χρησιμοποιούνται στην ΘΑΚΚ δεν εξαρτώνται από τις διαστάσεις (η βαθμωτή νόρμα είναι κανονικοποιημένη, ώστε να φτάσει στο 1 στην ΚΚ, ο σχετικός προσανατολισμός της δομής και του ρυθμού πλαστικής παραμόρφωσης κυμαίνεται από 1 έως -1) δεν υπάρχουν διαφορές στις τιμές αυτές καθαυτές.

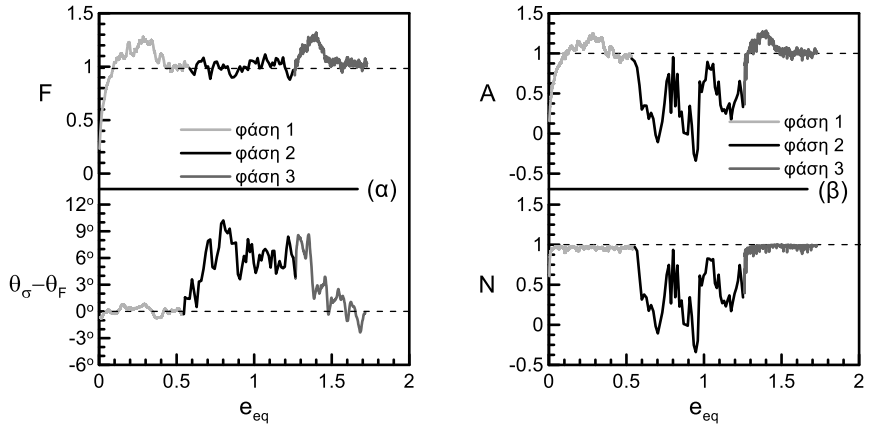

Σχήμα 13: Διαγράμματα ποσοτήτων δομής κατά την τριφασική φόρτιση με την φάση 3 για $\theta_\sigma = 90^o$ μετά από 1 κύκλο: (α) F και $\theta_\sigma - \theta_F$ (β) $A = F\mathbf{n}_F : \mathbf{n}$ και $N = \mathbf{n}_F : \mathbf{n}$

Μολαταύτα στη φάση 2 η υστέρηση μεταξύ των κυρίων κατευθύνσεων της δομής και της τάσης είναι προφανώς μεγαλύτερη σε 3Δ από ό,τι σε 2Δ, ενώ το ίδιο συμβαίνει και με τον ρυθμό πλαστικής τροπής. Και πάλι, όπως και στις 2Δ, ο ρυθμός πλαστικής τροπής στρέφεται πρώτος, ενώ η τάση ακολουθεί και η δομή έρχεται τελευταία. Οι διαφορές μεταξύ τους είναι σαφώς μεγαλύτερες.

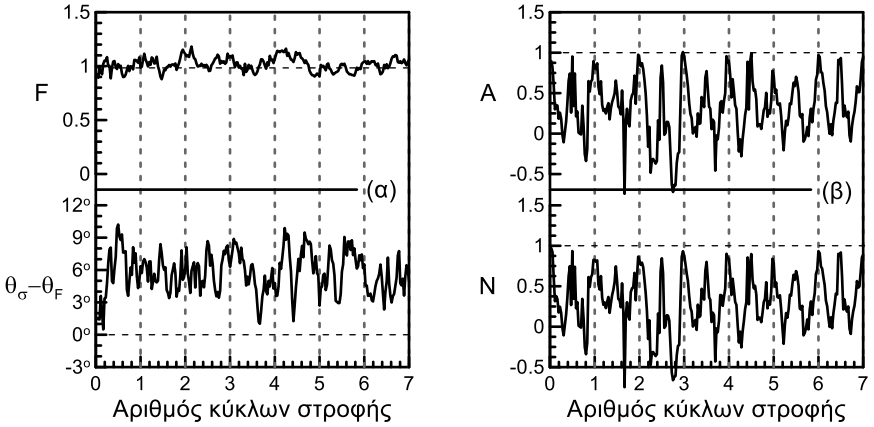

Σχήμα 14: Διαγράμματα ποσοτήτων δομής κατά την δεύτερη μόνο φάση, σε σχέση με τον αριθμό των κύκλων στροφής: (α) F και $\theta_\sigma - \theta_F$ (β) $A = F\mathbf{n}_F : \mathbf{n}$ και $N = \mathbf{n}_F : \mathbf{n}$.

Ο σχετικός προσανατολισμός μεταξύ του ρυθμού πλαστικής τροπής της δομής που ποσοτικοποιείται από το N κυμαίνεται από 1 έως 0 (με το μηδέν να σημαίνει ότι οι δύο τανυστές είναι κάθετοι μεταξύ τους) και παρουσιάζει σαφείς ταλαντώσεις σε σχέση με τους κύκλους στροφής (Σχήμα 14). Αυτές οι ταλαντώσεις δεν είναι τυχαίος θόρυβος και φαίνονται να ακολουθούν τις μεταβολές του δείκτη πόρων από συστολή προς διαστολή. Τέτοιου είδους ταλαντώσεις είχαν εμφανιστεί επίσης στις 2Δ, αλλά οι τιμές

που έλαβαν εκεί (από 0,8 έως 0,5) δεν επέτρεψαν να καταγραφούν με σαφήνεια, δεδομένου του αριθμητικού θορύβου της ανάλυσης.

6. Συμπεράσματα

Το ειδικό αριθμητικό πείραμα που πραγματοποιήθηκε και παρουσιάστηκε σε αυτή την εργασία, σε 2 και 3 διαστάσεις, είχε ως έναυσμα το γεγονός ότι η ΘΚΚ θεμελιώθηκε ελλείψει μιας παραμέτρου δομής, χαρακτηριστικό που έχει επικριθεί σοβαρά κατά το παρελθόν. Συγκεκριμένα η ΘΑΚΚ των Li & Dafalias (2012) αμφισβήτησε τις κλασσικές συνθήκες της ΘΚΚ προτείνοντας μία επιπλέον προϋπόθεση, παρέχοντας το κίνητρο για την παρούσα πειραματική διαδικασία.

Ως αποτέλεσμα το εν λόγω πείραμα προέκυψε ως αναγκαιότητα, προκειμένου να συγκριθούν οι δύο θεωρίες και οι υποθέσεις τους, οι οποίες είναι θεμελιώδους σημασίας για τους τομείς των κοκκωδών υλικών και της εδαφομηχανικής. Πραγματοποιήθηκε μία τριφασική πειραματική διαδικασία σε 2Δ και 3Δ, χρησιμοποιώντας τη ΜΔΣ. Αυτή η αριθμητική μέθοδος ήταν και ο μόνος τρόπος για να πραγματοποιήσουμε την επιθυμητή διαδικασία, καθώς οι φυσικοί περιορισμοί καθιστούν ένα τέτοιο φυσικό πείραμα πολύ δύσκολο, έως και αδύνατο. Η υλοποίηση των τριών φάσεων που έχει εφαρμοστεί σε κυκλικά (σε 2Δ) και σε σφαιρικά (σε 3Δ) διακριτά στοιχεία αποκάλυψε διάφορες πτυχές των χαρακτηριστικών του υλικού σχετικά με την απόκριση ενός κοκκώδους δείγματος, ειδικά στο καθεστώς Κρίσιμης Κατάστασης, τα οποία είναι εξαιρετικά ενδιαφέροντα και σημαντικά. Στη διαδικασία υλοποίησης αυτού του πειράματος επιλύθηκαν διάφορα τεχνικά ζητήματα εξελίσσοντας την πιθανή χρήση της ΜΔΣ, ειδικά στην περιοχή της ΚΚ.

Κατά τη διάρκεια της κύριας, δεύτερης φάσης, πραγματοποιήθηκε στροφή των κύριων αξόνων (ΚΑ) της τάσης, διατηρώντας τις κύριες τιμές που καθορίστηκαν από την ΚΚ, μια διαδρομή φόρτισης που δεν είχε επιτευχθεί ποτέ πριν. Αυτή η διαδρομή τάσεων παραβίασε μόνο την τρίτη συνθήκη που σχετίζεται με τη δομή στην Εξ. (11). Στη συνέχεια παρατηρήθηκε μια δραματική μείωση του δείκτη πόρων, σε αντίθεση με ό,τι προέβλεπε η κλασσική ΘΚΚ. Η ΚΚ εγκαταλείφθηκε σχεδόν άμεσα, όταν οι κύριοι άξονες της τάσης απέκλιναν από την αρχική διαμόρφωση του τριαξονικού φορτίου της φάσης 1, παρόλο που ο λόγος τάσεων και ο δείκτης πόρων βρίσκονταν στις τιμές της ΚΚ, και η υδροστατική τάση διατηρήθηκε σταθερή. Έτσι η τρίτη προτεινόμενη συνθήκη της

ΘΑΚΚ προκύπτει ως αναγκαία προσθήκη στις πρώτες δύο συνθήκες και οι τρεις μαζί είναι πλέον ικανές και αναγκαίες για την επίτευξη της ΚΚ.

Επιπρόσθετα με τη φόρτιση της φάσης 3 μια ακτινική φόρτιση τριαξονικού τύπου που πραγματοποιήθηκε μετά τη φάση 2, παρατηρήθηκε ότι το υλικό, υπό την ίδια υδροστατική πίεση θα φθάσει αναμφίβολα στην ίδια ΚΚ, όταν πληρούνται οι απαραίτητες συνθήκες. Ο δείκτης πόρων ανέκαμψε στην τιμή του την ΚΚ με άμεσο τρόπο, ενώ ο λόγος τάσεων αυξήθηκε σε μια μέγιστη τιμή, λόγω της συμπύκνωσης που σημειώθηκε κατά τη διάρκεια της φάσης 2, και στη συνέχεια έπεσε και πάλι στην τιμή του στην ΚΚ.

Η μακροσκοπική απόκριση του δείγματος συμπληρώθηκε από την παρατήρηση της εξέλιξης της δομής και άλλες παραμέτρους που ορίζονται από τη ΘΑΚΚ, δηλαδή τη νόρμα της δομής, τον σχετικό προσανατολισμό της κατεύθυνσης φόρτισης (που ορίζεται με βάση το ρυθμό πλαστικής τροπής) και της δομής και την Μεταβλητή Ανισοτροπίας Δομής (ΜΑΔ). Η δομή του εδάφους έχει ποσοτικοποιηθεί κυρίως μέσω των κάθετων διανυσμάτων των διεπαφών των σωματιδίων, όμως και η χρήση της δομής των κενών στην παρούσα περίπτωση δεν αναμένεται να αλλάξει τα αποτελέσματα ουσιωδώς, όπως αποδείχθηκε και στις αναλύσεις 2Δ.

Κατά τη διάρκεια της φάσης 1 και της φάσης 3 το ακτινικό φορτίο τριαξονικού τύπου, η τάση, ο ρυθμός τροπής και η δομή έγιναν συγγραμικά με τους κάθετους και οριζόντιους άξονες, ενώ ο λόγος τάσης αυξήθηκε και η ανισοτροπία της δομής έγινε ισχυρότερη. Τα πιο σημαντικά είναι τα αποτελέσματα της φάσης 2, όπου οι τιμές για τον λόγο τάσεων και τη νόρμα της δομής παρέμειναν σταθερές. Έτσι οι κύριες κατευθύνσεις των τανυστών απέκτησαν ιδιαίτερη σημασία, καθώς οι εντάσεις δεν άλλαξαν. Η κατεύθυνση του ρυθμού πλαστικής τροπής είναι η πρώτη που στρέφεται, ακολουθεί η τάση και η δομή βρίσκεται τελευταία. Η γωνιακή υστέρηση ήταν γενικά μεγαλύτερη μεταξύ του ρυθμού πλαστικής τροπής και της τάσης από ό,τι μεταξύ της τάσης και της δομής.

Ιδιαίτερη έμφαση δόθηκε στο σχετικό προσανατολισμό ρυθμού τροπής - δομής, και ως παράμετρος της ΘΑΚΚ. Η υστέρηση μεταξύ των κατευθύνσεων αυτών των δύο τανυστών φαίνεται να ταλαντώνεται, έτσι ώστε να τείνουν να είναι συγγραμικά στην αρχή και στη μέση κάθε κύκλου στροφής, ενώ τείνουν να αυξάνουν τη διαφορά φάσης μεταξύ των σημείων αυτών. Αυτή η παρατήρηση σχετίζεται και με την παρατηρούμενη

συστολή-διαστολή του δείκτη πόρων κατά τη διάρκεια της περιστροφής των ΚΑ. Επιπλέον, μετά από αρκετούς κύκλους, ο δείκτης πόρων σταθεροποιήθηκε σε μια ελάχιστη τιμή. Αυτές οι παρατηρήσεις συμφωνούν μακροσκοπικά με παρατηρήσεις από φυσικά πειράματα, ακόμη και αν τα τελευταία δεν ξεκίνησαν στην ΚΚ.

Τέλος, υπήρξε η δυνατότητα να συγκριθεί το ίδιο πείραμα σε 2 και 3 διαστάσεις, εξετάζοντας έτσι εάν οι 2Δ θα αρκούσαν για να αξιολογηθούν πλήρως τα φαινόμενα που περιγράφονται. Η περίπτωση 2Δ παρουσίασε σωστά τους γενικούς μηχανισμούς και τις έννοιες απαντώντας στο κύριο ερώτημα, όμως σημαντικές λεπτομέρειες, όπως η σημαντική συστολή του δείγματος κατά την στροφή των κυρίων αξόνων της τάσης στους αρχικούς 2 κύκλους, οι ταλαντώσεις του δείκτη πόρων και οι ταλαντώσεις της Μεταβλητής Ανισοτροπίας Δομής, είχαν κρυφτεί σε 2Δ, ενώ έγιναν εμφανείς σε 3Δ.

NATIONAL TECHNICAL
UNIVERSITY OF ATHENS
SCHOOL OF APPLIED MATHEMATICAL
AND PHYSICAL SCIENCES

Discrete Element Method simulations within Anisotropic Critical State Theory of granular materials

PHD THESIS

ALEXANDROS I. THEOCHARIS

Diploma in Civil Engineering NTUA

SUPERVISOR:

Y. F. DAFALIAS

Em. Prof. NTUA

Athens, June 2017

NATIONAL TECHNICAL
UNIVERSITY OF ATHENS
SCHOOL OF APPLIED MATHEMATICAL
AND PHYSICAL SCIENCES

Discrete Element Method simulations within Anisotropic Critical State Theory of granular materials

PHD THESIS

ALEXANDROS I. THEOCHARIS

Diploma in Civil Engineering NTUA

THREE-MEMBER CONSULTING COMMITTEE

1. Y. DAFALIAS
2. G. BOUCKOVALAS
3. A. PAPADIMITRIOU

SEVEN-MEMBER EXAM COMMITTEE

1. Y. DAFALIAS
2. G. BOUCKOVALAS
3. A. PAPADIMITRIOU
4. E. E. THEOTOKOGLOU
5. E. KONTOU - DROUGKA
6. F. DARVE
7. G. VIGGIANI

Athens, June 2017

Abstract

Critical State Theory (CST) has been the dominant paradigm of a constitutive framework in the soil mechanics and granular material community, since its creation 60 years ago. It is the main framework for most constitutive models concerning granular media, and predicts the steady state that granular materials will reach after extensive deformation during “continued shearing”. This state will be called henceforth Critical State (CS). CST implicitly assumes that, at that state, the material has no important fabric, because it makes no reference to it; however, recent research suggests that a particular strong anisotropic internal structure exists and meaningfully impacts soil’s behavior.

This work is primarily focused on the fabric of granular materials and, in particular, soil. Although soil’s internal structure, which we have come to call soil fabric, appears to be a key element in determining soil behavior, it started being widely researched only during the past two decades. Even though soil is a discrete medium, both in research and in practice, soil is usually modeled and analyzed based on continuum theories. This means that its internal grain structure, which determines soil’s macroscopic response in a crucial way, either is not accounted for, or it is represented by macroscopic internal variables of a continuous nature.

Fabric and its relation to the mechanical response of sand was shown to be so vital, that 5 years ago a new theory has been presented (Anisotropic Critical State Theory – ACST) enhancing the classical CST by adding a fabric-related parameter, as a necessary step towards rendering the theory complete by incorporating in its premises the role of fabric. ACST has been successfully applied as a framework for constitutive modeling, and the addition of fabric in the ACST framework indeed adds great simulative capabilities to the models using it. Nevertheless, despite its increased accuracy and applicability, the necessity of this new theory as an enhancement of the classical CST had not yet been proved, until today. The reason for this is that very special experimental conditions must apply in order to test if the aforementioned modification of CST is necessary, since, in a simple, typical situation (e.g. classical triaxial compression load) CST appears to be complete. However, for different, more complex, but still natural and frequently occurring loading paths (e.g. stress principal axes rotation) it is very difficult to assess whether CST conditions are complete.

In this work, Discrete Element Method (DEM) was used, a modern numerical method that can simulate a granular material at its discrete nature. Through a novel numerical experimental procedure, we conducted very specific 2-dimensional and 3-dimensional virtual experiments, and succeeded to prove that CST is indeed incomplete. The virtual sample was first brought to CS, and then stress Principal Axes (PA) rotation was imposed, keeping stress principal values fixed. The rotation induced void ratio reduction, thus, abandonment of CS, despite the fact the two CST conditions were satisfied at the initiation of the rotation process, since stress principal values were fixed and void ratio was at its critical state value. The recently proposed Anisotropic Critical State Theory (ACST) remedies this incompleteness of CST by enhancing its two conditions by a third one, related to the critical value of fabric anisotropy. This third condition is violated by the stress PA rotation and can explain the aforementioned void ratio reduction.

An extra third phase, similar to the initial triaxial radial path of phase 1, is applied to the sample at various stages of phase 2. It is concluded that the void ratio undoubtedly rebounds to its CS value, along with the stress ratio which reaches a peak value and then, also falls to its CS value. ACST can also explain the response of the sample during the second and the third loading phases, features that classical CST cannot address, since it lacks fabric anisotropy consideration. These loading phases have been implemented and compared in 2 and 3 dimensions, providing qualitatively the same mechanisms while the 3D analysis also provides results quantitatively comparable with real sands.

In conclusion, after the numerical experiment realized with the DEM, the three conditions of ACST are shown to be both necessary and sufficient for reaching and maintaining CS. In addition, the extra fabric condition proposed by ACST is verified, and ACST is proved to be a more complete and accurate theory for describing and predicting soil's behavior.

TABLE OF CONTENTS

Acknowledgements

I would like to express my gratitude to all the people who have contributed in many ways, all these years, in order for this work to be accomplished.

At first, I would like to gratefully thank my supervisor Prof. Yannis Dafalias, for his continuous support and guidance during my Ph.D. studies, and for the opportunity to conduct research with him. I could not have hoped for a better supervisor, both in terms of scientific excellence, but also in terms of personal character. I also thank Prof. George Bouckovalas for being an invaluable teacher, mentor and friend for many years now, since my undergraduate diploma. My sincere thanks to Prof. Achilleas Papadimitriou for a very fruitful collaboration and his excellent comments and suggestions. Special thanks to Prof. Cino Viggiani for his inspiring presence and contribution and to Prof. Marina Pantazidou for her mentorship.

In addition, many thanks along with my deep appreciation go to Dr. Manolis Vairaktaris, for his constant presence, comments, suggestions, and in general for the excellent collaboration we had.

Furthermore, my appreciation goes to the researchers of the laboratory of geomaterials and of the SOMEF group; I especially thank Alexandros and Nikos, Kostas and Myrsini for all the work we did and the fun we had together, and Yannis for his friendship and contribution during the past years. Another thank you goes to my friends, and in particular Petros, Kyriakos, Thodoris, Panagiotis, and Sotiris, for all the times we had together. A special thank you to my guitar teacher Morten and to Tina and Dimitris for their support.

This work would not be realized without the support of my parents, who are also to be credited for this achievement; I thank them for all their care, efforts, inspiration and encouragement. Additionally, a heartfelt thank you to my grandmother, my sister and my brother. Finally, I thank Elina for her love, her moral, as well as, practical support, and Sally for making every day happier.

The research leading to these results received funding from the European Research Council under the European Union's Seventh Framework Program FP7-ERC-IDEAS Advanced Grant Agreement n° 290963 (SOMEF); ERC is gratefully acknowledged.

Dedication

To my parents …

Chapter 1: Introduction

From the morning coffee and corn flakes to rice and nuts, from pharmaceuticals to agricultural fertilizers and cosmetics powders, we encounter, consume, and use granular materials numerous times every day. Indeed, granular materials are the most frequently occurring solid-state kinds of matter in nature. Sand and snow are also natural granular materials of great importance, as they are involved in major natural disasters and other potentially catastrophic events. All these seemingly very different forms of granular media have many common characteristics, which arise from the fact that they consist of solid grains that interact primarily with each other. Larger grains compose, in principle, non-cohesive materials (e.g. sand) while, as the grains tend to be smaller (e.g. less than 0.01mm), they also tend to be more cohesive (e.g. clay soil); the latter kind are often referred to as powders.

Granular media are a special case of matter. Though they are a collection of solid grains and only Newton laws and classical mechanics are needed to describe their mechanics, as an assembly they behave differently than solids, liquids or gases. They can flow like a fluid in an hourglass but they stand like a solid on a pile. They present a mixed behavior based on several factors such as the presence or absence of water, applied forces, boundary conditions etc.; under that perspective, they constitute a complex system rather than a single material. Their complex behavior along with their recurring appearance have attracted great research interest. Note that the grains in granular materials, such as soils and powders, are not extremely small (e.g. less than 1μm) and thus, no small-scale phenomena, such as thermal fluctuations or Brownian motions, occur. It is important to underline that various communities (e.g. soil mechanics, geotechnics, granular physics, powder technology) have worked throughout the years on granular materials but from different perspectives. Efforts have been made during the last 30 years to create a more multidisciplinary approach and unify the concepts and ideas employed in the discourse on granular materials.

Soil is itself a granular material of special interest, which, given its appearance at the earth's crust, has been called "the skin of the earth" (Miller, 1953). Since soil is literally the basis of our every step, it is indeed the foundation for modern human life; thus, we need to understand it especially well. Soil is a critical material for construction, mining,

landslides, and in general for almost every aspect of modern infrastructure and economic growth. Soil serves as the foundation for most constructions, it constitutes the environment for surface and deep mining, and it is the main construction material for infrastructures, such as roads and dams. Most importantly, soil materials are in many cases the critical culprits for large-scale failures and corresponding catastrophes (e.g. Fig 1.1), such as massive landslides, structural collapse, embankment failures, to name only a few. It is critical for the growth and, oftentimes, survival of human beings, that we become better at understanding and accurately predicting soil behavior.

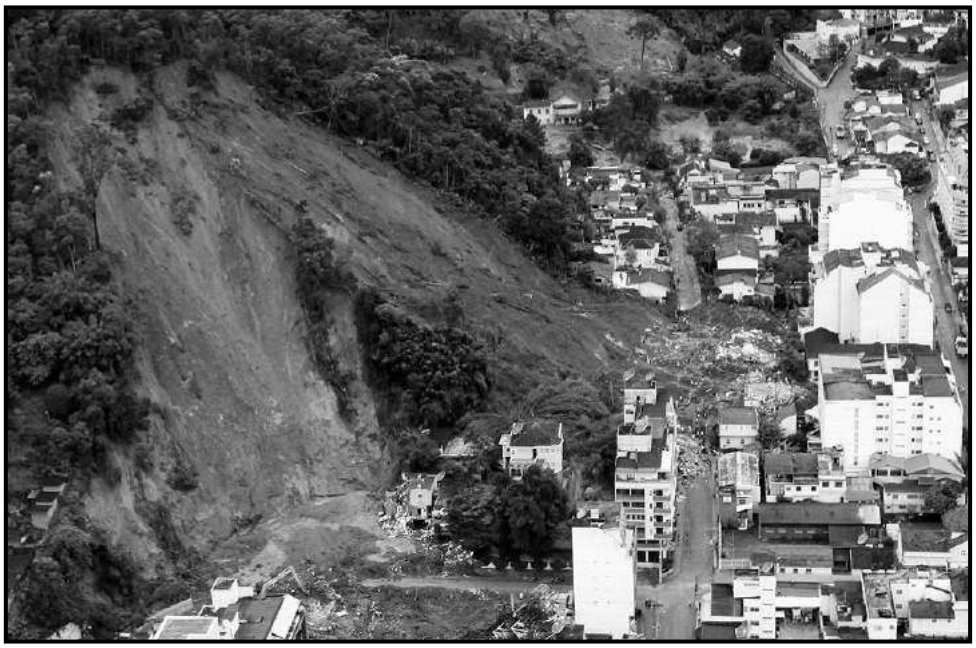

Fig. 1.1. Massive landslide failure in Nova Friburgo, 130 km north of Rio de Janeiro, Brazil, on January 13, 2011 (Shana Reis/AFP/Getty Images)

Soil mechanics was founded as a modern science at the beginning of 20th century. However, earlier contributions came from scientists and engineers on the more general framework of granular materials, unraveling fundamental aspects. Charles-Augustin Coulomb introduced friction as an element for the interactions between the grains (1773, 1781), Osborne Reynolds described dilation scientifically (1885, 1886) and James Clerk Maxwell had recognized the "memory effects" of granular media that he called "historical element" (Darwin, 1883). Making these general features more practical and adding to the soil mechanics knowledge, major contributions to earth-pressure theories, were made by Müller-Breslau *(*1906), Franzius, (1927), Krey (1936), Terzaghi (1925), and Fröhlich (1934); the father of soil mechanics is considered to be Karl von Terzaghi with his *b*ook

"Erdbaumechanik auf Bodenphysikalischer Grundlage", that was published in 1925. After these initial efforts, there has been great progress, specifically during the past 60 years, in the development of experimental, theoretical, and numerical tools that bring a new insight to granular media and geotechnics. Nevertheless, despite the considerable development and research that has been conducted until now, soil mechanics and geotechnical engineering are still considered to be mostly an empirical scientific field.

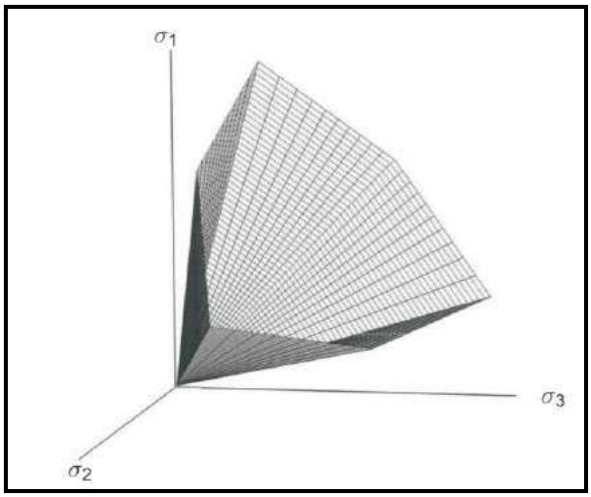

Fig. 1.2. Mohr-Coulomb failure surface in principal stress space

As far as the field of design in geotechnical engineering is concerned, the evolution of computational power and numerical techniques of the second half of 20th century, gave the capability to the geotechnical engineer and researcher to use complex methods and better predict the mechanical response of a soil mass, and consequently of the related soil-structure interaction. There has always been a need to better understand soils, to create constitutive models that can simulate their behavior and to be able to design and predict the soil's mechanical response for all the conditions and applications of engineering purpose. It is important to mention that in the development process of constitutive models, one numerical method, Finite Element Method (FEM), has played a significant role. Through FEM, it is possible to apply even the most complex constitutive models and evaluate the response of a continuum medium that behaves in this way; this provides the considerable power to evaluate, as well as, to use in practice any model to predict the behavior of a soil mass. In brief, FEM made all the complex constitutive models (considerably more complex than the very simple Mohr-Coulomb), and the complex geometries and conditions (i.e. cases that are almost impossible to manipulate by hand) applicable, with only a computational cost continuously reduced.

The first and most well-established law used for soils is the Mohr-Coulomb (Coulomb, 1776), a simple failure criterion that applies to materials where larger compressive, as opposed to tensile, strength is observed (Fig. 1.2); this criterion enhanced with an elastic-perfectly plastic response is the basic model, broadly applied even today, in geotechnics. More advanced constitutive models specialized for soils were proposed years later, to better describe their key features, such as the Drucker-Prager (Drucker & Prager, 1952), the Cam-Clay (Roscoe, Schofield& Wroth, 1958), and the modified Cam-Clay (Roscoe & Burland, 1968; (Fig. 1.3). Furthermore, several models have been proposed during the past decades for soils, that are adopting different modeling views (e.g. hypoelasticity, hyperelasticity, viscoelasticity, plasticity, viscoplasticity) trying to describe, as fully and accurately as possible, soil's mechanical behavior.

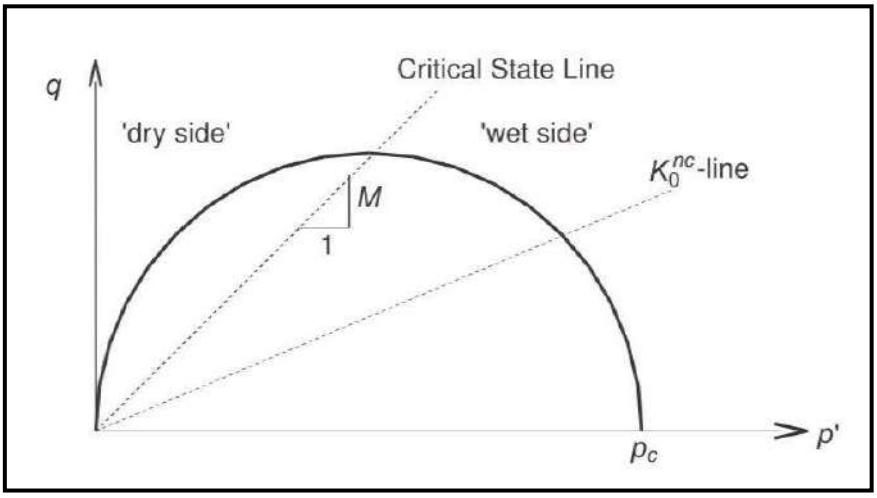

Fig. 1.3. Yield surface of the modified cam-clay model on p'-q plane

A milestone in the soil modeling has been the creation of the Critical State Theory (CST) or Critical State Soil Mechanics (CSSM) framework. Roscoe, Schofield and Wroth (1958) and Schofield and Wroth (1968) proposed a concise framework for the steady state condition reached after sufficient shearing for both clays and sands. This framework has been a central paradigm for the soil mechanics field and stands mostly successfully. Subsequently, CST is at the core of the clear majority of constitutive models specialized for sands and clays (the two major types of soil materials) (e.g. Vermeer, 1978; Manzari & Dafalias, 1997; Jeremic, Runesson & Sture, 1999; Dafalias, Papadimitriou & Li, 2004; Taiebat & Dafalias, 2008). These models are predominantly based on continuum theories of elasto-plastic materials and have been enhanced with pressure-dependent yielding, the possibility of plastic volume change, and dilatancy, which are key properties of soils.

The constitutive models focus on the macroscopic behavior of the soil mass, given that this macroscopic response best describes the consequences, i.e. failure and settlements. Nevertheless, it has been repeatedly stated that the structure of the grains of the soil and its micromechanical response are of importance for soil mechanics. Researching the granular media in its grain structure is the area where soil mechanics clearly overlaps other granular sciences. Features such as the packing properties, force distribution, local arrangements, instabilities, particles' shape, and many others that are important and emerge in the micromechanical analysis of granular structures, have been examined. This micromechanical analysis appears necessary to understand the nature of soils; in this vein, researchers have incorporated elements from the microstructure into the macroscopic behavior.

One such important and possibly key element of the soil behavior, widely considered in soil analysis and modeling during the past two decades, is the fabric of the soil. Even if soil is modeled based on continuum theories, it is a discrete medium, which indicates that it has an internal structure that determines in a crucial way its macroscopic response. Fabric can be defined as the internal structure of the soil, determined mainly by the shape and the contact network of particles, as well as, by the spatial distribution of voids. Advanced models have tried to incorporate fabric to simulate the structure of this discrete medium, and include it in a continuum model (Muhunthan, Chameau & Masad, 1996; Muhunthan & Chameau 1997; Li & Dafalias, 2002; Dafalias, Papadimitriou & Li, 2004; Li & Dafalias, 2012).

The types of soil fabric used in constitutive models according to the existing literature, are related to the particles' orientation, i.e. the way in which the major or minor axis of the grains is oriented (Fig. 1.4(a)), to the contact normal vectors fabric, i.e. the way in which the normal vectors of the contact planes are oriented (Fig. 1.4(b)), and to the void fabric, which refers to the spatial distribution of voids (Fig. 1.4(c)). These three types of fabric manifestation appear to be the most important expressions of soil structure. These three distinct types of fabric have been used separately in most of the existing literature, even if, due to the nature of the material and the definition of each fabric type, they seem to be qualitatively and quantitatively related. So far, little research exists comparing the types of fabric in a way that would reveal any possible relation between them.

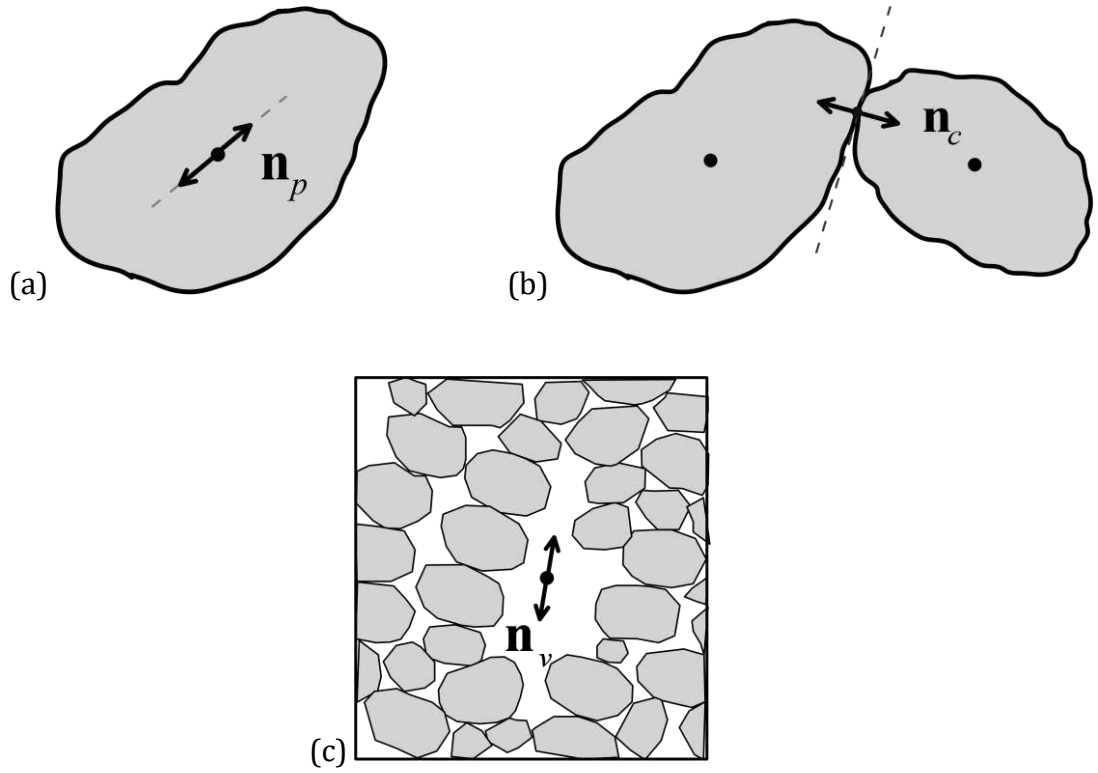

Fig. 1.4. (a) Fabric particle orientation defined by the unit vector $\mathbf{n}_p$ (b) Fabric contact normal defined by the unit vector $\mathbf{n}_c$ (c) void space

Fabric and its relation to the mechanical response of sand is so significant, that Li & Dafalias (2012) presented a theory (Anisotropic Critical State Theory – ACST) that extends the classical CST by adding a fabric-related parameter, considering this addition necessary to render the theory complete. Although ACST has been successfully applied as a framework for constitutive modeling, it has not up to this point been proven that distinctively has a "reason d'etre" far and beyond the classical CST that modified. The addition of fabric in the ACST framework provides great power to the models implementing it, but the theory *per se* has not been supported or disproved through experiments. Special conditions must apply to check if the modification of CST is necessary, as in the typical situations on which CST was built (e.g. classical triaxial compression experiment), is stands complete. However, for different and more complex loading paths that often appear in nature (e.g. stress principal axes rotation) it is not clear if CST conditions are complete and sufficient to guarantee reaching and maintaining Critical Sate (CS).

A major purpose of this thesis has been to produce an experiment that could resolve this ambiguity in a clear fashion. Such a test would create the conditions under which CST and

ACST could be challenged. This special experiment has been found to be the stress principal axes rotation, while keeping the principal stress values constant while being at Critical State (CS). Although at first glance this does not appear to be a very difficult experiment, it had not yet been done in the literature and its difficulties will be revealed and discussed in the sequel.

Due to the difficulty of the realization of the proposed procedure in physical experiments, that will be analyzed later, and since soil's fabric is very difficult to be measured in such experiments, the Discrete Element Method (DEM) has been used (Fig. 1.5) to model the experiments described. This numerical method has been applied in geomechanics since 1979 (Cundall & Strack., 1979), but it has been widely used and developed during the past 20 years. Its unique advantage, is that it constitutes a way of simulating a granular medium and its discrete nature, without needing to use a macroscopic constitutive model, in the absence of a continuum medium. This allows for analyzing a soil mass in its microstructural form in order to get results about the mechanical behavior under several conditions, and to reexamine the assumptions that are used by constitutive models. A disadvantage of DEM is that, as it deals with the solid particles of the discrete medium and the interactions between them, it is yet impossible to apply it on as many grains as there would be in boundary value problems; the computational cost would be unbearable for today's standards.

Hence, since it is not possible to use DEM to simulate a whole solid mass as is presented in real practice, DEM models include as many grains as possible (depending on the computational capabilities of the user) to deduce meaningful results for the mechanisms of soil response. Still, it has been proven many times that the number of particles used for simple experiments suffice to adequately capture the response of the granular materials simulated. Thus, DEM is the appropriate method to measure and describe the fabric evolution for a soil sample in a detailed manner, both qualitatively and quantitatively; it is a very useful tool that can produce results repeatedly, easily, quickly, and in a cost-effective way.

It is important to note that real experiments are irreplaceable, as the physical reality exists only there, without any simulation assumptions. All three types of fabric mentioned above (particle orientation, contact normal and void) could be quantified in physical experiments, e.g. using X-Ray capabilities. Furthermore, although the contact normal fabric is the most usual among constitutive modeling and will be primarily used herein,

it is the fabric that is the most difficult to define and measure physically. This type of fabric is based on the identification of the contact points and the definition of the contact tangent plane and the contact normal plane. This task may be an easy one for numerical experiments, where the geometry of the sample is fully predefined, but it is a difficult task for physical experiments (Jaquet, Andó, Viggiani& Talbot, 2013; Andò, Viggiani, Hall & Desrues, 2013).

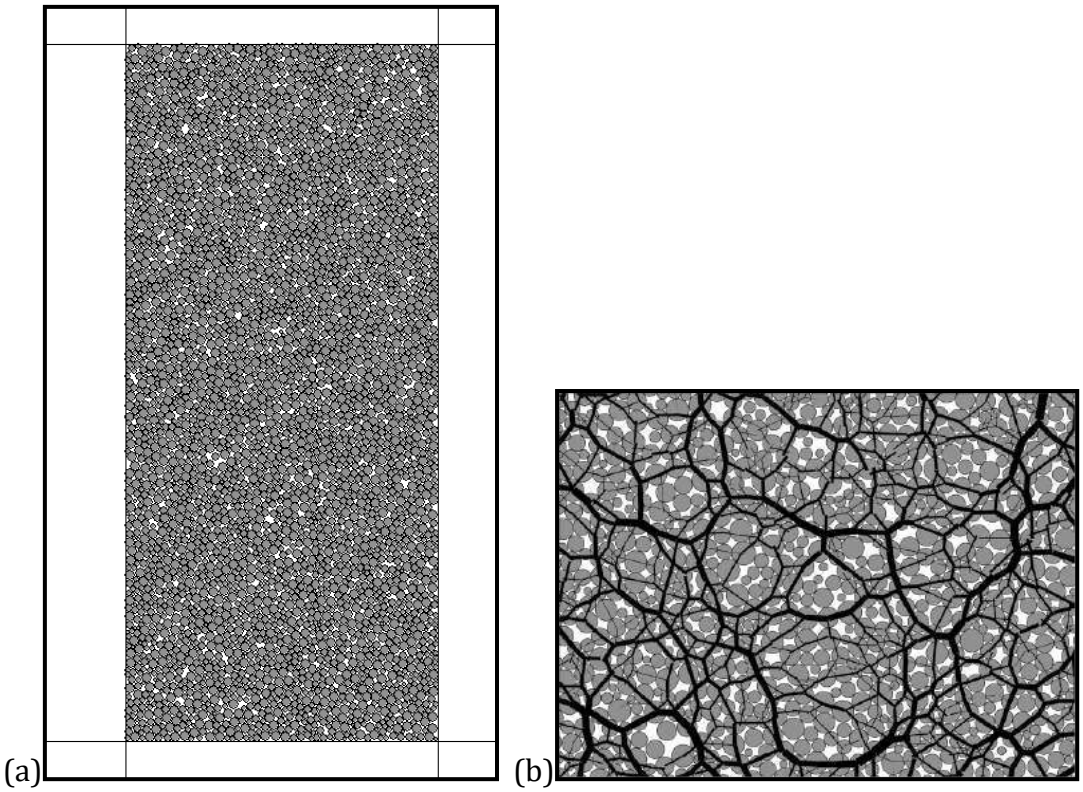

Fig. 1.5. (a) Initial condition for a 2D virtual experiment in vertical compression test in DEM simulation with the software PFC 2D© and (b) a part of this sample zoomed in (forces are with black and their width is proportional to the force's intensity)

More discussion on the fabric quantification possibilities will take place in the next Chapter (Chapter 2), and an extensive description of the ways in which fabric is quantified in general in granular mechanics will follow. Detailed analysis of the three fabric types will be given; furthermore, a new perspective based on existing scan line methods that are used to measure void fabric will be presented alongside a modified and a novel definition for void fabric quantification. In Chapter 3, Critical State Theory will be presented and Anisotropic Critical State Theory will provide the motive and the framework for the experiments and the analysis that follow. At Chapter 4, the 2D innovative virtual experiment by means of DEM will take place; this 2D representation of

granular material has been proven extremely useful for its easier - compared to 3D - interpretation and other advantages. The 2D experiment is founded on the stress Principal Axes rotation (named PA rotation). The analysis of this virtual experiment will reveal the incompleteness of CST and the remedy that ACST can provide. In addition, subsequent monotonic loading after the stress PA rotation phase will prove the very strong CS framework assumption. In Chapter 5, a similar experiment, as in 2D, will take place but in 3D; the 3 dimensions create some limitations on the procedure, but in principle this will also verify the incompleteness of CST. In implementing the 2D and 3D virtual experiments numerous technical difficulties have been overcome, creating new potential in load application procedures in DEM. Finally, the major conclusions will be drawn in Chapter 6.

Chapter 2: Fabric of granular media

2.1. The soil fabric

Soil is a multiphase granular material consisting of solid grains and voids. Particles constitute the solid phase of the soil mass, while the remaining part is the voids, which can be filled with liquid or gas. Thus, voids can be also separated into two sub-phases: the liquid and the gas phase. Usually in soil mechanics, the liquid is water and the gas is air, but other liquids or even gases can be present (e.g. oil or liquid wastes).

The typical phase diagram for soils is presented in Fig. 2.1 and subsequently solid, liquid and gas phases are defined; each phase is characterized by its mass and volume, properties that determine the corresponding density. General macroscopic parameters that are used to represent the relation between solid and void phase are porosity $n = V_v / V$ and void ratio $e = V_v / V_s = n/(1-n)$, where V_v is the volume of the voids, V_s is the volume of the solids, and $V = V_s + V_v$ is the total volume. These parameters define a straightforward way to quantify the relation between the solids and the voids and can be additionally used to characterize the soil's density. Notice that Fig. 2.1 provides the basic information about the phases of the medium, but does not describe the texture of each phase or how these phases interact with each other.

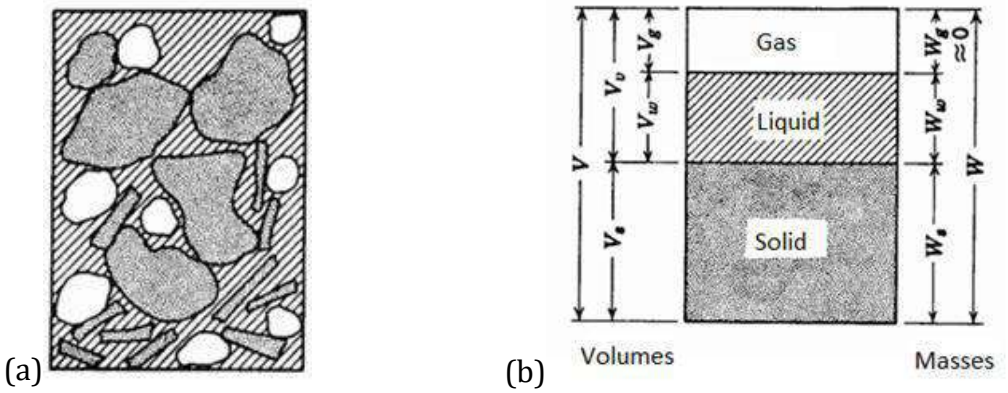

Fig. 2.1. (a) A random distribution of soil's phases and (b) the "phase diagram" of soils (Kavvadas, 2007)

Besides the multiphase character of the soils, another important aspect with a significant effect, especially on the anisotropic mechanical behavior, is the spatial distribution of the

solids and the associated voids. The term fabric is used to describe this texture, the overall spatial and geometric configuration of the soil elements (Brewer, 1964; Oda, 1972a).

2.1.1. Fabric's importance in soil mechanics

Fabric is known as an important determinant of the mechanical response of soils, especially their anisotropic behavior (Casagrande and Carrillo 1944; Arthur and Menzies 1972; Miura, Miura & Toki, 1986; Tatsuoka et al., 1986; Nakata et al., 1998). Some of the most profound experiments in this vein, that are briefly analyzed here to reveal fabric's importance to its full extend, are the experiments of Yoshimine, Ishihara & Vargas (1998); the authors conducted some undrained shear loading experiments on samples of Toyoura sand in a torsional apparatus.

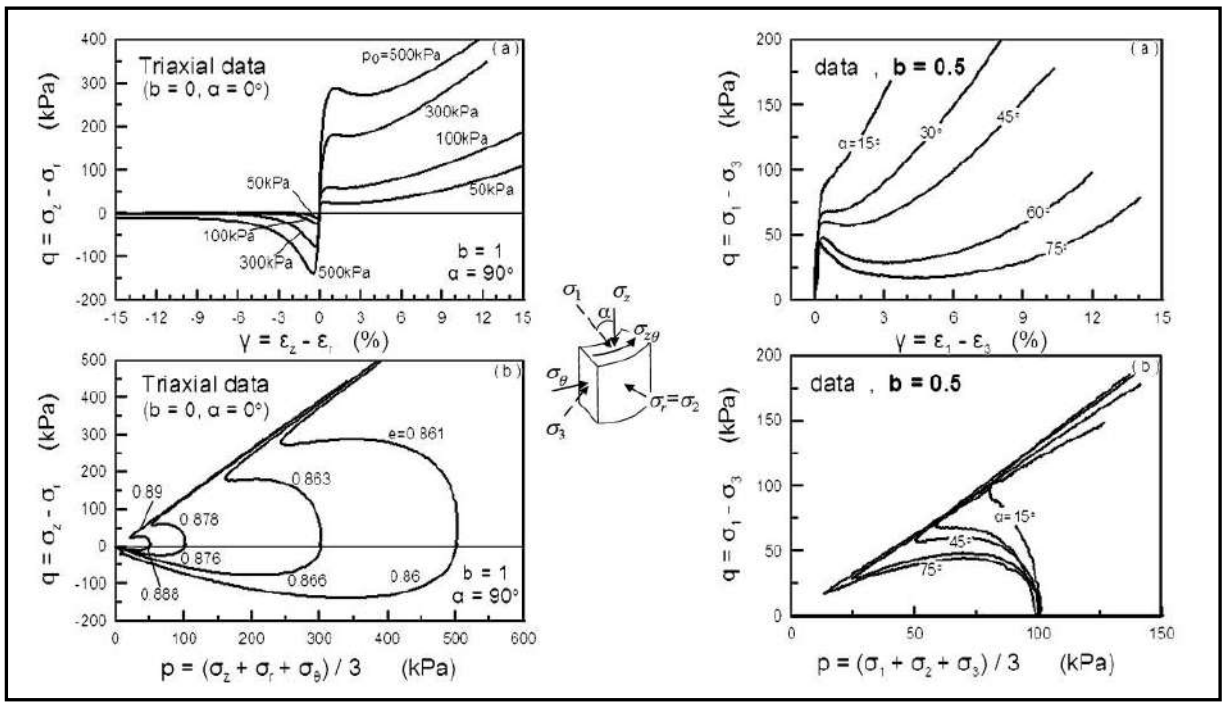

Fig. 2.2. Undrained response of sand samples loaded along different principal stress directions (Yoshimine et al., 1998)

Different values of the stress ratio b ($b=(\sigma_2-\sigma_3)/(\sigma_1-\sigma_3)$) and different orientations of the principal stress directions were applied to examine the response of non-cohesive soils; the results are represented in Fig. 2.2. The first column (left) shows the results concerning different stress ratio b values; different b values lead to triaxial extension or compression. The second column shows the results for constant $b=0.5$ and different

orientation of the principal stress directions; the direction is defined based on the angle α (see Fig. 2.2). The results presented in the first column of Fig. 2.2 are very much indicative of the great differences between the loading conditions of triaxial compression and extension for soils.

The figures of the second column of Fig. 2.2 present the significant importance of fabric, i.e. for different values of angle α, signifying different orientation of the principal stress axis, great differences in the response of the sample are observed. If we assume, as in the experiments, the same loading history, and consider only the different orientation of principal stress, the results diverge significantly. This is an indicative example of the fabric influence on the mechanical response of soil materials. The way the loading direction is oriented with respect to the fabric orientation (e.g. the particles' orientation principal axis) leads to significant differences in the final output. Another important conclusion that could be deducted from these experiments is that the Critical State (CS) conditions seem dependent on the fabric anisotropy and, specifically, on the relative position of the principal stress axis with respect to the orientation of fabric.

2.1.2. Fabric elements

Oda (1972a and 1972b), Satake (1982) and Kanatani (1984) were the first to understand and underline the importance of soil fabric and to initiate micromechanical research on the subject. Oda, Nemat-Nasser & Konishi (1985) and Satake (1992) suggested that the three important micromechanical fabric elements for the macromechanical behavior of the granular materials are the solid particles' orientation, the interparticle contacts, and the corresponding voids.

The particles, if they are non-spherical, as is almost always the case, have an axis of preferred orientation; this orientation can be defined either by the major axis in case of oval particles of rice-type, or by the minor axis when the particles tend to have a more platy type, such as lentils. The distribution of the preferred orientation of the grains is an essential element concerning the fabric of granular materials. In the case of pluviation under gravity of elongated grains without cohesion, the final sample would present an anisotropic particles' orientation distribution, with the major axis of the particles being parallel to the bedding plane (Fig. 2.3) and the minor axis being vertical to the bedding plane. This procedure, very usual in nature, would set the particles' orientation fabric (p-

fabric) to be significantly anisotropic at the very initial state of the material. P-fabric has been used extensively in the past for its simple interpretation, its intuitive nature (Oda, 1972a; Satake, 1982; Oda & Iwashita, 1999) and because it is the main element responsible for inherent fabric, i.e. anisotropy created during pluviation under gravity procedures. Nevertheless, it lacks considerable information on the sample's condition, since the particles' orientation is purely geometrical and not related with any macroscopic entities (such as stresses or strains). It remains however a very important element of fabric and it appears to be important for the anisotropic strength of soils (Fu & Dafalias, 2011a; Tong et al., 2014b).

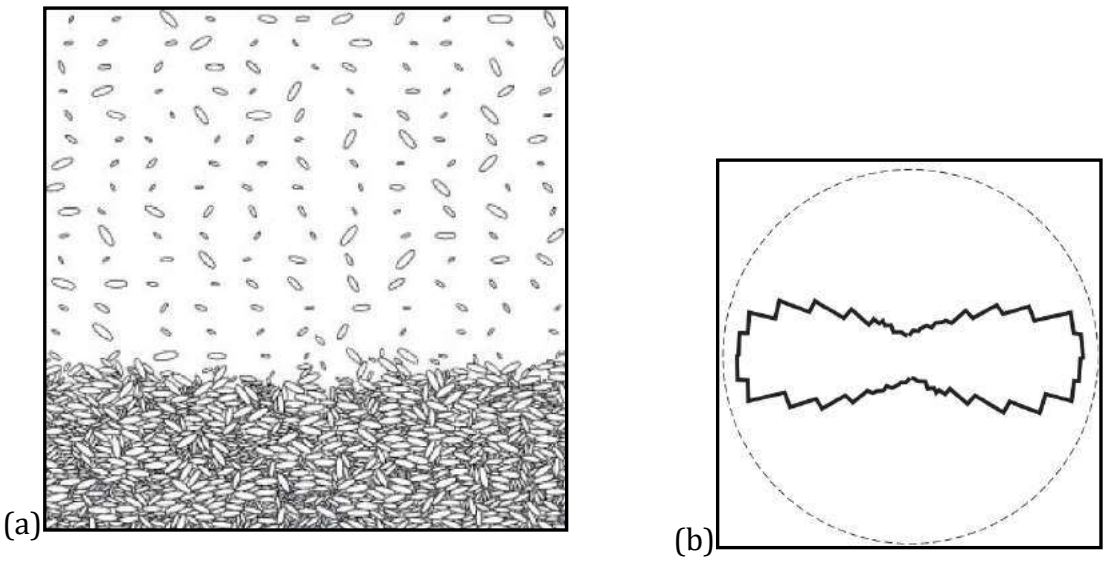

Fig. 2.3. (a) Part of a sample created with pluviation under gravity (Fu & Dafalias, 2011b) and (b) distribution of particle orientation at the end of the pluviation on a polar histogram

Of particular importance for the soil mass are the interparticle contacts, since the forces of the granular medium are transferred through these contacts (Fig. 2.4). The forces' transmission creates chains (force chains) that necessarily pass from the contacts and represent directly the forces' directions. The distribution of the contacts, of the vectors that describe the contacts, and the distribution of the force chains, define a type of contact based fabric. The simplest form of this fabric type is contact normal vector fabric and is defined based only on the unit vectors of each contact that originate from the contact and are vertical to the line (in 2D) or plane (in 3D) that passes through the contact and is tangent to the grains.

This fabric type is extremely popular due to its close relation with the forces, the force chains and the stresses, and the advantages that result from such fabric description (Thorton, 2000; Radjai & Azéma, 2009; Cambou, Jean & Radjai, 2009; Yishmiri & Soga, 2010; Azéma & Radjai, 2011; Li & Yu, 2013; Fu & Dafalias, 2015). In addition, this contact normal fabric (c-fabric), despite being in close association with the forces, it is only geometrically defined, and does not include forces *per se*, as is also the p-fabric. In the same example with pluviation under gravity conditions, as described for the p-fabric, the contacts are obviously preferring vertical alignment, as the main force transfer is made in the vertical direction. This is in accordance with the previous comment about p-fabric; as the particles are oriented horizontally, they contact each other primarily in the vertical direction (parallel to the minor axis of the particles) and less in the horizontal direction.

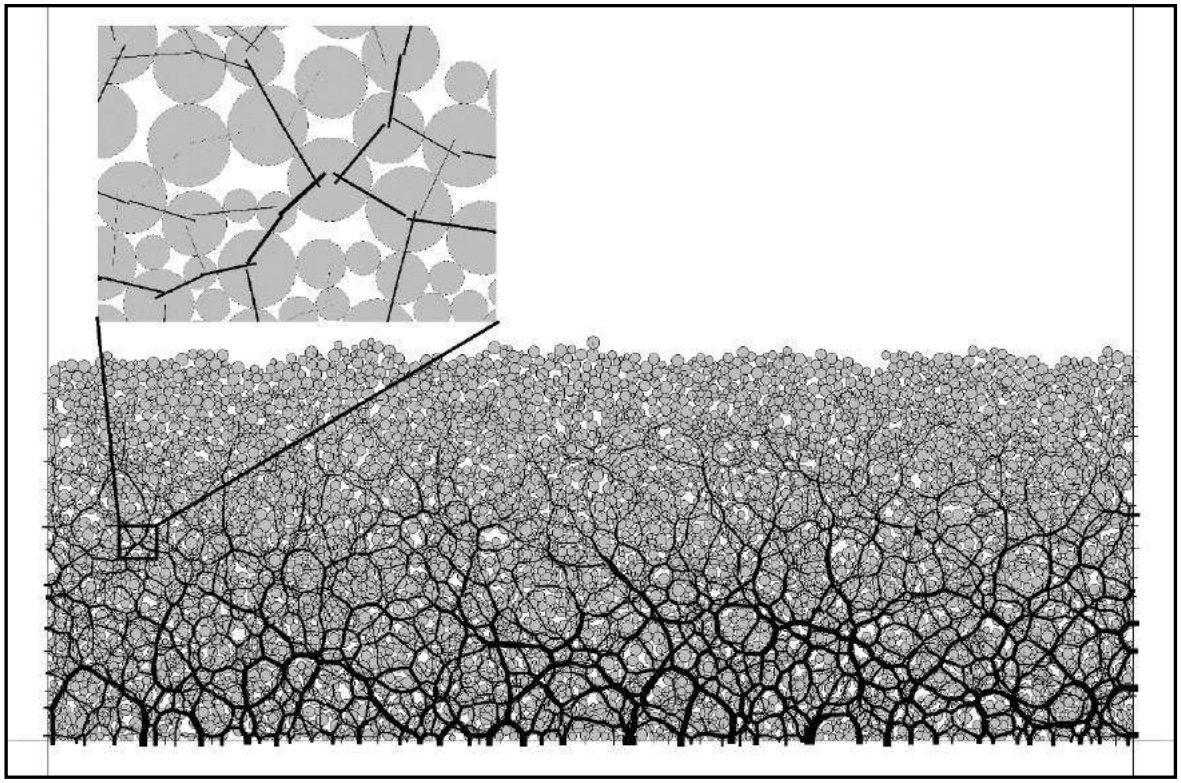

Fig. 2.4. Sample with circular particles pluviated under gravity; forces are with black and their width is proportional to the force's intensity

Finally, a very important element for the soil fabric are the voids between the particles; the void fabric is especially known to affect the hydraulic properties of porous materials. Obviously, the void space is in continuous interaction with the solid mass, as particle movements appear directly related to changes of voids. This means that change in the particles' orientation and contacts (i.e. the important fabric elements of the solid phase)

are directly reflected on the voids, at least from a physical point of view. As the solids and the voids are supplementary, the solid fabric elements and the void fabric elements are already related in a qualitative way.

Several different methods have been proposed to measure the fabric with respect to the voids (Oda et al., 1985; Konishi & Naruse, 1988; Muhunthan, Chameau & Masad, 1996; Kuo, Frost & Chameau, 1998; Kuhn, 1999; Li & Li 2009; Ghedia & O'Sullivan, 2012), because the voids are not easily defined in such a precise way as the solid elements. Different measuring approaches can possibly capture the same characteristics of the void space, with each one having its own advantages and disadvantages. More on this subject will be discussed in the sequel, where an existing void fabric measurement method will be reviewed and modified. Although void fabric is acknowledged to be of importance and is known to be related to the solid phase, the exact relationship between void and solid fabric has just started to attract greater research interest (Li & Li, 2009; Fu & Dafalias, 2011b; Theocharis et al., 2015; Fu & Dafalias, 2015).

Summarizing the above statements, soils consist of non-spherical, random-shaped solid particles that have a characteristic statistical distribution of the fabric quantities described above, which, along with the void space created between the solids, affect the mechanical response of the soil medium. The quantitative definitions of fabric that will be discussed in the rest of this chapter are a way to define the distributions so that the microstructure of the material and the important fabric elements described above, can be quantitatively considered for its response.

2.2. The soil fabric tensor

The most effective and physical way to describe fabric, is through the statistical distribution of the orientation of the different microstructural vector-like entities, based on the analysis of the fabric elements, such as particles' long axes, inter-particle contact normal directions, and void directions expressed by properly defined void vectors. Such fabric-related vectors are then used to define corresponding fabric tensors, which constitute the analytical means to express and quantify fabric and fabric anisotropy.

The most straightforward example that illustrates the simplicity and effectiveness of such a fabric tensor is the case of a 2-dimensional soil analysis; if a second order fabric tensor is used, then three characteristics of the fabric tensor are obtained, two principal values

and the principal angle. These properties schematically define an ellipse that shows most effectively the vectors' distribution through the major and the minor axis, and the angle of rotation of the ellipse. Tensors of higher ranks can be used for a more detailed analysis but for most applications, and for the sake of simplicity, a second order tensor is usually employed.

The fabric tensor seems to play an increasingly important role in constitutive modeling. It is a concise and physical way to thoroughly introduce the fabric into advanced constitutive models. Many researchers have tried to introduce the fabric as an extra variable in a soil constitutive model. Simple models incorporate only the initial state of fabric (Oda & Nakayama, 1989; Dafalias, Papadimitriou & Li, 2004); more advanced models try to introduce a fabric tensor evolution with respect to the properties of the model and the simulation (Li & Dafalias, 2012; Gao et al., 2014). In any case, the fabric parameters are becoming important for the constitutive definitions as the models attempt to describe more complex soil behavior.

The fabric feature of the soils seems to be of even greater importance when considering the Critical State Soil Mechanics (CSSM) framework. Recent advances show that CSSM lacks consideration of a fabric parameter (Li & Dafalias, 2012); this issue will be further discussed in Chapter 3. To fulfill the fabric quantification, it is fundamental to define a soil fabric tensor that can capture the macroscopic mechanical anisotropy and - at the same time - be representative of the material's microstructure.

2.2.1. Fabric based on the solid phase

2.2.1.1. Particle orientation

Soil particles are neither spherical nor ellipsoidal in shape, but it is still possible to define a major axis for their shape. For several grain shapes (such as in Fig. 2.5) a major axis can be calculated, considering the orientation of the soil grain.

Two unit vectors ($\mathbf{n}_p, -\mathbf{n}_p$) are then defined on the major axis (Fig 2.5), that are characteristic of the orientation of the grain. Based on these vectors, the particle orientation fabric of this one particle "p" equals $\mathbf{n}_p \otimes \mathbf{n}_p$ where $\otimes$ is the tensor product and only $\mathbf{n}_p$ (without $-\mathbf{n}_p$) is used. If both vectors are used, a factor 0.5 must be applied in front of the tensor product, yielding the exact same result.

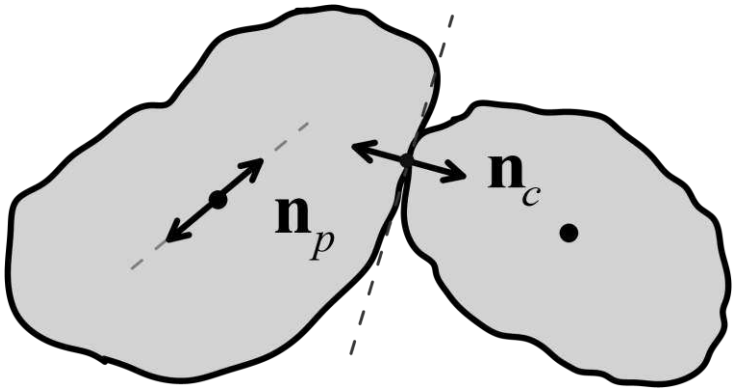

Fig. 2.5. Vectors that describe the microstructure of granular materials: $\boldsymbol{n}_{\mathrm{p}}$ for particle orientation, $\boldsymbol{n}_{\mathrm{c}}$ for contact normal

For a soil sample, the fabric tensor for particle orientation is defined as the sum of all the tensor products of all the soil grains (Oda, 1982; Satake, 1982; Kanatani, 1984):

$$\mathbf{G}_p = \frac{1}{N_p}\sum_{k_p=1}^{N_p} \mathbf{n}_p^{k_p} \otimes \mathbf{n}_p^{k_p} \tag{2.1}$$

$\mathbf{n}_p$ are the particle orientation vectors which describe the fabric, $\otimes$ is the tensor product, $\sum$ implies the summation over all the particles, k_p denotes the $k_p th$ particle, and N_p is the total number of the granular particles of the sample. In many cases, the deviatoric part of the fabric tensor is the most interesting part, given that it is free of the hydrostatic component and provides the very important fabric anisotropy. This deviatoric part is then defined in a 2D setting as:

$$\mathbf{F}_p = \mathbf{G}_p - \frac{1}{2}\mathbf{I} = \frac{1}{N_p}\sum_{k_p=1}^{N_p} \mathbf{n}_p^{k_p} \otimes \mathbf{n}_p^{k_p} - \frac{1}{2}\mathbf{I} \tag{2.2}$$

For a 3D setting, the coefficient 1/2 in front the identity tensor $\mathbf{I}$ should be substituted with 1/3.

In 2D space, the fabric tensor has two degrees of freedom, being traceless by definition (or having unit trace in the case of $\mathbf{G}_p$). Thus, the intensity of fabric anisotropy can be quantified using only the difference of the two principal values ($a_p = F_{pI} - F_{pII}$) and the principal direction, expressed by the angle between one characteristic axis (e.g. the horizontal) and the major principal direction (θ_p). This fabric intensity is very usual in DEM fabric analysis (Fu & Dafalias, 2011a; Yishmiri & Soga, 2011). Additionally, this fabric intensity proves to be qualitatively identical to the norm of the tensor

$F = \sqrt{tr\mathbf{F}^2} = \sqrt{2}|F_I| = \sqrt{2}|F_{II}| = (1/\sqrt{2})|F_I - F_{II}|$. Nevertheless, in 3D and in any general situation, the norm of the fabric tensor serves better to quantify the intensity of the anisotropy (Li & Dafalias, 2012).

In matrix notation, the vectors can be written explicitly in 3D and in Cartesian coordinates as:

$\mathbf{n}_p = \begin{pmatrix} n_{p1} \\ n_{p2} \\ n_{p3} \end{pmatrix}$. Thus, the tensor product for the vector $\mathbf{n}_p$ of the particle k_p and then for N_p particles, after the summation over all the particles, results to a tensor:

$$\mathbf{G}_p = \frac{1}{N_p}\sum_{k_p=1}^{N_p} \mathbf{n}_p^{k_p} \otimes \mathbf{n}_p^{k_p} = \frac{1}{N_p}\sum_{k_p=1}^{N_p} \begin{pmatrix} n_{p1}^{k_p} n_{p1}^{k_p} & n_{p1}^{k_p} n_{p2}^{k_p} & n_{p1}^{k_p} n_{p3}^{k_p} \\ & n_{p2}^{k_p} n_{p2}^{k_p} & n_{p2}^{k_p} n_{p3}^{k_p} \\ \textit{symmetric} & & n_{p3}^{k_p} n_{p3}^{k_p} \end{pmatrix} \qquad (2.3)$$

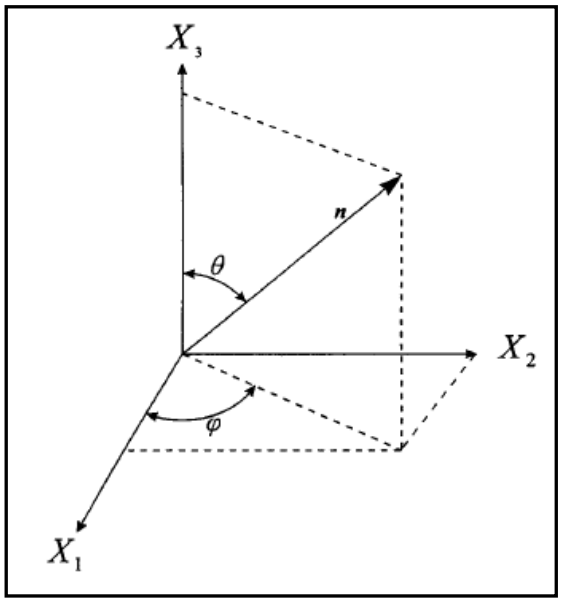

Fig. 2.6. Analysis of a vector in 3D in spherical coordinates

If the vectors are analysed in spherical coordinates, based on the angle φ and θ (Fig. 2.6), then:

$$\mathbf{n}_p = \begin{pmatrix} \sin\theta\cos\varphi \\ \cos\theta\sin\varphi \\ \cos\theta \end{pmatrix} \qquad (2.4)$$

From (2.3) and (2.4) the p-fabric tensor for spherical coordinates can be easily quantified as:

$$\mathbf{G}_p = \frac{1}{N_p}\sum_{k_p=1}^{N_p} \mathbf{n}_p^{k_p} \otimes \mathbf{n}_p^{k_p} =$$

$$\frac{1}{N_p}\sum_{k_p=1}^{N_p} \begin{pmatrix} \sin^2\theta^{k_p}\cos^2\varphi^{k_p} & \sin^2\theta^{k_p}\cos\varphi^{k_p}\sin\varphi^{k_p} & \sin\theta^{k_p}\cos\theta^{k_p}\cos\varphi^{k_p} \\ & \sin^2\theta^{k_p}\sin^2\varphi^{k_p} & \sin\theta^{k_p}\cos\theta^{k_p}\sin\varphi^{k_p} \\ \textit{symmetric} & & \cos^2\theta^{k_p} \end{pmatrix} \quad (2.5)$$

2.2.1.2. Contact normal vectors

Another way to define fabric based on the solid phase is through the plane that defines the direction of the contact (contact normal fabric). This plane (or line in 2D) is defined as the one passing through the contact point and being tangent to the particles in contact. Vertical on this plane (or line) initiating from the contact point, two unit vectors $\mathbf{n}_c$ and $-\mathbf{n}_c$ are defined, called contact normal vectors (Fig. 2.5).

Based on this definition of contact normal plane and of contact normal vectors, the fabric tensor for contact normal vectors (c-fabric) can be defined as (Oda, 1982; Satake, 1982; Kanatani, 1984):

$$\mathbf{G}_c = \frac{1}{N_c}\sum_{k_c=1}^{N_c} \mathbf{n}_c^{k_c} \otimes \mathbf{n}_c^{k_c} \quad (2.6)$$

where $\mathbf{G}_c$ is the fabric tensor for contact normal vectors, the subscript "c" denotes that the fabric quantification considers the contact normal vectors, $\mathbf{n}_c^{k_c}$ is the unit contact normal vector which describes the fabric for the $k_c th$ contact, and $\sum$ implies the summation over all the contacts N_c that exist between the N_p particles.

Following the same steps as in 2.1.1, the c-fabric tensor in spherical coordinates yields the expression:

$$\mathbf{G}_c = \frac{1}{N_c}\sum_{k_c=1}^{N_c} \mathbf{n}_p^{k_c} \otimes \mathbf{n}_p^{k_c} =$$

$$\frac{1}{N_c}\sum_{k_c=1}^{N_c} \begin{pmatrix} \sin^2\theta^{k_c}\cos^2\varphi^{k_c} & \sin^2\theta^{k_c}\cos\varphi^{k_c}\sin\varphi^{k_c} & \sin\theta^{k_c}\cos\theta^{k_c}\cos\varphi^{k_c} \\ & \sin^2\theta^{k_c}\sin^2\varphi^{k_c} & \sin\theta^{k_c}\cos\theta^{k_c}\sin\varphi^{k_c} \\ \textit{symmetric} & & \cos^2\theta^{k_c} \end{pmatrix} \quad (2.7)$$

where θ and φ are the spherical coordinates of vector $\mathbf{n}_c$ (Fig. 2.6).

2.2.2. Fabric based on the void phase

Another essential element for the fabric of granular media is the distribution and orientation of the voids. The quantification of the voids' characteristics is, in principle, very different from the description of the solid phase. This happens due to the fundamental differences between the two phases; the void space is solely the space not filled by solid particles. This leads to several issues for the void description, such as the non-convex and peculiar shape of the voids, and the continuous and random evolution of the void space, without any predefined shapes. Additionally, voids between grains, especially in 3D, are interconnected, such that in practice only one, or few, major voids exist. All these characteristics make the void phase very different in terms of fabric than the solid space. Nevertheless, it is obvious and it has been reported (Li & Li, 2009; Theocharis et al., 2015; Fu & Dafalias, 2015) that void and solid fabric are connected, as expected, and even quantitatively correlated. In brief, to quantify the void fabric all characteristics - such as size, shape, and connectivity of the voids - matter, while for the solids it is easier to distinguish only the shape of the particles or the connectivity of the contact normal vectors.

2.2.2.1. Void fabric methods

Due to its peculiar nature, void fabric has invited the application of several methods from different perspectives. Nevertheless, most methods are based on one of two primary concepts: One set of methods involves the use of lines (scan-lines) which scan the sample or a Representative Volume (RV) and quantify the solid and void segments; these will be called scan line methods (Oda et al., 1985; Kuo, Frost & Chameau, 1998; Ghedia & O'Sullivan, 2012). Another set of approaches uses graphs created through tessellation methods so that the granular assembly is replaced with a geometrical system; these are named here as tessellation methods (Kuhn, 1999; Li & Li, 2009).

Tessellation methods manage to produce a pure geometrical system based on a granular specimen, on which the mathematical modelling of a sample is possible (Bagi, 1996). The final system can vary based on the assumptions made and the aim of the tessellation; in principle, there are void cells that characterize the voids, based on the arrangement of

the related particles (e.g. Fig. 2.7(a)) and there can also exist solid cells that describe the particles. Usually, dual systems are created that account for both solids and voids; the most common such system is the Voronoi-Delaunay tessellation, where the one part describes the solids and the second part the voids (Fig. 2.7(b)). Notice that these geometrical structures have a deep theoretical background and are not aimed only at quantifying void fabric, but also at describing the internal structure of a granular medium in general; e.g. based on these structures, the tessellations strains on the granular medium can be defined (Satake, 1976; Satake, 1983; Bagi, 1996; Oda & Iwashita, 1999). Nevertheless, the void part of such a system is ideal for quantifying void fabric and has been used for this reason (Konishi & Naruse, 1988; Kuhn, 1999, Fu & Dafalias, 2015). More advanced tessellations (e.g. Li & Li, 2009) create more sophisticated mixed cells using the center of the grains and the contact points, so that each cell can be used for stress, strain and fabric determination. However, if someone wishes to focus solely on the void fabric, simpler schemes can provide sufficient information.

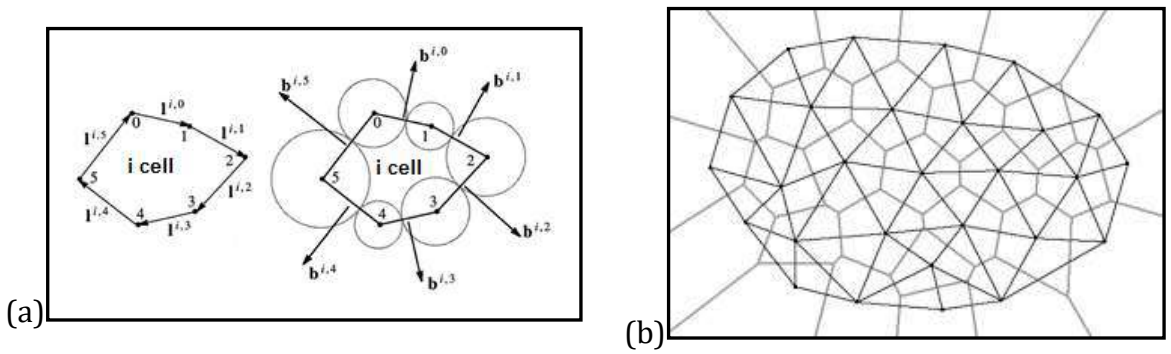

Fig. 2.7. (a) Branch vectors ($\mathbf{l}$) and normal to the void cell vectors ($\mathbf{b}$) defined based on ith (loop) void cell (Kuhn, 1999), (b) Voronoi-Delaunay tessellation (dots are the centers of the grains, triangles represent the voids and polygons the solids)

2.2.2.2. A modified and a novel scan line definitions

Oda et al. (1985) underlined the importance of voids and of void fabric anisotropy for granular materials, and provided the initial scan line concept and definition. The principal concept and the main parameters are presented schematically in Fig. 2.8. The sample of a granular material is scanned with parallel lines at inclination θ, maintaining a fixed distance "d" between neighboring lines; the scanning is repeated for small intervals of θ between limits covering the whole sample. The line segments defined between grain

boundaries during scanning can be characterized either as voids or as solids and, thus, the measured void length segments (l_i^θ) can adequately quantify the voids of the media. The lengths of these void segments, along with the corresponding unit vectors at inclination θ, determine the basic void vectors that are used for defining the corresponding scan line void fabric tensor. Oda et al. (1985) introduced the method in its most simplified way, by applying it directly onto snapshots of small-scale physical experiments. Ghedia and O'Sullivan (2012) presented advanced methods applying a scan line approach to digital images obtained from small-scale physical experiments and 2D DEM specimens.

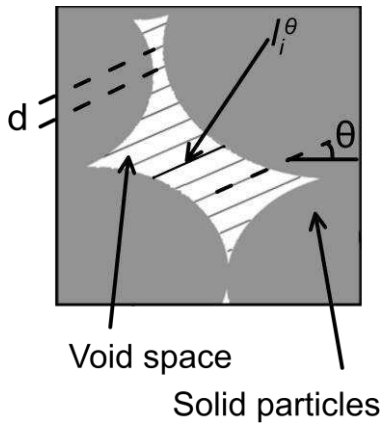

Fig. 2.8. Scan line concept and main parameters

The scan line idea is straightforward for both 2D and 3D analyses and has been implemented in several fields of research (Biscarini et al., 1997; Kahl et al., 2013), including geomechanics (Oda et al, 1985; Ghedia & O'Sullivan, 2012). It is important to emphasize the crucial operational difference between the scan line method and all other approaches in determining a fabric tensor: in the former case the measurements are made for all θ's (in practical terms at many discrete intervals of θ) and then are combined to obtain the value of a tensor, while in all other cases the measured quantities, e.g. contact normal distribution orientations, are fixed and measured once. Notice that while the scan line approach employed in this work uses a series of parallel scanning lines in different orientations, another type of "scan line method" exists, which introduces only one scan line that emanates from a point inside a representative volume in various orientations (Kuo, Frost & Chameau, 1998; Pietruszczak & Krucinski, 1998); hence, it is a different concept than the one discussed here.

Scan line is a rather simplified method that has so far been performed on images, a great advantage in the case of experimental measurements. Literature combining DEM experiments and the scan line method includes one case (Ghedia & O'Sullivan, 2012) where the method was applied to digital images obtained from DEM experiments. Scan line approaches have been systematically implemented and analyzed on precise data from computational experiments, e.g. Discrete Element Method (DEM), in a recent work by the author (Theocharis et al., 2017b). It is concluded that the application of existing scan line void fabric tensor definitions on DEM data, fails to provide compatible results with those produced using images, due to an inherent shortcoming of the original definition which has been proved analytically and numerically. To overcome this deficiency, Theocharis et al. (2017b), proposed, on the one hand, a modification of the original definition of the scan line void fabric tensor by introducing the concept of a "cut off" characteristic length, and, on the other hand, a novel void scan line fabric tensor definition based on the squared lengths of void scan line segments, for which comparisons were made among themselves and contact normal fabric tensors.

The primary outcomes of that research include the proof of the shortcomings of the scan line methods defined so far, and a proposition of two alternatives for a more concise scan line fabric tensor. The original scan line definition by Oda et al. (1985) is:

$$\mathbf{V}^{Oda} = 4\left(\frac{1}{L}\sum_{\theta=-90^0}^{\theta=90^0} l^{\theta}\mathbf{n}^{\theta}\otimes\mathbf{n}^{\theta} - \frac{1}{4}\mathbf{I}\right) \qquad (2.8)$$

where $\mathbf{n}^{\theta}$ is the unit vector along all scan line void vectors inclined at a specific angle θ, $\mathbf{I}$ is the identity tensor, $\mathbf{n}^{\theta}\otimes\mathbf{n}^{\theta}$ represents the tensor product of $\mathbf{n}^{\theta}$ by itself, l^{θ} is the mean length of scan line segments for each angle θ, and $L=\sum_{\theta=-90^0}^{\theta=90^0} l^{\theta}$ is the sum of all mean lengths l^{θ} over all θ, where the summation is executed in predefined intervals of θ within the angular domain $[-90^0, 90^0]$. The mean length of the scan lines l^{θ} provides the all-important weight of the tensors $\mathbf{n}^{\theta}\otimes\mathbf{n}^{\theta}$ and its orientation distribution characterizes the anisotropy. In case l^{θ} is equal for all θ, it will be eliminated from the numerator and the denominator of Eq. (2.8), emerging from the fact that L is a summation over all l^{θ}, and, by using integration over θ to accurately express the ensuing summation of $\mathbf{n}^{\theta}\otimes\mathbf{n}^{\theta}$

one obtains from Eq. (2.8) the half identity tensor $(1/2)\mathbf{I}$, corresponding to perfectly isotropic fabric.

The problem with this definition, as a similar and even more severe issue stands for the definition of Ghedia & O'Sullivan (2012), is that when the parallel scanning lines are too close (distance $d \to 0$), void segment lengths multiplied by the scanning distance d can be related to void areas. As a result, the final weight of the tensor becomes equal to the inverse $1/N_\theta$ of the total number of void scan line segments for each angle θ, thus not depending at all on the lengths of the void segments or the mean void length. This renders that scan line approach incapable of measuring the void anisotropy by means of DEM, as the very many small void segments interfere with the important - in terms of length - void segments, and the method results into obtaining a constantly isotropic fabric. The reader is referred to Appendix for a detailed proof of this conclusion. In real experiments these graphical scan line approaches are effective in detecting void fabric anisotropy because image analysis and other processes, by default, ignore many small segments for void anisotropy quantification (e.g. even in digital images, the size of the pixel constitutes the minimum void segment length that is taken in to account, while all void segments smaller than this are by default excluded from the calculation).

By simply modifying the original definition of Eq. (2.8) to neglect the void segments that are smaller than a characteristic minimum length ("cut off"), a void fabric tensor based on the scan line method that can adequately quantify fabric anisotropy is defined:

$$\mathbf{G}_v^{co} = \frac{1}{L}\sum_{\theta=-90^0}^{\theta=90^0} l^\theta \, \mathbf{n}^\theta \otimes \mathbf{n}^\theta; \quad L = \sum_{\theta=-90^0}^{\theta=90^0} l^\theta; \quad l^\theta = \frac{\sum_{i=1}^{N^\theta} l_i^\theta}{N^\theta} \quad \text{for } l_i^\theta > \text{"cut off" value} \qquad (2.9)$$

The same symbols as in Eq. (2.8) are used and l_i^θ is the length of an i_{th} void scan line segment along angle θ.

As analyzed in the previous section, the original definition of the scan line fabric tensor, with the mean length of the void segments being the all-important statistical weight, has the inherent shortcoming of elimination of any void vector length at the end; in particular the fact that void segment lengths multiplied by the scanning distance d can be related to void areas, is at the heart of the eventual length elimination and its substitution by $1/N^\theta$ as the corresponding weighting factor; the remedy of this shortcoming was the use of the "cut off" approach (Eq. 2.9). Based on this observation, a novel, very simple, more

physical and straightforward definition of a scan line void fabric tensor, that can overcome the shortcoming without the use of any "cut off" concept, is proposed. The proposition is based not on unit vectors along void segments weighted by the segments' length, but on not unit void vectors defined along void segments and having norm equal to the segments' length. Thus, the squared length (instead of length) of a void segment enters the definition of the void fabric tensor as the weighting factor of each $\mathbf{n}^{\theta} \otimes \mathbf{n}^{\theta}$, which cannot be eliminated by its connection to void surface area elements. One then can proceed in a step-by-step construction of the new void scan line fabric tensor as follows. Define the i_{th} void vector along θ by $\boldsymbol{v}_i^{\theta} = l_i^{\theta}\mathbf{n}^{\theta}$ where recall that l_i^{θ} is the length and $\mathbf{n}^{\theta}$ the unit vector of the i_{th} void scan line segment along angle θ. The crucial point is now the definition of the i_{th} void tensor along θ by $\boldsymbol{f}_i^{\theta} = \boldsymbol{v}_i^{\theta} \otimes \boldsymbol{v}_i^{\theta} = l_i^{\theta^2}\mathbf{n}^{\theta} \otimes \mathbf{n}^{\theta}$, where the squared length $l_i^{\theta^2}$ naturally appears as the weighting factor of this tensor. The next steps are straightforward and consistent with the concept of scan line approach, namely one first considers the combined effect of all void segments for a given θ, and then combines such effects for all θ' s. Hence, for a given θ the summation over i of all $\boldsymbol{f}_i^{\theta}$ yields the tensor $\boldsymbol{g}^{\theta} = (\sum_{i}^{N^{\theta}} l_i^{\theta^2})\mathbf{n}^{\theta} \otimes \mathbf{n}^{\theta}$, with the sum of the squared lengths along θ being the weighting factor of $\boldsymbol{g}^{\theta}$, and subsequently the summations of $\boldsymbol{g}^{\theta}$ over all θ, normalized by the sum of their weighting factors, yields the sought new scan line void fabric tensor as:

$$\mathbf{G}_{v2} = \frac{1}{\sum_{\theta=-90^0}^{\theta=90^0}\left(\sum_{i=1}^{N^{\theta}} l_i^{\theta^2}\right)} \sum_{\theta=-90^0}^{\theta=90^0}\left(\sum_{i=1}^{N^{\theta}} l_i^{\theta^2}\right)\mathbf{n}^{\theta} \otimes \mathbf{n}^{\theta} \qquad (2.10)$$

In this case, the weight of the fabric tensor, characterizing the distribution of the void orientations, is the square of the length of the void segments. This tensor appears to sufficiently quantify the void fabric anisotropy with or without the use of the cut off. Both of the above newly defined fabric tensors in Eqs. (2.9) and (2.10) can capture the void characteristic that would be expected from a fabric tensor and will be applied in the sequel for quantifying void fabric in 2D via DEM virtual experiments.

2.3. Fabric in biaxial and triaxial loading paths and stress principal axes rotation; experiments and the Discrete Element Method

This section is dedicated to the overview of the evolution of fabric elements and fabric anisotropy during typical loading paths that will be implemented in the next chapters. The experimental possibilities for quantifying the micromechanical property of fabric have been, in principle, dependent on, and hence also limited by, the numerical capabilities; initially material of the 2-dimensional kind has been used, such as photoelastic rods and schneebeli cylinders, as these materials are visually accessible due to their 2D nature and thus allow one to see and study fabric. Moreover, in 3D specimens, cutting out sections of the original samples was the only way to access the internal micromechanical characteristics (Oda, 1972a; Al-Shibli, Macari, & Sture, 1996; Frost & Kuo, 1996). The sample was "frozen" with resin or other material, and then slices were cut out of it. Those 2D slices were again visually accessible and with some basic image analysis, measurements were taken on the fabric properties.

These initial efforts and their conclusions were in many ways uncertain. More advanced experimental techniques, that have been used for the analysis of the texture of granular media in general, include x-ray radiography (Arthur & Dunstan, 1969a and 1969b; Nemat-Nasser & Okada, 2001), electrical conductivity and resistivity (Dafalias & Arulanandan, 1978; Dafalias & Arulanandan, 1979; Arulanandan & Dafalias, 1979), magnetic resonance imaging (Ng, Aube & Altobelli, 1997; Ng, Hu & Altobelli, 2006), laser-aided tomography, (Konagai et al., 1992; Konagai & Rangelow, 1994; Matsushima et al., 2003), and X-ray computed tomography (Desrues et al., 1996). X-ray CT seems to be a promising experimental tool (Latiere & Mazerolle, 1987; Colliat-Dangus, Desrues & Foray, 1988; Raynaud et al., 1989) that has become popular in experimental investigation of granular materials (Desrues et al., 1996; Chang, Matsushima & Li, 2003; Aste et al., 2004; Aste, 2005; Alshibli & Alramahi, 2006; Desrues, Viggiani & Besuelle, 2010) and will possibly answer questions and unravel mysteries on the fabric regime on real soils.

Until then, DEM is the major tool that provides results and mechanisms on the fabric response. Recent research has made several steps towards revealing the physical response of fabric through common and well-analysed loading paths. Furthermore, CS

and fabric has become one of the most popular topics in fabric analysis; fabric has been shown to be strongly anisotropic in Critical State (CS) as will be further analysed in Chapter 3. An increasing number of analyses confirm this result, as the interest is now focused on whether the CS value of this fabric anisotropy, usually calculated in DEM from c-fabric, is unique, or whether it is dependent on parameters of the experiments. Research so far supports the unique-value assumption (Fu & Dafalias, 2011b; Zhu et al, 2016; Yang & Wu, 2016) and renders CS fabric anisotropy pertinent only to the shear mode or Lode angle.

Before fabric reaches CS, where fabric is strongly anisotropic, the evolution of fabric is still under research, and is based on the original conditions and the loading path. In experiments, fabric tensor is difficult to calculate because of measurement uncertainties; furthermore, fabric evolution during an experiment demands for the calculation of the fabric in several steps. This is an ongoing work for the X-ray CT method combined with advanced image analysis; recent works are now pointing in this direction (Hall et al., 2010; Fonseca et al., 2012; Andò et al., 2013; Jaquet et al., 2013; Taylor, O'Sullivan & Sim, 2015; Fonseca et al., 2016).

2.3.1. Biaxial shear

The clear majority of the results existing on fabric measurements are for triaxial and biaxial experiments; 2-dimensional experiments that simulate the triaxial load paths will here be called biaxial experiments for our purposes. In general, the vertical stress is increased as the horizontal is either constant or decreases to maintain constant hydrostatic pressure; the vertical loads are usually applied through boundaries that are not allowed to deform (rigid), while the lateral pressure can be applied though rigid or flexible boundaries. For stress loading conditions, a servomechanism is usually implemented to control the boundaries' velocity.

2D biaxial experiments have been popular as the results from a 2D experiment - at least fabric-wise - are visually accessible and easily interpretable, while for the 3D soils, fabric is extremely difficult to measure. 2D biaxial physical experiments have taken place in the past on photoelastic rods (Drescher & De Jong, 1972; Oda & Konishi, 1974), and, more recently, in schneebeli materials (Calvetti, Combe & Lanier, 1997); these materials have the advantage that they do not simulate plane-strain or plane-stress conditions, but

rather constitute a pure 2D case. Additionally, 2D numerical simulation that would produce qualitatively similar results with 2D experiments, are extremely faster than the 3D, and the results are again more readily interpretable with the aid of the visual simplicity.

Oda (1972a, 1972b, 1988, 1999) has made measurements of fabric on real 2D experiments by taking snapshots of the biaxial and applying several fabric methods for all types of fabric. These results are not very coherent due to the very difficult measurement conditions, but are the first attempts to measure fabric in a real experiment. More recently Calvetti et al. (1997) made some fabric-type measurements on schneebeli rods using more sophisticated apparatus (see Joer et al., 1992).

Most results for fabric measurements come from DEM analysis, that is based on the 2D biaxial type presented for experiments with rods. While in physical experiments the most common fabric type is the p-fabric followed by the void fabric, named v-fabric, in DEM measurements the most common one is c-fabric. In experiments the orientation of the particles is clearly visible; furthermore, the experimental materials are sometimes designed to provide clear particle orientation, while voids are accessible through snapshots of the procedure. On the other hand, contact normal vectors have been almost impossible to measure so far, but, as they are closely related to chain forces and stresses, they have been extensively analyzed through numerical methods.

From all this experience - experimental and mainly DEM - the tendencies of the fabric are clear: during the biaxial loading the particles orient themselves parallel to the horizontal plane, i.e. perpendicular to the vertical loading axis, and contact normal vectors build a very strong preference parallel to the loading axis, and the voids follow the contact normal vectors in tending to align vertically (e.g. Fu & Dafalias, 2011b; Li, Yu & Li, 2011; Tong, Zhang & Zhou, 2013); they all reach a relatively strong anisotropy as the biaxial loading proceeds. This is also intuitive; as the load increases, the particles tend to obtain a more "stable" position. The principal axes of the fabric tensor of all three types always align with the stress principal axes (vertical and horizontal), even if at the beginning of the tests they might appear slightly non-coaxial.

It is important to distinguish the two cases of initially isotropic and initially anisotropic specimens, i.e. of samples created with pluviation under gravity (inherent fabric). Both types appear to reach a final strong anisotropy, but their evolution might appear slightly different (Wang et al., 2017). Additionally, the fabric of the dense specimens, follows the

stress ratio curve, i.e. fabric anisotropy stronger than the CS can be reached, and then, following the softening of the material reach the final CS value, which will be lower than the peak. In the case of loose specimens, fabric anisotropy monotonically evolves towards CS. The case of localization in shear bands (e.g. Vardoulakis, 1980) has also been studied in terms of fabric, but not in the same depth. Similar conclusions seem to apply, but only for the area inside the shear band where CS is reached (Fu & Dafalias, 2011b; Zhu et al., 2016). The part of the specimen outside the shear band is not as active and has a different fabric anisotropy.

2.3.2. Triaxial Shear

Typical triaxial experiments are most common in soil mechanics practice. They have also been used extensively for fabric analysis as they are well-analyzed in many respects. They are very similar to biaxial experiments with respect to soil response, and fabric response is, in principle, extremely similar between 2D and 3D. As mentioned above , slices from triaxial specimens have been used to quantify the fabric; resin has been used to "freeze" the samples, cut out slices, and then use these slices to make 2D fabric measurements. These results were the first hints on the discussion on how fabric looks like, and how it evolves in real soils. Modern techniques, predominately X-ray CT with advanced image analysis, could capture the micromechanical response of a soil under triaxial loading; however, few results exist on the evolution of the fabric elements using these techniques, as these techniques are very costly and are now being developed. For these reasons, DEM is still the main method used to extract conclusions on the mechanisms underlying fabric behavior.

The general trends concerning fabric evolution during typical triaxial experiments (and virtual experiments) are qualitatively the same with those in 2D. The response of the fabric elements (p-fabric, c-fabric and v-fabric) and the anisotropy of each one of them follows the same evolution as in 2D. The same observations are also valid when considering the application of p-fabric and v-fabric primarily in physical experiments and c-fabric in DEM. The bridge between these distinct types of fabric is still at an early stage of investigation; little research appears on this (Li & Li, 2009; Fu & Dafalias, 2011b; Fu & Dafalias, 2015; Theocharis et al., 2015), although it seems very important in revealing the

full picture of the micromechanical behavior and its relation to the macromechanical response.

2.3.3. Stress principal axes rotation

The rotation of the principal axes of stress with constant principal stress values is one of two cases called rotational shear (Wang, Dafalias & Shen, 1990); the other case is the variation of principal stress values with fixed stress axes, such that the stress orbit in π-plane is circular, but we will only deal with the first one here. Under this loading path, the principal values of stress are held constant while only its principal axes rotate. This loading path is usually applied in physical experiments through the hollow cylinder apparatus; results from stress PA rotation have been reported for several years in the literature, as this specific type of cyclic stress rotation is an important feature for failures (e.g. Ishihara & Towhata, 1983).

Several drained (Miura et al., 1986; Symes, Gens & Hight, 1988; Wijewickreme & Vaid, 1993; Tong et al., 2010) and undrained experiments (Ishihara & Yamazaki, 1984; Symes, Gens & Hight, 1984; Nakata et al., 1998; Yang, Li & Yang, 2007; Chen & Kutter, 2009) have been conducted. Results mostly focus on the evolution of strains, the accumulation of volumetric strain, and the non-coaxiality between the directions of stain increment and stress. The microscopic evaluation of this type of loading appears to be of interest, since the constant change of the principal axes of stress force the principal axes of strain and fabric to follow those of stress. This is fundamentally different from the previous loading paths, where the principal axes of stress remained fixed and those of strain fabric were always aligned with them.

Microscopic analysis of stress PA rotation has gained attention in the past years due to the obvious non-coaxiality between the stress and the strain during the loading. Besides this feature, fabric results have been reported that show the c-fabric and the void fabric to follow the rotation of the stress principal axes with a delay of a small angle, while its intensity seems to remain constant (Li & Yu, 2010; Fu & Dafalias, 2015). To the contrary the p-fabric for relatively elongated particles seems to resist extensive rotation when the stress PA rotate. Only through DEM it has been possible to assess this evolution of fabric during stress PA rotation. That provides a starting point for investigating fabric under the stress PA rotation; this loading path had not been applied in Critical State conditions until

in a recently published work by the author (Theocharis et al., 2017a), and the results seems to be of profound importance for the Critical State Theory. This subject will be analyzed in depth in the next chapters.

Chapter 3: Critical State Theory and its legacy

3.1. Classical Critical State Theory

The Critical State (CS) concept and the Critical State Theory (CST) have been introduced by Roscoe, Schofield & Wroth (1958) and by Schofield & Wroth (1968), in their landmark work more than half a century ago. The authors describe the CS as: "the concept that soil and other granular materials, if continuously distorted until they flow as a frictional fluid, will come into a well-defined critical state determined by two equations" (Schofield & Wroth, 1968 - Section 1.8, p. 12). These two equations refer to the macroscopic properties of the geomaterial, and are defined based on the stress and the volume. It follows, that when a granular medium is "distorted", i.e. extremely deformed under a load of some kind, it will reach a well-defined steady state.

3.1.1. The phenomenon of Critical State

The Critical State can be described as the state where a granular material keeps deforming in shear, at constant stress and volume. The analytical expression of this state then reads:

$$\dot{p}=0, \quad \dot{q}=0, \quad \dot{\varepsilon}_v=0, \quad \dot{\varepsilon}_q\neq 0 \tag{3.1}$$

where q is the deviatoric stress, p is the hydrostatic stress, ε_v the volumetric strain and ε_q is the deviatoric strain, the only macroscopic quantity evolving in CS; the superposed dot implies the material time derivative. The above Eq. (3.1) declares that when being at CS, the stress as well as the volumetric strain are constant with time.

Eq. (3.1) uses only the most important macroscopic variables of the state, i.e. the stress and the volume. Someone could introduce the very general case of CS, where all state variables relevant to a granular assembly would be unchangeable with time. That means if the state of the material is represented by means of a set of state variables $\mathbf{q}=[q1,q2,...]$, scalar or tensor-valued, the analytical expression of the critical state event is given by:

$$\dot{\mathbf{q}}=\mathbf{0} \tag{3.2}$$

Although Eq. (3.2) looks as a more complete definition for CS, in practice it may often be found that many variables have insignificant effect on critical states and that first order dependence of critical state on effective stress and volumetric packing may be sufficient. It is important to underline here that the CS is not an instantaneous event but a steady state; this is also clearly stated by Eq. (3.1) as the stress and the volume are declared constant with the evolution of time.

3.1.2. Critical State Theory (CST)

Roscoe, Schofield & Wroth (1958) and Schofield & Wroth (1968) described the phenomenon but also proposed a theory based on CS, which will be called the Critical State Theory (CST). This theory suggests two conditions, which are necessary and sufficient for CS to be reached and maintained. These two conditions are expressed by equations that were primarily defined in the triaxial space and in their original form they read:

$$q = \mathrm{M}p; \qquad \Gamma = v + \lambda \ln p \tag{3.3}$$

where q is the deviatoric stress, p is the hydrostatic stress, v is the specific volume of the material, and M, Γ and λ are soil material properties. The first part of Eq. (3.3) refers to stress quantities and declares that when being at CS, the deviatoric and the hydrostatic stress are linearly related through M, a constant dependent only on the material. The second part of Eq. (3.3) dictates that the specific volume v, which is the volume occupied by a unit volume of solid particles, depends uniquely on the hydrostatic pressure p at CS and decreases linearly as the logarithm of the hydrostatic pressure increases, while the sample always stays in CS. The two parts of Eq. (3.3) are qualitatively presented in Fig. 3.1.

The Critical State is not just a steady state that a granular material reaches under some particular loading procedure, but is a general “base of reference” for this kind of material. At any given soil sample, the question for the soil is whether it is “looser” or “denser” than the Critical State. “Looser” is the condition in which, under deformation, the material will eventually densify, its specific volume will decrease, i.e. decrease of the voids between the unit volume of grains will occur till reaching CS, and is referred to as ‘Wet’ in Fig. 3.1(b). On the other hand, “denser” is the opposite state, in which the sample will eventually dilate, i.e. the deformation will cause increase of specific volume till reaching

CS, possibly preceded by a small contraction; this is the 'Dry' area of Fig. 3.1(b). It is now clear that the Critical State is not merely a steady state, but a very important and powerful concept that dictates the response of the soil. This response constitutes the basis for the development of Critical State Theory (CST) or of the Critical State Soil Mechanics (CSSM) framework, a major achievement in soil mechanics.

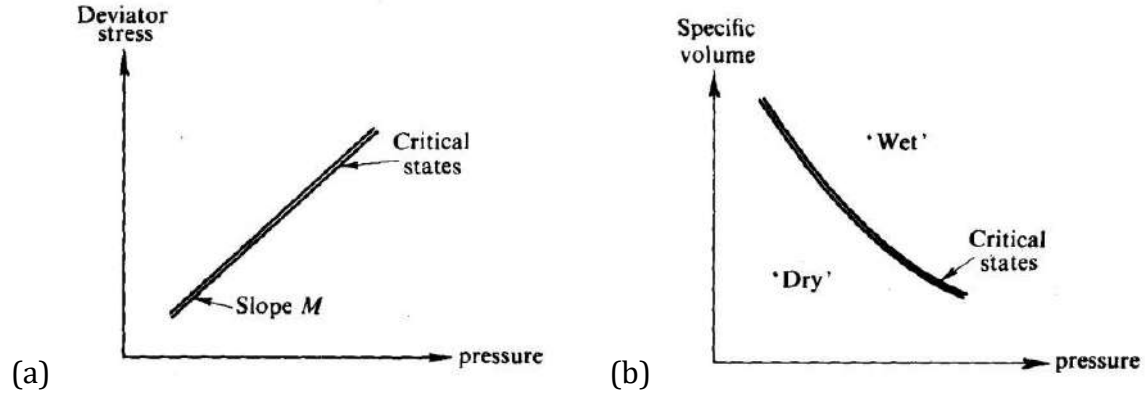

Fig. 3.1. Critical State after Eq. (2.1): (a) deviatoric vs hydrostatic pressure and (b) specific volume vs hydrostatic pressure (Schofield & Wroth, 1968 - Section 1.8, p. 12)

Another very common way to express CST is through the stress ratio and the void ratio; this is the most usable form in geotechnics and geotechnical engineering. Stress ratio is the ratio of the deviatoric stress over the hydrostatic stress; it is important to soil materials, as they are significantly pressure-dependent, and this ratio normalizes each stress condition with the important hydrostatic pressure. The void ratio is simply the volume of the voids over the volume of the solid grain for a representative volume of the granular medium, and is widely used in the place of the specific volume. Porosity, defined as the volume of the voids over the total volume of the representative volume, can be used interchangeably. All the volume quantities mentioned above are completely dependent variables and their relations are summarized in Table 3.1.

	Porosity n	Void ratio e	Specific volume v
Porosity n	1	$e/(1+e)$	$(1-v)/v$
Void ratio e	$n/(1-n)$	1	$v-1$
Specific volume v	$1/(1-n)$	$1+e$	1
Volumetric strain $\varepsilon_v = -(V_{fin}-V_{ini})/V_{ini}$	$(n_{ini}-n_{fin})/(1-n_{fin})$	$(e_{ini}-e_{fin})/(1+e_{ini})$	$(v_{ini}-v_{fin})/v_{ini}$

Table 3.1. Relations between volumetric-type quantities.

For the stress ratio and the void ratio parameters, Eq. (3.3) reads:

$$\eta=\frac{q}{p}=\eta_c=\mathrm{M}; \qquad e=e_c=\hat{e}_c(p) \tag{3.4}$$

Where η signifies the stress ratio, and η_c the Critical State ratio, which is by definition equal to M. Void ratio (e) is equal to e_c at CS; $\hat{e}_c(p)$ is used to underline that the CS void ratio is only dependent on the hydrostatic pressure. Eqs. (3.4) define a line in e-q-p space, called the Critical State Line (CSL). Often, however, it is the projection of this line on the e-p space, namely the second of Eqs. (3.4), that is called the CSL; we will adhere to this name here.

Eqs. (3.1), (3.3) and (3.4) are written in a form based on p and q, the deviatoric and hydrostatic stress. Initially, these parameters were only defined in classical triaxial space. Nevertheless, the generalization from triaxial to multiaxial space can easily be made. For example, in eq. (3.4) for multi-axial loading, one could substitute $\sqrt{(3/2)\mathbf{s}:\mathbf{s}}$ for q in the expression $\eta=\frac{q}{p}$, where $\mathbf{s}$ is the deviatoric part of the stress tensor, and renders M a function of the Lode angle determined by the shearing mode.

3.1.3. Critical State Theory in Experiments

The creation and foundation of CST has been based on experiments on reconstructed Weald clay (Roscoe, Schofield & Wroth, 1958), where the phenomenon has been systematically recorded. However, the CST, its principles and concepts, have then been extended to all granular media, i.e. cohesive materials, such as clays and non-cohesive materials, such as sands. Nevertheless, we must distinguish the results that will be presented, as these two material types exhibit two distinct responses. They may both come under the same CS framework, but the way they get there and the details are profoundly different, due to their fundamental structural differences. This section does not intend to give an extensive overview of the literature, but rather to briefly underline in principle, the sound base of CST and its relation to experimental results.

3.1.3.1. Critical State for Clays

Roscoe, Schofield & Roth (1968) gathered data for several drained and undrained triaxial compression tests on reconstituted Weald clay. Additional results have been presented in a concise way in Atkinson & Bransby (1978) and in Wood (1991). The data presented in Fig. 3.2 are for undrained tests and in Fig. 3.3 for drained, as they appear in Wood (1991), and support very well the Critical State Theory for clays. It is clear that during CS, the relation between p and q is linear, and that the volumetric strain in CS is dependent only on p.

During the triaxial experimental procedure, non-uniformities (such as shear bands) are very likely to develop. Thus, for the data presented, results of samples that developed such non-uniformities during loading, like heavy consolidated clays, were neglected; CS is then obvious for the points of all the experiments considered. From these figures, one can calculate the constants of Eq. (3.3) for this particular clay: $\mathrm{M}=0.872$, $\Gamma=2.072$ and $\lambda=0.091$. It is important to notice that the clay material reaches the same Critical State under drained and undrained conditions.

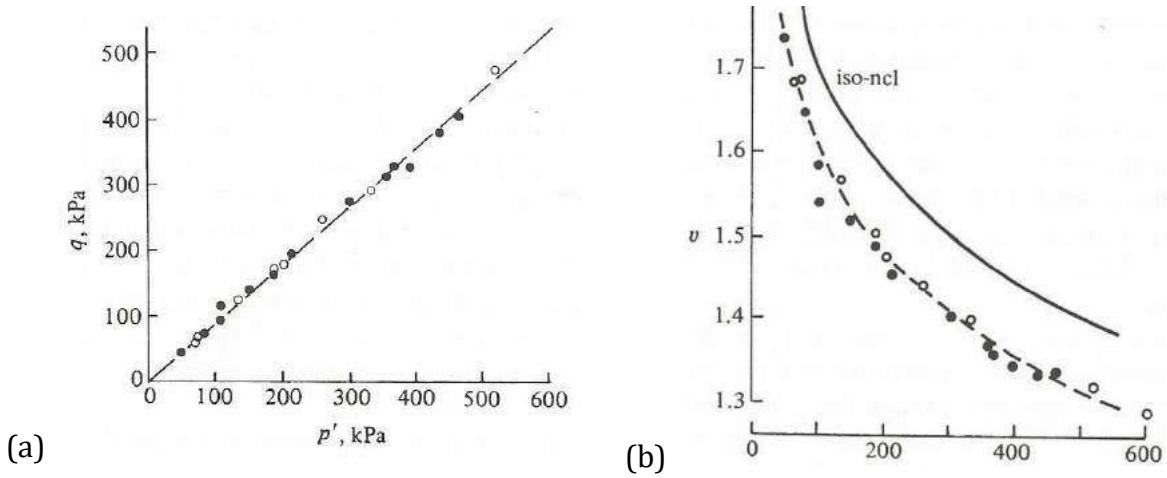

Fig. 3.2. Final points of triaxial undrained test on Weald clay (white circles are for normally consolidated and black for overconsolidated samples) (a) deviatoric vs hydrostatic pressure and (b) specific volume vs hydrostatic pressure (from Wood, 1991; after Roscoe et al., 1958)

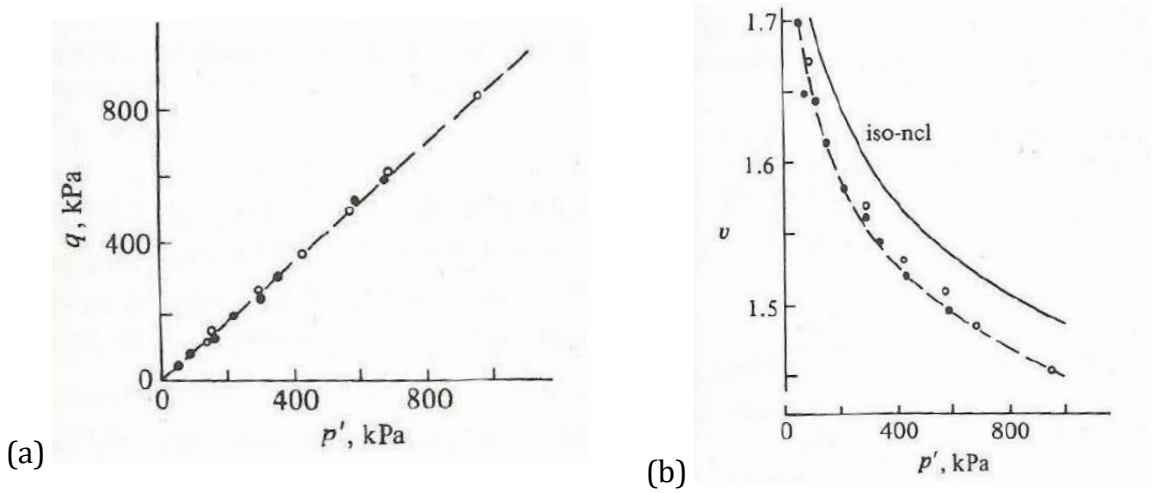

Fig. 3.3. Final points of triaxial drained test on Weald clay (white circles are for normally consolidated and black for overconsolidated samples) (a) deviatoric vs hydrostatic pressure and (b) specific volume vs hydrostatic pressure (from Wood, 1991; after Roscoe et al., 1958)

3.1.3.2. Critical State for Sands

For non-cohesive soils, it is more difficult to describe a definite CS experimentally, due to different failure modes, mainly shear bands, non-uniformities and instabilities during their loading procedure. Nevertheless, efforts support that CS is most likely the framework for these materials too. The steady state reached at large axial strains for a non-cohesive granular medium, is independent of the initial density (or void ratio) as shown in Fig. 3.4(a), for drained triaxial tests. When shear bands form, CS appears to be reached inside the shear band (Fig, 3.4(b)) where the deformation is localized. This implies that each material has a unique set of parameters that describe this state, independently of its initial condition and the loading procedure.

In addition, this steady state works again as a borderline, which defines if the material will dilate or compress. If the material is in denser state than the CS ('Dry'), it tends to increase its specific volume and dilate, while in looser conditions ('Wet') the opposite happens. It is now obvious that this steady state observed for sands, presents exactly the same properties as for clays, and is thus called Critical State. Experimental results, such as those for Chattahoochee sand (Vesic & Clough, 1968) presented in Wood (1991) (Fig. 3.5) are difficult to obtain due to the problems mentioned above, but still strongly support the CS concept.

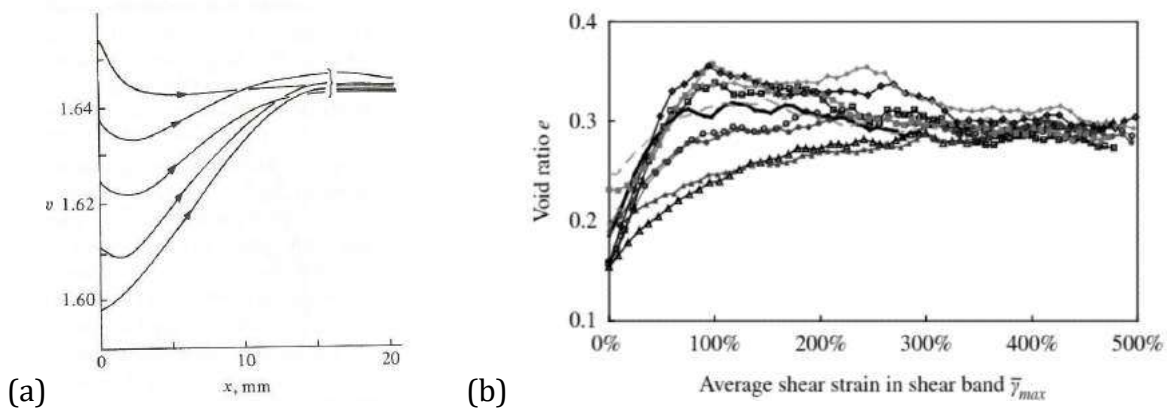

Fig. 3.4. (a) Specific volume vs shear strain for simple shear tests on 1mm diameter steel balls with normal stress 138kPa (from Wood, 1991; after Wroth, 1958) and (b) void ratio vs shear strain measured in shear band with different initial void ratio and fabric anisotropy for 2D DEM results of direct shear and elongated particles (Fu & Dafalias, 2011b)

Since this work focuses on the Critical State of sands, from this point on, the main focus will be given only on the Critical State of non-cohesive granular materials. Nevertheless, it is important to notice that CST is a unified theory for both clays and sands; although it had been primarily developed for clays, nowadays it is broadly accepted and extremely popular for sands as well.

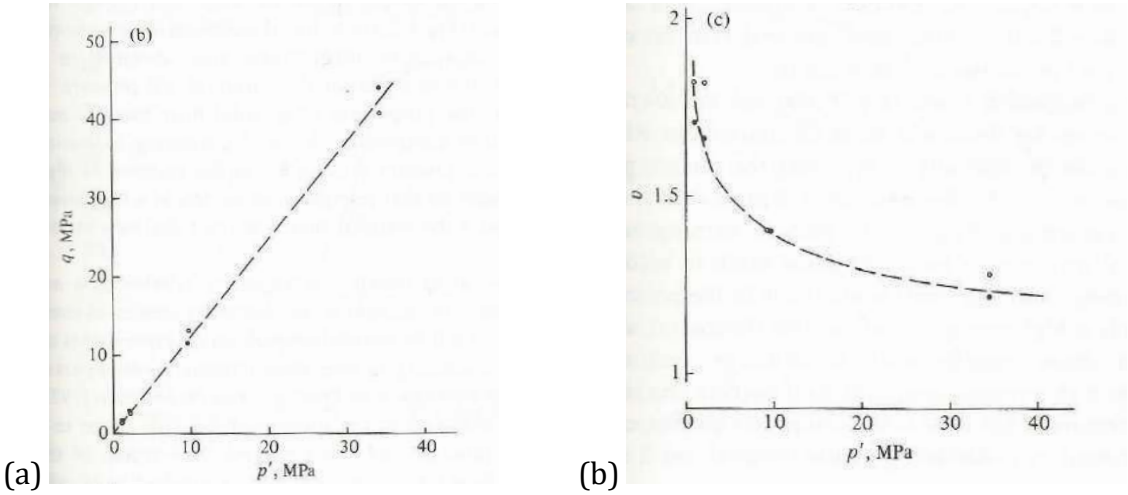

Fig. 3.5. End points of triaxial compression with constant mean effective stress (black circle for dense and white for loose samples): (a) deviatoric vs hydrostatic pressure and (b) specific volume vs hydrostatic pressure (Wood, 1991; data from Vesic & Clough, 1968)

3.1.4. Critical State in constitutive modelling

Critical State Theory, except from its value in understanding the response of granular materials as they approach CS failure, has been a very successful framework for constitutive modelling. Initially, Schofield & Wroth (1968) used the CST as a framework for a simple elastoplastic model named cam clay model. Roscoe & Burland (1968) modified the yield surface of the cam clay model and created the modified cam clay. These models have set a path for elastoplastic models within the CS framework.

Onwards, Critical State has been extremely popular and many models have been developed in the field of geotechnics and geomechanics within the CS framework throughout the years after its initial introduction (Scott, 1985; Gens and Potts, 1988; Jefferies, 1993; Wheeler and Sivakumar, 1995; Yu, 1998; Li and Dafalias, 2000; Lade, 2005; Wan, Pinheiro & Guo, 2011; Li and Dafalias, 2012; Zhao and Guo, 2013; Gao et al., 2014). For the past 50 years, soil constitutive modeling has flourished within CST, up to the point that constitutive models which do not fall into this framework are difficult to be accepted and are rarely used. Thus, CST is of great importance, not only for the understanding of the physical phenomena of granular materials, but also for their modeling and practical application.

3.1.5. Issues in Critical State Theory

As a theory-paradigm for the field, Critical State has attracted considerable criticism. It is important to keep in mind that, at the time CST was developed, no such theory was in place and the field of geomechanics was at its very preliminary stages. From that perspective, it was good practice to make simplified assumptions - without oversimplifying - given the restrictions in measurements and the limited amount of knowledge and experimental results at the time. Until its introduction though, several issues concerning CST have been raised, especially given that it is a theory initially based mainly on experimental results, without strong theoretical proof. The two major issues that have attracted research attention in recent years are the uniqueness of the Critical State Line, and the necessary and sufficient conditions for reaching and maintaining CS on it (Poulos, 1981; Chu, 1995; Riemer & Seed, 1997; Mooney, Finno & Viggiani, 1998; Li & Dafalias, 2012; Zhao & Guo, 2013).

3.1.5.1. Is Critical State Unique?

The uniqueness or not of CS is mostly attached to the CSL in $e-p$ space, i.e. to the unique value of void ratio (or specific volume) under a specific p, independently of the initial state and loading procedure; it seems now generally accepted that critical stress state is unique (e.g. Mooney et al., 1998). This problem has been researched, without a complete and definite proof yet to be attained. Many practical problems limit laboratory results so far: the development of shear bands, necking, and other non-uniformities, create a non-homogenous condition, as a result of which CS cannot be attained at the whole sample, and so only few specimens can truly reach CS. Varied and mixed boundary conditions (rigid walls, flexible membranes) make the situation complex in analysis; triaxial extension needs extremely large deformation to reach CS. All these complications compose a very difficult environment to create a variety of samples and situations where CS is measured in practice, and to result to a systematic analysis of this state. Nevertheless, some laboratory results indicate that CSL could be dependent on factors such as the stress path, the Lode angle, and the fabric of the samples (Vaid, Chung & Kuerbis, 1990; Mooney et al., 1998; Zhao & Guo, 2013). That means that CS may be unique only under restrictions, which would add a modification to the original CST or even some extra variables to the Critical State equations.

Discrete Element Method (DEM) (Cundall & Strack, 1979) is a rather new, promising, numerical tool that provides some answers in that vein. DEM will be discussed more in the next chapters; at this point, it is enough to mention that this numerical tool can apply many virtual loading conditions and give precise measurements in any area of the samples used, so that practical problems of real experiments, such as the creation of shear bands, could be overpassed. DEM research has already given convincing evidence of the uniqueness of CSL and the parameters this involves (Rothenburg & Kruyt, 2004; Sitharam & Vinod, 2008; Fu & Dafalias, 2011b; Yang & Luo, 2015; Yang & Wu, 2016).

3.1.5.2. Are Critical State conditions necessary and sufficient?

After presenting the principal concept of the CST, Schofield & Wroth (1968) describe in a more precise way the Critical State behavior. In section 6.8, p. 104-105, the CS is defined: "[…] ideal material that flows as a frictional fluid at constant specific volume, when and only when, the effective spherical pressure p and axial-deviator stress q satisfy […]"

herein, the Eq. (3.4). This assumption clearly suggests that Eq. (3.4) describe conditions necessary and sufficient ("when and only when") to define the Critical State.

This assumption is obviously also connected with the issue of uniqueness described above. The complete set of state variables that would precisely define the Critical State would also define the necessary and sufficient conditions for it. These two issues, although clearly related, are not the same problem; this difference may become apparent when it comes to constitutive modelling. In constitutive modelling one can have several CSLs depending on several parameters that could affect them. This means that multiple CSLs exist depending on some parameter (in Dafalias, Papadimitriou & Li (2004), this parameter was fabric). Although this perspective of CS does not provide uniqueness, the conditions met for each case are necessary and sufficient to reach CS.

3.2. Anisotropic Critical State Theory (ACST)

One of the basic assumptions of CST, has been the fact that, Schofield & Wroth (1968), in their effort to simplify their framework, have neglected the significance of the internal texture of the soil. As they explicitly assumed: "We will be concerned with isotropic mechanical properties of soil-material, particularly remoulded soil which lacks fabric." (Schofield & Wroth (1968) - Section 1.9, p. 14). This is represented in Eq. (3.4) by the fact that only void ratio is used, but no fabric-related quantity. This particular assumption, although it may have been reasonable or even necessary in order to build the paradigm of CST at the time, has attracted constructive criticism (Li & Dafalias, 2012; Dafalias, 2016).

Until recently, it seemed unclear whether the assumption for an isotropic fabric in CS was correct. Wood explicitly states (D.M. Wood, 2004 - section 2.6.1, p.86): "The exact nature of the fabric of the soil at a critical state is not clear". The isotropic nature of the fabric in CS, gave plausible grounds for keeping Critical State independent of the fabric. Although good reasons supported the anisotropic fabric in Critical State (Oda 1972a, 1972b), the dispute had begun. One easily can question the validity of this CS assumption, given that the soil response closely before reaching critical state has been repeatedly shown to be highly anisotropic (Nakata et al. 1998; Yoshimine et al. 1998; Oda & Iwashita, 1999) because of the fabric elements described in Chapter 2; thus, it would be unreasonable to assume that by reaching CS this rather strong anisotropy disappears.

During the last 20 years, several micro-structural pieces of evidence invariably show that in CS conditions fabric is anisotropic, and furthermore, strongly anisotropic (e.g. Masson & Martinez, 2001; Li & Li, 2009; Fu & Dafalias, 2011b). Hence, even though the quantifying element of fabric may change, the principle that fabric is anisotropic seems now evident. In contemporary research, it has become obvious that Critical State possesses some dependence on fabric, an extra variable that emerges as a necessity to this state. Thus, fabric actually seems of great importance for the CSSM framework; it has been stated that such influence of fabric in CST would be very important: "The influence of fabric on the anisotropic nature of Critical State and the uniqueness of CSL has profound implications for the universally accepted CSSM theory" (Seed et al., 2003).

Furthermore, Li & Dafalias (2012) suggested that the fabric parameter was missing from the classical CST and proposed an enriched theory that incorporates the fabric and its anisotropic critical state condition. If fabric is indeed such a missing link, then the classical CST conditions expressed from Eq. (3.4) would be rendered necessary but not sufficient, and the CSL would not be unique but dependent on the fabric anisotropy. Notice that the stress ratio remains independent of fabric anisotropy and only CSL seems to be fabric-dependent, a conclusion that some existing research also supports (Alarcon & Leonards, 1988; Dennis, 1988; DeGregorio, 1990; Mooney et al., 1998).

Thus, Li & Dafalias (2012) created the Anisotropic Critical State Theory (ACST), where the fabric is an added state parameter. This theory was formulated for granular materials as a general constitutive framework in a continuum approach, unrelated to any particular model, and lies within the broader rate-independent elastoplasticity field, exactly in the same spirit as the CST. At the core of ACST is fabric effect, which is expressed through the Fabric Anisotropy Variable (FAV) defined as:

$$A = \mathbf{F} : \mathbf{n} = F\mathbf{n}_F : \mathbf{n} = FN \tag{3.5}$$

where A is the FAV; $\mathbf{F}$ is the deviatoric fabric tensor (see also Chapter 2) that can be analyzed in norm (F) and a unit-norm direction tensor $\mathbf{n}_F$; $\mathbf{n}$ is the unit-norm loading direction tensor; scalar $N = \mathbf{n}_F : \mathbf{n}$ measures the relative orientation of $\mathbf{F}$ and $\mathbf{n}$ with the colon symbol (:) implying the trace of the product of the two adjacent tensors. In principle and for our purposes, the loading direction $\mathbf{n}$ is chosen along the deviatoric plastic strain rate tensor; this choice eliminates the need to associate it with specific models with yield and loading surfaces. Thus, the FAV quantifies fabric in terms of intensity and in terms of

its relative orientation with respect to the loading. The fabric intensity F is defined as the norm of the fabric tensor, normalized with it CS value. The evolution of $\mathbf{F}$ can be monitored in DEM based on its definition (see Chapter 2), while a continuum rate equation of its evolution has been suggested in Li and Dafalias (2012) motivated by DEM observations. If $\mathbf{F}$ is going to be used as an internal dissipative evolving variable in a continuum theory, it must be referred to a per unit volume measure to accommodate thermodynamic dissipation requirements, as elaborated extensively in a recent work by Li and Dafalias (2015).

Previous DEM studies (Li and Li, 2009; Fu and Dafalias, 2011b) have indicated that, as the fabric tensor evolves during plastic deformation, its direction $\mathbf{n}_F$ tends to align with $\mathbf{n}$ and becomes identical to it at CS (if it is not already equal to it), while the norm F, normalized with regards to the Lode angle θ_F of $\mathbf{F}$, defined by $\cos 3\theta_F = \sqrt{6} tr\, \mathbf{n}_F^3$, tends towards 1 at CS. Consequently at CS one has $N = N_c = \mathbf{n}_F : \mathbf{n} = \mathbf{n} : \mathbf{n} = 1$ (given the unit-norm property of both $\mathbf{n}_F$ and $\mathbf{n}$), $F = 1$ and $\mathbf{F} = \mathbf{F}_c = \mathbf{n}$; hence, based on the definition of A in Eq. (3.5), the third CS condition $A = A_c = 1$ follows. Thus, one can now write the three necessary and sufficient conditions of ACST for reaching and maintaining CS as:

$$\eta = \eta_c = (q/p)_c = M; \qquad e = e_c = \hat{e}_c(p); \qquad A = A_c = 1 \qquad (3.6)$$

The usefulness of ACST as a framework for constitutive modeling requires a few extra steps that address the dilatancy of granular assemblies accounting for the effect of fabric anisotropy. The state parameter $\psi = e - e_c$, introduced by Been & Jefferies (1985), determines the contracting ($\psi > 0$) or dilating ($\psi < 0$) state of a sample under shear, but does not account for fabric effects, as shown in a series of experiments by Yoshimine et al. (1998) (see also Chapter 2, section 1.2). The ACST introduces a very simple extension to the notion of the state parameter ψ in order to incorporate the effect of fabric, by defining a Dilatancy State Parameter (DSP) ζ in terms of ψ and A as:

$$\zeta = e - e_d = \psi - \hat{e}_A(e,p)(A-1) \qquad (3.7)$$

with $\hat{e}_A(e,p)$ an appropriate positive scalar-valued function of e, p (in the simplest case a constant). The ζ determines in $e-p$ space the so-called Dilatancy State Line (DSL), with e_d the void ratio on it at the current p. The ζ delineates between contractive ($\zeta > 0$) and dilative ($\zeta < 0$) states under shear, as ψ did in classical CST. At CS $A = A_c = 1$ according to the

third of Eqs. (3.6), and it follows from Eq. (3.7) that $\zeta = \psi$, $e_d = e_c$ and DSL = CSL. In essence, ζ substitutes for ψ in all constitutive features that depend on ψ, and together with A incorporate, in a simple and straightforward way, the effect of fabric anisotropy in CST. Use of ACST as a constitutive framework has been shown to produce very good results in simulating granular response with strong fabric anisotropy (Li and Dafalias, 2012; Gao et al, 2014; Papadimitriou et al, 2015).

3.3. CST completeness and the validity of ACST

While the notion of the FAV A has been very useful in constitutive modeling, to prove its necessity as a third CS condition entering Eqs. (3.6) one must be able to show that if the first two classical conditions are satisfied but not the third one, then CS cannot be reached and maintained. So far, by performing DEM simulations it has been observed that, when the first two conditions were met, the third condition $A = A_c = 1$ was always met concurrently and CS occurred (Fu and Dafalias, 2011b); and it had not been possible to generate a case where the first two conditions were reached without the third one also being reached simultaneously. Thus, one could conclude that the third condition is only a convenient supplement, which happens concurrently with the first two conditions at CS, but cannot be raised to the status of a necessary and independent third condition for CS to occur.

However, there is a way to counter argue this conclusion. So far, the DEM simulations started from an initial state where none of the three conditions were satisfied, while when CS was reached, all three were concurrently met. However, one can consider the exact opposite scheme of action in terms of initial state, namely starting from a CS, where all three conditions are satisfied, and modifying only the third condition so that it is violated in order to see if CS is maintained. If it is maintained, then the third condition is not a necessary addition to the first two, but only a convenient supplement in some cases. On the other hand, if CS is not maintained, then CST is incomplete and an extra condition must be added as a necessary, independent condition for CS, rendering all three conditions necessary and sufficient.

This being stated, the following thought experiment and related question is worth considering: a soil sample is loaded in triaxial compression until it reaches Critical State (CS), namely the state at which continuous deviatoric strain develops under fixed stresses

with no volume change. While being at CS, stress Principal Axes (PA) rotation is imposed, with the principal stress values kept fixed. The question that arises is: will the sample continue being at CS or not?

The thought experiment proposed, where the PA of stress rotate at CS while keeping the stress principal values constant, is exactly the experiment needed to address the issues raised in the preceding paragraph. The original question was whether the sample would continue being at CS or not when such rotation is imposed. Since the critical stress ratio condition ($\eta = \eta_c = M$) will not change for fixed principal stress values, and the void ratio is already at critical state value ($e = e_c$) for the given p that also remains same, if the classical CST conditions given by Eqs. (3.4) are sufficient for CS, then the sample must remain at CS during the rotation of stress PA and, accordingly, no void ratio change must be observed.

However, if one measures a void ratio change when stress PA rotation initiates, this means that Eqs. (3.4) are necessary but not sufficient to maintain CS and, therefore, classical CST is incomplete. In this case, something else must be happening during this process that moves the sample away from CS against the premises of classical CST. According to ACST this "something else" is related to the violation of the third, fabric-related, condition $A = A_c = 1$ in Eqs (3.6); how it is related, will be explained after the results of the stress PA rotation at CS are presented. Rotations of PA of stress and related observations on deformation characteristics have been presented before using DEM (e.g. Li and Yu, 2010; Tong et al, 2014a), but the distinguishing feature of the present work is that such rotation initiates at CS, a numerical experiment never attempted before.

The foregoing analysis on the issue of completeness or not of CST, as well as, the suggestion for a DEM experiment with rotation of the PA of stress at CS to confirm or deny such completeness and to validate the necessity for introducing ACST, were recently elaborated on a hypothetical basis by Dafalias (2016); one of the main objectives of the present work is the realization of this hypothetical proposal.

Chapter 4: 2D DEM virtual experiments – Proof of incompleteness of Critical State Theory and its Remedy

4.1. Introduction

Following the previous chapter's analysis on the incompleteness of Critical State Theory (CST), the importance of the proposed DEM experiment becomes evident. A question arises as to why such results had not yet appeared in the literature. Though physical experiments with stress principal axes rotation have been conducted (e.g. Miura et al., 1986; Tong et al., 2010), none has been presented initiating at Critical State (CS). In addition, though few 2D DEM virtual experiments do exist in stress PA rotation (Li & Yu, 2010; Tong et al, 2014a; Fu & Dafalias, 2015), there exist none in the CS. This happens mainly due to systematic issues that arise when a soil sample is under CS conditions; as suggested in Chapter 3, during CS the stress ratio and the volumetric strain are constant while the deviatoric strain is the only one evolving. That means that, by definition the sample is uncontrollable in terms of stress, as a slight increase would theoretically create infinite deviatoric strain. Furthermore, the successful access of CS is difficult, as discussed before, due to the occurrence of shear bands and other non-uniformities.

Consider that the successful realization of the described experimental procedures means that, not only the sample should reach CS, but also it should be in a condition to be loaded with stress PA rotation. The procedure presented below has been a systematic try to solve these problems and access the experiment in pursue. In succeeding the two phases (biaxial loading and stress PA rotation) another, third phase has been added for reasons that will become clear in the sequel. For the 2D setting, where the numerical experiments of this chapter will take place, only two principal stress and strain components exist, $\sigma_i (i=1,2)$ and $\varepsilon_i (i=1,2)$; the biaxial counterparts of the originally defined in triaxial variables p (hydrostatic pressure), q (deviatoric stress), ε_v (volumetric strain) and ε_q (deviatoric strain) are defined as $p=1/2(\sigma_1+\sigma_2)$, $q=\sigma_1-\sigma_2$, $\varepsilon_v=\varepsilon_1+\varepsilon_2$ and $\varepsilon_q=1/2(\varepsilon_1-\varepsilon_2)$.

4.2. Implementation issues

The 2D DEM analysis was executed using PFC 2D v4.0© (Itasca, 2013; Cundall and Strack, 1979). The virtual experiment presented herein employed circular particles (disks), whose properties are outlined in Table 4.1. The local damping ratio and the loading rate were determined through a sensitivity analysis to ensure quasi-static conditions and negligible effects on the final results. In particular, the value of the damping ratio 0.7 of type local, given in Table 4.1, is typical for biaxial experiments, in order to sufficiently dissipate the energy of the system, whereas the loading rate was controlled using two different approaches: (1) the inertial number, (Radjai & Dubois, 2011; Szarf et al, 2011), having a maximum value in the order of 10^{-5}, and (2) the maximum unbalanced force ratio (defined as the maximum ratio of mean unbalanced force over the mean contact force) measured in the order of 10^{-4} (Ai et al, 2013). Calculations were carried within a circular Representative Volume (RV), shown in black in Fig. 4.1(a), while circular volumes concentric with the RV and shown with light gray shade, are used to monitor and validate the results inside the main RV and, thus, ensure homogeneity of the samples. Compressive stresses and strains are considered positive according to the usual soil mechanics convention.

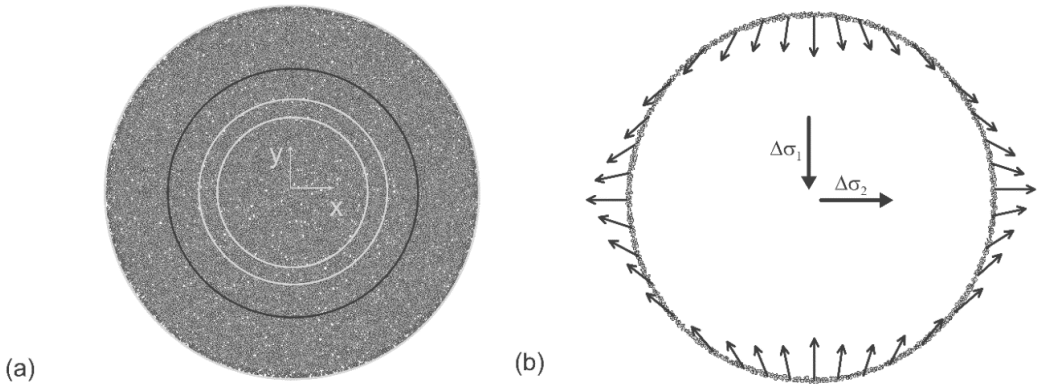

Fig. 4.1. (a) Configuration of particles for initially circular sample, its REV in black and concentric circles in gray where results were monitored (b) Velocity field applied at the boundary particles to achieve the stress changes $\Delta\sigma_1$ and $\Delta\sigma_2$ as shown

Common practice for boundary conditions in 2D virtual DEM experiments employs either rigid walls for strain-controlled experiments (e.g. Li & Li, 2009), or particle-defined

membranes simulating flexible walls (e.g. Fu & Dafalias, 2015). However, here the strain-controlled boundary of the sample is formed using boundary particles on which a velocity field is applied using a servomechanism (e.g. Calvetti, 2008; Huang et al., 2014). This servomechanism controls the convergence of the stress state in the RV to a specified stress state. Fig. 4.1(b) illustrates the application of a velocity field shown by vectors applied on the boundary particles of the sample, to implement a desired loading that consists of a vertical compressive stress increase $\Delta\sigma_1 (> 0)$ and a horizontal stress decrease $\Delta\sigma_2 (<0)$; the directions of velocities vary progressively from vertical to horizontal in order to reflect the foregoing loading**.**

Number of grains	20,000
Average grain radius (m)	0.001
coefficient of uniformity (Cu = d_{60}/d_{10}); r_{min} (m); r_{max} (m)	1.8 ; 0.0005 ; 0.0015
Out of plane length of the grain assembly (t) (m)	1
Radius of circular specimen (m)	0.165
Isotropic and mean pressure (kPa)	200
k_n (N/m)	$5x10^8$
k_n / k_s (N/m)	1
Surface friction (disk-disk; disk-boundary disk)	0.5; 0.0
Damping ratio	0.7

Table 4.1 Particles properties for 2D DEM experiments

The use of the boundary particles allows imposing stress PA rotation on a virtual DEM sample by directly rotating the applied velocity field. This choice facilitates the development of stress PA rotation at a high stress ratio, particularly when reaching CS. Based on theoretical considerations stress-controlled methods (e.g. Tong et al., 2014a) can hardly control the deformation of the sample when reaching CS; additionally, strain-controlled boundaries using rectangular or polygonal-shaped rigid elastic walls (e.g. Li et al, 2013) may induce arching when significant strains of the samples are considered.

The strain rate calculation (actually the rate of deformation as the symmetric part of the velocity gradient) is based on a best-fit approach already implemented in PFC 2D v.4.0,

which provides the strain rate tensor at every time-step of the simulation inside the RV (Liao, 1997; ITASCA, 2008). As already stated, the stress PA rotation is achieved by adjusting iteratively a velocity field applied to the boundary particles, for the resulting stress state in the RV to converge with the desired stress state with rotated PA. This convergence process is repeated for each increment of the stress PA rotation, lasts multiple time-steps and induces variability (of numerical nature) to the related strain rate values. Hence, a proper averaging procedure over multiple time-steps (during each convergence process) is considered to obtain the strain rate tensor.

The randomness of the grains' creation inside the initially circular sample led to an initially isotropic fabric. This isotropic fabric was sustained to a large extend, after isotropic compression with mean stress $p = 200\text{kPa}$ was applied to the virtual soil specimen. Subsequently a three-phase loading sequence was applied to the sample whose response is described in the following.

4.3. Macroscopic results

4.3.1. Phase 1: Biaxial loading till CS

Biaxial loading was applied by increasing the compressive major principal stress σ_1 along the vertical y-axis and decreasing by an equal amount the minor principal stress σ_2 along the horizontal x-axis, keeping p constant; hence, with reference to Fig. 4.1(b) one has $\Delta\sigma_1 = -\Delta\sigma_2 > 0$. Because the direction of the principal stresses remained constant throughout the test, a velocity field with fixed directions was applied at the boundary particles. The macroscopic response of the initially circular sample is presented in Figs. 4.2(a and b) with black lines, and exhibits a typical stress-strain and volumetric response for initially loose granular samples. The virtual sample reached CS at around 10% of axial (compressive) strain along the y-axis, and calculations continued all the way to 30% strain, while the stress and void ratios maintained their CS values of $\eta = \eta_c = M \approx 0.57$ and $e = e_c = \hat{e}_c(200\text{kPa}) \approx 0.23$. In order to avoid bias due to initial sample shape and boundary conditions, the same kind of loading was also applied to an elliptical sample with boundary particles, and a rectangular sample with rigid walls; both samples with ratio of major (vertical) to minor (horizontal) axis equal to 2, using the same parameters

of Table 4.1. The results are included in Figs. 4.2(a and b) as lines with different shades of gray and show similar response, thus, validating non-existence of bias.

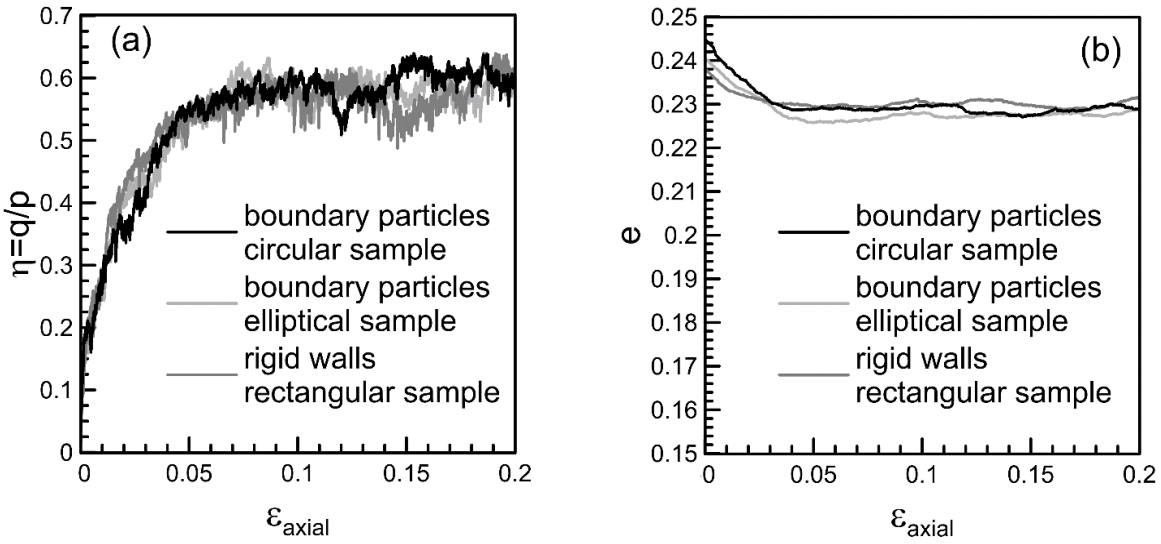

Fig. 4.2. Effect of initial geometry and boundary conditions on the macroscopic response of phase 1 biaxial tests on an initially loose sample: (a) stress ratio η and (b) void ratio e, versus vertical axial strain ε_{axial}

4.3.2. Phase 2: Stress PA rotation

Rotation of stress principal axes (PA) keeping the principal stress values σ_1, σ_2 constant was imposed on the specimen, when it reached 20% axial strain during Phase 1 loading, while being undoubtedly at critical state (CS). The stress PA rotation is quantified by the varying angle θ_σ of σ_1 axis with respect to the vertical y-axis, which increases by 180^o for each full cycle of rotation. Fig. 4.3 shows schematically the stress path followed during the stress PA rotation in the σ_{xy} versus $(\sigma_{yy}-\sigma_{xx})/2$ stress space, which is tangential to the circumference of a circle with constant radius equal to $(\sigma_1-\sigma_2)/2$. Since the sample is at CS where $q/p=M$, it follows that the radius also equals $(1/2)Mp$ (recall definition of q, p in 2D after section 4.1). The angle of the radius with the $(\sigma_{yy}-\sigma_{xx})/2$ axis equals $2\theta_\sigma$.

The small inserts show the orientation of the stress components in real space. The DEM servomechanism defines the appropriate rotating velocity field applied at the boundary particles, to obtain the stress PA rotation by controlling the periodical variation of the

stress components σ_{xx}, σ_{yy}, σ_{xy} as shown in Fig. 4.4(a), with the normal stresses at double the frequency of the shear stress.

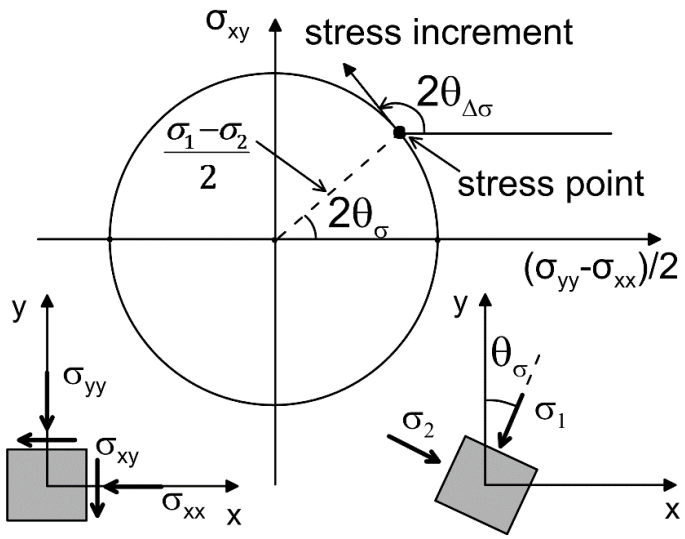

Fig. 4.3. Illustration of stress path in the shown stress space for rotation of stress PA during phase 2 loading and schematic presentation of stress components in real space

Fig. 4.4(b) is a key figure; it shows a reduction of the void ratio and associated volumetric strain during the stress PA rotation. The void ratio decreased continuously, cycle after cycle from its critical state value $e_c = 0.23$, to a value close to $e = 0.188$, which corresponds to a volumetric contraction strain of 3.4% from initiation of PA rotation, at a decreasing rate heading towards stabilization after 15 cycles. This result embodies a most important conclusion: *the initial reduction of void ratio from its CS value at the very start of the PA rotation is the key observation that invalidates the completeness of classical CST conditions in Eq. (3.4)*. The reason why this is the case was fully explained at the end of Chapter 3, particularly in the subsection entitled "3.3 CST completeness and the validity of ACST", and will not be repeated here. It suffices to say that at the end of phase 1 loading where CS was reached and just before initiation of the stress PA rotation with fixed principal stress values, the two CS conditions of Eq. (3.4) were satisfied, and yet CS was abandoned at the initiation of the rotation. It will be shown that the new ACST can explain the foregoing response, based on the third CS condition on fabric of Eq. (3.6).

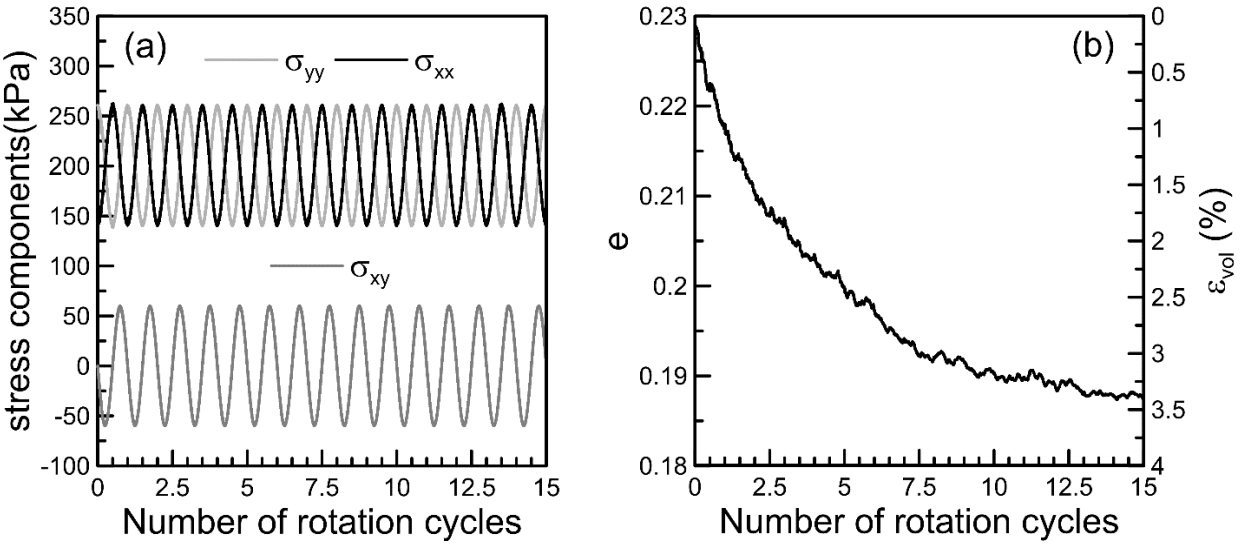

Fig. 4.4. (a) Variation of stress components and (b) Variation of void ratio and volumetric strain, with cycles of stress PA rotation during phase 2 loading

4.3.3. Phase 3: Biaxial loading after stress PA rotation and overview of all phases

Phase 3 loading imposed biaxial loading as in phase 1, but "rotated" by an angle θ_σ of σ_1 axis with respect to the vertical y-axis, where the preceding stress PA rotation stopped at the end of phase 2. The purpose of this radial loading is to investigate what happens with the stress ratio and the void ratio, which was reduced during the preceding stress PA rotation, and to examine if CS is reached again and how. To examine the effect of the angle of the preceding rotation on the response, two different radial loading paths were performed at angles θ_σ of 210^o (30^o after 1 full circle) and 0^o after 10 full cycles (of 180^o each).

With the objective of having an overview of the response from the beginning, the results of phase 3 loading will be presented together with the results of the previous two phases in common plots of Figs. 4.5 and 4.6 for the aforementioned two choices of θ_σ, respectively. For a unified representation of all test results, the equivalent cumulative deviatoric strain measure $e_{eq} = \int \sqrt{(1/2)\dot{e}_{ij}\dot{e}_{ij}}\,dt$, with e_{ij} the deviatoric strain in two dimensions, is used as a reference strain for the whole experiment, initiating after the application of isotropic compression $p = 200\text{kPa}$. In all these plots, the part for phase 1 will be denoted by light gray, for phase 2 by black and for phase 3 by darker gray.

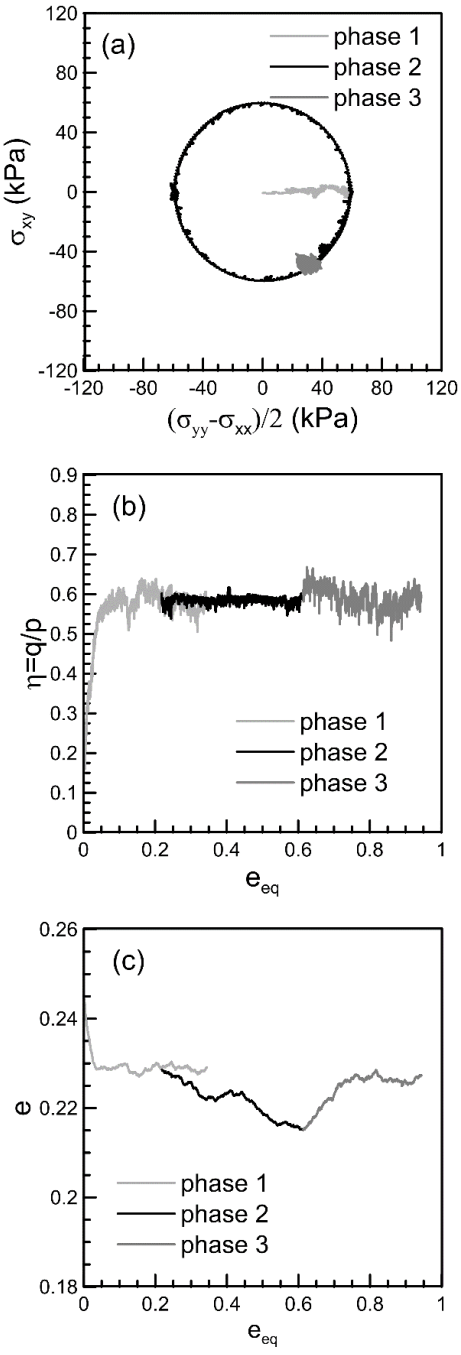

Fig. 4.5. Plots during the full three-phase loading sequence with phase 3 at $\theta_\sigma = 210^o$: (a) the stress path (b) the stress ratio q/p versus e_{eq} (c) the void ratio e versus e_{eq}

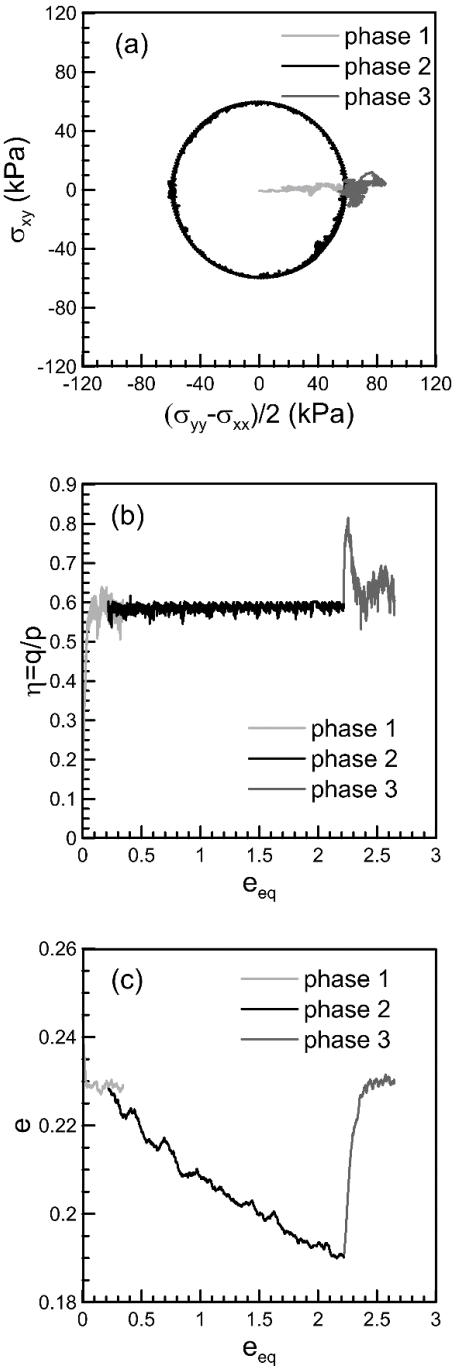

Fig. 4.6. Plots during the full three-phase loading sequence with phase 3 at $\theta_\sigma = 0^o$ after 10 cycles: (a) the stress path (b) the stress ratio q/p versus e_{eq} (c) the void ratio e versus e_{eq}

Recall that the initiation of phase 2 took place at an intermediate stage of phase 1 at axial strain $\varepsilon_{axial} = 20\%$; thus, the initiation points of the black plots of phase 2 will appear at such intermediate points of the light gray color plots of phase 1, accounting for the fact e_{eq} substitutes for ε_{axial} used in phase 1. Phase 3 darker-gray plots will continue directly after the black plots of phase 2.

Figs. 4.5(a) and 4.6(a) show the stress path in the σ_{xy} versus $(\sigma_{yy} - \sigma_{xx})/2$ stress space as presented in Fig. 4.3 during all three phases, the third one for $\theta_\sigma = 210^o$ and 0^o (after 10 cycles), respectively. Recall that at CS the radius of the circular stress path equals $(1/2)Mp$; the DEM calculation of the critical stress ratio yields $(q/p)_c = \eta_c = M = 0.57$, thus, with $p = 200kPa$ the value of the radius is 57kPa. The light-gray radius, black circumference and gray line radial segments outwards the circumference, as well as corresponding cluster of points at CS, vividly represent the stress history during each one of the three phases, correspondingly. The outwards radial segments (imperceptible in Fig. 4.5(a) but clearly visible in Fig. 4.6(a)) describe the increase of stress ratio at the initiation of phase 3, as clearly seen in the subsequent Figs. 4.5(b) and 4.6(b). Fluctuations in regard to shapes of line segments and circumference are due to numerical effects of the servomechanism, which controls stress evolution via velocity field on the boundary particles.

Figs. 4.5(b) and 4.6(b) show the variation of stress ratio $\eta = q/p$ with e_{eq}, with expected fluctuations inherent to DEM, during all three phases (large-scale difference in the horizontal e_{eq} axis). The overlapping of the black lines with the light gray ones reflects the aforementioned fact that phase 2 (black lines) begun at an intermediate point of phase 1 (light-gray lines). Regardless of the θ_σ value at the end of phase 2 loading, the stress ratio η is equal to its critical state value M, but immediately upon initiation of phase 3 loading there is an increase of η above M (beginning of gray lines in Figs. 4.5(b) and 4.6(b)), with such an increase being significantly more pronounced after the more extensive densification in the case of $\theta_\sigma = 0^o$ following 10 cycles, and then falls back and stays at $\eta = M$.

Finally, Figs. 4.5(c) and 4.6(c) present the variation of the void ratio during the full loading sequence for the choices of angle θ_σ equal to 210^o and 0^o following 10 cycles,

respectively. The main observation is again the reduction of the void ratio during stress PA rotation shown by the black lines, quite more pronounced in Fig. 4.6(c) than 4.5(c). In particular, at the very beginning of phase 2 the same argument used in conjunction with Fig. 4.4(b), apply to deny completeness of classical CS conditions of Eq. (3.4). One very interesting new piece of information is provided by phase 3 loading: the void ratio rebounds to its critical state value and stays there, i.e. the volume reduction observed during the preceding stress PA rotation is reversed in full, and this happens regardless of the preceding cycles, the associated values of θ_σ and the resulted e_{eq}; in conjunction with $\eta = M$ this implies that CS has been restored.

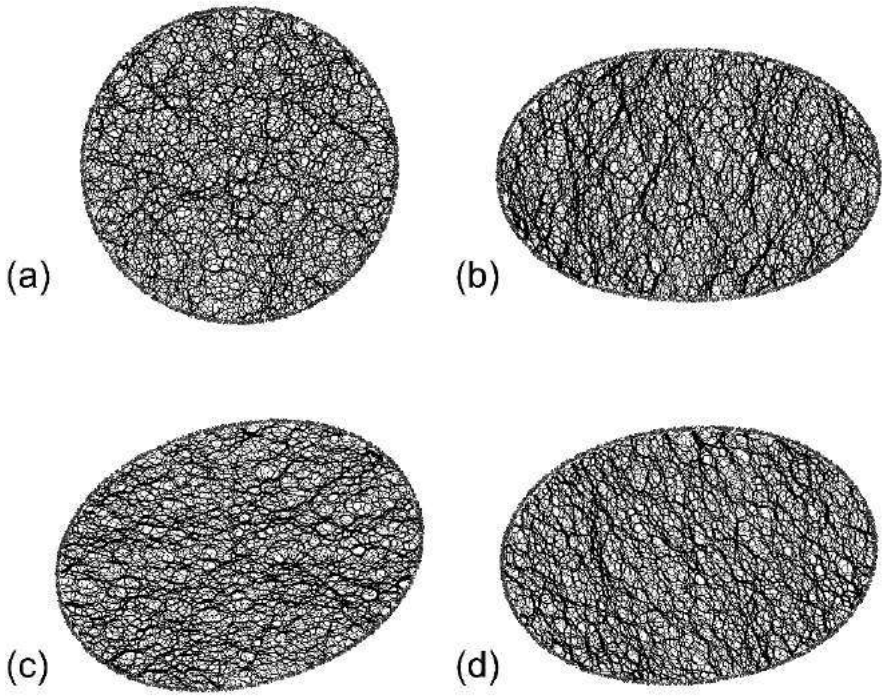

Fig. 4.7. Sample with boundary particles and contact forces at (a) end of isotropic compression; (b) end of Phase 1 (sample at CS); (c) Phase 2 after stress PA rotation $\theta_\sigma = 90^o$; (d) Phase 3 for stress PA rotation $\theta_\sigma = 210^o$

Finally, no shear bands or other inhomogeneity were observed for all samples and loading procedures in this work. Fig. 4.7 presents the deformed samples and the contact forces in specific loading instances: (1) the end of isotropic compression [Fig. 4.7(a)], (2) the end of Phase 1 when the sample is at CS [Fig. 4.7(b)], (3) during Phase 2 and in particular for $\theta_\sigma = 90^o$ [Fig. 7(c)], and (4) during Phase 3 at $\theta_\sigma = 120^o$ [Fig. 4.7(d)]; the

thickness of the line segments along contact forces corresponds, as usual, to the magnitude of those forces, and the same scale is used in all subfigures. The observed spatial distribution of the contact forces' network attests to the homogeneity of stresses in all loading phases.

4.4. Fabric evolution during the 2D DEM experiment

So far, the results of the DEM experiment proved the incompleteness of classical CST, by showing the insufficiency of the two classical CS conditions of Eqs. (3.4) to maintain CS. It is important to propose an alternative theory that will be complete and able to explain and incorporate such results. As already mentioned this alternative theory appears to be the ACST by Li and Dafalias (2012) outlined earlier, and the novel element of its foundation is the role of fabric at CS. Thus, the evolution of the fabric and quantities relevant to ACST during the foregoing experiment will be briefly presented in this section and illustrated in common plots for all three phases of loading following the same color scheme of light-gray, black and darker-gray for phases 1, 2, and 3, correspondingly. For clarity, the plots for phase 1 will be shown till 20% axial strain when the transition to phase 2 takes place, unlike in previous figures where the phase 1 plots continued all the way to 30% strain.

4.4.1. Contact normal fabric

The fabric tensor $\mathbf{F}$ is firstly calculated by Eq. (2.6), for contact normal fabric. The $\mathbf{F}$ will be quantified by two entities: its norm F given by $F=\sqrt{tr\mathbf{F}^2}=\sqrt{2}|F_I|=\sqrt{2}|F_{II}|=(1/\sqrt{2})|F_I-F_{II}|$ and the stress-fabric angle lag $\theta_\sigma-\theta_F$ measuring the difference of the angle θ_F of its eigenvector with the major principal value F_I, from the angle θ_σ of the σ_1 axis (see Fig. 4.3), with both angles in reference to the vertical y-axis. The loading direction $\mathbf{n}$ has been defined after Eq. (3.5).

Figs. 4.8(a) and 4.9(a) show the plots of F and $\theta_\sigma-\theta_F$ during all three phases, the third one at $\theta_\sigma=210^o$ and 0^o (after 10 cycles), respectively. The F increases from zero to its CS value $F_c=1$ during phase 1 as fabric anisotropy develops, stays equal to 1 during phase 2 (within the expected DEM fluctuations) despite the fact the material abandons

CS as shown in Figs. 4.5(c) and 4.6(c) by the reduction of void ratio from its CS value, and then after a rather dramatic initial increase above 1 at the initiation of phase 3, it falls back to its CS value $F_c = 1$. Just a reminder that the value of F is normalized by its CS value, that is why $F_c = 1$; its actual calculated value at CS is $F_c = 0.085$.

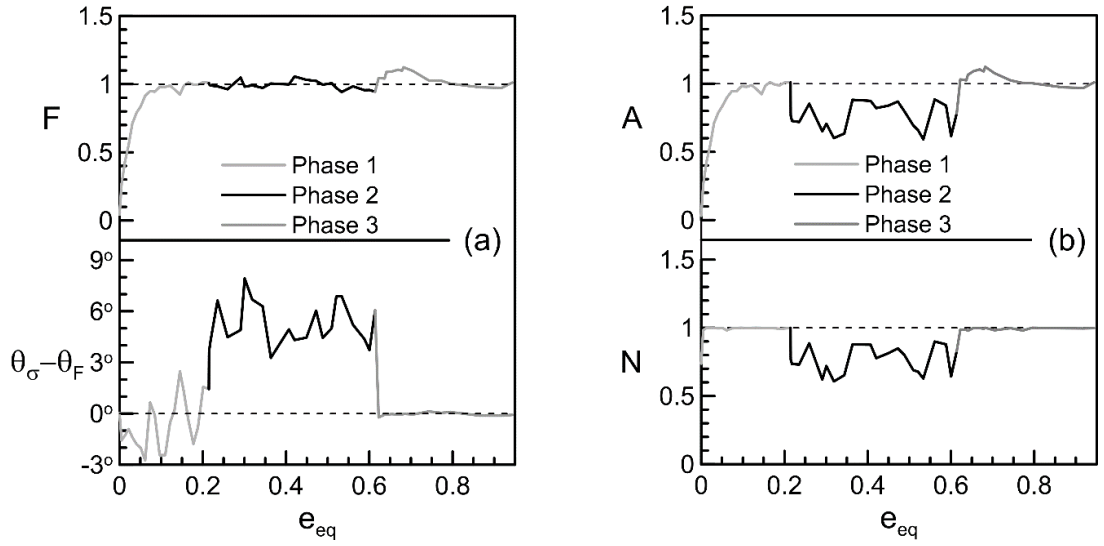

Fig. 4.8. Plots of contact normal fabric entities during the full three-phase loading sequence with phase 3 at $\theta_\sigma = 210^o$: (a) F and $\theta_\sigma - \theta_F$ (b) $A = F\mathbf{n}_F : \mathbf{n}$ and $N = \mathbf{n}_F : \mathbf{n}$

On the same figures the $\theta_\sigma - \theta_F$ remains at an average value of 0^o during the biaxial loadings of phases 1 and 3; during phase 1 there are some fluctuations between -3^o and 3^o because the sample is quite loose and has a more unstable evolving granular structure, while during phase 3 $\theta_\sigma - \theta_F$ is almost zero with no fluctuations (denser sample). During phase 2 the η fluctuates between 3^o and 8^o or both cases of θ_σ; its increase from M (on average during phase 1) occurs by a rather fast transition within the first quarter of the first cycle of phase 2 (Fig. 4.10a), and so does its reversal back to 0^o at the transition from phase 2 to 3. The foregoing discussion shows that the PA of the fabric tensor are coaxial with the PA of the stress tensor during phases 1 and 3, while during phase 2 the two pairs of PA rotate together, with the PA of fabric following those of stress with a phase lag of about $\theta_\sigma - \theta_F = 5^o$ on average.

While the PA of stress can change abruptly by the investigator, those of fabric tensor evolve progressively since the directions of inter-granular normal vectors cannot change abruptly; here, however, the stress direction does not change abruptly but progressively

when the PA begin to rotate from their orientation at the end of phase 1, and they are followed by the PA of fabric tensor with a constant phase lag on average. Similar results for stress and fabric PA rotation have been presented in the literature but not initiating at CS, such initiation being the most important differentiating feature the present work. Particularly in Li & Yu (2010) and Fu & Dafalias (2015) the fabric anisotropy intensity, defined by $\alpha_F = \sqrt{2F}$, remains approximately fixed during the rotation, while $\theta_\sigma - \theta_F$ fluctuates from -4^o to 8^o and from 5^o to 8^o for the foregoing two references, respectively, very close to the present findings.

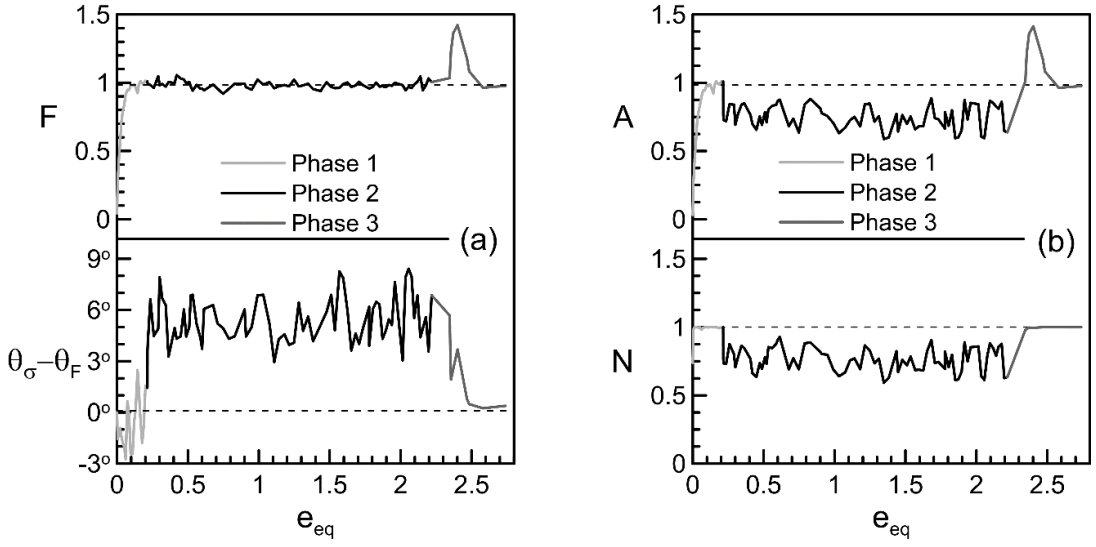

Fig. 4.9. Plots of contact normal fabric entities during the full three-phase loading sequence with phase 3 at $\theta_\sigma = 0^o$ after 10 cycles: (a) F and $\theta_\sigma - \theta_F$ (b) $A = F\,\mathbf{n}_F : \mathbf{n}$ and $N = \mathbf{n}_F : \mathbf{n}$

Fig. 4.8(b) and 4.9(b) show the plots of N and A during all three phases, the third one at $\theta_\sigma = 210^o$ and 0^o (after 10 cycles), respectively. During phases 1 and 3 $N = 1$,while during phase 2, N fluctuates around 0.8. Based on Eq. (3.5) one has $N = \mathbf{n}_F : \mathbf{n} = \cos 2\varphi$ with $\varphi = \theta_n - \theta_F$ the angle between the directions of $\mathbf{n}$ and $\mathbf{F}$ (via $\mathbf{n}_F$), expressed by the difference of the angles θ_n and θ_F of their major PA with respect to the vertical y-axis. Therefore $\theta_n - \theta_F = (1/2)\cos^{-1} N$ which yields $\theta_n - \theta_F = 0$ for $N = 1$ during phases 1 and 3 implying coaxiality of $\mathbf{F}$ and $\mathbf{n}$, and $\theta_n - \theta_F = 18^o$ for $N \simeq 0.8$, approximately, during phase 2, implying the PA of $\mathbf{F}$ follow by an angle lag of 18^o those of $\mathbf{n}$ during the rotation

of the PA of stress. Recalling that during phase 2 one has $\theta_\sigma - \theta_F = 5^o$ on average, it follows that $\theta_n - \theta_\sigma = 18^o - 5^o = 13^o$, i.e. the PA of stress follow by an angle lag of about 13^o the PA of $\mathbf{n}$ during the rotation of the former. In summary during phases 1 and 3 the PA of stress, $\mathbf{F}$ and $\mathbf{n}$ are all coaxial, with fast transition to and from phase 2 (Fig 4.10b) during which the PA of $\mathbf{F}$ follow the PA of stress by an angle lag of 5^o, while the PA of stress in turn follow the PA of $\mathbf{n}$ by an angle lag of 13^o, as all three pairs of PA rotate simultaneously.

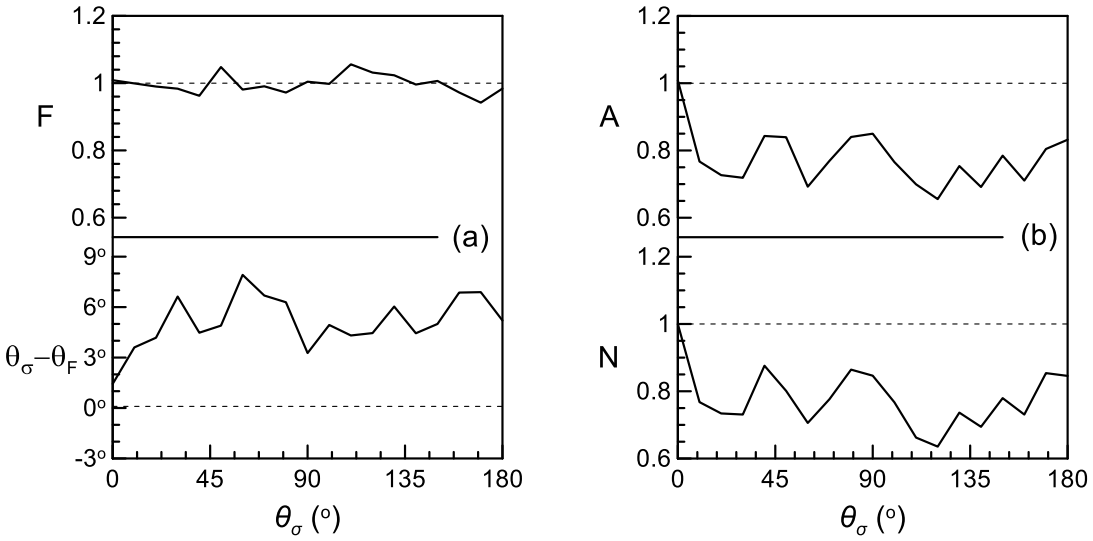

Fig. 4.10. The first cycle of Phase 2, showing the fast transition from Phase 1 during the first quarter; Plots of fabric entities: (a) F and $\theta_\sigma - \theta_F$, (b) $A = F\mathbf{n}_F : \mathbf{n}$ and $N = \mathbf{n}_F : \mathbf{n}$

Based on the preceding summary, the FAV $A = A_c = 1$, on average, at the end of phases 1 and 3, where CS is established since the critical stress ratio and void ratio are reached as seen in Figs. 4.5(b and c), 4.6(b and c). During phase 2 one has $A \simeq 0.8 < 1$ for both Fig. 4.8(b) and 4.9(b), while during the first part of phase 3 $A \simeq 1.1 > 1$ for Fig. 4.8(b), and $A \simeq 1.25 > 1$ for Fig. 4.9(b), on average. Since $A = FN$ from Eq. (3.5), the plot of A is very close to N when $F \approx 1$ on average at the end of phase 1, during phase 2 and finally towards the end of phase 3. These observations about the values of A and F during the three-phase loading will be instrumental in interpreting the response based on the premises of ACST in the sequel.

4.4.1. Void scan line fabric

The same fabric analysis has been conducted for the void fabric as for the contact normal fabric. Both equations defined in Chapter 2 for the scan line void fabric have been used for the quantification of void fabric; Eq. (2.9) for the modified classical scan line and Eq. (2.10) with the novel squared length scan line tensor. For both cases the "cut off" has been defined as the minimum radius of the smallest grain for the uniform distribution of the grains. The results are presented in the exact same form as for the contact normal fabric in Figs. 4.10 and 4.11, for F and $\theta_\sigma - \theta_F$, and N and A during all three phases, respectively, the third one only at $\theta_\sigma = 0^o$ (after 10 cycles). It appears that qualitatively, the use of the void fabric in lieu of the contact normal, justifies a similar conclusion. In general, the response of the void fabric is the same as that of the contact normal, but the scan line void fabric presents, in principle, more fluctuations. This observation could be expected given the completely different definitional approach between, on the one hand, the extremely accurate definition of contact normal fabric in DEM, and, the more "rough" and experimental-type definition of the scan line void fabric on the other.

In Figs 4.11(a) and 4.12(a) the norm of the fabric tensor F appears to be constant, on average, as is the contact normal fabric norm, though with significant fluctuations around its average value. Still, there is no tendency for the norm to increase or decrease. In addition, the difference of the fabric angle with respect to the stress principal angle $\theta_\sigma - \theta_F$ has a change from 8^o to 20^o for classical scan line and 0^o to 15^o for the squared scan line. This result, including the aforementioned fluctuations, reveals that the void fabric rotates with more delay than the contact normal fabric. This reveals an expected feature of the void fabric; the contact normal vectors, as they follow the evolution of stresses very closely, have a slight delay from the stresses (5^o on average) while the void fabric delays even more (12^o for the classical scan line and 8^o for the squared length). Voids need more time to evolve after the contact normal vectors have evolved, given that they need the grains to rotate and change position. This could be considered an advantage of the scan line method in properly quantifying the voids, as contact-based void fabric tensors would probably provide an evolution more similar to the contact normal fabric (see also Fu & Dafalias, 2015).

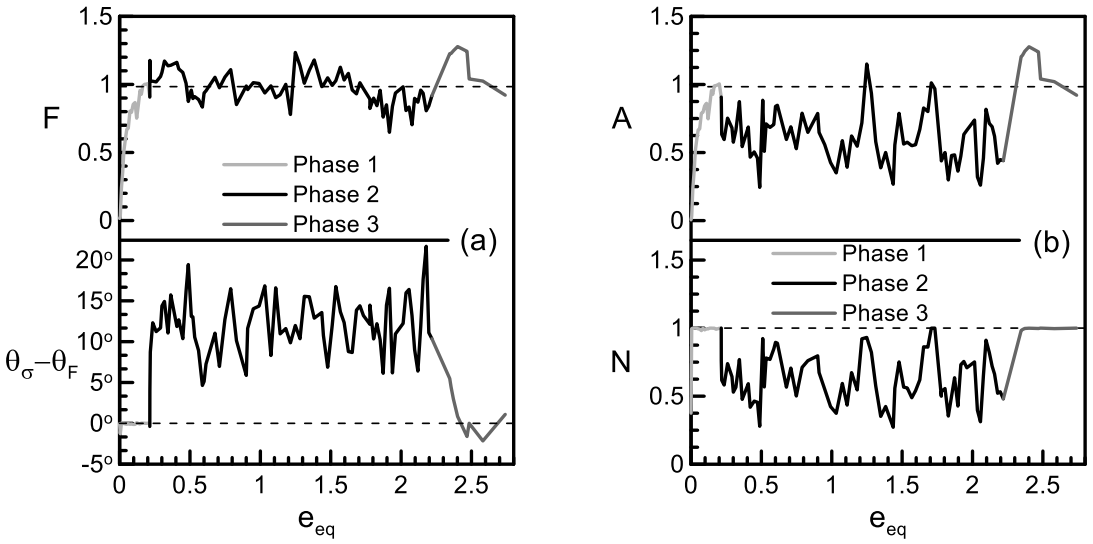

Fig. 4.11. Plots of fabric entities during the full three-phase loading sequence, for scan line void fabric, with phase 3 at $\theta_\sigma = 0^\circ$ after 10 cycles: (a) F and $\theta_\sigma - \theta_F$ (b) $A = F\mathbf{n}_F : \mathbf{n}$ and $N = \mathbf{n}_F : \mathbf{n}$

In Figs 4.11(b) and 4.12(b) the evolution of the N leads to the same conclusions, i.e. the greater delay of the void fabric, this time with respect to the strain rate, along with greater fluctuations than the contact normal fabric. In addition, the evolution of A supports the same comments as in the prequel for the contact normal fabric. In summary, the scan line void fabric supports the qualitative results of the contact normal fabric and could be used interchangeably in the foregoing interpretation of the results.

Closing this section, it should be mentioned that, in order to exclude bias of the results due to various levels of pressure and strain at the end of phase 1, or due to the initial circular shape of the sample, the same numerical experiment was performed for different p values on circular samples and after axial strains of 4%, 8% and 13% for phase 1 (different stress ratio), and on elliptical samples after axial strains of 15%, 17%, 19% and 20% for phase 1 (again different stress ratio). With small variations, the results were the same as the ones for circular sample at $p = 200\text{kPa}$ after axial strain of 20% before the initiation of phase 2.

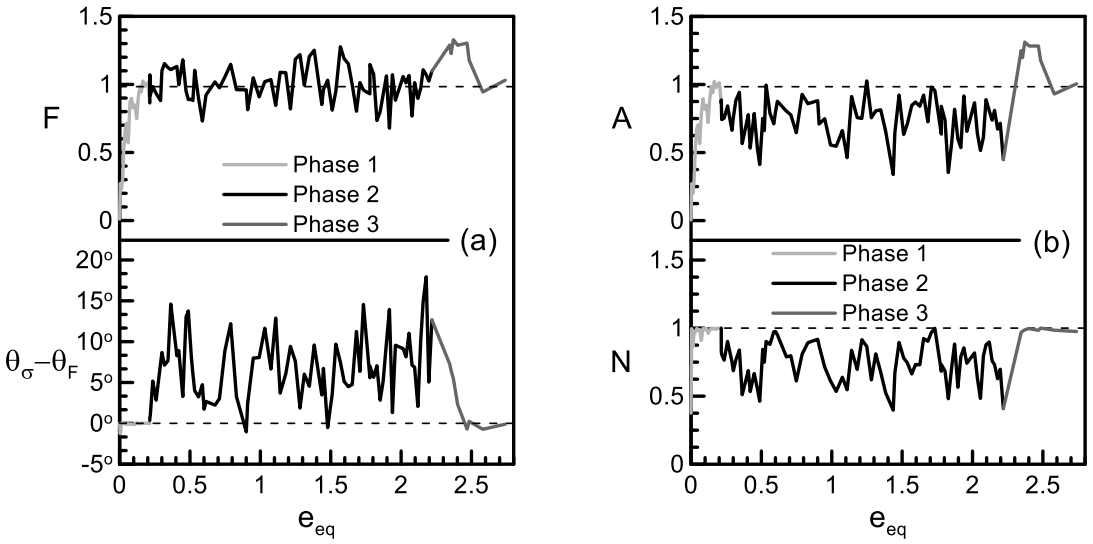

Fig. 4.12. Plots of fabric entities during the full three-phase loading sequence, for squared scan line void fabric, with phase 3 at $\theta_\sigma = 0^o$ after 10 cycles: (a) F and $\theta_\sigma - \theta_F$ (b) $A = F\mathbf{n}_F : \mathbf{n}$ and $N = \mathbf{n}_F : \mathbf{n}$

4.5. Explanation of DEM experiment results by ACST

The foregoing experimental-numerical DEM results on the reduction of void ratio at the initiation of the stress PA rotation, while classical CS conditions expressed by Eqs. (3.4) were satisfied, constitute a clear counterexample to their completeness, and show that classical CS conditions may be necessary but not sufficient to maintain CS. However, it is important, not only to conclude that CST is incomplete, but to also see if the proposed ACST can explain these results during phase 2, as well as, the additional ones during phases 1 and 3. The task of the present section is to argue that this is indeed the case.

In very simple terms the essence of ACST is, on one hand, the introduction of the third condition in Eqs. (3.6) (i.e. the satisfaction of $A = A_c = 1$ by the FAV A) and on the other hand the definition of the DSP ζ in terms of A in Eq. (3.7) as the quantity that signifies dilative response if negative, and contractive if positive. In other words, the ζ in ACST plays the role that the state parameter ψ played in CST, and brings the effect of fabric anisotropy via A into dilation. Therefore, it was suggested that a constitutive model constructed within the framework of CST, can be incorporated within ACST, simply by replacing ζ for ψ wherever the latter appeared in the model.

Such a constitutive model with explicit dependence on ψ was introduced by Manzari and

Dafalias (1997), and modified by Li and Dafalias (2000) and Dafalias and Manzari (2004). Restricting description to triaxial space for simplicity (there is of course generalization to multiaxial space in the foregoing references), the dilatancy D (ratio of plastic volumetric to plastic deviatoric strain rate) and plastic modulus K_p were given by:

$$D = d(M^d - \eta) \tag{4.1a}$$

$$K_p = h(M^b - \eta) \tag{4.1b}$$

with d and h positive model parameters and where the dilatancy stress ratio M^d (better known as the phase transformation line) and the bounding or peak stress-ratio M^b depend on ψ according to $M^d = Me^{m\psi}$ and $M^b = Me^{-n\psi}$, respectively, with m and n positive model constants; at CS when $\psi = 0$ it follows that $M^d = M^b = M$. As mentioned above these constitutive features that satisfy CST as functions of ψ, can instead satisfy ACST by simply substituting ζ for ψ and obtaining:

$$M^d = Me^{m\zeta} \tag{4.2a}$$

$$M^b = Me^{n<-\zeta>} \tag{4.2 b}$$

with dilatancy D and plastic modulus K_p given always by Eqs. (4.1). One key observation is that by introducing ζ into Eqs. (4.1a) and (4.2b), one takes the bold step of introducing fabric anisotropy via A (see eq. (3.7)) into dilatancy and hardening response, a step that has been shown to be of great simulative value. In Eq. (4.2b) a small modification was made compared to the suggestion in Li and Dafalias (2012), namely the $<-\zeta>$ was used instead of $-\zeta$ in the expression for M^b, following the original proposition in Manzari and Dafalias (1997) to use $<-\psi>$ instead of $-\psi$ for M^b, thus, always maintaining $M^b \geq M$ for any sign of ζ in Eq. (4.2b) based on the action of the Macaulay brackets $<>$; the reason for this modification will become evident in the sequel.

The best way to confirm that ACST can predict the response during the 3-phase loading sequence is to relate such response for the two choices of θ_σ as illustrated in Figs. 4.5 and 4.6 for the stress-strain relations, to the fabric evolution shown in Figs. 4.8 and 4.9, respectively, via the constitutive equations of ACST. It will be seen that Eqs. 3.7, 4.1 and 4.2 suffice to explain the observed response during the 3-phase loading within ACST. Please note the very large difference in the scale of the e_{eq} on the horizontal axes for the two choices of θ_σ that has a

strong effect on the way plots appear. To avoid repetition, the previously presented descriptions of Figs. 4.5, 4.6, 4.8 and 4.9 will be considered known.

4.5.1. Phase 1

During phase 1 loading of the rather loose sample, there is coaxiality of stress, $\mathbf{F}$ and $\mathbf{n}$, thus $N=\mathbf{n}_F:\mathbf{n}=1$, and simultaneously F and A progressively approach their CS values of 1 as $\eta\to M$. It follows from Eq. (3.7) that eventually $\zeta=\psi=0$, therefore, Eqs. (4.2) yield $\eta\to M^d=M^b=M$. Consequently, it follows from Eqs. (4.1) that $D=0$ and $K_p=0$, leading to zero volumetric and continuously accumulating shear strain, respectively; thus, CS is straightforwardly obtained.

4.5.2. Phase 2

During phase 2 loading when the stress PA begin to rotate, the most important event is the non-coaxiality of the PA of $\mathbf{F}$ and $\mathbf{n}$, which results in the key observation that $A=FN=N=\mathbf{n}_F:\mathbf{n}=0.8<1$ given that $F=1$. Consequently, the third condition of Eq. (3.6) is violated and according to ACST the sample must abandon CS. Indeed, with $A<1$ and $\psi=0$ at the initiation of PA rotation (recall the sample is at CS then where $\psi=0$ and $\eta=M$), Eq. (3.7) yields $\zeta>0$. Therefore, $M^d=Me^{m\zeta}>M$ from Eq. (4.2a) and with $\eta=M$, Eq. (4.1a) yields $D=d(M^d-\eta)=d(M^d-M)>0$ which implies volume reduction; hence, the void ratio reduction shown in Figs. 4.5(c) and 4.6(c). The classical CST would have used $\psi=0$ instead of $\zeta>0$ in Eqs. (4.2), thus, $M^d=M$ and, with $\eta=M$, Eq.(4.1a) would have yielded $D=0$; accordingly, no volume reduction would begin at the initiation of PA rotation and CS would have been maintained, contrary to the DEM results. As the rotation of stress PA continues, progressive reduction of volume and void ratio occurs because ζ continues to be positive as $A<1$; hence, $M^d>M$ and $D>0$, but at a reducing pace. This is because the reduction of void ratio from its CS value induces a $\psi=e-e_c<0$, which when inserted in Eq.(3.7) progressively diminishes the positive value of ζ that tends towards 0, thus, $M^d\to M$ and $D\to 0$, arresting volume reduction; reference to Fig. 4.4(b) confirms it. In parallel observe that with $\zeta>0\Rightarrow<-\zeta>=0$. Thus, Eq. (4.2b) yields

$M^b = M$ and with $\eta = M$ Eq. (4.1b) yields $K_p = 0$ (perfect plastic response). Had one not introduced the Macaulay brackets in Eq. (4.2b), $\zeta > 0$ would have induced $M^b < M$, and from Eq. (4.1b) it concludes that $K_p = h(M^b - \eta) = h(M^b - M) < 0$, which implies softening. Also η must have been reduced from its value M, an event that is not, and cannot be, observed during the DEM simulation since the principal stress values are kept fixed. Hence, the use of $< >$ in Eq. (4.2b) is justified according to the original proposition by Manzari and Dafalias (1997).

4.5.3. Phase 3

When phase 3 loading begins, first $\mathbf{n}$ becomes coaxial with the stress to induce biaxial radial loading, and then $\mathbf{F}$ evolves and becomes coaxial with $\mathbf{n}$ and stress, as seen from $\theta_\sigma - \theta_F$ going to zero quite fast in Figs. 4.8(a) and 4.9(a) during the transition from phase 2 to phase 3. Hence, coaxiality between $\mathbf{F}$ and $\mathbf{n}$ resumes as shown by $N = \mathbf{n}_F : \mathbf{n} = 1$ in Figs. 4.8(b) and 4.9(b). Since $F = 1$, one also has $A = FN = 1$, and with $\psi = e - e_c < 0$ from the previous phase, Eq. (3.7) yields $\zeta < 0$. Consequently, it follows from Eq. (4.2) that $M^d < M$ and $M^b > M$, hence, with $\eta = M$ one has from Eq. (4.1) that $D < 0$, thus, dilation, and $K_p > 0$, implying hardening. This is exactly what is observed as phase 3 starts in Figs. 4.5(c) and 4.6(c) with an abrupt increase of void ratio, and in Figs. 4.5(b) and 4.6(b) with a sharp increase of stress ratio η above M as it tends towards $M^b > M$; both dilation and hardening are more intense for Fig. 4.6 since the sample has reduced its volume more than once in Fig. 4.5, due to larger number of cycles of PA rotation.

The theoretical explanation of the continuation of phase 3 loading requires an equation of evolution of the fabric tensor norm F that is shown to increase above 1 in Figs. 4.8(b) and 4.9(b) before it falls back to 1. Such an equation was given in Li and Dafalias (2012) but it has not been investigated extensively and, moreover, is not within the goals of this work to address. It suffices to consider the consequences of the increase of F above 1; with $N = 1$ due to coaxiality, $F > 1$ results into $A = FN = F > 1$; thus, with $\psi = e - e_c < 0$ Eq. (3.7) yields an even more negative value of ζ that maintains $M^d < M$ and $M^b > M$, thus, $D < 0$ and $K_p > 0$ and therefore, dilation and hardening continue, ψ becomes less

negative, and so does ζ. As a result, M^b decreases towards M, while the increasing η eventually exceeds the decreasing M^b causing $K_p < 0$ from Eq. (4.1b). Softening thus occurs, as manifested by the falling value of η in Figs. 4.5(b) and 4.6(b) until it reaches M. F and A return to their CS values of 1, as shown at the end of phase 3 in Figs. 4.8(b) and 4.9(b), and the void ratio returns to its CS value by fully recovering its reduction during phase 2 loading (Figs. 4.5(c) and 4.6(c)) with $\zeta = \psi = 0$ from Eq. (3.7). Thus, CS is reached again.

The explanation of the DEM results by ACST in this section is not a simulation by a constitutive model nor was it intended to be, since no full constitutive formulation is provided. Eqs. (3.6) and (3.7) are fundamental equations of ACST and together with the generic constitutive Eqs. (4.1) and (4.2), can be incorporated within various specific constitutive modeling approaches one might choose within ACST. Nevertheless, it will be a challenge to simulate by a constitutive model, the various response characteristics observed during the 3 phases of the DEM experiment.

4.6. Conclusions

The main task of this chapter was two-fold: on the one hand to prove that the classical Critical State Theory (CST) is incomplete because its two conditions on critical values of stress ratio and void ratio are necessary but not sufficient for CS to occur and be maintained, and, on the other hand, to offer a remedy for this incompleteness by employing the recently proposed Anisotropic Critical State Theory (ACST) by Li and Dafalias (2012), which addresses the role of fabric at CS. The novelty of ACST is the introduction of the third condition in Eqs. (3) on the critical state value of Fabric Anisotropy Variable (FAV), that, together with the first two on stress and void ratios, are necessary and sufficient for CS to occur. The ACST was proposed several years ago, and its benefits have been confirmed by the simulative success of constitutive models within its framework. However, one fundamental theoretical point was missing: its main novelty, namely the third condition of Eqs. (3) on FAV, was always reached concurrently with the first two, thus, the question as to whether this third condition on the fabric is an independent and necessary addition or merely a convenient and useful supplement to the first two remained an-answered. It was possible to obtain an answer by following the

methodology suggested by Dafalias (2016), according to which, instead of trying in vain to reach the first two conditions without the occurrence of the third in order to test its role, one can start from CS, where all three conditions are satisfied, and then simply violate the third one only.

This was achieved by imposing a rotation of the principal axes (PA) of stress at CS, keeping the principal stress values fixed in a virtual experiment by means of DEM, which violated only the fabric-related third condition in Eq. (3.6). A dramatic reduction of void ratio was then observed, contrary to what would be expected by the classical CST. According to CST, since both classical CS conditions on stress and void ratios were satisfied at the initiation of such stress PA rotation, no void ratio change should have occurred. From this it follows that classical CST is incomplete, since its two conditions are necessary but not sufficient to maintain CS, while the third condition proposed by ACST becomes a necessary addition to the first two, and all three are both necessary and sufficient for CS. Furthermore, the 3-phase loading sequence, with phase 2 being the one where the stress PA rotate, provided additional information. In particular, the CS resumed during phase 3, when radial loading was applied again by total rebound of void ratio to its CS value, and similarly for the fabric related variable A and the stress ratio, which, after an initial increase, both decreased to their CS values (Figs. 4.5(b), 4.6(b), 4.8(b) and 4.9(b)).

The foregoing results of the virtual DEM experiment would suffice to show that CST is incomplete, but equally important is that ACST can predict the aforementioned behavior throughout the 3-phase loading by accounting for the effects of evolution of the fabric tensor norm and "direction", all possible to evaluate within the DEM analysis. The prediction was based on the new fabric-related condition on FAV in Eqs. (3.6), in conjunction with the introduction of the Dilatancy State Parameter (DSP) defined in Eq. (3.7) in terms of A and the well-known State Parameter ψ, as well as some generic constitutive ingredients for the dilatancy and the plastic modulus within ACST. Thus, ACST offers a remedy for the incompleteness of CST and, furthermore its structure can predict the DEM response while CST fails to do so.

It is true that CST and its two conditions given by Eq. (3.4) were developed based on monotonic triaxial loading with fixed principal stress directions, and then extended to general stress space (Appendix C in Schofield and Wroth, 1968). However, all considerations of CST as a framework for various constitutive modeling approaches

presume that CST and its conditions given by Eq. (3.4) are valid for all loading paths that may include change of principal stress directions; otherwise CST would not be an appropriate constitutive framework for general loading. In this case, the conditions expressed by Eq. (3.4) are considered necessary when CS occurs, while their sufficiency, while assumed, has never been demonstrated (Schofield and Wroth, 1968). It is within this enlarged perception for the applicability of CST under general loading that the present work was able to prove the incompleteness of CST, and the insufficiency of Eq. (3.4) for defining CS, as well as to offer a remedy by proving the ACST, with its three necessary and sufficient conditions.

Chapter 5: 3D DEM virtual experiments

5.1. Introduction

In this chapter, the 2D virtual experiment of Chapter 2 will be extended in 3D. One would ask why is it necessary to extend the results already obtained in 2D in 3D, or, alternatively, why was it worth obtaining results in 2D at all in the first place, instead of examining the phenomenon directly in 3D. On the second question, the reasons for 2D results are mainly related to two key factors: the significant difference in terms of running time, as 2D analysis is vastly more rapid (and so the 2D DEM software are still more broadly used than 3D), as well as, the more straightforward interpretation of the 2D results. The 2D DEM simulations have considerably reduced computational times with respect to their 3D counterparts; this is due to the fewer degrees of freedom for each particle in 2D, the more difficult 3D rigid body dynamics, and the greater number of contacts per particle in 3D. Thus, in cases where physical reality allows it, 2D simplifications can elucidate the mechanisms that underline several physical phenomena, at considerably lower cost. In addition, 2D results can be represented on a plane (chain forces, velocities etc.), and this direct visualization of information enables valuable insight to mechanisms that are often impossible to visualize in 3D.

2D DEM has proved to be an adequate tool for approaching several problems (e.g. Fu & Dafalias, 2011a; Fu & Dafalias, 2011b; Tong et al., 2014a; Tong et al. 2014b), and is currently used extensively; for this reason, during the past years, 2D results have been consistently more than 3D. Nevertheless, 2D analysis obviously lacks the 3rd dimension, which implies that any 2D result is purely qualitative. Therefore, conclusions extracted from 2D can be only qualitatively assessed in terms of mechanisms and concepts, and this sometimes means that such results should be re-established in 3 dimensions. In such cases, even though the 2D analysis is incomplete, it can form a great basis on which the 3D results can be built and interpreted, with the aid of 2D visualization; great caution is needed when 2D results are used without 3D extension. Quantitatively, in 3D, mass properties, the values of void ratios and coordination number (average number of contacts per particle) are expected to be very different, as well as, extra arching possibilities that are attached to the 3rd dimension. Thus, 3D analysis should follow any important results extracted from 2D, such as the incompleteness of a theory. An

additional gain of this step is the comparison of the frequently applied 2D DEM with the 3D results, on an important experiment.

Although the concepts and principles for the present experimental procedures were similar as in 2D, the consideration of the 3rd dimension posed many practical challenges. At first, visualization of the results is more difficult and, in many cases, might create more confusion than clarity. In addition, one extra axis means three additional components in terms of the – symmetrical – second order tensors (stress, strain rate and fabric). Thus, there exist three principal values and three related principal eigenvectors that need at least two parameters in order to be defined (e.g. two angles in terms of spherical coordinates); still only one norm can be used to quantify the intensity of the tensor (see also Li & Dafalias, 2012). Furthermore, the implementation of a boundary velocity field, as was implemented in 2D, added important complexity to the existing models and algorithms. The technical details of the application of practically all the special methods that were used in the 2D case, as described in the previous chapter, were extended in 3D; the concepts built in 2D had significantly paved the way towards this extension.

The three experimental phases applied in this case were: phase 1 a triaxial load, phase 2 the stress Principal Axes (PA) rotation in Critical State (CS), and phase 3 a radial load, similar to the initial triaxial load of phase 1. The results were expected to be qualitatively similar with those obtained in 2D. Physical experimental results appear in literature where a stress PA rotation had been applied, only before CS (e.g. Miura et al., 1986; Tong et al., 2010), and can be compared with our 3D DEM virtual experiment. Only one publication exists on 3D DEM that includes stress PA rotation before Critical State (Yang, Li & Yu, 2015). This makes obvious the novel nature of the results that will be presented in the sequel, along with the totally new concept of stress PA rotation in 3D and in CS. For the 3D setting, where the numerical experiments presented in this chapter took place, the three principal stress and strain components are $\sigma_i (i=1,2,3)$ and $\varepsilon_i (i=1,2,3)$; the variables p (hydrostatic pressure), q (deviatoric stress), ε_v (volumetric strain), and ε_q (deviatoric strain) are defined as $p=1/3\left(\sigma_1+\sigma_2+\sigma_3\right)$, $q=\sqrt{\left(\left(\sigma_1-\sigma_2\right)^2+\left(\sigma_2-\sigma_3\right)^2+\left(\sigma_1-\sigma_3\right)^2\right)/2}$, $\varepsilon_v=\varepsilon_1+\varepsilon_2+\varepsilon_3$ and $\varepsilon_q=2/3\sqrt{\left(\left(\varepsilon_1-\varepsilon_2\right)^2+\left(\varepsilon_2-\varepsilon_3\right)^2+\left(\varepsilon_1-\varepsilon_3\right)^2\right)/2}$.

5.2. Implementation issues

Most of the implementation issues are very similar, at least conceptually, with the 2D implementation; chapter 4, section 2 is the main reference for the following analysis. For the realization of the numerical experiment, PFC 3D v5.0 was used (Itasca, 2015). This numerical code is the closest possible to the 2D presented in the previous chapter, to ensure that no great software differences affect the results from 2D to 3D. It is a DEM code applying the molecular dynamics method, with very similar numerical methodologies as in the 2D version, extended in 3D (Itasca, 2015). The particles were spherical in shape and their properties are outlined in Table 5.1. The same analysis as in 2D was needed for the damping coefficient (type local with damping ratio value 0.7), the inertial number and the mechanical ratio. The inertial number is defined slightly differently due to the third dimension (Radjai & Dubois, 2011) but again must be less than 10^{-5}. Compressive stresses and strains are considered positive according to the soil mechanics convention.

The 2D success on the boundary type implementation led the way for imposing the 3D boundary conditions. A 3D velocity field, that must consider the three principal axes and the targeted stresses, was applied on boundary particles. A servomechanism controlled the intensity of the velocity field based on the measured stresses in a spherical RV containing approximately 1,600 particles (Fig. 5.1(a)); this RV is used for all the measured quantities and concentric spherical RVs were used to validate the main one and to ensure homogeneity of the sample during all types of loading. Fig. 5.1(b) illustrates the application of the velocity field to the boundary particles of the sample to implement a desired triaxial type loading that consists of a vertical compressive stress increase $\Delta\sigma_1 (> 0)$ and a horizontal stress decrease in both x and y axes $\Delta\sigma_3 = \Delta\sigma_2 (< 0)$; the directions of velocities vary progressively from vertical to horizontal to reflect the foregoing loading**.** Notice that the two horizontal stresses were defined as equal; this is not a prerequisite for the successful application of the boundary velocities but was used for simplicity, and on the basis of the usual triaxial experimental procedure. It is though possible to apply any three different stress increments.

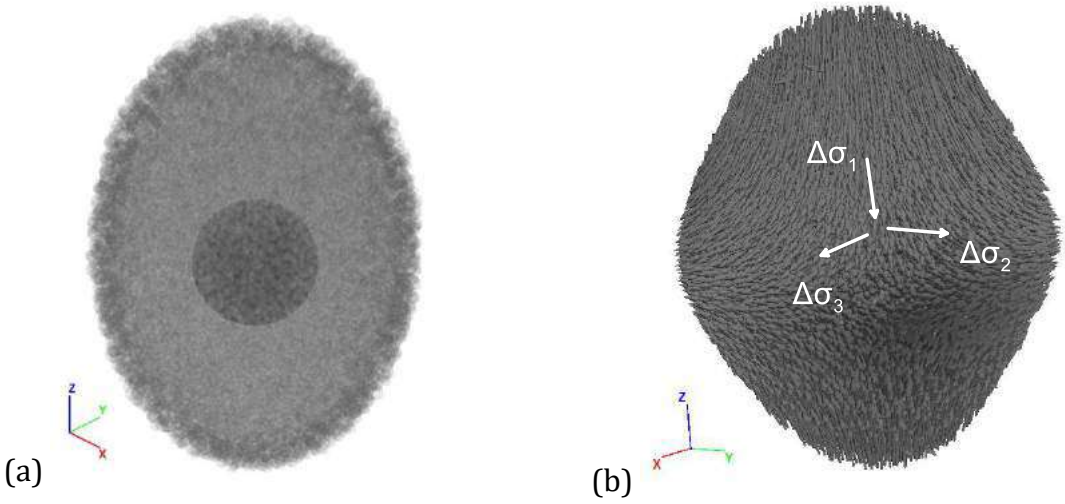

Fig. 5.1. (a) Configuration of particles for initially ellipsoidal sample and its RV in black; the particles are presented partially transparent: light-grey are the particles inside the sample, darker-grey the boundary particles (b) Velocity field applied at the boundary particles to achieve the stress changes $\Delta\sigma_1$, $\Delta\sigma_2$ and $\Delta\sigma_3$ as shown

The stresses and strains were calculated according to the same concept as in 2D; the stresses are based on the typical DEM formula that has been derived rigorously for quasi-static granular materials (Love, 1927; Weber, 1966; Goddard, 1977; Christoffersen et al., 1981; Rothenburg and Selvadurai, 1981). The strains were calculated through a best-fit approach (Liao, 1997; ITASCA, 2008). The final strain rate calculation (equal to the rate of deformation as the symmetric part of the velocity gradient) is based on a proper averaging procedure over multiple time-steps, similarly as in 2D. An initially isotropic fabric was created by random grain creation inside an initial, elliptical in shape, sample; the isotropic compression produced insignificant changes to this isotropic fabric. The elliptical shape of the sample supported the homogeneity through the isotropic compression procedure; thus, the samples reached the end of this preliminary phase as homogeneous as possible and with isotropic fabric. The 3-phase loading was then applied and its response is described in the sequel.

A literature review reveals that different DEM parameters can produce similar response for the triaxial experiment and that the full calibration of a DEM sample is not necessarily a one to one relation. Nevertheless, some general guidelines follow, concerning the importance of each DEM simulation parameter, with focus on the present loading paths. In principle, the choice of the boundaries can support or discourage the creation of a shear band; e.g. flexible boundaries clearly favor the creation of shear bands, and so are

rejected by default. Particles' shape has been chosen to be spherical for simplicity, as the special experiment presented through phase 2 and phase 3 is completely new, and effects such as particles' shape and initial inherent fabric should be added at future steps. With spherical particles, only contact normal fabric and void fabric exist, which promotes simplicity in the fabric analysis. The simple shape of the particles, which is in contrast with real soils, is mainly balanced with the values for the friction and the rolling friction coefficients.

Number of grains	35,840
Average grain radius (m)	0.0009
coefficient of uniformity (Cu = d_{60}/d_{10}); r_{min} (mm); r_{max} (mm)	1.9; 0.12; 0.6
Elliptical specimen's half axes z - y - x (m)	0.02 - 0.0134 - 0.0134
Isotropic and mean pressure (kPa)	200
Particles' density (kg/m^3)	2600
k_n (N/m)	10^5
k_s / k_n (N/m)	0.25
Friction coefficient (sphere-sphere; sphere-boundary sphere)	0.3; 0.0
Rolling friction coefficient (sphere-sphere; sphere-boundary sphere)	0.3; 0.0
Damping ratio	0.7

Table 5.1. Particles properties for 3D DEM experiments

Micromechanical stiffness (normal stiffness k_n and tangential stiffness k_s) and friction (surface friction with or without added rolling resistance and rolling friction coefficient) are the main parameters calibrated that define the material. The normal stiffness is mostly important for the stress-strain curve while the tangential stiffness is important for the initial, linear part; for that reason, no particular attention needed to be paid in the tangential stiffness for our analysis, as we are mostly focused on CS, i.e. large deformation. Rolling friction can account for the simplified shape of the particles along with any surface irregularities of the grains; it appears that rolling friction along with friction can create a

rather realistic response in terms of the evolution of stress and void ratio. Both friction coefficients have a significant influence on the peak and post peak response of the stress. The damping definition is a critical issue, as the energy dissipated from friction is very insignificant compared to the real energy consumption. The typical damping for quasi-static conditions is of type "local", i.e. applied as an extra force on each particle and is proportional to the acceleration. This type of damping is appropriate for our analysis, as only acceleration motion is damped, while any steady-state motion remains unaffected (Itasca, 2008). Finally, particles' density was equal to 2600kg/m^3, a typical value for soil particles.

5.3. Macroscopic results

5.3.1. Phase 1: Triaxial loading until CS

Phase 1 is a triaxial type loading and was applied through the increase of the vertical stress $\Delta\sigma_1$, and the decrease of the two horizontal stresses $\Delta\sigma_2$ and $\Delta\sigma_3$, so that the hydrostatic pressure p ($p=1/3(\sigma_1+\sigma_2+\sigma_3)$) remained constant. Notice that these three stresses (the vertical and the two horizontal) are also the principal ones and that the horizontal ones are defined to be equal ($\Delta\sigma_2=\Delta\sigma_3$) throughout the phase 1 procedure, as in a classical triaxial test. As a result, all the stress changes were defined through one variable change, i.e. $\Delta\sigma_2=\Delta\sigma_3=3/2p-1/2\Delta\sigma_1$, as p always equals 200kPa.

The stress increments were applied through a servomechanism based on the main RV (Fig. 5.1(a)). The macroscopic evolution (stress and void ratio) of phase 1 is presented in Fig. 5.2; the stress ratio (Fig. 5.2(a)) reaches a peak value at approximately 8% of vertical axial strain and then presents a softening behavior until 25% of axial strain, when it reaches its CS value, $M\approx1.1$. The stress ratio softening is not monotonic but fluctuations appear which are not considered to be important for the uniformity or the homogeneity of the sample.

The specimen has been checked and does not present one persistent shear band but rather some smaller non-uniformities develop and vanish due to the velocity controlled boundary particles. That implies that in total, the sample remains homogeneous and the measurements obtained are valid for the whole specimen. In addition, the void ratio (Fig.

5.2(b)) presents in principle a dilative response. Initially there is a slight volumetric compression of 0.5% until approximately 7% of axial strain, and then the dilative behavior of the material takes over. The value of the axial strain is not atypical for the peak strength to take place; literature of experiments and DEM analysis show that in 3D this peak is expected to be somewhere between 2% and 10% of axial strain (Oda 1972a; Oda, 1972c; Belheine et al., 2009; Carraro et al., 2009; Yang & Wu, 2016). The continuing dilation until CS, reaches a total volumetric strain of 1.75% and the critical void ratio becomes $e = e_c = \hat{e}_c(200\text{kPa}) \approx 0.70$.

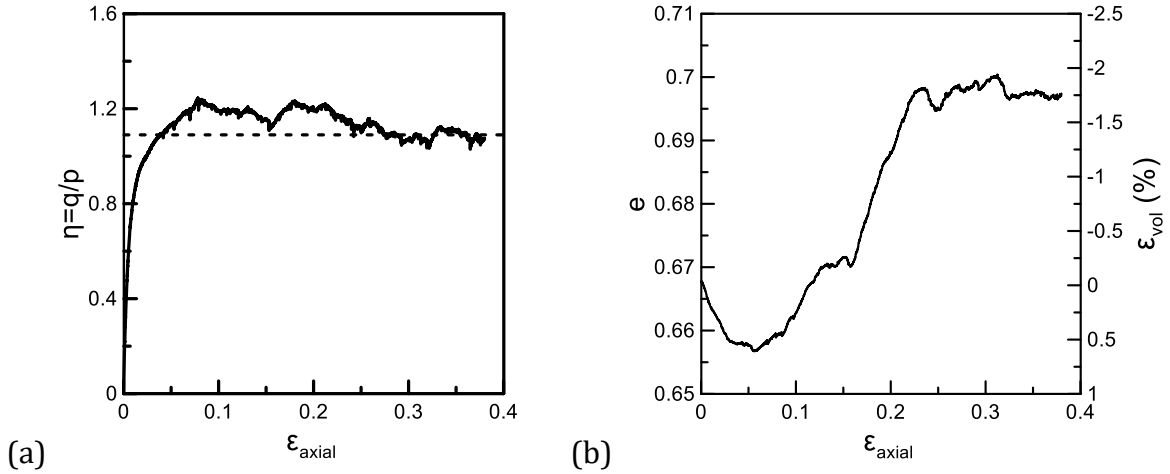

Fig. 5.2. The macroscopic response of phase 1 triaxial test on an initially medium dense sample: (a) stress ratio η and (b) void ratio e, versus vertical (z-axis) axial strain ε_{axial}

This behavior is not atypical for a medium loose - medium dense specimen, governed by its dilative response. The key factors here are the homogeneity of the sample that remains until CS, so that phase 2 can take place, and the realistic response of the granular material. The spherical particles, along with the distribution chosen and the initial void ratio are close to real sub-rounded sands, such as Ottawa sand. The parameters described in Table 5.1 are chosen in order for the material to be quantitatively close to reality and not only qualitatively similar. Under that perspective, the results and the governing mechanisms can be evaluated in a more realistic framework and can be further used for quantitative comparisons with real sands.

Standard Ottawa sand, Ottawa ASTM 20-30, Ottawa F-110 and other similar sands, have distributions very close to the one used in this work (e.g. Salgado, Bandini & Karim, 2000; Santamarina & Cho, 2001; Cole, 2014). In addition, the critical state void ratio ($\hat{e}_c(200\text{kPa}) \approx 0.70$) has the same value as measured in Santamarina & Cho (2000). The

total volumetric strain (1.75%) and its evolution is also quantitatively in the order expected for a triaxial test and a sand with such characteristics (e.g. Oda, 1972c; Salgado et al., 2000; Carraro, Prezzi & Salgado, 2009). The critical stress ratio ($M \approx 1.1$) is close to the range reported for Ottawa sand in Carraro et al. (2009) and Salgado et al. (2000) where it takes values from 1.15 to 1.25. Toyoura sand is another type of sand frequently used for triaxial experiments, and is more angular with respect to Ottawa, but with similar distribution (e.g. Verdugo & Ishihara, 1996). This sand provides slightly larger critical stress ratio ($M \approx 1.25$) and critical state void ratio ($\hat{e}_c(200\text{kPa}) \approx 0.85$) (Dafalias et al., 2004; Yoshimine, Ishihara & Vargas, 1998; Yoshimine & Ishihara, 1998); this could be attributed mainly to the different shape of the particles of this sand. It becomes obvious that the results obtained from our simulation lie within the normal quantitative results for real sands. A full calibration procedure has not taken place as the exact recreation of a particular sand's response is not in the scope of this work.

	Cil & Alshibli (2014).	Kozicki, Tejchman & Mühlhaus (2014)	Calvetti (2008)	Kozicki & Tejchman (2011)	Gu, Huang & Qian (2014)	Yang, Li & Yu (2015)
Boundary type	Flex.	Flex.	Rigid walls	Rigid walls	Rigid walls	Rigid walls
Particles' Shape	spheres	spheres	spheres	spheres	spheres	spheres
k_n (N/m)	$2\ 10^6$	$\approx 3\ 10^5$	$2.5\ 10^5$-$4.2\ 10^5$	$7.5\ 10^6$-10^7	$2\ 10^4$	10^5
k_s / k_n (N/m)	0.5	0.25	0.25	0.3	1	1
Friction coefficient	0.26	various	0.32-0.35	0.3-0.8	0.5	0.5
Rolling friction coefficient	0	0	Inhibited rotation	various	0	0
Damping ratio	N/A	various	0.7	0.3	0.7	0.7
Particles' density (kg/m^3)	920	N/A	N/A	2600	N/A	N/A

Table 5.2. Particles properties for 3D DEM triaxial experiments in literature

From the DEM perspective, the parameters used for the simulation (Table 5.1) are also typical, for this quasi-static type simulation. Several 3D DEM virtual experiments exist

that simulate the triaxial loading test. Some of them use membrane – type boundaries to better simulate the physical triaxial experiment (Cheung & O'Sullivan, 2008; Cil & Alshibli, 2014; Kozicki, Tejchman & Mühlhaus, 2014) or periodic boundaries (Sitharam & Vinod, 2009), while most implement rigid walls (Ng, T. T., 2009; Belheine et al., 2009; Widuliński, Kozicki, & Tejchman, 2009; Yan & Dong, 2011; Yimsiri & Soga, 2011; Lee, Hashash & Nezami, 2012; Guo & Zhao, 2013; Gu, Huang & Qian, 2014; Li & Yu, 2014); none of them uses the special boundary particles implemented herein. Parameters of simulations that implemented similar micromechanical and DEM concepts for triaxial load in the literature, are summarized in Table 5.2; thus, it becomes clear that the parameters of this implementation lie within the usual values of the existing literature.

5.3.2. Phase 2: Stress PA rotation in CS

After the triaxial type load of phase 1, a 2nd phase was applied for the stress Principal Axes (PA) rotation, while keeping the principal stress values fixed. Phase 1 was stopped at 30% of axial strain where it is clearly in CS (see Figure 5.2); at the end of phase 1 the three principal axes were fixed on the two horizontals (x, y) and the vertical (z) axes due to the triaxial concept. We initially needed to define the way that the PA of stress would rotate; in general, the choice of the potential PA rotation of stress is restricted only by the principal axes at the end of the triaxial load and in case of symmetry (as the case of triaxial) an infinite number of equivalent PA rotations of stress can take place. In this work, the simplest case was chosen and so the stress principal axes rotation took place on the x - z plane, on which the two principal axes were rotating, while the third principal axis (y - axis) remained fixed.

As a result, the stress value on the y axis remained constant and equal to the minor principal value it had at the end of phase 1, and thus the shear stresses that are out of x-z plane remain equal to zero. Infinite combinations are possible for the evolution of the stresses defined on the x-y-z axes based on the stress PA rotation load path and the principal stress values but we chose the simplest one for theoretical and practical reasons. The numerical scheme that was implemented, is capable of any of these infinite rotations in any planes, should the generalization of the procedures is needed for some future purpose.

All three principal stress values were kept constant throughout the procedure. As a result of all the above, the stress PA rotation can be easily overviewed as in Fig. 5.3, which is practically the same as Fig. 4.3, with one change from the y-axis in 2D to the z-axis for 3D; the out of x-z plane principal stress, parallel to the y axis, remains constant in value and in orientation and the extra shear stresses equal to zero. These simplifications create an experimental environment which represents the simplest extension of the 2D virtual experiment; under that perspective, the results and conclusions can be more easily compared between the 3D and the 2D cases.

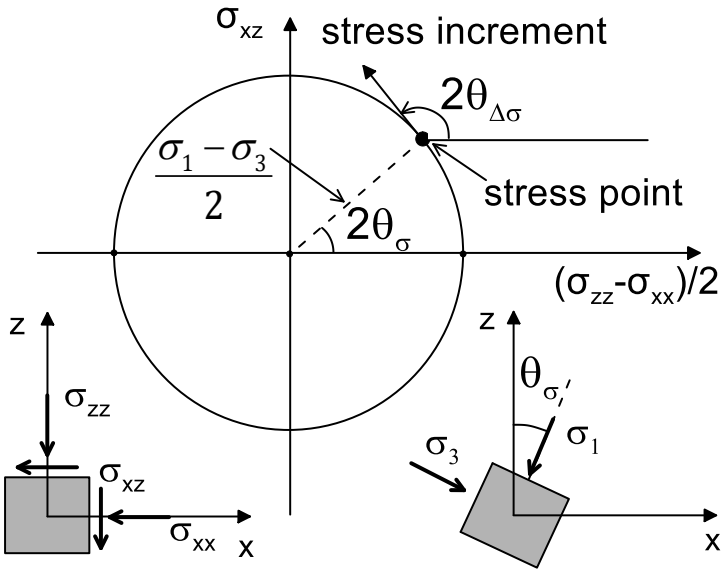

Fig. 5.3. Illustration of stress path in the shown stress space for rotation of stress PA during phase 2 loading and schematic presentation of stress components in real space

The application of the PA rotation is based on the rotation of the applied velocity field. The results from the second phase are presented in Fig. 5.4 in terms of stress components and volumetric strain; the similarities with the 2D case are profound (see also Fig. 4.4). As the rotation takes place on the x - z plane, the σ_{xx} and the σ_{zz} are the two normal stresses who change their values continuously along with the shear σ_{xz}, in order for the σ_1 and the σ_3 to remain constant. Additionally, the two out of plane shear stresses (σ_{xy}, σ_{yz}) are practically zero and the third principal stress, which is along the y axis ($\sigma_{yy} = \sigma_2$) remains approximately constant (Fig. 5.4(a)). The measured stress components confirm that the stress PA rotation has been successfully applied to the sample. The results of Fig. 5.4(a) are exactly similar with those of Fig 4.4(a), with the addition of the extra stress components of the third dimension, which are constant.

The volumetric strain that corresponds to the PA rotation (Fig. 5.4(b)) presents many similarities with the 2D response, but also some important differences. The main message extracted from the 2D case concerning the incompleteness of CST stands totally supported by the 3D results. Qualitatively, the general trend is profoundly compressive, while the compression of the sample continues until it reaches a void ratio minimum. Interestingly, the 3D sample needs half the number of rotation cycles of the 2D to reach the minimum PA rotation value. This relates to another major difference: in the 3D case 2/3 of the volumetric strain change happened during the first 2 cycles, and only 1/3 happened at the next 3 cycles; this reveals that the major part of the compression due to the PA rotation takes place at the very beginning of the phase, while a second smoother and smaller part of the volumetric strain change takes place later. A totally different trend was revealed at the 2D case (Fig. 4.4(b)) where the volumetric change was smooth and the change of the slope of the volumetric evolution was progressively decreased until the reach of the minimum void ratio. This difference is attributed to the increased degree of freedom of motion of particles in 3D.

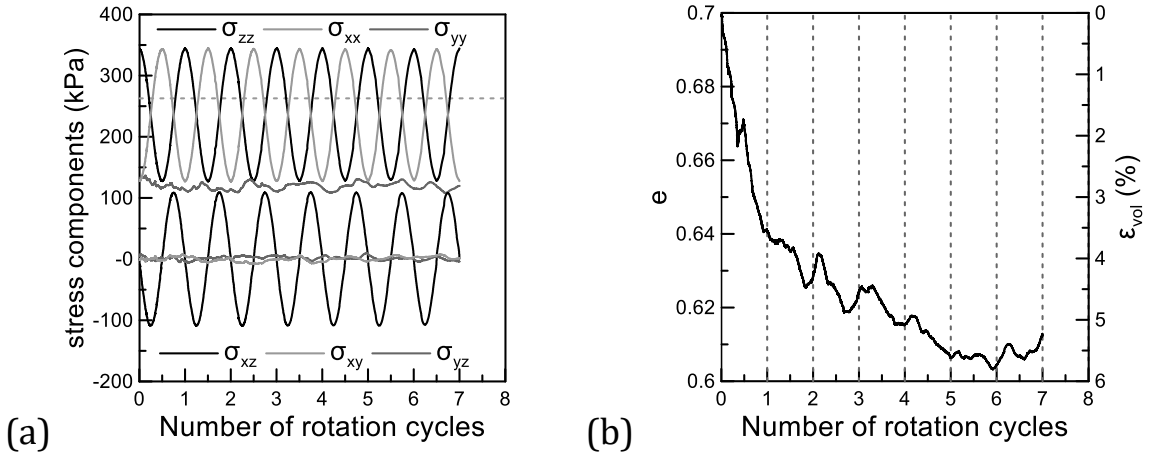

Fig. 5.4. (a) Variation of stress components and (b) Variation of void ratio and volumetric strain, with number of cycles of stress PA rotation during phase 2 loading

In addition, the evolution of the volumetric strain in 3D presents great dilation between rotation cycles, a phenomenon not observed during the 2D where the dilation was minor. Dilation with maximum value of 0.5% of volumetric strain, can be clearly observed at the middle of the 1st cycle and in the beginning of all the other cycles (2nd until 6th). It is noticed that the servo-control of the stress is possible to have affected these results, in terms of their appearance with respect to the rotation cycles, given that the volumetric strain is a purely geometrical measurement and thus, directly affected by the precise

loading boundary conditions. Finally, quantitatively, the 3D void ratio and its change are, as expected due to the different dimensions, larger and very different from the 2D void ratio and the total volumetric strain at the end of the PA rotation is almost double from the 2D. Again, as in the 2D case, most important for the goals of this investigation is the dramatic contraction at the very initiation of the stress PA rotation while the two classical CST condition hold true, and accordingly one would have expected no change of the void ratio. This expectation is proven to be entirely inaccurate, thus, showing the lack of sufficiency of the two classical CST conditions to maintain CS.

It should be mentioned that similar DEM results with the present ones were shown in Tong et al. (2014), but with two major differences. Firstly, the DEM code there was 2D and second, the stress PA rotation begun at a state quite before CS, since the goal there was not to disprove the insufficiency of the CST to maintain CS in such type of loading. Several physical experiments exist with results discussing stress PA rotation, but only before CS. The comparison of our results with these physical experiments is informative and is done with extreme caution, due to all the reasons discussed in the prequel. Additionally, there are several differences attributed to alterations in the rotation procedure and the properties of the materials used in experiments; we focus only on the comparison for the volumetric strain which is the main parameter of interest. Qualitatively, all results from stress PA rotation present the same trend towards volumetric compression with small periods of dilation. Tong et al. (2010) have done an extensive experimental program on PA rotation before CS for various loading parameters, focusing mainly on the importance of the intermediate stress (Fig. 5.5). The results, reveal very similar trends with Fig. 5.4; a great part of the compression takes place during the first and the second cycle, while afterwards follows a smooth evolution of the volumetric strain until reaching a minimum void ratio.

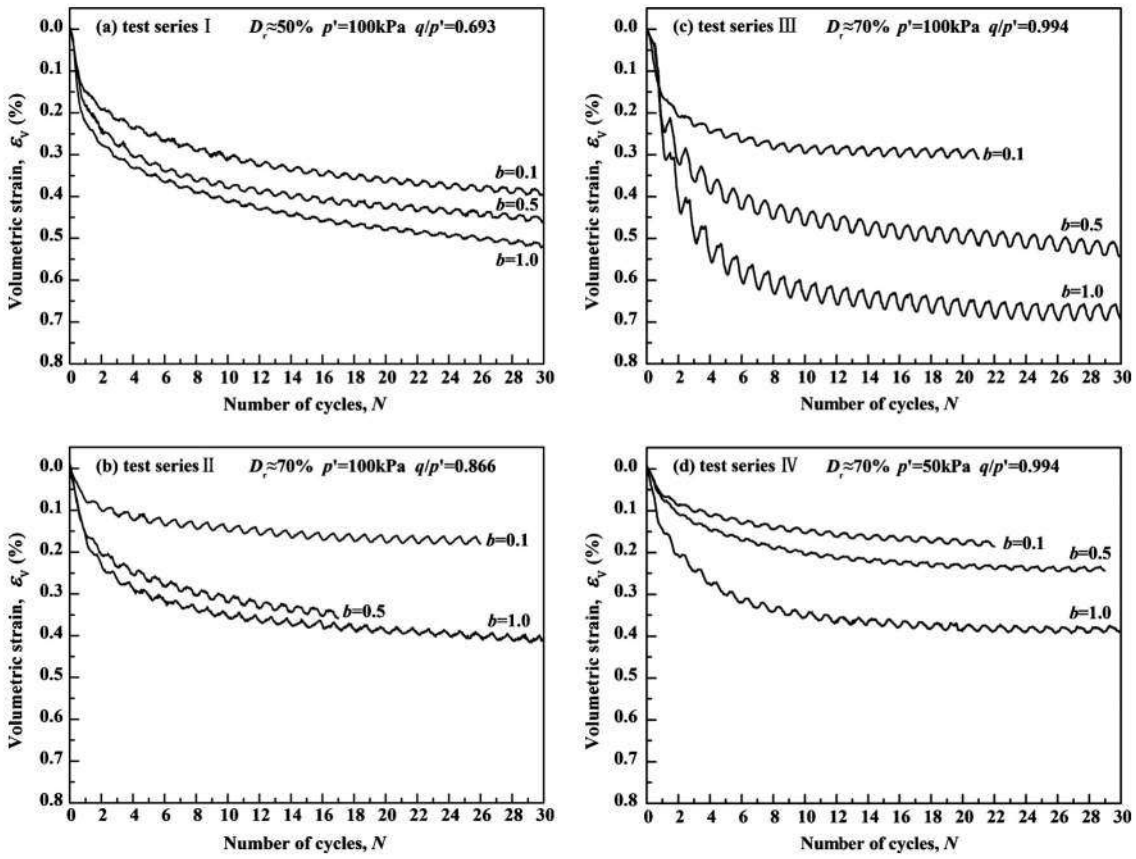

Fig. 5.5 Volumetric strain evolution for stress PA rotation in physical experiments; from Tong et al., 2010

The maximum number of cycles needed to reach the final void ratio value varies, but ranges from 10 to 20 cycles; this is not very different from the 7 cycles we needed to reach minimum void ratio. A periodic change between dilation and compression appears, with compression being the general trend, that our simulation has also revealed. The values of the volumetric strain are larger in our case but this can be attributed to the larger hydrostatic value that appears to importantly affect the volumetric strain (series III vs series IV) and the fact that our sample is in CS condition. The exact same observation stands for the results of Miura et al. (1986) (Fig. 5.6) Vaid et al. (1990) showed that monotonic compression without dilation happened for half a cycle while Wijewickreme and Vaid (1993) have reached with Ottawa sand (ASTM-C-109) volumetric strain 0.9% for half a cycle of rotation, quantitatively very similar to ours. Other physical experiments with stress PA rotation have not completed many cycles to be comparable with the present results and many are difficult to use due to very different properties.

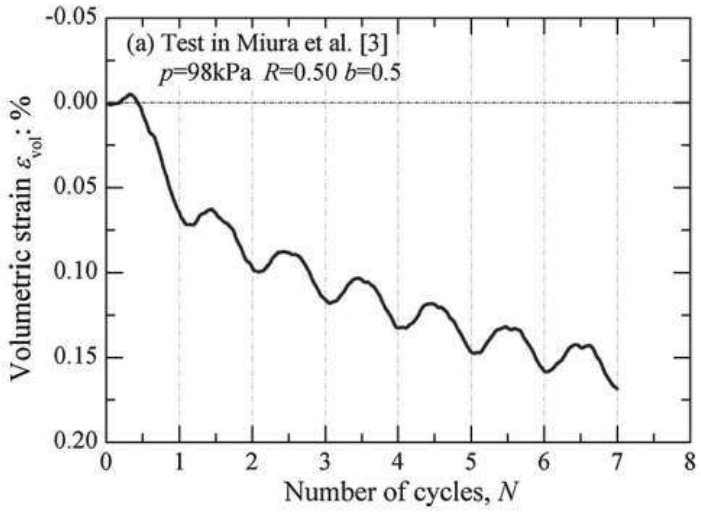

Fig. 5.6. Volumetric strain evolution for stress PA rotation in physical experiment; from Tong et al., 2014a; after Miura et al., 1986

5.3.3. Phase 3: Triaxial loading after stress PA rotation and overview of all phases

A phase 3 followed phase 2 of stress PA rotation, to check for the response of the sample in a similar fashion as done in 2D. This third phase consists of a triaxial type loading similar as in phase 1, but rotated by an angle θ_σ of the σ_1 axis with respect to the vertical y-axis, where the preceding stress PA rotation stopped. For a unified representation of all test results, the equivalent cumulative deviatoric strain measure $e_{eq} = \int \sqrt{(2/3)\dot{e}_{ij}\dot{e}_{ij}}\,dt$ with e_{ij} the deviatoric strain in three dimensions, is used as a reference strain for the whole experiment, as also happened in 2D, initiating after the application of isotropic compression $p = 200\text{kPa}$. In all these plots, the part for phase 1 will be denoted by light gray, for phase 2 by black. Recall that the initiation of phase 2 took place at an intermediate stage of phase 1 at axial strain $\varepsilon_{axial} = 30\%$, thus, the initiation points of the black plots of phase 2 will appear at such intermediate points of the light gray color plots of phase 1, accounting for the fact e_{eq} substitutes for ε_{axial} used in phase 1. Phase 3 plots will continue directly after the black plots of phase 2.

Phase 3 has started from several intermediate points of phase 2; in Fig. 5.7 are presented the results for phase 3 at $\theta_\sigma = 90^\circ$, at $\theta_\sigma = 0^\circ$ after 1 cycle, at $\theta_\sigma = 90^\circ$ after 1 cycle and after 2 cycles. The main deformation as also the main volumetric strain changes has taken

place during these initial two cycles of rotation and thus, the results for phase 3 starting in these cycles are representative. Very large deformation of the sample has taken place after the 2 cycles, which implies extra difficulties to run phase 3, without any gain in the interpretation of the results.

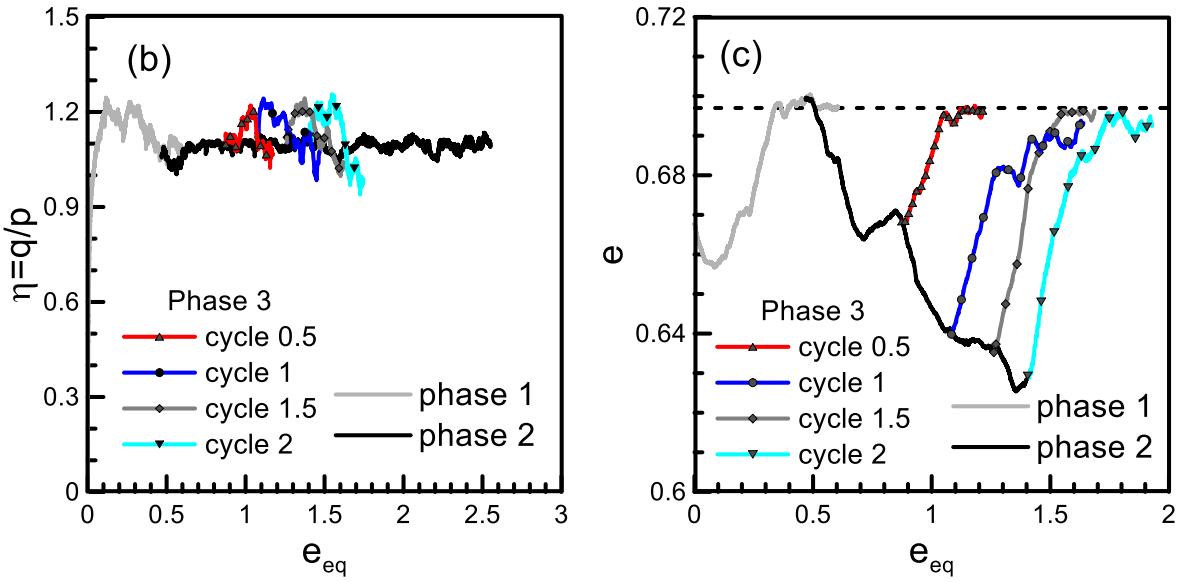

Fig. 5.7. Plots during the full three-phase loading sequence with phase 3 at $\theta_\sigma = 90^o$, at $\theta_\sigma = 0^o$ after 1 cycle and after 2 cycles: (a) the stress path (b) the stress ratio q/p versus e_{eq} (c) the void ratio e versus e_{eq}

From Fig. 5.7(b), it is concluded that the macroscopic response when phase 3 is started on half cycles (i.e. $\theta_\sigma = 90^o$ and same after 1 cycle) is better, due to the deformation of the sample. When phase 1 stopped, the sample was nearly a spherical sample, as was intended from the initial ellipsoidal shape configuration of the specimen (Fig. 5.8(a)). As the PA of stress rotated on the x-z plane, the sample was majorly deformed in the out of plane y-axis, in order for the y stress to remain constant and principal (Fig.5.8(b)); additionally, the deformation on the z axis was larger than the one on the x axis, since at the beginning and the end of each rotation cycle the major principal value lies on this axis. The limitations presented on the deformation arise due to the existence of the third dimension; in the 2D case this limitation did not exist, since the particles could not move out of the 2D plane. From these observations, it is concluded that the best loading angle to proceed with the phase 3 load, would be the with $\theta_\sigma = 90^o$.

At the end of phase 1, the two horizontal normal stresses were equal and equal to the

minor principal stress $\sigma_{yy} = \sigma_{xx} = \sigma_3$ while the vertical stress was the major one $\sigma_{zz} = \sigma_1$ When the stress PA rotation takes place on the x-z plane, the major and the minor principal values change their respective axes, from z to x and back. As a result, when phase 2 is stopped at $\theta_\sigma = 90^o$ (half cycle) , σ_{xx} is equal to the major principal stress value due to the PA rotation, while $\sigma_{yy} = \sigma_{zz}$ are equal to the minor principal value and the loading is triaxial compression with the major stress increment ($\Delta\sigma_1$) lying on the x axis while the two minor on the y and z axes.

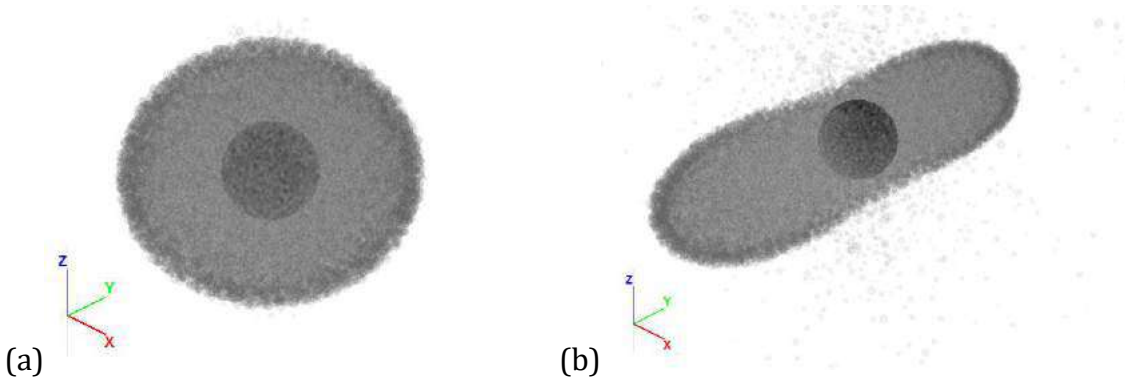

(a) (b)

Fig. 5.8. Deformed sample(a) when phase 1 triaxial load is stopped and (b) when phase 2 loading ends; the spherical RV is in black, the particles are presented partially transparent: light-grey are the particles inside the sample, darker-grey the boundary particles

Nevertheless, from all the results in Fig. 5.7 it can be easily concluded that, as the triaxial-type loading of phase 1 is repeated after phase 2 (through phase 3), and after the sample has abandoned CS, the sample returns to the same CS. Notice that pressure p does not change during all the three-phase procedure, and thus critical void ratio e_c, which is a unique function of p , remains the same for the whole experiment, from the beginning till the end. For $\theta_\sigma = 90^o$ both after 0 and 1 cycle of rotation void ratio clearly returns to its CS value while the stress ratio reaches a peak and then also fall to its CS value.

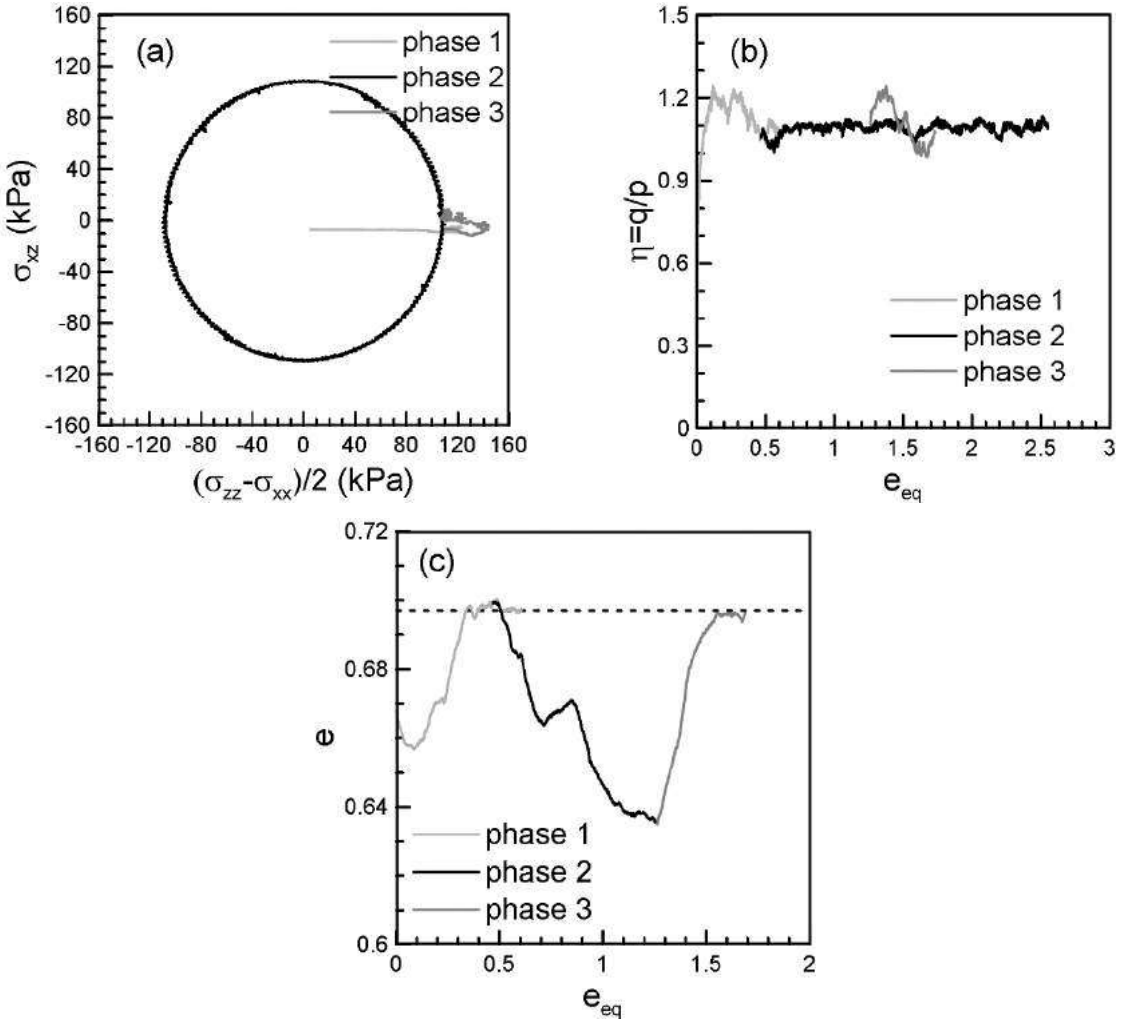

Fig. 5.9. Plots during the full three-phase loading sequence with phase 3 at $\theta_\sigma = 90^o$ after 1 cycle: (a) the stress path (b) the stress ratio q/p versus e_{eq} (c) the void ratio e versus e_{eq}

For $\theta_\sigma = 0^o$ after 1 and 2 cycles the results are not similarly clear, due to the deformation of the sample (Fig. 5.7). For $\theta_\sigma = 0^o$ after 1 cycle the void ratio does not reach the CS value due to extreme deformation before this, but it has a tendency towards the CS; for $\theta_\sigma = 0^o$ after 2 cycles the void ratio reaches CS with some fluctuations. The stress ratio for all cases reaches a peak value, very similar to the one for phase 1, and then falls on CS.

The primary results for the foregoing analysis are provided for an angle of rotation of the stresses $\theta_\sigma = 90^o$; this is dictated by the deformation pattern of the sample during phase 2 as discussed. The results presented in Fig. 5.9 are for all three loading phases, with phase 3 initiating at $\theta_\sigma = 90^o$ after one cycle of PA rotation. The response is qualitatively

the same as in 2D; the specimen was in a denser state than the CS and as a result the void ratio (Fig. 5.9(c)) evolves in dilation, with a quick pace, until it reaches its CS value while the stress ratio (Fig. 5.9(b)) is increased to its peak value and then falls back to its CS value. The 3D results come to confirm the 2D simulations that have produced, qualitatively the same trends.

5.4. Fabric evolution during the 3D DEM experiment

Following the analysis of the macroscopic results, the incompleteness of the CST is again undoubtedly confirmed, on this chapter with a 3D virtual experiment. The results of Fig. 5.9. leave no room for doubt on the Critical State conditions that are clearly reached at the end of both radial monotonic loadings, in phase 1 and 3, and the abandonment of the CS during the non-radial monotonic loading of phase 2. The classical CST conditions are obviously necessary for CS to be attained but are proved not to be sufficient, as in phase 2 they are not enough for the sample to stay in CS. The ACST, as a major motivation of this work, is again examined in the sequel of this section. The fabric analysis follows the same principles as in the 2D experiments, with the addition of the extra fabric components of the third dimension.

Fabric during the 3-phase loading has been quantified by the means of contact normal vectors and the results presented in the following are all based on contact normal fabric. The analysis can be easily extended from 2D to 3D, as the parameters of ACST, i.e. the fabric norm (F), the coaxiality quantification of the fabric and the loading direction (N) and the Fabric Anisotropy Variable (A) are all scalar values that are calculated in 3D in the same way as in 2D (see also Eq. 3.5). The second order tensors measured in the 3D case for fabric and loading direction (in terms of plastic strain rate) produce no extra information in that vein. The only clear difference concerns the evaluation of the non coaxiality of stress and fabric (angle lag $\theta_\sigma - \theta_F$ in 2D); in 3D, the second order tensors have three principal axes, that translates into two angles needed to characterize the axes orientation, e.g. in spherical coordinates.

Nevertheless, the approach we decided that simplified the stress PA rotation, i.e. keeping the intermediate principal stress on the y-axis principal and constant in value, simplifies also this analysis, without loss of generality, as the same analysis could be made during any stress path like the one of phase 2, with the proper transformation of the tensors.

Given that the intermediate principal axis is fixed on the y axis, the intermediate principal axis of strain and fabric is also fixed on the same axis. This observation was confirmed by the calculation of the principal eigenvectors of the stress, strain and fabric tensors during the stress PA rotation and simplifies the analysis as only the angle difference that lies on the plane x-z, where the PA rotation takes place. As a result, only one angle can be used for stress and for fabric, the angle on the x-z plane that is defined from the vertical, z axis. Thus, the results presented in Fig. 5.10 have the same axes as in Fig. 4.8 and Fig. 4.9 for the 2D case. In Fig. 5.10(a) are presented the fabric norm (upper diagram) that is normalized with its CS value and the angle lag of fabric and stress (lower diagram), on the x-z plane where the stress PA rotation took place. In Fig. 5.10(b) are the relative orientation of fabric and loading direction (N)(lower diagram) and the FAV (upper diagram), which is the combination of the two plots for the norm F and the relative orientation N. For the uniform presentation of the three phases, the total equivalent plastic strain is again used. These are the figures used in the following analysis and they will not be repeated for clarity.

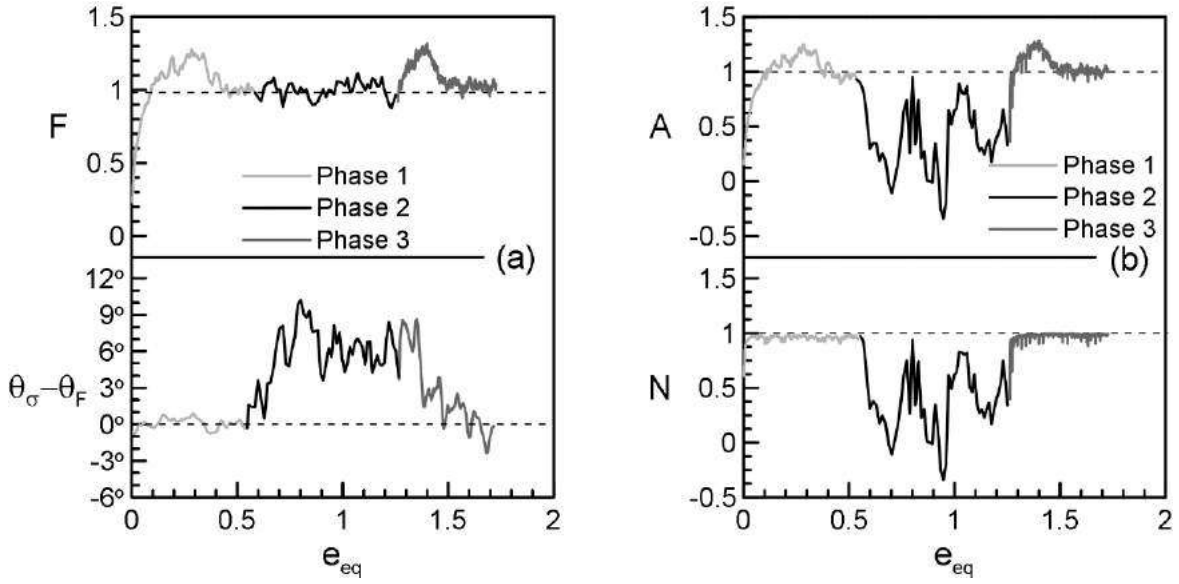

Fig. 5.10. Plots of fabric entities during the full three-phase loading sequence with phase 3 at $\theta_\sigma = 90^\circ$ after 1 cycle: (a) F and $\theta_\sigma - \theta_F$ (b) $A = F\,\mathbf{n}_F : \mathbf{n}$ and $N = \mathbf{n}_F : \mathbf{n}$

During the triaxial load of phase 1, the fabric norm F, following the evolution of the stress ratio, reaches a peak value 1.3 times greater that its CS value and after 0.4 of equivalent strain, falls to its CS value. The fabric, the strain and the stress tensor are all coaxial during phase 1. The FAV, following the norm reaches a value greater than 1 ($A \approx 1.3$), and when

CS conditions are reached, it falls back to 1 meeting the two classical CS conditions concurrently. This is the expected evolution for such a triaxial experiment, for a medium dense sample that presents dilation and peak stress ratio larger than its CS stress ratio.

When phase 2 initiates, the three tensors become non-coaxial very rapidly. Fabric follows the rotation of stress with an angle lag that fluctuates from 4^o to 9^o; this is very similar with the angle lag presented for the 2D simulation. The norm of the fabric during phase 2 remains constant on average and the relative orientation N becomes less than 1. On the 3D results, N cannot be directly related to an angle between the strain and the stress tensor, but when $N=1$ the two tensors are coaxial while when $N<1$ the two tensors have some lag. The FAV has the same evolution as N, as the fabric norm is constant; thus $A<1$ and the third of the conditions of the ACST (Eq. 3.6) is violated. This results in the abandonment of the CS as it is measured in the void ratio (Fig. 5.4(b)).

Although the CS condition have been abandoned, after the radial monotonic loading phase 3 they are quickly restored. The relative orientation N returns to 1 and the stress and strain rate to coaxiality very rapidly, while the fabric requires more time in order to become coaxial with the stress. This appears because the fabric norm F again reaches the same peak value 1.3 before it falls back to 1 and this evolution delays the reorientation of the fabric on the, fixed on phase 3, stress axes. In summary during phases 1 and 3 the PA of stress, $\mathbf{F}$ and $\mathbf{n}$ are all coaxial, with fast transition to and from phase 2 during which the PA of $\mathbf{F}$ follow the PA of stress by an angle lag of 4^o to 9^o, and all three pairs of PA rotate simultaneously.

Additionally, it is of importance to examine the second phase alone, to analyze the evolution of the ACST parameters with respect to the cycles of rotation. In Fig. 5.11 the same parameters as in Fig. 5.10 are presented only for the second phase and with respect to the cycles of stress PA rotation. From Fig. 5.11(b) it can be concluded that the fabric - plastic strain rate relative orientation N (relative orientation of fabric and plastic strain rate in 3D, expressed through the trace of the product of the two tensors) presents oscillations which are not random nor just noise of the DEM.

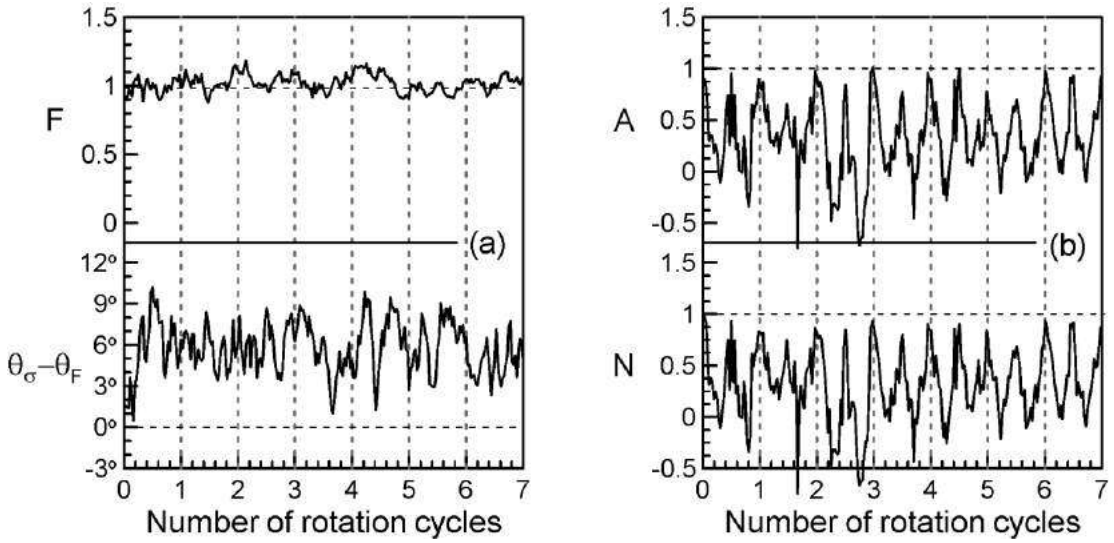

Fig. 5.11. Plots of fabric entities during the whole phase 2 loading with respect to the number of rotation cycles: (a) F and $\theta_\sigma - \theta_F$ (b) $A = F\mathbf{n}_F : \mathbf{n}$ and $N = \mathbf{n}_F : \mathbf{n}$

Similarly with the evolution of the void ratio, at the beginning but also at the middle of each cycle, N becomes equal to 0.9 while in between these areas it becomes very smaller than 1 and close to zero (even slightly negative). These oscillations have physically occurred and declare that fabric and plastic strain rate do have a non-coaxiality that is not constant but oscillates with respect to the stress PA rotation cycles. One very possible and natural reason for this behavior, that appears in this experiment and would distinguish these two direction (i.e. $\theta_\sigma = 0^o$ and $\theta_\sigma = 90^o$) are the principal directions of fabric, which initially is strongly anisotropic (due to being in CS) and its axes are fixed and aligned with those of stress and strain rate in vertical and horizontal direction. As a result, fabric appears to "go quicker" and catch up with the plastic strain rate when approaching these special directions, while it "stays behind" when deviating from them.

5.5. Analysis of non coaxiality angle between unit fabric direction and unit plastic strain direction in 3D

5.5.1. Angle derivation from the eigenvectors

We define φ as the angle lag between the unit plastic strain rate principal axes and the unit fabric principal axes that lie on the x-z plane, i.e. the rotation plane of the stress PA

rotation. This is the only existing angle between the principal axes of these two tensors in 2D, but in 3D is the angle on the rotation plane, which is directly related to the 2D case. To directly calculate this angle, the principal axes of the two tensors that lie on the x-z plane are needed. We plot in Fig. 5.12 and Fig. 5.13 the components of the unit fabric direction tensor and of the unit plastic strain rate direction tensor. Based on these components we can conclude that the two principal axes lie on the x-z plane while one principal axis is constantly parallel to the y axis; these results are also supported by the calculation of the principal values and the relevant eigenvectors (not presented here).

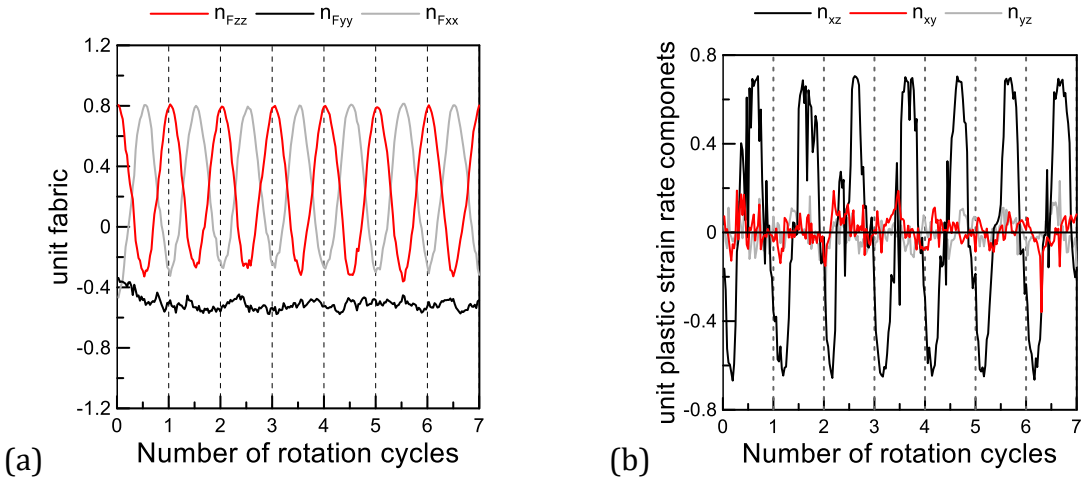

Fig. 5.12. Fabric tensor's (a) normal and (b) shear components

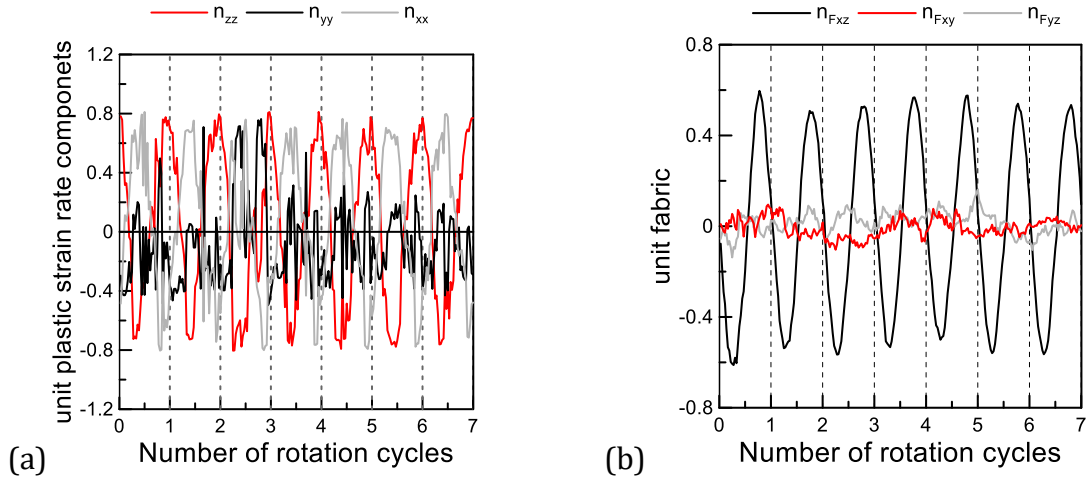

Fig. 5.13. Plastic strain rate tensor's (a) normal and (b) shear components

Thus, the procedure to calculate φ is as follows: the eigenvectors of the unit fabric direction tensor and of the unit plastic strain rate direction tensor are calculated; the eigenvector that relates to the major principal value and lies always on the x-z plane is

chosen for each tensor and its angle with respect to the vertical axis is calculated. These angles are presented in Fig. 5.14(a) where θ_n is the angle for the unit plastic strain rate and θ_F for the unit fabric tensor; finally, the difference between these two angles, which is the angle $\varphi = \theta_n - \theta_F$, is calculated. This calculated φ is presented in Fig. 5.14(b).

We can mostly focus on the evolution of φ after cycle 4, as at these cycles the entities have been mostly stabilized for phase 2. It is accepted that the initial 1-3 cycles are transition cycles and thus the results for fabric and strain rate are more difficult to interpret and more difficult to use; still they show the same tendencies but with more fluctuations and more noise. It can be concluded that the angle φ has an average value of 20^o but oscillates $\pm 10^o$ degrees around that value.

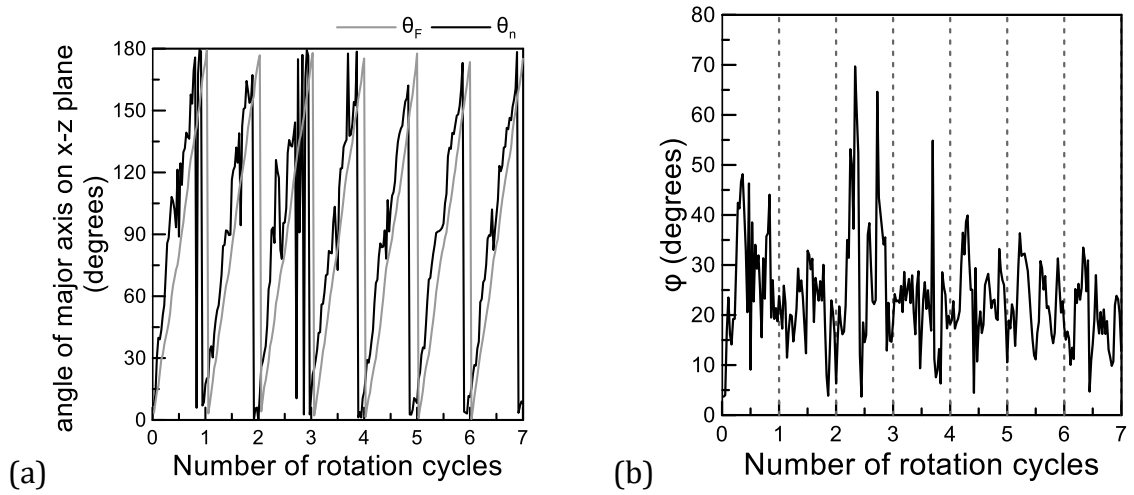

Fig. 5.14. (a)The angle of the major principal axis for the unit fabric direction tensor and the unit plastic strain rate direction tensor with respect to the vertical axis and (b) angle φ based on the eigenvectors of the two tensors

This same angle φ is presented for the 2D case in Fig. 5.15 for comparison. The average value is again approximately 20^o but the oscillations are $\pm 5^o$ degrees and are not as clear as for 3D; this small value for the oscillations in 2D could not easily be determined whether it represents noise or not, but as the same behavior is observed in 3D, then the same conclusion can be derived.

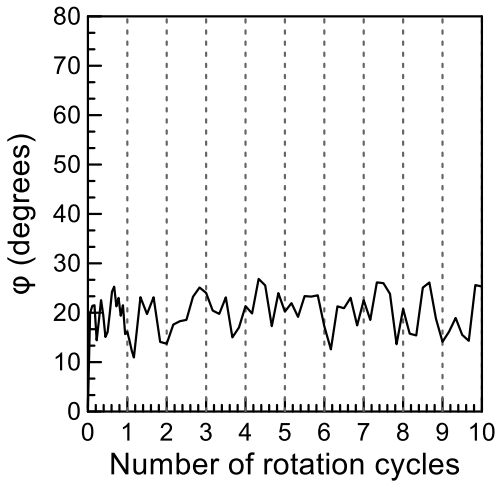

Fig. 5.15. Angle φ of the 2D DEM virtual experiment

5.5.2. Indirect angle derivation from N

The angle φ could also be derived indirectly through N. The following analysis has as ultimate purpose to relate $N = \mathbf{n}_F : \mathbf{n}$ with φ; under this approach it will be possible to reveal the mechanisms of the evolution of N in 3D. Recall that in 2D, N can be directly related to φ as $N = \cos(2\varphi)$, but this is not the case in 3D, as will be proved.

The unit fabric tensor direction can be expressed on its principal axes by its three principal values as:

$$\mathbf{n}_F = \begin{pmatrix} n_{F1} & 0 & 0 \\ 0 & n_{F2} & 0 \\ 0 & 0 & n_{F3} \end{pmatrix} \tag{5.1}$$

Also, the unit plastic strain rate tensor direction can be expressed on the same axes, the principal axes of the fabric tensor. Remember that for the phase 2 of loading, i.e. the stress PA rotation, the intermediate principal axis of the stress tensor, related with the second principal value σ_2, remains fixed on the y axis and that the PA rotation takes place only on the x-z plane and the other two principal axes, related to σ_1 and σ_3, are always on the x-z plane. Thus, we conclude that also for the unit plastic strain rate tensor and for the fabric tensor, the second principal axis remains fixed on the y axis, as the whole scheme of PA rotation takes place on x-z plane; this is also based on the analysis of the components of the two tensors and of their eigenvectors, as discussed in the prequel and in Figs. 5.12 and 5.13.

As a result, we can now express the unit plastic strain rate components with a constant second principal axis (but not necessarily constant second principal value); based on the angle difference φ, which is the angle between the principal axes of the unit plastic strain rate and the fabric on the x-z plane, on the eigenvectors of the fabric tensor that yields:

$$\mathbf{n} = Q\begin{pmatrix} n_1 & 0 & 0 \\ 0 & n_2 & 0 \\ 0 & 0 & n_3 \end{pmatrix}Q^T = \begin{pmatrix} \cos\varphi & 0 & \sin\varphi \\ 0 & 1 & 0 \\ -\sin\varphi & 0 & \cos\varphi \end{pmatrix}\begin{pmatrix} n_1 & 0 & 0 \\ 0 & n_2 & 0 \\ 0 & 0 & n_3 \end{pmatrix}\begin{pmatrix} \cos\varphi & 0 & -\sin\varphi \\ 0 & 1 & 0 \\ \sin\varphi & 0 & \cos\varphi \end{pmatrix} =$$
$$= \begin{pmatrix} n_1\cos^2\varphi + n_3\sin^2\varphi & 0 & (-n_1+n_3)\cos\varphi\sin\varphi \\ 0 & n_2 & 0 \\ (-n_1+n_3)\cos\varphi\sin\varphi & 0 & n_1\cos^2\varphi + n_3\sin^2\varphi \end{pmatrix} = \begin{pmatrix} n_1' & 0 & n_{13}' \\ 0 & n_2 & 0 \\ n_{31}' & 0 & n_3' \end{pmatrix} \quad (5.2)$$

where $Q = \begin{pmatrix} \cos\varphi & 0 & \sin\varphi \\ 0 & 1 & 0 \\ -\sin\varphi & 0 & \cos\varphi \end{pmatrix}$ is the rotation matrix for rotation only on the x-z plane, and φ is the angle on the x-z rotation plane between the principal axes of the two tensors. Notice that the second principal value n_2 is not affected by the rotation angle lag between unit plastic strain rate and fabric, as assumed.

Thus, N, written on the principal axes on the fabric, becomes:

$$N = \mathbf{n}_F : \mathbf{n} = trace\left(\begin{pmatrix} n_{F1} & 0 & 0 \\ 0 & n_{F2} & 0 \\ 0 & 0 & n_{F3} \end{pmatrix}\begin{pmatrix} n_1' & 0 & n_{13}' \\ 0 & n_2 & 0 \\ n_{31}' & 0 & n_3' \end{pmatrix}\right) = n_{F1}n_1' + n_{F2}n_2 + n_{F3}n_3' = \quad (5.3)$$
$$= (n_1 n_{F1} + n_3 n_{F3})\cos^2\varphi + (n_1 n_{F3} + n_3 n_{F1})\sin^2\varphi + n_2 n_{F2}$$

The part $n_{F1}n_1' + n_{F3}n_3'$ is equal to what would be derived by a 2D analysis on the x-z plane where the eigenvectors of n_1, n_3, n_{F1}, n_{F3} all lie, but it cannot be written similarly as for the 2D case (as $\cos 2\varphi$). This happens because the equations of the tensors' properties are different for 2D and 3D and there are the components along the y axis which add the last term in the last member of Eq. (5.3).

In 2D we would have only two principal values for the fabric and the unit plastic strain rate tensor: $\begin{matrix} n_1 + n_2 = 0 \\ n_1^2 + n_2^2 = 1 \end{matrix}$ and $\begin{matrix} n_{F1} + n_{F2} = 0 \\ n_{F1}^2 + n_{F2}^2 = 1 \end{matrix} \Rightarrow n_1, n_2 = \pm\sqrt{2}/2 \;, n_{F1}, n_{F2} = \pm\sqrt{2}/2$

In 3D, we have three principal values and thus:

$$\begin{aligned} n_1 + n_2 + n_3 &= 0 \\ n_1^2 + n_2^2 + n_3^2 &= 1 \end{aligned} \tag{5.4a}$$

and

$$\begin{aligned} n_{F1} + n_{F2} + n_{F3} &= 0 \\ n_{F1}^2 + n_{F2}^2 + n_{F3}^2 &= 1 \end{aligned} \tag{5.4b}$$

as both unit fabric and unit plastic strain rate tensors are traceless and unit-norm. Furthermore, if we proceed on the 3D, after Eq. (5.4a) it results that:

$$\begin{aligned} n_2 &= -n_1 - n_3 \\ n_{F2} &= -n_{F1} - n_{F3} \end{aligned}$$

and Eq. (5.3) then easily becomes:

$$N = (n_1 n_{F1} + n_3 n_{F3})(1 + \cos^2\varphi) + (n_1 n_{F3} + n_3 n_{F1})(1 + \sin^2\varphi) \tag{5.5}$$

Focus now only on one of the two tensors, the unit plastic strain rate. By using Eq. (5.4a) we can express everything based on n_2, because the eigenvector that is related with n_2 and n_{F2} is constant and parallel to the y axis for the whole phase 2. Thus:

$$\left.\begin{aligned} n_1 + n_2 + n_3 &= 0 \\ n_1^2 + n_2^2 + n_3^2 &= 1 \end{aligned}\right\} \Rightarrow \left.\begin{aligned} n_1 &= -n_3 - n_2 \\ (-n_3 - n_2)^2 + n_2^2 + n_3^2 &= 1 \end{aligned}\right\} \Rightarrow \left.\begin{aligned} n_1 &= -n_3 - n_2 \\ 2n_3^2 + 2n_2 n_3 + 2n_2^2 - 1 &= 0 \end{aligned}\right\} \tag{5.6}$$

Now, solving $2n_3^2 + 2n_2 n_3 + 2n_2^2 - 1 = 0$ for n_3 (n_2 is considered known):

$\Delta = 4n_2^2 - 4\cdot 2\cdot(2n_2^2 - 1) = 4n_2^2 - 16n_2^2 + 8 = 8 - 12n_2^2$, and so:

$$n_3 = \frac{-2n_2 \pm \sqrt{8 - 12n_2^2}}{2\cdot 2} = \frac{-2n_2 \pm \sqrt{4(2 - 3n_2^2)}}{2\cdot 2} = \frac{-2n_2 \pm 2\sqrt{2 - 3n_2^2}}{2\cdot 2} = \frac{-n_2 \pm \sqrt{2 - 3n_2^2}}{2}$$

Thus:

$$\left.\begin{aligned} n_3 &= \frac{-n_2 \pm \sqrt{2 - 3n_2^2}}{2} \\ n_1 &= -n_3 - n_2 \end{aligned}\right\} \Rightarrow \left.\begin{aligned} n_3 &= \frac{-n_2 \pm \sqrt{2 - 3n_2^2}}{2} \\ n_1 &= -\frac{-n_2 \pm \sqrt{2 - 3n_2^2}}{2} - \frac{2n_2}{2} \end{aligned}\right\} \Rightarrow \left.\begin{aligned} n_3 &= \frac{-n_2 \pm \sqrt{2 - 3n_2^2}}{2} \\ n_1 &= \frac{-n_2 \mp \sqrt{2 - 3n_2^2}}{2} \end{aligned}\right\}$$

And so finally:

$$n_3 = \frac{-n_2 \pm \sqrt{2 - 3n_2}}{2} \quad \text{and} \quad n_1 = \frac{-n_2 \mp \sqrt{2 - 3n_2}}{2} \tag{5.7}$$

The conclusion of Eq. (5.7) stands the same for n_{F1}, n_{F2} and n_{F3}.

Check that for Eq. (5.7):

$n_1 + n_3 = -n_2$

$n_1^2 + n_3^2 = 1 - n_2^2$

Also check that in triaxial compression and extension, which is by definition an axisymmetric loading: $n_1 = \sqrt{2/3}$ & $n_2 = n_3 = -1/\sqrt{6}$ and $n_1 = -\sqrt{2/3}$ & $n_2 = n_3 = 1/\sqrt{6}$, respectively.

Now remember the equation (5.5) for *N* and based on (5.7) we find that:

$$n_1 n_{F1} + n_3 n_{F3} = \frac{n_2 n_{F2}}{2} + \frac{\sqrt{2-3n_2^2}\sqrt{2-3n_{F2}^2}}{2} = N' \quad (5.8)$$

$$n_1 n_{F3} + n_3 n_{F1} = \frac{n_2 n_{F2}}{2} - \frac{\sqrt{2-3n_2^2}\sqrt{2-3n_{F2}^2}}{2} = N'' \quad (5.9)$$

(check also that $n_1 n_{F1} + n_3 n_{F3} + n_1 n_{F3} + n_3 n_{F1} = n_2 n_{F2}$ as it should be).

Finally, by replacing (5.8), (5.9) in (5.5) we end up with an equation for *N* that contains only the angle φ and the principal values for the unit plastic strain rate and the fabric tensors which lie on the y axis (the principal value n_2 and n_{F2}):

$$N = N'(1+\cos^2\varphi) + N''(1+\sin^2\varphi) = N' + 2N'' + (N' - N'')\cos^2\varphi \quad (5.10a)$$

$$N' = \frac{n_2 n_{F2}}{2} + \frac{\sqrt{2-3n_2^2}\sqrt{2-3n_{F2}^2}}{2} \quad (5.10b)$$

$$N'' = \frac{n_2 n_{F2}}{2} - \frac{\sqrt{2-3n_2^2}\sqrt{2-3n_{F2}^2}}{2} \quad (5.10c)$$

Also based on (5.10a):

$$N = N' + 2N'' + (N' - N'')\cos^2\varphi \Rightarrow \cos^2\varphi = (N - N' - 2N'')/(N' - N'') \Rightarrow$$

$$\varphi = \operatorname{acos}\left(\sqrt{(N - N' - 2N'')/(N' - N'')}\right) \quad (5.10d)$$

It was not necessary to derive the intermediate Eq. (5.5) for *N* in order to obtain Eqs. (10); the initial Eq. (5.3) of *N* could also be directly used, but for clarity we derived Eq. (5.5) that is similar to the initial form of Eq. (5.10a). This equation is based only on the assumption that the second eigenvector for both the unit plastic strain rate tensor and the fabric tensor lie on the same axis. In our case, this axis is the y axis while the rotation of the eigenvectors 1 and 3 takes place on the x-z plane.

From the DEM analysis, we can measure n_2 and n_{F2}, and result in a relation only between *N* and φ. The three principal values of the fabric are presented in Fig. 5.16. As expected

from the triaxial load of phase 1, when stress PA rotation initiates the fabric major principal value is equal to $\sqrt{2/3}$ (≈ 0.8146) while the two minors are equal to $-1/\sqrt{6}$ (≈ -0.4073); this occurs as these three value must satisfy Eq. (5.4a) and (5.4b).

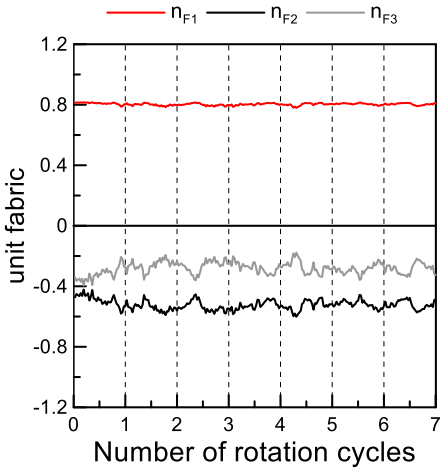

Fig. 5.16. Fabric tensor's principal values

It is important to notice here the theoretical importance of the equations (5.4a) and (5.4b) on the evolution of these principal values. It is interesting to relate n_2 and n_3 with n_1 so that based on the value of n_1, which is obviously the more stable in value in Fig. 5, the other two are analytically calculated. For this purpose, the solving procedure is the same as for Eqs. (5.6) and (5.7) because of the symmetry of Eq. (5.4a) and these relations then yield:

$$n_3 = -\frac{n_1}{2} \pm \frac{\sqrt{2-3n_1^2}}{2}$$
$$n_2 = -\frac{n_1}{2} \mp \frac{\sqrt{2-3n_1^2}}{2} \qquad (5.11)$$

It results that the values of n_1, n_2 and n_3 are related in such a way that only one of them needs to be defined and then the other two are analytically calculated. Based on Eq. (5.11) we can assume n_1 which is the major principal value and is the more stable in terms of DEM measurements, and calculate the other two. If n_1 fluctuates even slightly from its value, then the other two deviates a lot from their respected values. In Fig. 5.17 the allowed values of n_1, n_2 and n_3 are presented which satisfy Eq. (5.11), when n_1 varies from $\sqrt{2/3}$ (this is the maximum allowed value for n_1) to 0.79; n_2 is assumed to have

always the positive sign in Eq. (5.11) without loss of generality). The horizontal axis of Fig. 5.17 is just measuring the number of values and is not of importance.

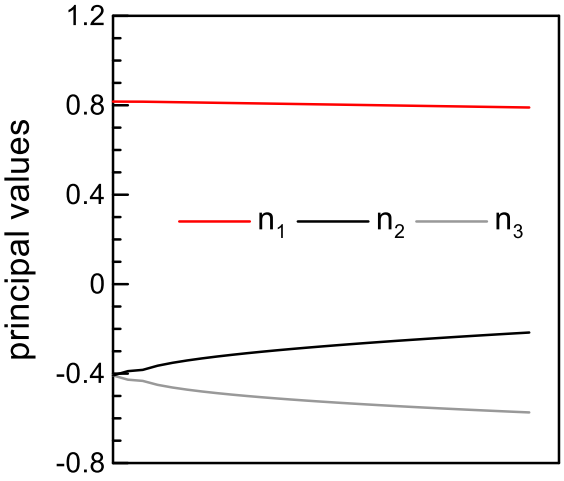

Fig. 5.17. The allowed combinations between the principal values of the tensors based on Eq. (5.4a); n_1 varies from $\sqrt{2/3} \approx 0.8146$ to 0.79

Based on this discussion, the principal values for the unit fabric tensor are considered constant for phase 2 and they are calculated to fit the evolution presented in Fig. 5.16:

$$n_{F1} = 0.80\,; \qquad n_{F2} = -0.2586\,; \qquad n_{F3} = -0.5414 \tag{5.12}$$

For the calculation of these values, n_{F1} is primarily estimated from the DEM measurements and then n_{F2} and n_{F3} are calculated based on Eq. 5.11. The fit of these values with the measured DEM values is presented in Fig. 5.18.

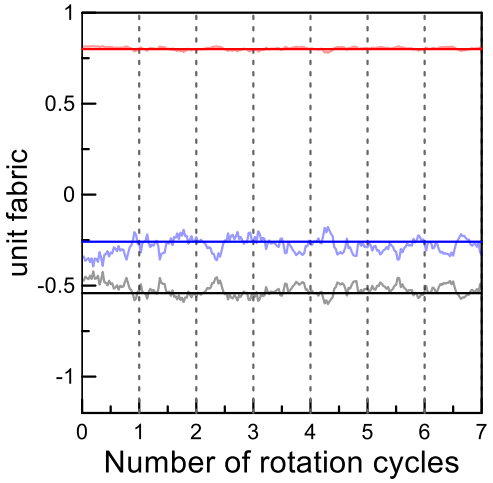

Fig. 5.18. Fabric tensor's principal values and their chosen constant values

The evolution of the unit plastic strain rate appears different than the one for the fabric and due to the more extreme fluctuations, it is more difficult to interpret it. From Fig. 5.13(a) when the stress PA rotation initiates $n_{zz} = \sqrt{2/3}$ and $n_{xx} = n_{yy} = -1/\sqrt{6}$ similarly to the fabric normal components, as it is expected. From the shear components, Fig. 5.13(b), it is concluded that the only shear unit plastic strain rate component lies on the x-z plane and that the axis y is principal axis for the unit plastic strain rate.

After having confirmed the basic assumption, we procced to Fig. 5.19 to observe the principal values of the unit plastic strain rate tensor. The value of n_2 should be decided to be used with Eq. (5.10) and Eq. (5.12) for the calculation of φ. Again Eq. (5.11) are used for the relation among the three principal values.

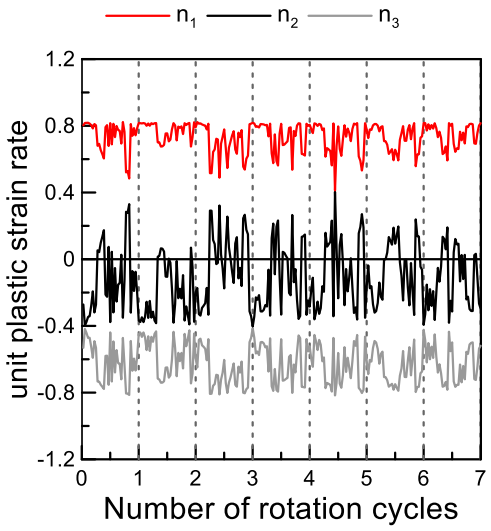

Fig. 5.19. Unit plastic strain rate tensor's principal values

After Fig. 5.19 two cases have been examined for the evolution of the principal values of the unit plastic strain rate; for the first case, the principal values have a constant value throughout phase 2 while for the second case an evolution is decided. These two cases and their results now follow.

5.5.2.1. Case 1: constant n_2 value

Based on Fig. 5.19 three constant principal values for phase 2 are calculated to fit the respected evolution. Thus:

$$n_1 = 0.75\,; \qquad n_2 = -0.0955\,; \qquad n_3 = -0.6545 \tag{5.13}$$

These values are based on the estimation of n_1 from the DEM measurements and then n_{F2} and n_{F3} are calculated based on Eq. 5.11; though this is the main procedure, all three principal values must fit well with their DEM measurements. The fit for these principal values of the unit plastic strain rate is presented in Fig. 5.20(a).

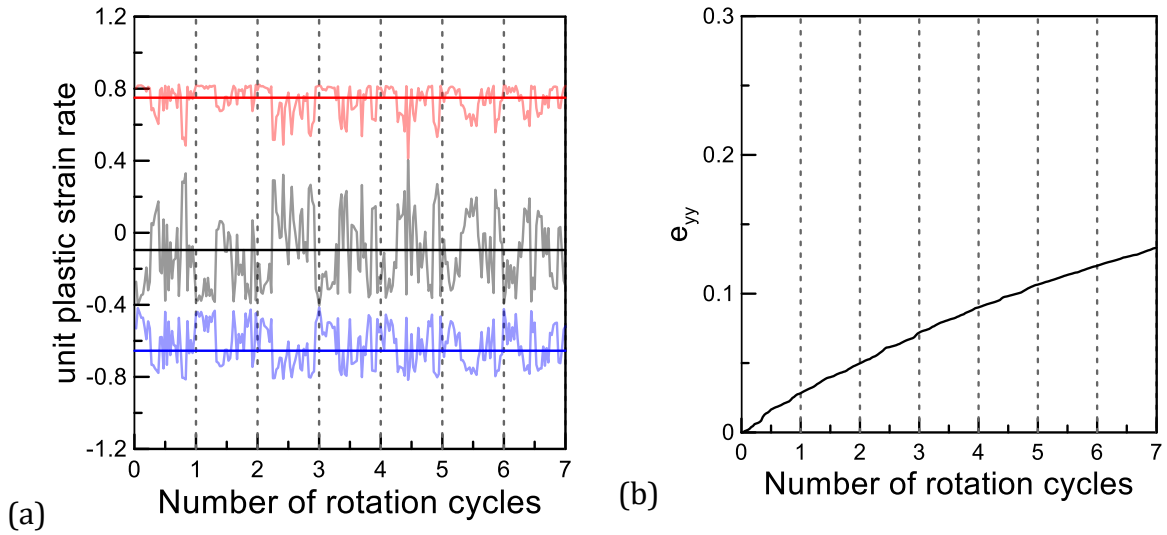

Fig. 5.20. (a) Unit plastic strain rate principal values along with their constant values chosen for phase 2 (b) strain evolution of the sample on y axis based on constant $n_2 = -0.0955$

That approach produces increase of strain in the y axis, which is the one parallel to the eigenvector of n_2. This happens because the value for the n_2 corresponds to a value for the plastic strain rate de_2 through the norm of the plastic strain rate tensor. That leads to an evolution for de_2 that produces strain on the y axis, as was observed in the experiment, because: $e_2 = \int de_2 = \text{constant} = e_{yy}$. The results of the Fig. 5.20(b) are based on the constant value of n_2 multiplied with the norm of the plastic strain rate tensor; this would introduce $n_2 \cdot norm(d\mathbf{e}) = de_2$ and this suggests that we get the increase of strain on the y axis. This evolution is qualitatively consistent with the observed evolution of the strain on the y axis, where the second principal value lies during the stress PA rotation on the DEM sample.

Based on Eqs. (5.10), (5.12) and (5.13), ($n_2 = -0.0955$ and $n_{F2} = -0.2586$) the following calculations yield the relation between *N* and angle φ:

$N' = 0.9544$ and $N'' = -0.9297$

$$N = -0.905 + 1.8838\cos^2\varphi \qquad (5.14)$$

and

$$\varphi = \text{acos}\left(\sqrt{(N + 0.905)/1.8838}\right) \qquad (5.15)$$

This equation directly connects *N* and φ, and based on the calculated *N* Fig. 5.21(a) follows. Fig. 5.22(b) is the angle φ measured from the eigenvectors of the two tensors presented for comparison (same as Fig. 5.14(b)). A good agreement is presented between these two methods for φ calculation.

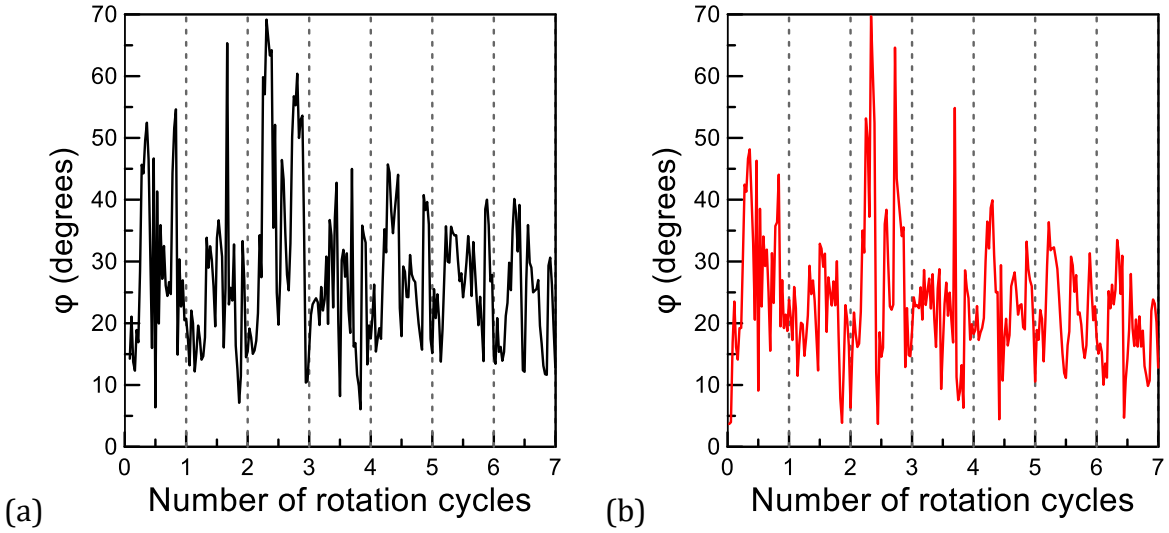

Fig. 5.21. (a) Angle lag φ on x-z plane based on N and constant $n_2 = -0.0955$ and (b) φ calculated from eigenvectors, versus the number of rotation cycles

5.5.2.2. Case 2: evolving n_2

On this case, the principal values of the unit plastic strain rate tensor are considered evolving during phase 2, i.e. stress PA rotation. A trigonometric evolution is chosen to describe the unit plastic strain rate principal values; the results are presented in Fig. 5.22. For the equation of n_2 it is necessary to introduce the angle of the stress rotation on the x-z plane θ_σ, and so:

$$n_2 = -1/(2\sqrt{6}) - 1/(2\sqrt{6})\cos(2\theta_\sigma) \tag{5.16}$$

The other two equations for n_1 and n_3 are directly calculated based on Eq. (5.7). This fit is presented in Fig. 5.22(a). Based on Eq. (5.16) we can now calculate similarly as for case 1 the evolution of the strain e_{yy}; the results are presented in Fig. 5.22(b).

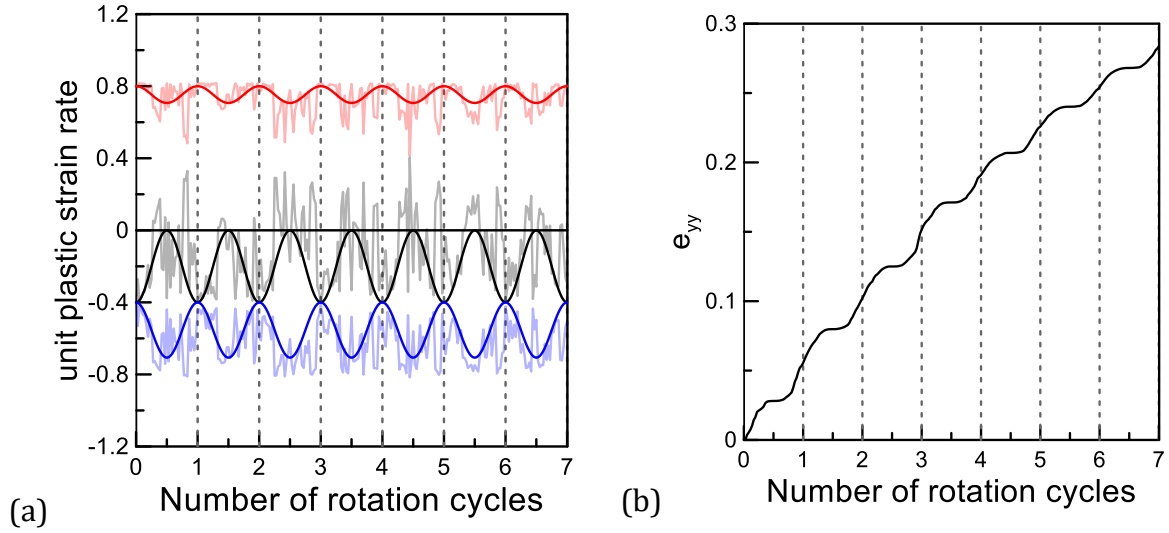

Fig. 5.22. (a) The trigonometric fits on the evolution of unit plastic strain rate tensor's principal values and (b) strain evolution of the sample on y axis based on evolving n_2

Based on Eq. (5.10), (5.12) and (5.16) ($n_2 = -1/(2\sqrt{6}) - 1/(2\sqrt{6})\cos(2\theta_\sigma)$ and $n_{F2} = -0.2586$), the following calculations yield the relation between *N* and angle *φ*:

$$N' = 0.0264(1+\cos(2\theta_\sigma)) + 0.6624\sqrt{1.833 - 0.25\cos(2\theta_\sigma) - 0.1667\cos^2(2\theta_\sigma)}$$

$$N'' = 0.0264(1+\cos(2\theta_\sigma)) - 0.6624\sqrt{1.833 - 0.25\cos(2\theta_\sigma) - 0.1667\cos^2(2\theta_\sigma)}$$

$$\varphi = \operatorname{acos}\left(\sqrt{\frac{(N - 0.0792(1+\cos(2\theta_\sigma)) + 0.6624\sqrt{1.833 - 0.25\cos(2\theta_\sigma) - 0.1667\cos^2(2\theta_\sigma)})}{(1.3248\sqrt{1.833 - 0.25\cos(2\theta_\sigma) - 0.1667\cos^2(2\theta_\sigma)})}}\right) \tag{5.17}$$

This leads to an equation that directly connects *N* and *φ*, and based on the calculated *N*, Fig. 5.23(a) follows. Fig. 5.35(b) presents angle *φ* calculated by the eigenvectors of the two tensors (same as Fig. 5.12(b)) and is used for comparison. Again, a good agreement is presented between these two methods of calculation of *φ*.

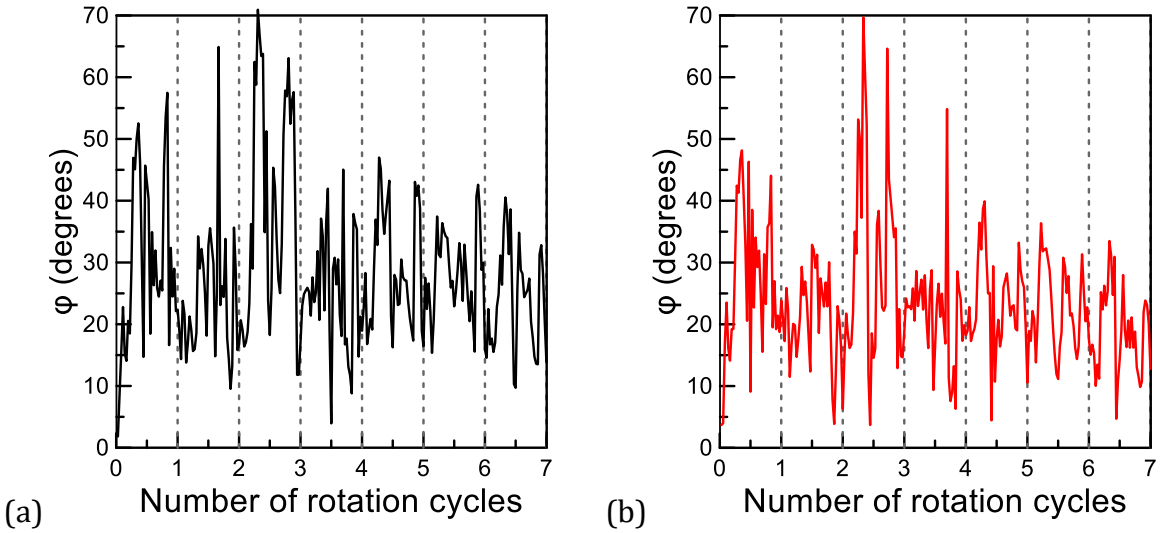

Fig. 5.23. (a) Angle lag φ on x-z plane based on N and evolving $n_2 = -1/(2\sqrt{6}) - 1/(2\sqrt{6})\cos(2\theta_\sigma)$ and (b) φ calculated from eigenvectors, versus the number of rotation cycles

5.6. Discussion

Up to this point, it has become clear that the conditions of CST for reaching and maintaining CS (Eq. 3.4) are incomplete, in the sense that they are necessary but not sufficient. The ACST is a theory that has come to fill this incompleteness with one extra condition, elegantly defined by Eq. (3.6). Besides the Critical State conditions per se, ACST has come to propose some scalar values that can explain and quantify in a physical way the possible reasons for dilation-contraction response, i.e. the void ratio evolution, through the dilatancy defined in section 4.5, as well as for the hardening and softening of the material, through the plastic modulus. The equations for the dilatancy as well as for the plastic modulus are repeated here:

$$D = d(M^d - \eta) \tag{4.1a}$$

$$K_p = h(M^b - \eta) \tag{4.1b}$$

$$M^d = Me^{m\zeta} \tag{4.2a}$$

$$M^b = Me^{n<-\zeta>} \tag{4.2 b}$$

In the heart of ACST is the FAV A, which incorporates two elements: the fabric anisotropy intensity and the relative orientation between the fabric and the loading direction (quantified as the plastic strain rate direction). Another parameter, is the Dilatancy State

Parameter (DSP) - ζ (see also Eq. 3.7 and Chapter 3, section 2) the equation of which is repeated here for simplicity:

$$\zeta = e - e_d = \psi - \hat{e}_A(e,p)(A-1) \qquad (3.7)$$

with $\hat{e}_A(e,p)$ an appropriate positive scalar-valued function of e, p (in the simplest case a constant). This parameter has been used in section 4.5 for the explanation of the results of the 2D DEM virtual experiments within the ACST. Eq. (3.7) physically suggests that dilation-compression is related through ζ to the density state of the sample with respect to its CS value (through ψ), and to the fabric in term of intensity (norm) and relative direction, of fabric, with respect to the loading (herein plastic strain rate) via A. This would be intuitive and natural as previous researchers have qualitatively suggested similar explanations (e.g. Tong et al., 2010) for the void ratio evolution. From an experiment as the one practiced herein, it is possible to extract all the information concerning A, ψ but the term $\hat{e}_A(e,p)$ is unknown. The calibration of this parameter would require more than the results obtained in this work, as the direct evolution of the void ratio is based on the dilatancy D, which has also a second parameter for calibration, the parameter m (see Eq. 4.1a and 4.2a).

Still, it is possible to assume a constant value for the $\hat{e}_A(e,p)$ and calculate the evolution of ζ, mainly during phase 2, which has been the non-typical loading phase. On this discussion, the results from phase 1 and phase 2 are presented on Fig. 5.24(a) for three different constant values of $\hat{e}_A$: 0.1, 0.35 and 1. The results are all plotted versus the equivalent strain for uniform presentation of the two phases; from bottom to top the constant $\hat{e}_A$ value increases. For all the plots, the vertical grey zones mark the areas where dilation takes place while the white zones where compression happens; these zones are not calculated but merely concluded from the void ratio evolution.

On Fig. 5.24(b) are presented the void ratio, the state parameter ψ and the FAV for the same phases (phase 1 and phase 2). On the bottom diagram lies the evolution of A, the same as presented in Figs. 5.10 and 5.11. Above the FAV A, is the state parameter ψ; it becomes clear that the evolution of ψ is exactly the same as for the void ratio as ψ is merely the difference of the void ratio with its CS value, that is constant for the whole experiment (given the constant p). As a result, ψ totally follows the evolution of the void

ratio and is constantly negative; this state parameter can only declare where the sample stands with respect to the CSL.

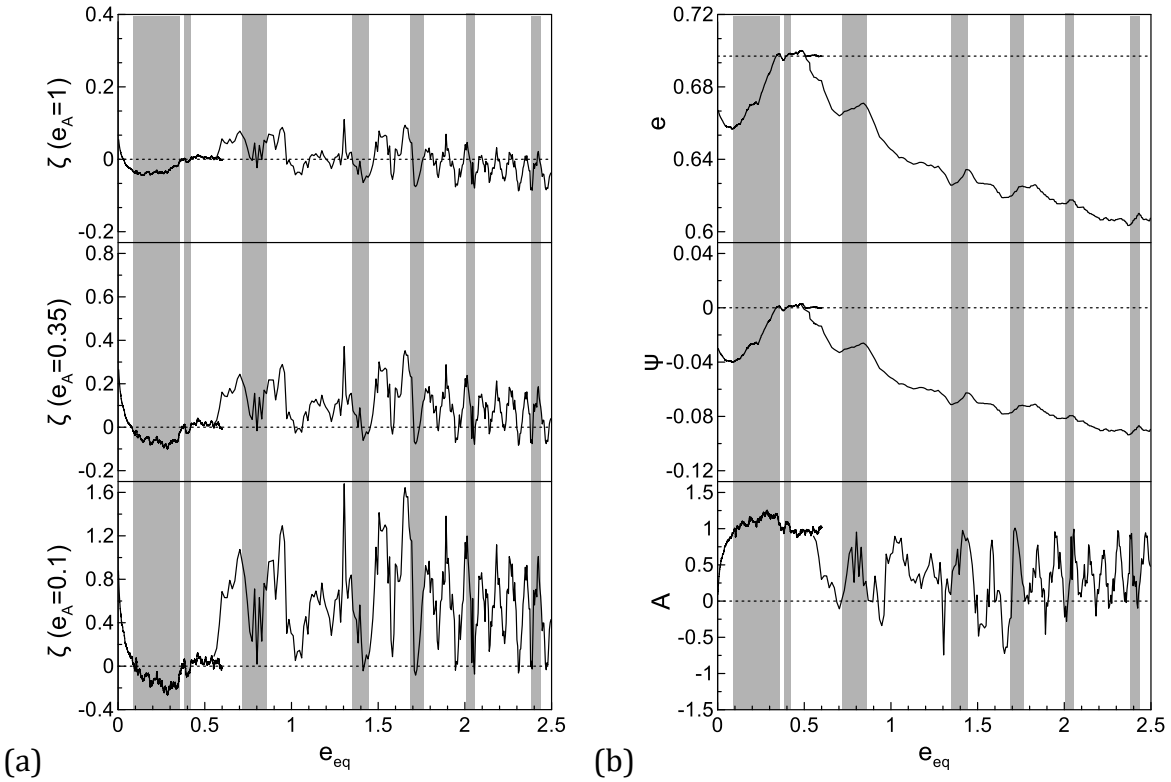

Fig. 5.24. (a) Dilatancy State Parameter for three values of the function $\hat{e}_A$ (b) void ratio and plots of entities related to ACST (FAV A, state parameter ψ) during the loading sequence of phase 1 and phase 2 for; the grey zones define the area where dilation appears

5.6. Conclusions

In this chapter, the 2D virtual experiment presented in the previous one has been extended in 3 dimensions. Though the implementation was very similar conceptually, the practical application per se has been different and several technical issues had to be solved. The results were expected to be qualitatively similar to those from the 2D, but also different due to the extra dimension. Besides the very interesting and important conclusions from the results of this virtual experiment, this has been also an opportunity to compare 2D and 3D DEM; most of the times only the one of the two approaches is used (usually only 2D without 3D) and so, with these results some conclusions can be drawn also on the differences that the addition of the (real) third dimension might carry.

At first, the major conclusions drawn from the 2D virtual experiments, i.e. the incompleteness of the CST and the support of this by the proposed remedy of Li and Dafalias (2012), are even more supported by the 3D results. The same mechanisms are revealed in the abandonment of the CSL during the stress PA rotation that render the classical CST incomplete. Additionally, similar general trends from 2 to 3 dimensions apply in the macroscopic and microscopic analysis. These are mostly the similarities of 2D and 3D DEM applications, that primarily validate the conclusions of Chapter 4, as these conclusions were of conceptual form.

Furthermore, the 3D DEM experiment and the subsequent analysis, revealed significant similarities with macroscopic results from physical experiments and other details, that the 2D DEM could not capture accurately. The triaxial procedure of phase 1 has a macroscopic response that is very realistic, presenting dilation and a small softening, and the values obtained for the Critical State parameters are very close to those of real sands. Thus, the results are quantitatively comparable to those of physical experiments with similar materials. The void ratio evolution during phase 2 has the clear tendency for overall contraction but with clear phases of, smaller in intensity, dilation, as in physical experiments, a fact that did not appear in 2D. Additionally, the contraction of phase 2 was mostly realized during the two initial cycles of rotation, as the rest of the rotation was significant less in overall volumetric change. The overall volumetric change of phase 2 seems to be greater than in experiments with sands; still reasons appear that could support these differences but further research could be needed to clarify this issue.

Moreover, phase 3 reveals the return to the CS, under the same p value, as was also suggested in 2D. Clearly, no matter where is the orientation of the triaxial loading, for the same hydrostatic pressure, the material will return to the same CS, as expected. This conclusion supports the independence of the CS on the loading path, as even if the intermediate phase 2 forces the sample to abandon CS, the material still recognizes the same CS.

The fabric analysis of the 3-phase procedure reveals similar trends with the 2D ones. As the scalar values used in ACST are not dimension dependent (fabric norm is normalized to go to 1 in CS, relative orientation of fabric and plastic strain rate varies from 1 to -1 accounting for coaxiality) there are no difference in these values. Though, in phase 2, the lag between the fabric and the stress is obviously larger in 3D than in 2D and the same happens for the plastic strain rate. Again, as in 2D, the plastic strain rate is the first to rotate, while the stress follows and the fabric comes last; the lags though between them are clearly larger. The relative orientation between fabric and plastic strain rate quantified by N, goes from 1 to 0 (0 meaning conceptually that the two are perpendicular to each other), and presents clear oscillations with respect to the cycles of rotation; these oscillations appear to follow nicely the void ratio variations from contraction to dilation. The oscillations of N have appeared also in 2D, but the values that N obtained there (from 0.8 to 0.5) did not allow to be definite about their appearance given the numerical noise of the analysis.

By analyzing N it has been revealed that the evolution of the non-coaxiality angle between the unit fabric direction and the unit plastic strain rate direction tensors defined on the rotation plane, does not present great differences with respect to the 2D case. The different evolution presented for N in 3D is due to the different form this takes and not on major differences on the angle lag φ. The calculation of this angle φ based on N has initiated a discussion on the evolution of the principal values of the unit fabric and the unit plastic strain rate tensors. Based on this, it can be concluded that these principal values evolve differently during stress PA rotation than in triaxial loading.

Finally, a brief but very interesting discussion on the Dilatancy State Parameter (DSP - ζ) of Li & Dafalias (2012) supports the fact that, this parameter is related to the evolution of the void ratio. Furthermore, the dilative or contractive response of a material to a certain loading, appears to be directly related with the DSP, which is based on the state parameter ψ that declares the relation of the sample's condition with CS and the FAV A

which in terms is a function of the relative orientation of plastic strain rate and fabric anisotropy and of fabric intensity. This parameter seems like an elegant way to include in one the CS (with ψ), the fabric anisotropy intensity (with norm F) and the loading direction (in terms of plastic strain rate) through its relationship with the fabric direction (with N).

Chapter 6: Conclusions

6.1. Summary – Conclusions

Critical State Soil Mechanics has been a framework-paradigm for the mechanical response of granular materials and soil mechanics since its introduction six decades ago. Two analytical conditions were explicitly proposed for reaching and maintaining Critical State (CS), those of Eq. (3.4), that refer to the stresses and the volumetric strain; they constitute the basis for Critical State Theory (CST) and have since been considered necessary and sufficient for reaching and maintaining CS. The special virtual experiment that has been realized and presented in this work, in 2 and 3 dimensions, has been inspired by the fact that CST lacks a fabric parameter, a feature that has been constructively criticized in the past. In particular, the Anisotropic Critical State Theory (ACST) of Li & Dafalias (2012) has challenged the completeness (in the sense of being necessary and sufficient) of the classical conditions put forth by CST, by proposing an extra, third condition, providing the motivation for the present experimental procedure. It should be mentioned that this third condition was originally introduced in order to address a strongly anisotropic response, rather than to show the incompleteness of CST as it is done in this work and in a recent publication by Theocharis et al (2017a). The aforementioned experiment was conceived, in order to compare the two theories and their assumptions, which are of fundamental nature for the fields of granular material and soil mechanics.

A three-phase experimental procedure took place in 2D and 3D using the Discrete Element Method (DEM). The first phase consisted of a constant-p biaxial (in 2D) or triaxial (in 3D) compression; the second phase applied the stress principal axes rotation with fixed principal stress values initiating at Critical State, and constituted the most important part of the procedure; the third phase was the resumption of the initial biaxial or triaxial compression loading for several orientations of the principal stress axes. The use of DEM has been the only way to conduct the desirable procedure, as physical limitations make such an experiment very difficult, if not impossible, to realize in the physical world. The three-phase loading that has been applied on circular (in 2D) and spherical (in 3D) discrete elements, revealed several aspects of the materials' characteristics concerning the response of a granular sample, especially at the regime of

Critical State, which are of extremely interesting and important nature. In the process of realizing this virtual experiment, several technical issues have been resolved, evolving and expanding the potential use of DEM, especially near the CS.

During the key phase 2 of the virtual experiment, a stress principal axes (PA) rotation took place, keeping the principal stress values fixed and initiating at CS, a loading path that has never been attempted before. This path violated only the fabric-related third condition, the new ACST condition, while keeping the two classical CST conditions satisfied at the initiation of rotation. A dramatic reduction of void ratio was then observed, contrary to what would be expected based on classical CST; CS was abandoned almost instantaneously when the principal axes of stress deviated from the initial configuration of the phase 1 triaxial load, even though the stress ratio and the void ratio were in their CS values and the hydrostatic stress was kept constant. It follows that classical CST is incomplete because its two conditions are necessary but not sufficient to maintain CS, and an addition to Eq. (3.4) is necessary; thus, the third condition of ACST is added to the first two CST conditions and all three are then both necessary and sufficient for CS to be reached and maintained.

During phase 3 loading, a radial loading of triaxial type was applied after phase 2 and the material reached the same CS when the necessary conditions were met. The void ratio rebounded to its CS value in a direct way, while the stress ratio increased to a peak value, due to the densification that took place during phase 2, and, afterwards, fell back to its CS value.

The macroscopic results in general agree well with observations from physical experiments where same stress paths were applied, even though, on this work, the stress PA rotation initiated at CS. Additional fabric insight has been given to these macroscopic results, due to the DEM flexibility. Along with the macroscopic response of the sample, the fabric evolution has also been monitored through a fabric tensor. In particular, we have used the fabric parameters defined within ACST, i.e. the fabric norm F, the relative orientation of fabric and loading direction (defined in terms of plastic strain rate), the Fabric Anisotropy Variable (FAV) A and the Dilatancy State Parameter ζ. The fabric of the granular samples has been quantified primarily through the contact normal fabric; additionally, only for the 2D case, the scan line method has been implemented for measuring void fabric. The void scan line fabric tensor definitions used herein include crucial modifications and improvements with respect to previous work on the scan line

method. It can be concluded that, at least in the context of this work, the contact normal and the void scan line fabric led to very similar results.

Most interesting are the results of phase 2, stress PA rotation initiating at CS, considering the changes of the principal axes of the stress, the plastic strain rate and the fabric. On the 2D DEM virtual experiment, the results presented a fast transition from phase 1 and phase 3 to and from phase 2, during which the PA of fabric follow the PA of stress by an angle lag of 5^o on average, while the PA of stress in turn follow the PA of plastic strain rate by an angle lag of 13^o, as all three pairs of PA rotate almost simultaneously. On the 3D case, we observe the same fast transition to and from phase 2 while the plastic strain rate, stress and fabric tensors rotate following the same sequence as in 2D. However, on 3D it became obvious that the three tensors do no keep a constant lag while rotating, but oscillate significantly. The angle lag was in general greater between the rotating directions of the plastic strain rate and the stress, than those of the stress and the fabric. Focus has been given on the plastic strain rate - fabric relative orientation, through N. The lag between these two quantities appears to oscillate in such a fashion that plastic strain rate and fabric tend to be coaxial at the beginning and in the middle of each rotation cycle, while they tend to be strongly non-coaxial in between. This observation can be related to the oscillations of contraction-dilation of the void ratio during the stress PA rotation.

Finally, valuable information was obtained by comparing the same experiment in 2 and 3 dimensions, thus examining if the 2D analysis could suffice and fully evaluate the phenomena described. On one side, the 2D DEM virtual experiment correctly captured the general mechanisms and concepts, correctly answering the principal question of whether CST was incomplete and whether ACST could be an accurate remedy. On the other side, vital details, such as the significant contraction of the sample during the first 2 cycles of the stress PA rotation, the oscillations of contraction-dilation of the void ratio and the oscillations of the FAV A, have been obscured in 2D, while plainly revealed in 3D.

6.2. Discussion – Further research

This work answered some important questions, yet other queries exist that require further research. At first, there are two major effects that could be added to the analysis in order to solidify the results. The one is the shape of the particles, which in this work

were circular in shape in 2D and spherical in 3D; changes of the particles' shape have been shown to play a key role in granular materials' response. Although such an alteration in the analysis is not expected to modify the primary conclusions of this work, it would be necessary to validate them and to examine any differences that might occur in the results. Additionally, we assumed an initially isotropic fabric for all the samples; this could be changed so that the specimen is initially anisotropic, as in cases of pluviation under gravity. It is quite possible that such a variation would not affect results at CS, but it would be important to analyze the response of the sample before the CS and during phase 2 and 3 where the material has abandoned CS, and thus such a difference on the initial conditions may affect the details of the response.

Another crucial issue that arises and is at the heart of ACST, and any other fabric-related analysis, is which type of fabric and which fabric tensor would be most efficient in order to explain and quantify the material's mechanical response. Due to the nature of circular and spherical particles, only contact normal and void fabric exists. These two fabric types appear to be directly related with respect to this type of particles and can possibly be used interchangeably, thus being of no major importance which one of the two is implemented. However, when elongated particles are used, all three fabric elements appear to play a vital role to a specimen's response. In this regime, of elongated or irregular particles, more research is needed concerning the fabric elements, their relations, and their importance to the material's mechanical response.

Furthermore, in this work only the 2D scan line method has been used, as a relevant 3D method is not yet completely developed. Such a 3D scan line method should be implemented, following the path that has been paved by this research in 2D. This would provide a proper way to measure the void fabric in 3 dimensions; 3D methods for void fabric are especially needed for physical experiments where the quantification of contact normal is difficult and still seems uncertain. With such tools, it becomes possible to quantify fabric and all of its elements, in simulations and in real materials.

Finally, it is worth noting that one could argue on the way of remedying the incompleteness of CST, and examine the possibility of adding an alternative third condition in order to create the necessary and sufficient conditions for reaching and maintaining CS. Specifically, since this incompleteness is related to the lack of a condition that corresponds to the CS feature of a constant deviatoric strain rate direction, another possible third condition could be one that would not allow any change in the direction of

the plastic strain rate. If this demand for fixed plastic strain rate directions could be formulated by means of an adequate mathematical expression, then this new set of conditions would also be necessary and sufficient. However, the fact that such fixity of strain rate direction must be defined in regard to the sample (e.g. one could superpose a rigid body rotation to the whole sample and change the strain rate direction, but not intrinsically), leaves no much room for a third condition much different than the one proposed in ACST. Nevertheless, ACST provides a framework that, not only remedies the CST, but also introduces the concept of fabric and of anisotropy in several aspects of the material's mechanical response, thus providing a more complete overall framework for modeling and understanding the mechanical behavior of granular materials.

References

1. Ai, J., Langston, P. A., & Yu, H. (2014). Discrete element modeling of material non-coaxiality in simple shear flows. *International Journal for Numerical and Analytical Methods in Geomechanics,* 38(6), 615-635.
2. Alarcon, A., & Leonards, G. A. (1988). Liquefaction evaluation procedure-discussion. *Journal of geotechnical engineering*, *114*(2), 232-236.
3. Alshibli, K. A., & Alramahi, B. A. (2006). Microscopic evaluation of strain distribution in granular materials during shear. *Journal of geotechnical and geoenvironmental engineering*, *132*(1), 80-91.
4. Al-Shibli, K., Macari, E., & Sture, S. (1996). Digital imaging techniques for assessment of homogeneity of granular materials. *Transportation Research Record: Journal of the Transportation Research Board*, (1526), 121-128.
5. Anandarajah, A., Kuganenthira, N. (1995). Some aspects of fabric anisotropy of soil. *Géotechnique, 45*(1), 69–81.
6. Andò, E., Viggiani, G., Hall, S. A., & Desrues, J. (2013). Experimental micro-mechanics of granular media studied by X-ray tomography: recent results and challenges. *Géotechnique Letters*, *3*(3), 142-146.
7. Arthur, J. R. F., & Dunstan, T. (1969a). Radiography measurements of particle packing. *Nature*, *223*(5205), 464-468.
8. Arthur, J. R. F., & Dunstan, T. (1969b). Radiological techniques developed to describe particle packing. *Powder Technology*, *3*(1), 195-207.
9. Arthur, J. R. F., & Menzies, B. K. (1972). Inherent anisotropy in a sand. *Géotechnique*, *22*(1), 115-128.
10. Arulanandan, K. and Dafalias, Y.F., "Significance of Formation Factor in Sand Structure Characterization," Letters in Applied and Engineering Sciences, International Journal of Engineering Science, Vol. 17, pp. 109-112, 1979.
11. Aste, T. (2005). Variations around disordered close packing. *Journal of Physics: Condensed Matter*, *17*(24), S2361.
12. Aste, T., Saadatfar, M., Sakellariou, A., & Senden, T. J. (2004). Investigating the geometrical structure of disordered sphere packings. *Physica A: Statistical Mechanics and its Applications*, *339*(1), 16-23.

13. Atkinson, J. H., & Bransby, P. L. (1977). *The mechanics of soils, An introduction to critical state soil mechanics*, London: McGraw Hill.
14. Azéma, E., & Radjai, F. (2011). Force chains and contact network topology in packings of elongated particles. *Physical Review E*, *85*(31083).
15. Bagi, K. (1996). Stress and strain in granular assemblies. *Mechanics of Materials*, *22*(3), 165–177.
16. Been, K., & Jefferies, M. G. (1985). A state parameter for sands. *Géotechnique*, 35(2), 99–112.
17. Belheine, N., Plassiard, J. P., Donzé, F. V., Darve, F., & Seridi, A. (2009). Numerical simulation of drained triaxial test using 3D discrete element modeling. *Computers and Geotechnics*, *36*(1), 320-331.
18. Biscarini F., Samori P., Greco O. and Zamboni R. (1997). Scaling behavior of anisotropic organic thin films grown in high vacuum. *Physical review letters, 78*(12), 2389.
19. Brewer, R. (1964). *Fabric and mineral analysis of soils*, USA: John Wiley & Sons.
20. Calvetti, F. (2008). Discrete modeling of granular materials and geotechnical problems. *European Journal of Environmental and Civil Engineering*, *12*(7-8), 951-965.
21. Calvetti, F., Combe, G., & Lanier, J. (1997). Experimental micromechanical analysis of a 2D granular material: relation between structure evolution and loading path. *Mechanics of Cohesive-Frictional Materials*, *2*(1997), 121–163.
22. Cambou, B., Jean, M., & Radjai, F. (2009). *Micromechanics of Granular Materials (ISTE)*. London: Wiley
23. Carraro, J. A. H., Prezzi, M., & Salgado, R. (2009). Shear strength and stiffness of sands containing plastic or nonplastic fines. *Journal of geotechnical and geoenvironmental engineering*, *135*(9), 1167-1178.
24. Casagrande, A., & Carrillo, N. (1944). Discussion on Study of Failure Envelope Soils. *Journal of the Soil Mechanics and Foudations Division", ASCE*, *89*, 243.
25. Chang, C. S., Matsushima, T., & Lee, X. (2003). Heterogeneous strain and bonded granular structure change in triaxial specimen studied by computer tomography. *Journal of engineering mechanics*, *129*(11), 1295-1307.
26. Chen, Y. R., & Kutter, B. L. (2009). Contraction, dilation, and failure of sand in triaxial, torsional, and rotational shear tests. *Journal of engineering mechanics*, *135*(10), 1155-1165.

27. Cheung, G., & O'Sullivan, C. (2008). Effective simulation of flexible lateral boundaries in two- and three-dimensional DEM simulations. *Particuology*, *6*(6), 483–500.
28. Christoffersen, J., Mehrabadi, M.M., Nemat-Nasser, S. (1981). A micromechanical description of granular material behaviour. *Journal of Applied Mechanics-ASME 48*, 339–344.
29. Chu, J. (1995). An experimental examination of the critical state and other similar concepts for granular soils. *Canadian Geotechnical Journal*, *32*(6), 1065-1075.
30. Cil, M. B., & Alshibli, K. A. (2014). 3D analysis of kinematic behavior of granular materials in triaxial testing using DEM with flexible membrane boundary. *Acta Geotechnica*, *9*(2), 287–298.
31. Cole, D. M. (2014). Laboratory observations of frictional sliding of individual contacts in geologic materials. *Granular Matter*, *17*(1), 95–110.
32. Colliat-Dangus, J. L., Desrues, J., & Foray, P. (1988). Triaxial testing of granular soil under elevated cell pressure. In *Advanced triaxial testing of soil and rock*. ASTM International.
33. Coulomb, C. A. (1773). Essai sur un application de règles de maximis et minimis à quelques poblèmes de staique relatifs à l'architecture. *Acad. R. Sci. Mem. Math. Phys. Acad. R. Sci.*, Paris, 7, 343–382.
34. Coulomb, C. A. (1776). An attempt to apply the rules of maxima and minima to several problems of stability related to architecture. *Mémoires de l'Académie Royale des Sciences*, *7*, 343-382.
35. Coulomb, C. A. (1781). Théorie des machines simples. *Acad. Sci.*, 10, 166–331.
36. Cundall, P. A., & Hart, R. D. (1992). Numerical modeling of discontinua. *Engineering Computations*, *9*(2), 101-113.
37. Cundall, P. A., & Strack, O. D. (1979). A discrete numerical model for granular assemblies. *Géotechnique*, *29*(1), 47-65.
38. Dafalias, Y.F. and Arulanandan, K., "The Structure of Anisotropic Sands in Relation to Electrical Measurements," Mechanics Research Communications, Vol. 5, pp. 325 330, 1978.
39. Dafalias, Y.F. and Arulanandan, K., "Electrical Characterization of Transversely Isotropic Sands," Archives of Mechanics, Vol. 31, pp. 723-739, 1979.
40. Dafalias, Y. F., Papadimitriou, A. G., & Li, X. S. (2004). Sand plasticity model accounting for inherent fabric anisotropy. *Journal of Engineering Mechanics*, *130*(11), 1319-1333.

41. Dafalias, Y.F. (2016). Must Critical State Theory be revisited to include fabric effects?. *Acta Geotechnica,* DOI: 10.1007/s11440-016-0441-0.
42. Dafalias, Y.F., & Manzari, M.T. (2004). A simple plasticity sand model accounting for fabric change effects, *Journal of Engineering Mechanics, ASCE, 130*(6), 622-634.
43. Dafalias, Y.F., and Taiebat, M. (2014). Rotational hardening with and without anisotropic fabric at critical state. *Géotechnique*, *64(6),* 507-511.
44. Daouadji, A., & Hicher, P.Y. (2010). An enhanced constitutive model for crushable granular materials. *International Journal for Numerical and Analytical Methods in Geomechanics, 34*(6), 555-580.
45. Darwin, G. H. (1883). On the horizontal thrust of a mass of sand. *Minutes of the Proc. Institution of Civil Engineering*, Vol. 71, Institution of Civil Engineering (ICE), London, 350–378.
46. DeGregorio, V. B. (1990). Loading systems, sample preparation and liquefaction, *Journal of Geotechnical Engineering, 116*(5), 805–821.
47. Dennis, N. D. (1988). Liquefaction Evaluation Procedure: Discussion, *Journal of Geotechnical Engineering, 114*(2), 241–243.
48. Desrues, J., Chambon, R., Mokni, M., & Mazerolle, F. (1996). Void ratio evolution inside shear bands in triaxial sand specimens studied by computed tomography. *Géotechnique*, *46*(3), 529-546.
49. Desrues, J., Viggiani, G., & Besuelle, P. (Eds.). (2010). *Advances in X-ray Tomography for Geomaterials* (Vol. 118). John Wiley & Sons.
50. Drescher, A., & De Jong, G. D. J. (1972). Photoelastic verification of a mechanical model for the flow of a granular material. *Journal of the Mechanics and Physics of Solids*, *20*(5), 337-340.
51. Drucker, D. C., & Prager, W. (1952). Soil mechanics and plastic analysis or limit design. *Quarterly of applied mathematics*, *10*(2), 157-165.
52. Fonseca, J., Coop, M. R., O'Sullivan, C., & Lee, P. D. (2012). Quantifying the evolution of soil fabric during shearing using directional parameters. *Géotechnique*, *63*(10), 1–13.
53. Fonseca, J., Nadimi, S., Reyes-Aldasoro, C. C., O'Sullivan, C., & Coop, M. R. (2016). Image-based investigation into the primary fabric of stress-transmitting particles in sand. *Soils and Foundations*, *7* (October).
54. Franzius, O. (1927). *Der Grundban* (Vol. 3). Springer.

55. Fröhlich, O.K. (1934). *Druckverteilung im Baugrunde*. Verlag von Julius Springer, Wien, Austria.
56. Frost, J. D., & Kuo, C. Y. (1996). Automated determination of the distribution of local void ratio from digital images. *Geotech. Test. J. 19*(2), 107-119.
57. Fu, P., & Dafalias, Y. F. (2011a). Study of anisotropic shear strength of granular materials using DEM simulation. *International Journal for Numerical and Analytical Methods in Geomechanics*, *35*(10), 1098–1126.
58. Fu, P., & Dafalias, Y. F. (2011b). Fabric evolution within shear bands of granular materials and its relation to critical state theory. *International Journal for Numerical and Analytical Methods in Geomechanics*, *35*(18), 1918-1948.
59. Fu, P., & Dafalias, Y. F. (2015). Relationship between void- and contact normal-based fabric tensors for 2D idealized granular materials. *International Journal of Solids and Structures*, *63*, 68–81.
60. Gao, Z., Zhao, J., Li, X.S., &Dafalias, Y.F. (2014). A Critical State Sand Plasticity Model Accounting for Fabric Evolution. *International Journal for Numerical and Analytical Methods in Geomechanics, 38* (4), 370-390.
61. Gens, A., & Potts, D. M. (1988). Critical state models in computational geomechanics. *Engineering Computations*, 5(3), 178-197.
62. Ghedia, R., & O'Sullivan, C. (2012). Quantifying void fabric using a scan-line approach. *Computers and Geotechnics*, *41*, 1–12.
63. Goddard, J., 1977. An elastohydrodynamics theory for the rheology of concentrated suspensions of deformable particles. *Journal of Non-Newtonian Fluid Mechanics, 2*, 169–189.
64. Gu, X., Huang, M., & Qian, J. (2014). DEM investigation on the evolution of microstructure in granular soils under shearing. *Granular Matter*, *16*(1), 91-106.
65. Guo, N., & Zhao, J. (2013). The signature of shear-induced anisotropy in granular media. *Computers and Geotechnics*, *47*, 1-15.
66. Hall, S. a., Bornert, M., Desrues, J., Pannier, Y., Lenoir, N., Viggiani, G., & Bésuelle, P. (2010). Discrete and continuum analysis of localised deformation in sand using X-ray μCT and volumetric digital image correlation. *Géotechnique*, *60*(5), 315–322.
67. Huang, X., Hanley, K. J., O'Sullivan, C., & Kwok, C. Y. (2014). Exploring the influence of interparticle friction on critical state behaviour using DEM. *International Journal for Numerical and Analytical Methods in Geomechanics*, *38*(12), 1276-1297.

68. Ishihara K, Towhata K. (1983). Sand response to cyclic rotation of principal stress directions as induced by wave loads. *Soils and Foundations, 23*(4), 11–26.
69. Ishihara K, Yamazaki A. (1984). Analysis of wave-induced liquefaction in seabed deposits of sand. *Soils and Foundations, 24*(3), 85–100.
70. ITASCA (2008). Particle Flow Code in Two Dimensions. *Users' Manual: Theory and Background*. Minneapolis, MN, 3.13–3.16.
71. ITASCA (2015). Particle Flow Code in Two and Three Dimensions. PFC 5.0 Documentation. Minneapolis, MN.
72. ITASCA Consulting Group, Inc. (2013). *PFC— Particle Flow Code, Ver. 4.0*. Minneapolis, MN.
73. ITASCA Consulting Group, Inc. (2015). *PFC— Particle Flow Code, Ver. 5.0*. Minneapolis, MN.
74. Jaquet, C., Andó, E., Viggiani, G., & Talbot, H. (2013). Estimation of separating planes between touching 3D objects using power watershed. In *International Symposium on Mathematical Morphology and Its Applications to Signal and Image Processing* (pp. 452-463). Springer Berlin Heidelberg.
75. Jefferies, M. G. (1993). Nor-Sand: a simple critical state model for sand. *Géotechnique*, *43*(1), 91-103.
76. Jeremic, B., Runesson, K., & Sture, S. (1999). A model for elastic-plastic pressure sensitive materials subjected to large deformations. *International Journal of Solids and Structures*, *36*(31), 4901-4918.
77. Joer, H., Lanier, J., Desrues, J., & Flavigny, E. (1992). "1γ2ε": A New Shear Apparatus to Study the Behavior of Granular Materials.
78. Kahl W.A., Hinkes R., Feeser V. and Holzheid A. (2013). Microfabric and anisotropy of elastic waves in sandstone–An observation using high-resolution X-ray microtomography. *Journal of Structural Geology, 49*, 35-49.
79. Kanatani, K. (1984). Distribution of directional data and fabric tensors, *International Journal of Engineering Science*, *12*(2), 149–164.
80. Kavvadas, M. J. (2007). *Soil Mechanics - course textbook*. National Technical University of Athens.
81. Konagai, K., Rangelow, P. (1994). Real-time observation of dynamic changes in the fabric of granular material structures through Laser-Aided Tomography. In:

Proceedings of the 10th European Conference Earthquake Engineering, Vienna, pp. 459–465

82. Konagai, K., Tamura, C., Rangelow, P., Matsushima, T. (1992). Laser-aided tomography: a tool for visualization of changes in the fabric of granular assemblage. *Structural engineering/earthquake engineering, 9*(3), 193–201
83. Konishi, J., Naruse, F., 1988. A note on fabric in terms of voids. Micromechanics of granular materials. In: Satake, M., Jenkins, J.T. (Eds.), Proc. *U.S.–Japan Seminar on the Micromechanics of Granular Materials*, Elsevier, Amsterdam, Sendai-Zao, Japan, pp. 39–46.
84. Kozicki, J., & Tejchman, J. (2011). Numerical simulations of sand behaviour using DEM with two different descriptions of grain roughness. In *II International Conference on Particle-based Methods—Fundamentals and Applications. Particles*.
85. Kozicki, J., Tejchman, J., & Mühlhaus, H. (2014). Discrete simulations of a triaxial compression test for sand by DEM. *International Journal for Numerical and Analytical Methods in Geomechanics*, *38*, 1923–1952.
86. Krey, H. (1936). Erddruck, Erwiderstand "Earth Pressure Resistance and bearing of soils" W. *Ernst, Berlin*, 143-146.
87. Kuhn, M. R. (1999). Structured deformation in granular materials. *Mechanics of Materials*, *31*(August 1998), 407–429.
88. Kuo, C.-Y., Frost, J. D., & Chameau, J.-L. (1998). Image analysis determination of stereology based fabric tensors. *Geotechnique*, (4), 515–525.
89. Lade, P. V. (2005). Overview of constitutive models for soils. In J.A. Yamamuro & V.N. Kaliakin (Eds.) *Soil constitutive models: Evaluation, selection, and calibration* Paper presented at the Proceedings of the Geo-Frontier Conference (US), Austin, Texas (pp.1-34).
90. Latiere, H. J., & Mazerolle, F. (1987). The X-ray scanner. A tool for the examination of the intravoluminal crystalline state of aluminum. *Engineering Fracture Mechanics*, *27*(4), 413-463.
91. Lee, S. J., Hashash, Y. M., & Nezami, E. G. (2012). Simulation of triaxial compression tests with polyhedral discrete elements. *Computers and Geotechnics*, *43*, 92-100.
92. Li, X. S., & Dafalias, Y. F. (2000). Dilatancy for cohesionless soils. *Géotechnique*, *50*(4), 449-460.
93. Li, X. S., & Dafalias, Y. F. (2002). Constitutive modeling of inherently anisotropic sand

behavior. *Journal of Geotechnical and Geoenvironmental Engineering, ASCE,128*(10), 868-880.

94. Li, X. S., & Dafalias, Y. F. (2012). Anisotropic critical state theory: role of fabric. *Journal of Engineering Mechanics*, *138*(3), 263-275
95. Li, X. S., & Dafalias, Y. F. (2015). Dissipation consistent fabric tensor definition from DEM to continuum for granular media. *Journal of the Mechanics and Physics of Solids*, *78*, 141-153.
96. Li, X., & Li, X. S. (2009). Micro-macro quantification of the internal structure of granular materials. *Journal of engineering mechanics*, *135*(7), 641-656.
97. Li, X., & Yu, H. S. (2009). Influence of loading direction on the behavior of anisotropic granular materials. *International Journal of Engineering Science*, *47*(11), 1284-1296.
98. Li, X., & Yu, H. S. (2010). Numerical investigation of granular material behaviour under rotational shear. *Géotechnique*, *60*(5), 381-394.
99. Li, X., & Yu, H. S. (2013). On the stress-force-fabric relationship for granular materials. *International Journal of Solids and Structures*, *50*(9), 1285–1302.
100. Li, X., Yu, H. S., & Li, X. S. (2013). A virtual experiment technique on the elementary behaviour of granular materials with discrete element method. *International Journal for Numerical and Analytical Methods in Geomechanics*, *37*(1), 75-96.
101. Liao, C. (1997). Stress–strain relationship for granular materials based on the hypothesis of best fit. *Int. J. Solids Structures,* 34 (31,32), 4087–4100.
102. Love, A.E.H. (1927). A Treatise of Mathematical Theory of Elasticity. Cambridge University Press, Cambridge.
103. Manzari, M.T. & Dafalias, Y.F. (1997). A Critical State two-surface plasticity model for sands. *Geotechnique, 47*(2), 255-272.
104. Masson, S., & Martinez, J. (2001). Micromechanical analysis of the shear behavior of a granular material. *Journal of Engineering Mechanics*, *127*(10), 1007-1016.
105. Matsushima, T., Hidetaka, S., Yosuke, T., Yasuo, Y. (2003). Grain rotation versus continuum rotation during shear deformation of granular. *Soils Foundations. 43*(4), 95–106
106. Miller, A. (1953). *The skin of the earth*. London: Methuen And Co. Ltd.
107. Miura K, Miura S, Toki S. (1986). Deformation behavior of anisotropic sand under principal stress axes rotation. *Soils and Foundations, 26*(1), 36–52.

108. Mooney, M. A., Finno, R. J., & Viggiani, M. G. (1998). A unique critical state for sand? *Journal of Geotechnical and Geoenvironmental Engineering*, *124*(11), 1100-1108.

109. Muhunthan, B., & Chameau, J. L. (1997). Void fabric tensor and ultimate state surface of soils. *Journal of geotechnical and geoenvironmental engineering*, *123*(2), 173-181.

110. Muhunthan, B., Chameau, J. L., & Masad, E. (1996). Fabric effects on the yield behavior of soils. *Soils and foundations*, *36*(3), 85-97.

111. Muller-Breslau, H. (1906). *Erddruck auf Stutzmauert*. Stutgart: Alfred Kroner.

112. Nakata Y, Hyodo M, Murata H, Yasufuku N. (1998). Flow deformation of sands subjected to principal stress rotation. *Soils and Foundations, 38*(2),115–128.

113. Nemat-Nasser, S., & Okada, N. (2001). Radiographic and microscopic observation of shear bands in granular materials. *Géotechnique*, *51*(9), 753-766.

114. Ng, T. T. (2009). Discrete element method simulations of the critical state of a granular material. *International Journal of Geomechanics*, *9*(5), 209-216.

115. Ng, T., Aube, D., Altobelli, S. (1997). 3-D MRI Experiment of Granular Material. In: *Proceedings of Symposium on Mechanical Deformation and Flow of Particulate Materials*, pp. 189–198. Evanston, Illinois

116. Ng, T., Hu, C., Altobelli, S. (2006). Void Distributions in Samples of a Granular Material. In: *Proceedings of GeoShanghai, Site and Geomaterial Characterization*, pp. 104–111. Shanghai

117. Oda, M. & Konishi, J. (1974). Microscopic deformation mechanism of granular material in simple shear. *Soils Foundation*, *14*(4), 25–38.

118. Oda, M. (1972a). Initial fabrics and their relations to mechanical properties of granular material. *Soils and foundations*, *12*(1), 17-36.

119. Oda, M. (1972b). The mechanism of fabric changes during compressional deformation of sand. *Soils and Foundations*, *12*(2), 18.

120. Oda, M. (1972c). Deformation mechanism of sand in triaxial compression tests. *Soils and Foundations*, *12*(4), 45-63.

121. Oda, M. (1982). Fabric tensor for discontinuous geological materials. *Soils and Foundations, Japanese Society of Soil Mechanics and Foundation Engineering*, *22*(4), 96–108.

122. Oda, M., & Iwashita, K. (1990). *Mechanics of Granular Materials*. Rotterdam: Balkema Publishers.

123. Oda, M., & Nakayama, H.: Yield function for soil with anisotropic fabric. Journal of Engineering Mechanics, 115(1), 89-104. (1989).

124. Oda, M., Nemat-Nasser, S., & Konishi, J. (1985). Stress-induced anisotropy in granular masses. *Soils and Foundations*, *25*(3), 85–97.

125. Papadimitriou, A.G., Dafalias, Y.F., & Li, X.S. (2015). Sand model within anisotropic critical state theory with evolving fabric. In M. K. Kenichi Soga, Krishna Kumar, Giovanna Biscontin (Ed.), *International Symposium on Geomechanics from Micro to Macro* (pp. 627–632). CRC press Taylor and Francis group, London.

126. Pietruszczak, S., & Krucinski, S. (1998). Description of anisotropic response of clays using a tensorial measure of structural disorder. *Mechanics of Materials*, *8*(2–3), 237–249.

127. Poulos, S. J. (1981). The steady state of deformation. *Journal of Geotechnical and Geoenvironmental Engineering*, *107*(ASCE 16241 Proceeding).

128. Radjai Farhang, Dubois Frédéric (2011) *Discrete-element modeling of granular materials.* Wiley-Iste.

129. Radjai, F., & Azéma, E. (2009). Shear strength of granular materials. *European Journal of Environmental and Civil Engineering*, *13*(2), 203–218.

130. Raynaud, S., Fabre, D., Mazerolle, F., Geraud, Y., & Latière, H. J. (1989). Analysis of the internal structure of rocks and characterization of mechanical deformation by a non-destructive method: X-ray tomodensitometry. *Tectonophysics*, *159*(1), 149-159.

131. Reynolds, O. (1885). On the dilatancy of media composed of rigid particles in contact. *Philosophical Magazine Series, 20*(127), 469–481.

132. Reynolds, O. (1886) Experiments showing dilatancy, a property of granular material, possibly connected with gravitation, *Proc. Royal Institution of Great Britain*.

133. Riemer, M. F., & Seed, R. B. (1997). Factors affecting apparent position of steady-state line. *Journal of Geotechnical and Geoenvironmental Engineering*, *123*(3), 281-288.

134. Roscoe, K. H., Schofield, A., & Wroth, C. P. (1958). On the yielding of soils. *Géotechnique*, *8*(1), 22-53.

135. Roscoe, K., & Burland, J. B. (1968). On the generalized stress-strain behaviour of wet clay, U.K.

136. Rothenburg, L., & Kruyt, N. P. (2004). Critical state and evolution of coordination number in simulated granular materials. *International Journal of Solids and Structures*, *41*(21), 5763–5774

137. Rothenburg, L., Selvadurai, A.P.S. (1981). A micromechanical definition of the Cauchy stress tensor for particulate media. Paper presented in Selvadurai, A.P.S. (Ed.), *Proceedings of the International Symposium on Mechanical Behaviour of Structured Media*, Ottawa, Canada, pp. 469–486.

138. Salgado, R., Bandini, P., & Karim, A. (2000). Shear strength and stiffness of silty sand. *Journal of Geotechnical and Geoenvironmental Engineering*, *126*(5), 451-462.

139. Santamarina, J. C., & Cho, G. C. (2001). Determination of critical state parameters in sandy soils—simple procedure, *Geotechnical Testing Journal, GTJODJ, 24*(2), 185–192.

140. Satake, M. (1978). *Constitution of mechanism of granular materials through graph representation.* Theoretical and Applied Mechanics. 26, University of Tokyo Press, pp. 257-266.

141. Satake, M. (1982). Fabric tensor in granular materials. In L. H. (eds) (Ed.), *IUTAM Symposium on Deformation and Failure of Granular Materials* (pp. 63–68). Delft: Amsterdam: Vermeer PA.

142. Satake, M. (1983), Fundamentals quantities in the graph approach to granular materials, J.T. Jenkins and M. Satake (eds.) in: *Mechanics of Granular Materials: New Models and Constitutive Equations*, Amsterdam: Elsevier.

143. Schofield, A. N., & Wroth, C. P. (1968). *Critical State Soil Mechanics*. London: McGraw-Hill.

144. Scott, R. F. (1985). Plasticity and constitutive relations in soil mechanics. *Journal of Geotechnical Engineering*, *111*(5), 559-605.

145. Seed RB, Cetin KO, Moss RES, Kammerer A, Wu J, Pestana J, Riemer M, Sancio RB, Bray JD, Kayen RE, Faris A (2003) Recent advances in soil liquefaction engineering: A unified and consistent framework. *26th Annual Los Angeles Geotechnical Spring Seminar of ASCE Geo-Institute*, Long Beach, CA

146. Sitharam, T. G., & Vinod, J. S. (2008). Critical state behaviour of granular materials from isotropic and rebounded paths: DEM simulations. *Granular Matter*, *11*(1), 33–42. Zhu, H., Nguyen, H. N. G., Nicot, F., & Darve, F. (2016). On a common critical state in localized and diffuse failure modes. *Journal of the Mechanics and Physics of Solids*, *95*(May), 112–131

147. Sitharam, T. G., & Vinod, J. S. (2009). Critical state behaviour of granular materials from isotropic and rebounded paths: DEM simulations. *Granular matter*, *11*(1), 33-42.

148. Symes MJ, Gens A, Hight DW. (1984). Undrained anisotropy and principal stress rotation in saturated sand. *Géotechnique, 34*(1), 11–27.

149. Symes MJ, Gens A, Hight DW. (1988). Drained principal stress rotation in saturated sand. *Géotechnique, 38*(1), 59–81. 5.

150. Szarf, K., Combe, G., & Villard, P. (2011). Polygons vs. clumps of disks: a numerical study of the influence of grain shape on the mechanical behavior of granular materials. *Powder Technology,* Special Issue: Papers presented to the Symposium STPMF 2009, Science and Technology of Powders and Sintered Materials, 279–288.

151. Taiebat, M., & Dafalias, Y. F. (2008). SANISAND: simple anisotropic sand plasticity model. *International Journal for Numerical and Analytical Methods in Geomechanics*, *32*(8), 915-948.

152. Tatsuoka, F., Ochi K., Fujii, S., & Okamoto, M. (1986). Cyclic undrained triaxial and torsional shear strength of sands for different sample preparation methods. *Soils and Foundations*, *26*(3), 23-41.

153. Taylor, H. F., O'Sullivan, C., & Sim, W. W. (2015). A new method to identify void constrictions in micro-CT images of sand. *Computers and Geotechnics*, *69*, 279–290.

154. Terzaghi, K. (1925). *Erdbaumechanik auf bodenphysikalischer Grundlage*.

155. Theocharis A., Vairaktaris E., Fu P., & Dafalias Y.F. (2015). Comparison of fabric tensors for granular materials. fabric. In M. K. Kenichi Soga, Krishna Kumar, Giovanna Biscontin (Ed.), *International Symposium on Geomechanics from Micro to Macro* (pp. 153–158). CRC press Taylor and Francis group, London.

156. Theocharis, A. I., Vairaktaris, E., Dafalias, Y. F., & Papadimitriou, A. G. (2017a). Proof of Incompleteness of Critical State Theory in Granular Mechanics and Its Remedy. *Journal of Engineering Mechanics*, 04016117.

157. Theocharis, A. I., Vairaktaris, E., Dafalias, Y. F. (2017b). Scan line void fabric anisotropy tensors of granular media, *Granular Matter*, under review.

158. Thorton, C. (2000). Numerical simulations of deviatoric shear deformation of granular media. *Géotechnique*, *50*(1), 43–53.

159. Tong, Z. X., Zhang, J. M., Yu, Y. L., & Zhang, G. (2010). Drained deformation behavior of anisotropic sands during cyclic rotation of principal stress axes. *Journal of Geotechnical and Geoenvironmental Engineering*, *136*(11), 1509-1518

160. Tong, Z., Fu, P., Dafalias, Y. F., & Yao, Y. (2014a). Discrete element method analysis of non-coaxial flow under rotational shear. *International Journal for Numerical and*

Analytical Methods in Geomechanics, *38*(14), 1519-1540.

161. Tong, Z., Fu, P., Zhou, S., & Dafalias, Y. F. (2014b). Experimental investigation of shear strength of sands with inherent fabric anisotropy. *Acta Geotechnica*, *9*(2), 257–275.
162. Vaid, Y. P., Chung, E. K. F., & Kuerbis, R. H. (1990). Stress path and steady state. *Canadian Geotechnical Journal*, *27*(1), 1-7.
163. Vaid, Y. P., Sayao, A., Hou, E., & Negussey, D. (1990). Generalized stress-path-dependent soil behaviour with a new hollow cylinder torsional apparatus. *Canadian Geotechnical Journal*, *27*(5), 601-616.
164. Vardoulakis, I. (1980). Shear band inclination and shear modulus of sand in biaxial tests. *International Journal for Numerical and Analytical Methods in Geomechanics*, *4*(2), 103-119.
165. Verdugo, R., & Ishihara, K. (1996). The steady state of sandy soils. *Soils and foundations*, *36*(2), 81-91.
166. Vermeer, P. A. (1978). A double hardening model for sand. *Géotechnique*, *28*(4), 413-433.
167. Vesic, A. S., & Clough, G. W. (1968). Behavior of granular materials under high stresses. *Journal of Soil Mechanics & Foundations Div*.
168. Viggiani, G., Andò, E., Jaquet, C., & Talbot, H. (2013). Identifying and following particle-to-particle contacts in real granular media: An experimental challenge. In A. Yu, K. Dong, R. Yang, & S. Luding (Eds.), *AIP Conference Proceedings* (Vol. 1542, No. 1, pp. 60-65). AIP.
169. Wan, R. G., Pinheiro, M., & Guo, P. J. (2011). Elastoplastic modelling of diffuse instability response of geomaterials. *International Journal for Numerical and Analytical Methods in Geomechanics*, *35*(2), 140-160.
170. Wang, Z. L., Dafalias, Y. F., & Shen, C. K. (1990). Bounding surface hypoplasticity model for sand. *Journal of engineering mechanics*, *116*(5), 983-1001.
171. Wang, R., Fu, P., Zhang J.-M., Dafalias, Y.F. (2017). Evolution of various fabric tensors for granular media towards the critical state", *Journal of Engineering Mechanics*, in press.
172. Watkins, J. C., & Fukushima, E. (1988). High-pass bird-cage coil for nuclear-magnetic resonance. *Review of scientific instruments*, *59*(6), 926-929.
173. Weber, J. (1966). Recherches concernant les contraintes intergranulaires dans les milieux pulvérulents. *Bulletin de Liaison des Ponts-et-chaussées*, *20*, 1-20.

174. Wheeler, S. J., & Sivakumar, V. (1995). An elasto-plastic critical state framework for unsaturated soil. *Géotechnique*, *45*(1), 35-53.

175. Wijewickreme D & Vaid YP. (1993). Behavior of loose sand under simultaneous increase in stress ratio and principal stress rotation. *Canadian Geotechnical Journal 30*, 953–964.

176. Wood, D. M. (1991). *Soil behaviour and critical state soil mechanics*. Cambridge: Cambridge university press.

177. Wood, D. M. (2004). *Geotechnical modelling* (Vol. 1). CRC Press.

178. Wroth, C. P. (1958). Soil behaviour during shear–existence of critical void ratios. *Engineering*, *186*, 409-413.

179. Yan, W. M., & Dong, J. (2011). Effect of particle grading on the response of an idealized granular assemblage. *International Journal of Geomechanics*, *11*(4), 276-285.

180. Yang ZX, Li XS, Yang J. (2007). Undrained anisotropy and rotational shear in granular soil. *Géotechnique, 57*(4), 371–384

181. Yang, D. S., X. Li, and H. S. Yu. (2015). Fabric evolution of 3D granular materials in rotational shear. In M. K. Kenichi Soga, Krishna Kumar, Giovanna Biscontin (Ed.), *International Symposium on Geomechanics from Micro to Macro* (pp. 85–90). CRC press Taylor and Francis group, London.

182. Yang, J., & Luo, X. D. (2015). Exploring the relationship between critical state and particle shape for granular materials. *Journal of the Mechanics and Physics of Solids*, *84*, 196–213

183. Yang, Z. X., & Wu, Y. (2016). Critical State for Anisotropic Granular Materials: A Discrete Element Perspective. *International Journal of Geomechanics*, (May).

184. Yimsiri, S. & Soga, K. (2010). DEM analysis of soil fabric effects on behaviour of sand. *Géotechnique*, *60*(6), 483–495.

185. Yimsiri, S., & Soga, K. (2011). Effects of soil fabric on behaviors of granular soils: Microscopic modeling. *Computers and Geotechnics*, *38*(7), 861-874.

186. Yoshimine, M., & Ishihara, K. (1998). Flow potential of sand during liquefaction. *Soils and Foundations*, *38*(3), 189-198.

187. Yoshimine, M., Ishihara, K., & Vargas, W. (1998). Effects of principal stress direction and intermediate principal stress on undrained shear behavior of sand. *Soils and Foundations*, *38*(3), 179-188.

188. Zhao, J., & Guo, N. (2013). Unique critical state characteristics in granular media considering fabric anisotropy. *Géotechnique*, *63*(8), 695.

189. Zhao, J., Li, X. S., & Dafalias, Y. F. (2014). A critical state sand plasticity model accounting for fabric evolution. *International journal for numerical and analytical methods in geomechanics*, *38*(4), 370-390.

190. Zhu, H., Nguyen, H. N. G., Nicot, F., & Darve, F. (2016). On a common critical state in localized and diffuse failure modes. *Journal of the Mechanics and Physics of Solids*, *95*(May), 112–131.

Appendix

Scan line void fabric tensor definitions and their shortcomings

1. Scan line void fabric tensor in existing literature

The following definitions and notations are introduced, where the notations may differ from those of the original contributions we refer to, in order to unify the presentation: l_i^θ is the length of an i_{th} void scan line segment along angle θ; N^θ is the total number of scan line segments at an angle θ; $L_\theta = \sum_{i=1}^{N^\theta} l_i^\theta$ is the sum of all void scan line segments l_i^θ along θ; $l^\theta = L^\theta / N^\theta$ is the mean length of scan line segments for each angle θ; $L = \sum_{\theta=-90^0}^{\theta=90^0} l^\theta$ is the sum of all mean lengths l^θ over all θ, where the summation is executed in predefined intervals of θ within the angular domain $[-90^0, 90^0]$; and N^v denotes the total number of voids. A summation over θ, in the limit of very small intervals of θ, is equivalent to integration over θ in the chosen angular domain since the original scan line void definitions in Oda et al. (1985) were given in terms of integrals. Therefore, an appropriately dense set of intervals of θ should be chosen when summation is executed, in order to approach the result of integration. Different angular domains than the chosen $[-90^0, 90^0]$ may be considered, as long as they cover all directions θ within a sample, such as $[0^0, 180^0]$ or $[0^0, 360^0]$, with no loss of the essence of final conclusion in this work.

Void fabric is quantified using a corresponding scan line void fabric tensor based on all void segments in all directions; the original definition of this void fabric tensor was proposed by Oda et al (1985) for 2D and reads:

$$\mathbf{V}^{Oda} = 4\left(\frac{1}{L}\sum_{\theta=-90^0}^{\theta=90^0} l^\theta \mathbf{n}^\theta \otimes \mathbf{n}^\theta - \frac{1}{4}\mathbf{I}\right) \qquad (1)$$

where $\mathbf{n}^\theta$ is the unit vector along all scan line void vectors inclined at a specific angle θ, $\mathbf{I}$ is the identity tensor and $\mathbf{n}^\theta \otimes \mathbf{n}^\theta$ represents the tensor product of $\mathbf{n}^\theta$ by itself. Same

Eq. (1) with ½ substituting for ¼ in front of the identity tensor was used in Kuo et al. (1998).

Ghedia and O'Sullivan (2012) modified the first part in parentheses of Eq. (1) to define a scan line void fabric tensor by:

$$\mathbf{V} = \frac{1}{L} \sum_{\theta=-90^0}^{\theta=90^0} \bar{l}^{\theta} \mathbf{n}^{\theta} \otimes \mathbf{n}^{\theta} \qquad (2)$$

Where $\bar{l}^{\theta} = L^{\theta} / N^{v}$ is the mean total length of voids along θ per void and acts as the weighting factor for the tensors $\mathbf{n}^{\theta} \otimes \mathbf{n}^{\theta}$ (contrast this to $l^{\theta} = L^{\theta} / N^{\theta}$ entering Eq. (1)). Notice than unlike usual definitions, the L does not equal the sum of the weighting factors $\bar{l}^{\theta}$ in Eq. (2).

We will adopt only the first part in parentheses of Eq. (1), as is, for scan line void fabric tensor definition, which is very similar and compatible to existing definitions for other types of solid phase fabric tensors, as well as for a more recent but different void phase fabric tensor definition by Fu and Dafalias (2015), and reads:

$$\mathbf{G}_{v} = \frac{1}{L} \sum_{\theta=-90^0}^{\theta=90^0} l^{\theta} \mathbf{n}^{\theta} \otimes \mathbf{n}^{\theta} \qquad (3)$$

Hence, the mean length of the scan lines l^{θ} for each angle θ, provides the weight of the tensors $\mathbf{n}^{\theta} \otimes \mathbf{n}^{\theta}$ and its orientation distribution characterizes the anisotropy. In case l^{θ} is equal for all θ, it will be eliminated from numerator and denominator of Eq. (3), emerging from the fact that L is a summation over all l^{θ}, and by using integration over θ to express accurately the ensuing summation of $\mathbf{n}^{\theta} \otimes \mathbf{n}^{\theta}$, one obtains from Eq. (3) the half identity tensor $(1/2)\mathbf{I}$ corresponding to perfectly isotropic fabric.

2. Analytical proof of shortcomings of existing scan line void fabric tensors

The definitions of Eqs. (1) and (3), based on weights related to lengths of void vectors (or void segments), gives rise to an important implication that leads to an inherent shortcoming regarding the accurate quantification of void fabric anisotropy; an even greater shortcoming applies to the definition by Eq. (2). These shortcomings will be proved in the sequel by analytical means; 2D conditions are assumed, but the conclusion applies as well to 3D.

When the assumed fixed distance d between pairs of parallel scan lines multiplies a scan line segment l_i^θ, it yields the differential area element $\delta A_{vi} = l_i^\theta d$ of the total void surface area A_v in 2D. Based on the previous definitions, it follows by summation over all i's for a given θ, and in the limit case as $d \to 0$ and $N^\theta \to \infty$, that:

$$A_v = \sum_{i=1}^{N^\theta} \delta A_{vi} = \sum_{i=1}^{N^\theta} l_i^\theta d = L^\theta d = N^\theta l^\theta d = \text{constant} \tag{4}$$

With $l^\theta d = A_v / N^\theta$ from Eq. (4), it follows that $Ld = \sum_{\theta=-90^0}^{\theta=90^0} l^\theta d = A_v \sum_{\theta=-90^0}^{\theta=90^0} (1/N_\theta)$. Thus, multiplication of numerator and denominator of Eq. (3) by d and use of the foregoing expressions for $l^\theta d$ and Ld, eliminates the common factor A_v yielding the expression:

$$\mathbf{G}_v = \frac{1}{\sum_{\theta=-90^0}^{\theta=90^0} \left(\frac{1}{N^\theta}\right)} \sum_{\theta=-90^0}^{\theta=90^0} \left(\frac{1}{N^\theta}\right) \mathbf{n}^\theta \otimes \mathbf{n}^\theta \tag{5}$$

Surprisingly any notion of void length disappears from the form of Eq. (5), despite the fact the void fabric tensor was defined in Eqs. (1) and (3) on the basis of void length segments. Instead, the weighting factors of the tensors $\mathbf{n}^\theta \otimes \mathbf{n}^\theta$ are limited to the inverse $1/N_\theta$ of the total number of the void scan line segments for each angle θ, and do not depend on the lengths of the void segments or the mean void length. However, there is an indirect and subtle connection between void length segments and N^θ, because the latter implies a certain orientation arrangement of the long and short axes of voids. This happens for example simply because one needs a greater number N^θ to cover the same surface void area A_v if scan lines at a fixed distance d cross the voids along their short axes than along their long axes. The appearance of $1/N_\theta$ constitutes a serious shortcoming concerning the quantification of fabric anisotropy (Theocharis et al., 2017b). In regard to the definition of Eq. (2) an even more serious shortcoming appears. Recalling that $\bar{l}^\theta = L^\theta / N^v$ (N^v is the total number of voids), $l^\theta = L^\theta / N^\theta$ and $l^\theta d = A_v / N^\theta$, it follows that $\bar{l}^\theta d = (N^\theta / N^v) l^\theta d = A^v / N_v$. In the following derivation, the distance d is assumed to be small enough so that the number of voids crossed during scanning in any orientation θ is the same and equal to the total number of voids N^v. Multiplication now of numerator and denominator of Eq. (2) by d and use of the foregoing expression for

$l^{\theta}d$ and the previous expression $Ld = A_v \sum_{\theta=-90^0}^{\theta=90^0} (1/N_{\theta})$, eliminates the common factor A_v and yields the expression $\mathbf{V} \approx \left(N^{v} \sum_{\theta=-90^0}^{\theta=90^0} \frac{1}{N^{\theta}} \right)^{-1} \frac{1}{2}\mathbf{I}$, where the half identity tensor $(1/2)\mathbf{I}$ appeared by integration over θ as shown after Eq. (3) for the case of same l^{θ} for all θ; the symbol ≈ is used instead of = to simply express the approximation of the summation over θ to the implied accurate integration. The result implies that $\mathbf{V}$ is always an isotropic tensor, a serious drawback of Eq. (2) that is intended to measure anisotropy.

The exact same conclusion and shortcoming of the foregoing definition of void fabric tensor can be reached for a three-dimensional sample. In this case, the scan lines are positioned at equal distance among themselves in three dimensions, which implies that each line can be considered as the axis of a rectangular prism with area a normal to the scan line. If the length of all scan lines in a given angle θ is multiplied by the area a and the limit is taken as the number of scan lines tends to infinity while a tends to zero, the result of the product is the void volume V_v of the sample in lieu of the void surface area A_v in two dimensions, which is of course the same for every orientation θ. In analytical terms it implies an equation equivalent to Eq. (4) in 3D, where V_v substitutes for A_v and a for d, while the summation will take place over a spherical stereo-angular domain in 3D instead of a planar angular domain in 2D. Thus, what follows afterwards is the same as in two dimensions and the corresponding equation to Eq. (5) will be identical in form with aforementioned differences for 3D, as compared to 2D.